

Methanol Barrier Layers: Modified Membrane Electrode Assemblies for the Improvement of Direct Methanol Fuel Cell Performance

A thesis submitted to the University of Manchester for the degree of

Doctor of Philosophy

in the Faculty of Engineering and Physical Sciences

2015

Chatkaew Chailuecha

School of Chemical Engineering and Analytical Science

Contents

| | |
|---|-----------|
| Figures | 10 |
| Tables | 16 |
| Abstract | 19 |
| Declaration of authorship | 20 |
| Copyright statement | 21 |
| Acknowledgements | 22 |
| Symbols | 25 |
| Abbreviations | 28 |
| 1 Introduction and objectives | 30 |
| 1.1 Introduction | 30 |
| 1.2 Motivation | 33 |
| 1.2.1 Green electricity | 34 |
| 1.2.2 Fuel cell for green electricity | 35 |
| 1.2.2.1 Portable applications | 35 |
| 1.2.2.2 Stationary applications | 36 |
| 1.2.2.3 Transportation applications | 37 |
| 1.2.3 Fuel cell cost | 38 |

| | | |
|----------|--|-----------|
| 1.3 | Objective | 38 |
| 1.4 | Outline of thesis | 40 |
| 2 | Fuel cell | 41 |
| 2.1 | History of fuel cell | 41 |
| 2.2 | Principle of fuel cell | 43 |
| 2.3 | Different Types of Fuel Cell | 43 |
| 2.3.1 | Proton Exchange Membrane Fuel Cell (PEMFC) | 47 |
| 2.3.1.1 | Principles of Operation | 47 |
| 2.3.1.2 | Fuel Cell Voltages | 47 |
| 2.3.2 | Solid oxide fuel cell (SOFC) | 49 |
| 2.3.3 | Molten carbonate fuel cell (MCFC) | 51 |
| 2.3.4 | Phosphoric acid fuel cell (PAFC) | 51 |
| 2.3.5 | Alkaline fuel cell (AFC) | 52 |
| 2.4 | Direct methanol fuel cell (DMFC) | 56 |
| 2.4.1 | Electrochemical reaction | 56 |
| 2.4.2 | Thermodynamics | 58 |
| 2.4.2.1 | Gibbs free energy | 58 |
| 2.4.2.2 | Reversible potential | 59 |
| 2.4.2.3 | Open circuit voltage | 60 |
| 2.4.2.4 | Maximum efficiency | 61 |
| 2.4.3 | Performance | 64 |
| 2.4.3.1 | Part I: Activation loss | 64 |
| 2.4.3.2 | Part II: Ohmic loss | 66 |
| 2.4.3.3 | Part III: Mass transport loss | 66 |
| 2.4.3.4 | Methanol crossover | 68 |
| 2.5 | Components of a direct methanol fuel cell (DMFC) | 69 |
| 2.5.1 | Membrane electrode assembly (MEA) | 69 |
| 2.5.1.1 | Gas diffusion layer | 70 |

| | | |
|----------|--|-----------|
| 2.5.1.2 | Catalyst layer | 71 |
| 2.5.1.3 | Electrolyte membrane | 75 |
| 2.5.1.4 | Proton hopping or the Grotthuss mechanism . . . | 76 |
| 2.5.1.5 | Diffusion or vehicular mechanism | 76 |
| 3 | Development of the direct methanol fuel cell (DMFC) | 78 |
| 3.1 | Development of direct methanol fuel cell to reduce activation loss | 79 |
| 3.1.1 | Improvements in anodic catalyst materials | 80 |
| 3.1.2 | Improvements in cathodic catalyst materials | 81 |
| 3.1.3 | Improvements in catalyst support materials | 82 |
| 3.2 | Development of direct methanol fuel cell to reduce ohmic loss . . | 83 |
| 3.2.1 | Ohmic loss in Nafion electrolyte membrane | 83 |
| 3.3 | Development of direct methanol fuel cells to reduce mass transfer loss | 84 |
| 3.3.1 | Mass transport through the membrane | 84 |
| 3.3.2 | Mass transport at the electrodes | 85 |
| 3.3.2.1 | Improvements in electrode morphology | 85 |
| 3.3.2.2 | Improvements in the reactant flow field | 86 |
| 3.4 | Development of direct methanol fuel cell to reduce methanol cross- over | 88 |
| 3.4.1 | Methanol crossover in Nafion membrane | 88 |
| 3.4.1.1 | Water uptake | 90 |
| 3.4.1.2 | Electro-osmotic coefficient of the membrane . . . | 90 |
| 3.4.1.3 | Membrane selectivity | 91 |
| 3.4.2 | Improvements in polymer electrolyte membranes | 91 |
| 3.4.2.1 | Conventional Nafion composite membranes . . . | 92 |
| 3.4.2.2 | Alternative membranes | 108 |
| 3.4.2.3 | Multilayered membranes | 111 |
| 3.4.3 | Incorporating methanol barrier layers into MEAs | 112 |

| | | |
|----------|--|------------|
| 3.4.3.1 | Introduction to methanol barrier layer | 112 |
| 4 | Fabrication of membrane electrode assembly (MEA) and exper- | |
| | imental system | 115 |
| 4.1 | Standard membrane electrode assembly fabrication | 115 |
| 4.1.1 | Gas diffusion layer (GDL) | 118 |
| 4.1.1.1 | Carbon ink preparation | 118 |
| 4.1.1.2 | Spraying the gas diffusion layer | 119 |
| 4.1.2 | Catalyst layer (procedure I) | 121 |
| 4.1.2.1 | Anode catalyst ink preparation | 121 |
| 4.1.2.2 | Cathode catalyst ink preparation | 122 |
| 4.1.2.3 | Spraying the catalyst layer | 124 |
| 4.1.3 | Binding layer | 124 |
| 4.1.3.1 | Spraying the binding layer | 124 |
| 4.1.4 | Membrane treatment | 125 |
| 4.1.5 | Hot pressing | 127 |
| 4.2 | DMFC experimental system | 127 |
| 4.2.1 | DMFC operation | 129 |
| 4.2.2 | DMFC assembly | 130 |
| 4.3 | Fabrication of modified MEAs (procedure I) | 131 |
| 4.3.1 | Modified MEA using methanol barrier layer | 131 |
| 4.3.2 | Methanol barrier layer preparation | 132 |
| 4.3.2.1 | Inorganic suspension | 133 |
| 4.3.2.2 | Nafion/inorganic composite | 133 |
| 4.3.3 | Incorporating the methanol barrier layer onto the anode . | 135 |
| 4.4 | Fabrication of new modified membrane electrode assemblies (pro- | |
| | cedure II) | 136 |
| 4.4.1 | New standard MEA fabrication | 136 |
| 4.4.1.1 | New anode catalyst ink preparation | 136 |

| | | |
|----------|---|------------|
| 4.4.1.2 | New cathode catalyst ink preparation | 137 |
| 4.4.2 | New modified MEAs | 138 |
| 5 | Results and discussion I: Performance of standard and modified membrane electrode assemblies | 140 |
| 5.1 | Standard membrane electrode assembly operation | 140 |
| 5.1.1 | Influence of cell temperature on performance of STD1 using 1 M methanol solution | 141 |
| 5.1.2 | Influence of methanol concentration on performance of STD1 using 2 M and 4 M methanol solution | 143 |
| 5.1.3 | Influence of methanol and oxygen flow rate on STD1 per- formance using 1M methanol solution | 147 |
| 5.1.4 | Influence of catalyst loading | 150 |
| 5.1.5 | Summary of optimum conditions for MEA operation . . . | 152 |
| 5.2 | Modified MEAs Operations | 153 |
| 5.2.1 | Preparation of titanate | 154 |
| 5.2.2 | The Comparison Performance of the STD1 and the modi- fied MEAs with 1 M Methanol | 157 |
| 5.2.3 | The Comparison Performance of the STD1 and the modi- fied MEAs with 2 M Methanol | 158 |
| 5.2.4 | The Comparison Performance of the STD1 and the modi- fied MEAs with 4 M Methanol | 160 |
| 5.2.5 | Contact Angle Measurement | 161 |
| 5.2.6 | Summary | 163 |
| 6 | Results and discussion II: Performances of new standard and new modified MEAs | 165 |
| 6.1 | New standard MEA operation | 165 |
| 6.1.1 | Influence of methanol concentration on the performance of STD3 using 1M, 2M and 4M methanol solution | 167 |

| | | |
|----------|---|------------|
| 6.1.2 | The consistency of MEA fabricating by procedure II | 169 |
| 6.1.3 | The performance of new-standard MEA (STD3) in comparison with conventional-standard MEA (STD1) | 171 |
| 6.1.4 | Effect of the different catalyst preparation over the different catalyst manufacturing | 180 |
| 6.2 | New modified MEAs operations | 181 |
| 6.2.1 | Performance of new modified MEAs containing Nafion/-montmorillonite barrier layer at 1 M methanol concentration | 182 |
| 6.2.1.1 | Open circuit voltage | 182 |
| 6.2.1.2 | Power density | 183 |
| 6.2.1.3 | Limiting current density | 185 |
| 6.2.2 | Performance of new modified MEAs containing Nafion/-montmorillonite barrier layer at 2 M methanol concentration | 186 |
| 6.2.2.1 | Open circuit voltage | 186 |
| 6.2.2.2 | Power density | 187 |
| 6.2.2.3 | Limiting current density | 188 |
| 6.2.3 | Performance of new modified MEAs containing Nafion/-montmorillonite barrier layer at 4 M methanol concentration | 189 |
| 6.2.3.1 | Open circuit voltage | 189 |
| 6.2.3.2 | Power density | 190 |
| 6.2.3.3 | Limiting current density | 192 |
| 6.3 | Summary | 192 |
| 7 | Conclusions and suggestions for future work | 195 |
| 7.1 | Conclusions | 195 |
| 7.1.1 | Methanol barrier layer for the improvement of DMFC performance | 196 |
| 7.1.1.1 | Tortuosity factor | 198 |
| 7.1.1.2 | Organophobic character | 200 |

| | | |
|----------|---|------------|
| 7.1.2 | Modification of the catalyst morphology for the improvement of DMFC performance | 201 |
| 7.1.2.1 | Procedure for the membrane electrode assembly preparation | 201 |
| 7.1.2.2 | Optimum Inorganic loading in the methanol barrier layer | 201 |
| 7.2 | Future Work | 202 |
| 7.2.1 | Characterisation of proton conductivity | 204 |
| 7.2.2 | Characterisation of methanol permeability | 204 |
| A | Performances of the membrane electrode assemblies | 233 |
| A.1 | Experimental results of the standard membrane electrode assemblies | 233 |
| A.1.1 | Polarization and power density curves of the standard 2 (STD2) using 1M, 2M and 4M methanol concentration . . | 233 |
| A.1.2 | Polarization and power density curves of the the standard 3 (STD3) using 1M, 2M and 4M methanol concentration . | 237 |
| A.1.2.1 | Optimised methanol and oxygen flow rate of the the standard 3 (STD3) | 241 |
| A.1.3 | Polarization and power density curves of the standard 5 (STD5) using 1M, 2M and 4M methanol concentration . . | 241 |
| A.1.4 | Performances of standard membrane electrode assemblies . | 247 |
| A.2 | Experimental results of the modified membrane electrode assemblies | 251 |
| A.2.1 | Polarization and power density curves of the modified membrane electrode assemblies at 1 M methanol concentration | 251 |
| A.2.2 | Polarization and power density curves of the modified membrane electrode assemblies at 2 M methanol concentration | 256 |
| A.2.3 | Polarization and power density curves of the modified membrane electrode assemblies at 4 M methanol concentration | 260 |
| A.2.4 | Performances of the modified membrane electrode assemblies | 264 |

| | | |
|----------|---|------------|
| A.3 | Experimental results of the new modified membrane electrode assemblies | 267 |
| A.3.1 | Polarization and power density curves of the new modified membrane electrode assemblies at 1 M methanol concentration | 267 |
| A.3.2 | Polarization and power density curves of the new modified membrane electrode assemblies at 2 M methanol concentration | 271 |
| A.3.3 | Polarization and power density curves of the new modified membrane electrode assemblies at 4 M methanol concentration | 274 |
| A.3.4 | Performances of the new modified membrane electrode assemblies | 277 |
| B | Contact angle measurement | 280 |
| B.1 | Contact angle measurement between water droplet and the barrier layers | 280 |
| B.2 | Contact angle measurement between 1 M methanol droplet and the barrier layers | 282 |
| B.3 | Contact angle measurement between 2 M methanol droplet and the barrier layers | 283 |
| C | Presentations | 284 |

List of Figures

| | | |
|------|---|----|
| 1.1 | Global scale of greenhouse gas emissions in 2004 divided by Gas . | 31 |
| 1.2 | Global scale of greenhouse gas emissions in 2004 divided by Source | 31 |
| 1.3 | Greenhouse gases emissions of the European Union in 1990-1912 . | 33 |
| 1.4 | Share of renewable energy in global electricity production in 2011 | 35 |
| 1.5 | Schematic of a fuel cell based combined heat and power (CHP) system | 36 |
| 1.6 | Model of Fuel cell vehicle based on the Honda 2005 FCX | 37 |
| 2.1 | The first fuel cell | 42 |
| 2.2 | Nafion | 43 |
| 2.3 | Fuel cell components | 44 |
| 2.4 | The system of proton exchange membrane fuel cell (PEMFC) . . | 48 |
| 2.5 | The system of solid oxide fuel cell (SOFC) | 50 |
| 2.6 | The system of Molten carbonate fuel cell (MCFC) | 52 |
| 2.7 | The system of phosphoric acid fuel cell (PAFC) | 53 |
| 2.8 | The system of alkaline fuel cell (AFC) | 54 |
| 2.9 | The oxidation-reduction reactions and the charge transfer direction of fuel cells | 55 |
| 2.10 | Components of DMFC | 57 |
| 2.11 | Comparison of ideal fuel cell and Carnot efficiencies | 63 |
| 2.12 | Polarization curve and power density curve of fuel cell | 65 |
| 2.13 | Influence of voltage losses on the overall fuel cell j - V performance | 68 |

| | | |
|------|--|-----|
| 2.14 | Influence of methanol crossover on the overall fuel cell j - V performance | 69 |
| 2.15 | DMFC membrane electrode assembly | 70 |
| 2.16 | Reaction mechanism of methanol oxidation | 72 |
| 2.17 | Activation energy of reaction without and with catalyst | 73 |
| 2.18 | Methanol oxidation at Pt surface | 73 |
| 2.19 | CO oxidation at Pt-Ru surface | 74 |
| 2.20 | Microstructure of fuel cell catalyst | 74 |
| 2.21 | Water channel morphology of hydrated Nafion | 75 |
| 2.22 | Proton transportation in Nafion membrane | 77 |
| 3.1 | Polarization curve | 78 |
| 3.2 | Potential loss in DMFC | 79 |
| 3.3 | Different flow fields for direct methanol fuel cell | 87 |
| 3.4 | The affinity between the SiO_2 -F and the fluorocarbon backbone of Nafion | 93 |
| 3.5 | Proposed proton transport pathways in composite membrane | 95 |
| 3.6 | Crystal structure of montmorillonite | 97 |
| 3.7 | Polymeric aggregates in Nafion and Nafion/MMT membrane | 100 |
| 3.8 | Crystal structure of titanate ($\text{Na}_2\text{Ti}_3\text{O}_7$) | 102 |
| 3.9 | Cross-section of titanate nanotubes | 103 |
| 3.10 | Crystal structure of mordenite | 107 |
| 3.11 | Multilayer membrane form on Nafion | 111 |
| 3.12 | Cross-section of Nafion/5 wt% mordenite composite membrane | 113 |
| 3.13 | Cross-section of Nafion/functionalized mordenite barrier layer | 113 |
| 4.1 | Standard MEA fabrication | 116 |
| 4.2 | Standard MEA layers | 117 |
| 4.3 | Carbon ink | 119 |
| 4.4 | Sintering | 121 |

| | | |
|------|--|-----|
| 4.5 | Anode ink | 122 |
| 4.6 | Cathode ink | 123 |
| 4.7 | Binding ink | 125 |
| 4.8 | Membrane treatment | 126 |
| 4.9 | Experimental system | 128 |
| 4.10 | DMFC assembly | 130 |
| 4.11 | Standard MEA layers | 131 |
| 4.12 | Inorganic suspension | 134 |
| 4.13 | Nafion/inorganic composite | 135 |
| 4.14 | New anode ink | 137 |
| 4.15 | New cathode ink | 138 |
| 5.1 | Performance of STD1 at 1 M methanol | 142 |
| 5.2 | Performance of STD1 at 2 M methanol | 144 |
| 5.3 | Performance of STD1 at 4 M methanol | 145 |
| 5.4 | STD1 maximum power densities at different methanol concentrations | 146 |
| 5.5 | Performances of STD1 at different methanol flow rates | 148 |
| 5.6 | Performances of STD1 at different air flow rates | 149 |
| 5.7 | Comparison of maximum power densities of STD1 and STD2 | 151 |
| 5.8 | Methanol barrier layer | 153 |
| 5.9 | XRD patterns of titanate | 155 |
| 5.10 | SEM image of titanate | 155 |
| 5.11 | Comparison of maximum power densities of STD1 and modified MEAs at 1 M methanol | 158 |
| 5.12 | comparison of maximum power densities of STD1 and modified MEAs at 2 M methanol | 159 |
| 5.13 | Comparison of maximum power densities of STD1 and modified MEAs at 4 M methanol | 160 |
| 5.14 | Comparison contact angle of water, 1 M and 2 M methanol | 161 |

| | | |
|------|---|-----|
| 5.15 | Relation of contact angle and maximum power density at 1 M methanol | 162 |
| 5.16 | Relation of contact angle and maximum power density at 1 M methanol | 163 |
| 6.1 | Comparison of STD3 maximum power densities at methanol concentrations of 1-4 M | 167 |
| 6.2 | Comparison of STD3 open circuit voltages at methanol concentrations of 1-4 M | 168 |
| 6.3 | The comparison of STD3 limiting current densities at methanol concentrations of 1-4 M | 169 |
| 6.4 | Reproducibility of MEA fabricating by procedure II | 170 |
| 6.5 | Maximum power densities of STD1 and STD3 | 171 |
| 6.6 | Power density curve of STD1 and STD3 at 2 M methanol concentration and 80 °C | 173 |
| 6.7 | Polarization curve of STD1 and STD3 at 2 M methanol concentration and 80 °C | 174 |
| 6.8 | The OCV of STD1 and STD3 | 175 |
| 6.9 | Limiting current densities of STD1 and STD3 | 177 |
| 6.10 | Triple phase boundaries inside the catalyst layer | 179 |
| 6.11 | Open circuit voltage of STD3 compared to new modified MEAs containing MMT at 1 M methanol | 183 |
| 6.12 | Power densities of STD3 compared to new modified MEAs containing MMT at 1 M methanol | 184 |
| 6.13 | Limiting current densities of STD3 compared to new modified MEAs containing MMT at 1 M methanol | 186 |
| 6.14 | Open circuit voltage of STD3 compared to new modified MEAs containing MMT at 2 M methanol | 187 |
| 6.15 | Maximum power densities of STD3 compared to new modified MEAs containing MMT at 2 M methanol | 188 |

| | | |
|------|---|-----|
| 6.16 | Limiting current densities of STD3 compared to new modified MEAs containing MMT at 2 M methanol | 189 |
| 6.17 | Open circuit voltage of STD3 compared to new modified MEAs containing MMT at 4 M methanol | 190 |
| 6.18 | Maximum power densities of STD3 compared to new modified MEAs containing MMT at 4 M methanol | 191 |
| 6.19 | Limiting current densities of STD3 compared to new modified MEAs containing MMT at 4 M methanol | 192 |
| 7.1 | Migration of proton and methanol molecule through the composite layer | 198 |
| 7.2 | Description of tortuosity factor | 199 |
| 7.3 | Determination of contact angle at the interface between water droplet and solid surface | 200 |
| 7.4 | Nafion | 202 |
| A.1 | Performance of STD2 at 1 M methanol | 234 |
| A.2 | Performance of STD2 at 2 M methanol | 235 |
| A.3 | Performance of STD2 at 4 M methanol | 236 |
| A.4 | Performance of STD3 at 1 M methanol | 238 |
| A.5 | Performance of STD3 at 2 M methanol | 239 |
| A.6 | Performance of STD3 at 4 M methanol | 240 |
| A.7 | The Performances of STD3 at different methanol flow rates | 242 |
| A.8 | The Performances of STD1 at different air flow rates | 243 |
| A.9 | Performance of STD5 at 1 M methanol | 244 |
| A.10 | Performance of STD5 at 2 M methanol | 245 |
| A.11 | Performance of STD5 at 4 M methanol | 246 |
| A.12 | Performance of 0.50% MOR at 1 M methanol | 252 |
| A.13 | Performance of 0.50% ZY at 1 M methanol | 253 |
| A.14 | Performance of 0.50% MMT at 1 M methanol | 254 |

| | |
|--|-----|
| A.15 Performance of 0.50% TN at 1 M methanol | 255 |
| A.16 Performance of 0.50% MOR at 2 M methanol | 256 |
| A.17 Performance of 0.50% ZY at 2 M methanol | 257 |
| A.18 Performance of 0.50% MMT at 2 M methanol | 258 |
| A.19 Performance of 0.50% TN at 2 M methanol | 259 |
| A.20 Performance of 0.50% MOR at 4 M methanol | 260 |
| A.21 Performance of 0.50% ZY at 4 M methanol | 261 |
| A.22 Performance of 0.50% MMT at 4 M methanol | 262 |
| A.23 Performance of 0.50% TN at 4 M methanol | 263 |
| A.24 Performance of 0.25% MMT at 1 M methanol | 268 |
| A.25 Performance of 0.50% MMT at 1 M methanol | 269 |
| A.26 Performance of 1.00% MMT at 1 M methanol | 270 |
| A.27 Performance of 0.25% MMT at 2 M methanol | 271 |
| A.28 Performance of 0.50% MMT at 2 M methanol | 272 |
| A.29 Performance of 1.00% MMT at 2 M methanol | 273 |
| A.30 Performance of 0.25% MMT at 4 M methanol | 274 |
| A.31 Performance of 0.50% MMT at 4 M methanol | 275 |
| A.32 Performance of 1.00% MMT at 4 M methanol | 276 |
| | |
| B.1 Contact angle measurement between water droplet and the barrier layers | 281 |
| B.2 Contact angle measurement between 1 M methanol droplet and the barrier layers | 282 |
| B.3 Contact angle measurement between 2 M methanol droplet and the barrier layers | 283 |

List of Tables

| | | |
|-----|---|-----|
| 1.1 | Global Warming Potential (GWP) of greenhouse gases relative to carbon dioxide | 32 |
| 1.2 | Electricity generated from renewable energy sources | 34 |
| 1.3 | Summarised the target cost for fuel cell technology in the United States [32] | 39 |
| 2.1 | Classification of fuel cells | 45 |
| 2.2 | Classification of fuel cells | 46 |
| 3.1 | Characteristics of Nafion membranes | 88 |
| 3.2 | Methanol permeability and proton conductivity of Nafion membranes | 89 |
| 3.3 | DMFC power density of Nafion/silica composite membranes . . . | 96 |
| 3.4 | DMFC power density of Nafion/montmorillonite composite membranes | 101 |
| 3.5 | DMFC power density of Nafion/titanate composite membranes . . | 106 |
| 3.6 | DMFC power density of SPSF/filler composite membranes | 110 |
| 4.1 | Composition of carbon ink for producing two GDLs | 119 |
| 4.2 | Composition of anode catalyst ink for producing two electrodes . | 122 |
| 4.3 | Composition of cathode catalyst ink for producing two electrodes | 123 |
| 4.4 | Composition of binding ink for producing two electrodes | 125 |
| 4.5 | Modified MEAs | 132 |
| 4.6 | Composition of inorganic suspension | 133 |

| | | |
|------|---|-----|
| 4.7 | Composition of Nafion/inorganic composite | 134 |
| 4.8 | Composition of new anode catalyst ink for producing one electrode | 137 |
| 4.9 | Compositions of new cathode catalyst ink for producing one electrode | 138 |
| 4.10 | New modified MEAs | 139 |
| 5.1 | Parameters of DMFC operation for STD1 | 141 |
| 5.2 | Parameters of DMFC operation for STD2 | 150 |
| 5.3 | Modified MEAs | 157 |
| 5.4 | The best improvement in maximum power densities of the modified MEAs relative to STD1 | 163 |
| 5.5 | Contact angles measured from the barrier layers featuring with 0.5% ZY and 0.5% MMT at 2M methanol | 164 |
| 6.1 | The parameters of STD3 operation | 166 |
| 6.2 | The parameters of STD1, STD3 and STD5 fabrication | 180 |
| 6.3 | the new modified MEAs containing Nafion/inorganic barrier layer (a) is wt% inorganic relative to Nafion 117 membrane (b) is wt% inorganic relative to total weight of the barrier layer . | 181 |
| 6.4 | Improvement in maximum power density of 0.25% MMT relative to STD3 | 184 |
| 6.5 | Reduction in maximum power density of 0.50% MMT and 1.00% MMT relative to STD3 | 185 |
| 6.6 | Improvement in maximum power density of 0.25% MMT relative to STD3 | 187 |
| 6.7 | Reduction in maximum power density of 0.50% MMT and 1.00% MMT relative to STD3 | 188 |
| 6.8 | Improvement in maximum power density of 0.25% MMT relative to STD3 | 191 |
| 6.9 | Reduction in maximum power density of 0.50% MMT and 1.00% MMT relative to STD3 | 191 |

| | | |
|------|---|-----|
| 6.10 | Parameters for standard MEA fabrication | 193 |
| 7.1 | Comparison the performances of DMFCs incorporated with montmorillonite | 197 |
| 7.2 | Performances of DMFCs incorporated with graphene oxide | 203 |
| A.1 | Performances of Standard 1 (STD1) | 247 |
| A.2 | Performances of Standard 2 (STD2) | 248 |
| A.3 | Performances of Standard 3 (STD3) | 249 |
| A.4 | Performances of Standard 4 (STD4) | 250 |
| A.5 | Performances of Standard 5 (STD5) | 251 |
| A.6 | Performances of the modified membrane electrode assemblies containing 0.50% mordenite (0.50% MOR) | 264 |
| A.7 | Performances of the modified membrane electrode assemblies containing 0.50% zeolite Y (0.50% ZY) | 265 |
| A.8 | Performances of the modified membrane electrode assemblies containing 0.50% montmorillonite (0.50% MMT) | 266 |
| A.9 | Performances of the modified membrane electrode assemblies containing 0.50% titanate (0.50% TN) | 267 |
| A.10 | Performances of the modified membrane electrode assemblies containing 0.25% montmorillonite (0.25% MMT) | 277 |
| A.11 | Performances of the modified membrane electrode assemblies containing 0.50% montmorillonite (0.50% MMT) | 278 |
| A.12 | Performances of the modified membrane electrode assemblies containing 1.00% montmorillonite (1.00% MMT) | 279 |

Abstract

The direct methanol fuel cell (DMFC) performance has been improved via two approaches. The first approach reduces methanol crossover in the membrane electrode assemblies (MEAs) by incorporating a methanol barrier layer onto an anode electrode of the MEA. The second approach increases the triple phase boundaries via the modified morphology of catalyst layers in the MEA.

Methanol barrier layers containing a composite layer of Nafion/mordenite (MOR), Nafion/zeolite Y (ZY), Nafion/montmorillonite (MMT) or Nafion/titanate (TN) were distributed onto the anode of an MEA. The performance of these MEAs were tested in a single cell DMFC for temperatures between 30–80 °C and methanol concentrations of 1 M–4 M and compared with a standard MEA to identify changes in power output. At 2 M methanol concentration and 80 °C, the MEAs featuring with Nafion/0.50 wt% MMT and Nafion/0.50 wt% TN delivered higher power densities, 19.76% and 26.60%, respectively, than that of standard MEA.

The catalyst morphology has been adjusted by the dilution of catalyst ink to prevent an agglomeration of catalyst particles, resulting in the increased triple phase boundaries which are the phases for electrochemical reactions and for the transportation of electron and proton products. The new-standard MEA presented the best improvement in power density of 81.15% over the conventional counterpart at 80 °C and 2 M methanol concentration. This modified procedure was further utilised for MEAs fabrication.

Further investigation has been carried out by the selected Nafion/MMT layer. The MMT loading of 0.25 wt%–1.00 wt% were incorporated onto the barrier layer where the Nafion/0.25 wt% MMT layer illustrated the best performance. This MEA attributed the highest power density of 69.14 mW cm⁻² which is 2.76% higher than 67.23 mW cm⁻² of the new-standard MEA at 80 °C and 2 M methanol concentration. The best improvement in power density, 27.09%, was obtained at low temperature and low methanol concentration of 30 °C and 1 M. The power density was 25.30 mW cm⁻² when compare to 19.91 mW cm⁻² of the new-standard MEA.

These results suggest that the methanol barrier layer and the modified morphology of catalyst layer accomplish the aim of improving DMFC performance.

Declaration of authorship

No portion of the work referred to in this thesis has been submitted in support of an application for another degree or qualification of this or any other university, or other institute of learning.

Signed: Chatkaew Chailuecha

Date: 9 November 2015

Copyright statement

- i. The author of this thesis (including any appendices and/or schedules to this thesis) owns certain copyright or related rights in it (the “Copyright”) and s/he has given The University of Manchester certain rights to use such Copyright, including for administrative purposes.
- ii. Copies of this thesis, either in full or in extracts and whether in hard or electronic copy, may be made **only** in accordance with the Copyright, Designs and Patents Act 1988 (as amended) and regulations issued under it or, where appropriate, in accordance with licensing agreements which the University has from time to time. This page must form part of any such copies made.
- iii. The ownership of certain Copyright, patents, designs, trade marks and other intellectual property (the “Intellectual Property”) and any reproductions of copyright works in the thesis, for example graphs and tables (“Reproductions”), which may be described in this thesis, may not be owned by the author and may be owned by third parties. Such Intellectual Property and Reproductions cannot and must not be made available for use without the prior written permission of the owner(s) of the relevant Intellectual Property and/or Reproductions.
- iv. Further information on the conditions under which disclosure, publication and commercialisation of this thesis, the Copyright and any Intellectual Property and/or Reproductions described in it may take place is available in the University IP Policy (see <http://documents.manchester.ac.uk/DocuInfo.aspx?DocID=487>), in any relevant Thesis restriction declarations deposited in the University Library, The University Library’s regulations (see <http://www.manchester.ac.uk/library/aboutus/regulations>) and in The University’s policy on Presentation of Theses

Acknowledgements

I have made so many efforts to achieve my research target even though I usually have health problems over a study period. I would never be able to finish my thesis without the help from supervisor, friends and family.

I would like to express my sincere appreciation to my supervisor, Dr. Stuart Holmes, for his encouragement, guidance and support over my study period.

I gratefully acknowledge financial support by the Ministry of Science and Technology, Thai government and also thank you my work place, the University of Phayao, for giving me an opportunity to study in the PhD programme.

The staffs at the University of Manchester especially John Riley, Paul Rothwell, Patricia Turnbull, thank you for providing invaluable assistance. I do appreciate them for spending their time solving my technical problems, no matter how much they were.

My warm thanks to all my Ph.D. classmate: Craig Dawson, Nuria De Las Heras, Sutida Marthosa, Geraint Minton, Ashley Moore, David de Haro, Kwame Nkrumah-Amoako and Prabhuraj Balakrishnan who support me both in academic and lifestyle.

I would like to thank Chaiwat Prapainainar, Apichaya Theampetch and Chemical Engineering Department, Faculty of Engineering, King Mongkuts of University Technology North Bangkok (KMUTNB), Thailand for their support.

In addition, my deepest gratitude goes to my friends: Jomhadhyasnidh Bhongsatiern, Poonsuk Poosimma, Piyawadee Rohitarachoon, Tyun Sirikitputtisak, Patcharapan Siriwat, Chuleeporn Paa-rai for their precious friendship. They stayed by my side in both happy and disappointing moments. They took very good care of me every time I encountered my neurological health problems which made me contemporarily unable to move the right side of my body. At that time, they voluntarily became my right arm in every meaning.

I am thankful to all my friends: Patty and Jop, Yong and Koh, Ice and Martin, Palm and Ake, Au and Tam, Tiew and Win, Note and Bil, Bua, Yong, Aoi Jeab and Pak whom I have shared so much memories and activities.

From my heart, I wish to thank Thai students in Manchester for their kind help and cooking: Ranit, Note, Jeab, New, Tom, Moji, Fluke, Chinno, Oak and Neo.

Also I am grateful to my childhood friends: Gade, Jupp, and Oui for their communication with my family as well as my friends in the University of Phayao: Jing, Koy and Som for their coordination with my work place over the time I am studying. They can make me laugh in every situation.

All profoundly appreciate to my Mom and Dad, Songsri Chailuecha and Khamphuang Chailuecha, who give me unconditional love and support. I am grateful to my brother, Chatchai Chailuecha, with his encouragement and taking care parent when I am far away from home.

Dedicated

To the attempt on my own,

hope in my soul,

love from my beloved family and best friends

Symbols

| | |
|---------------------------|--|
| A | area (cm^2) |
| ASR | area-specific resistance ($\Omega \text{ cm}^2$) |
| C_m | methanol concentration (mol dm^{-3}) |
| D_m | diffusion coefficient ($\text{cm}^2 \text{ s}^{-1}$) |
| d' | actual distance that a penetrant must travel |
| d | the shortest distance that a penetrant would have travelled in the absence of inorganic layer |
| $E_{\text{reversible}}$ | reversible potential of fuel cell |
| E° | reversible potential at standard temperature and pressure (298 K and 1 atm) |
| F | Faraday constant ($96,485 \text{ J V}^{-1}\text{mol}^{-1}$) |
| G | Gibbs free energy |
| G_f | Gibbs free energy of formation |
| $G_{f, \text{products}}$ | Gibbs free energy of formation of products |
| $G_{f, \text{reactants}}$ | Gibbs free energy of formation of reactants |
| \bar{g}_f | Gibbs free energy per mole of chemical species |
| \bar{g}_f° | Gibbs free energy per mole at standard temperature and pressure (298 K and 1 atm) |
| H | enthalpy |
| \bar{h}_f | enthalpy per mole of chemical species |
| i | current (A) |
| j | current density (A cm^{-2}) |
| j_0 | exchange current density |

| | |
|----------------|---|
| j_L | limiting current density |
| J | Joule |
| J_{lim} | limiting methanol crossover current density (mA cm^{-2}) |
| J_D | methanol diffusion crossover current (mA cm^{-2}) |
| J_t | transitional methanol diffusion crossover current (mA cm^{-2}) |
| k_{dl} | drag coefficient for J_{lim} |
| k_{dt} | drag coefficient for $[J_t\sqrt{t}]$ |
| L | length of inorganic layer |
| l | membrane thickness |
| mol | mole |
| M | Molar (mole/Lite) |
| n | number of electrons transferred per mole of reactant |
| Pt | platinum |
| η_{act} | activation loss |
| η_{ohmic} | ohmic losses |
| η_{conc} | concentration loss |
| R | gas constant ($8.314 \text{ J mol}^{-1} \text{ K}^{-1}$) |
| r | resistance |
| S | entropy |
| S | Siemens (unit of electric conductance) |
| T | temperature (K) |
| t | time (s) |
| u | ratio of local methanol concentration to C_m |
| V | voltage |
| W | width of inorganic layer |
| W_{cell} | work done by the fuel cell |
| $Work_{ICE}$ | reversible work of the internal combustion engines |
| W_{dry} | weight of the dry membrane |
| W_{wet} | weight of the fully hydrated membranes |
| x_{ri} | mole fraction of methanol in the membrane |
| y | fraction distance |

| | |
|-------------------------------|--|
| α | charge transfer coefficient |
| γ^{sv} | the solid-vapor surface tension |
| γ^{sl} | solid-liquid interfacial surface tension |
| γ^{lv} | liquidvapor surface tension |
| θ | contact angle ($0^\circ < \theta < 180^\circ$) |
| τ | tortuosity factor |
| Φ_s | volume fraction of the sheets |
| ξ | total fluid drag coefficient |
| ε | efficiency of fuel cell |
| $\varepsilon_{\text{Carnot}}$ | Carnot efficiency |

Abbreviations

| | |
|----------------|---|
| 3-MPTMS | 3-mercaptopropyltrimethoxy silane |
| 1,3-PS | 1,3-propane sulfone (1,3-PS) |
| AFC | Alkaline fuel cell |
| AMPS | 2-acrylamido-2-methylpropanesulfonic acid |
| CoTMMP | cotetramethoxyphenylporphyrin |
| CHP | combined heat and power |
| CP | conducting polymer |
| CV | cyclic voltammetry |
| DMFC | direct methanol fuel cell |
| EU | European Union |
| EMF | electromotive force |
| EPS | emergency back-up power supply |
| FCV | fuel cell vehicle |
| GDL | gas diffusion layer |
| GHG | greenhouse gases |
| GMPTS | γ -glycidoxypropyltrimethoxysilane |
| GO | graphene oxide |
| GWP | Global Warming Potential |
| HFC | hydrofluorocarbon |
| IPA | isopropanol |
| LBL | layer-by-layer |
| MCFC | Molten carbonate fuel cell |
| MEA | membrane electrode assembly |

| | |
|---------------|---|
| MMT | montmorillonite |
| MOR | mordenite |
| MPL | microporous layer |
| NASA | National Aeronautics and Space Administration |
| OCV | open circuit voltage |
| ORR | oxygen reduction reaction |
| PAFC | Phosphoric acid fuel cell |
| PBI | polybenzimidazole |
| PEEK | poly(etheretherketone) |
| PEMFC | Proton Exchange Membrane Fuel Cell |
| PFC | perfluorocarbon |
| PFSA | perfluorosulfonic acid |
| PmPD | poly(<i>m</i> -phenylenediamine) |
| PSF | polysulfone |
| PTFE | polytetrafluoroethylene |
| RF | radiative forcing |
| SEM | scanning electron microscope |
| SOFC | Solid oxide fuel cell |
| SPSF | sulfonated polysulfone |
| STA | silicotungstic acid |
| STD | standard |
| STP | standard temperature and pressure |
| TBP | triple phase boundary |
| TEM | transmission electron micrograph |
| TN | titanate |
| UNFCCC | United Nations Framework Convention on Climate Change |
| XRD | X-ray diffraction |
| YSZ | yttrium stabilized zirconia |
| ZY | zeolite Y |

Chapter 1

Introduction and objectives

1.1 Introduction

The rise in sea level as a result of polar ice melting may strike much closer to home and make us realise the power of climate change [1–3]. Climate system composes of living things, land surface, snow and ice, oceans and other bodies of water and the characteristic part of climate which is the atmosphere [4]. Human behaviour has changed the atmospheric composition by releasing greenhouse gas into the atmosphere [4, 5]. “Greenhouse gas is a gas that absorbs and emit infrared radiation” [6]. The presence of greenhouse gas suppresses radiation emitted from the Earth’s surface to the space resulting an increase in global surface temperature. Hence, the environmental challenges especially climate change and global warming are contributing to the global concern.

Human activities are the major sources of human-made greenhouse gas which is classified into 4 main groups. The primary source of carbon dioxide (CO_2) are from burning of fossil and biomass especially the inefficient combustion of fossil fuels. Methane (CH_4) and nitrous oxide (N_2O) are from agricultural activities. The major source contributed fluorinated gases (hydrofluorocarbons (HFCs), perfluorocarbons (PFCs), and sulfur hexafluoride (SF_6)) are industrial processes and

refrigeration [7]. The global greenhouse gas emissions in 2004 specified by gas species are presented in Figure 1.1 while their categorised by source are displayed in Figure 1.2.

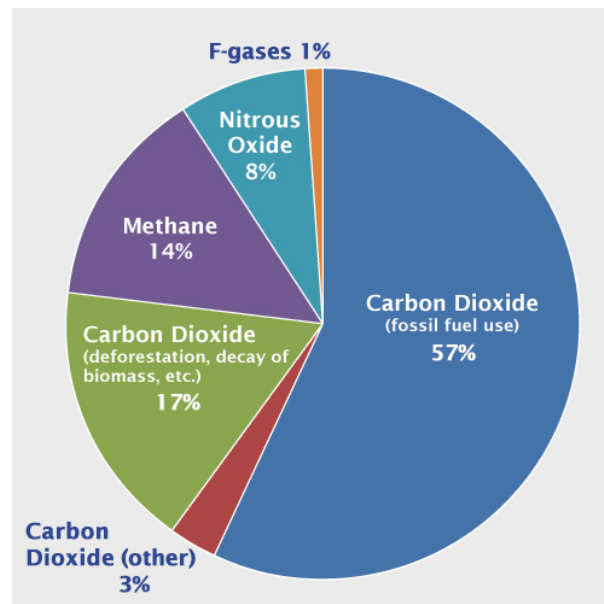


FIGURE 1.1: Global scale of greenhouse gas emissions in 2004 divided by Gas [7]

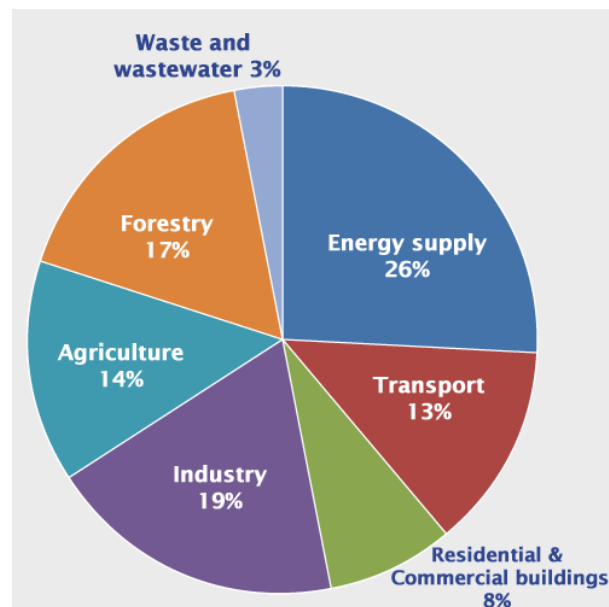


FIGURE 1.2: Global scale of greenhouse gas emissions in 2004 divided by Source [7]

The potentials of greenhouse gases on the climate system have been considered under the Global Warming Potential (GWP) index. There is a metric related to molecular weight, atmospheric lifetime, and radiative forcing (RF) of the greenhouse gases [7–9].

TABLE 1.1: Global Warming Potential (GWP) of greenhouse gases relative to carbon dioxide

| Greenhouse gases | Lifetime (years) | Radiative efficiency ($\text{W m}^{-2} \text{ ppb}^{-1}$) | Global Warming Potential for 100-years |
|--|------------------|---|--|
| Carbon dioxide (CO_2) | N/A | 1.4×10^{-5} | 1 |
| Methane (CH_4) | 12 | 3.7×10^{-4} | 25 |
| Nitrous oxide (N_2O) | 114 | 3.03×10^{-3} | 298 |
| Hydrofluorocarbons (CHF_3) | 270 | 0.19 | 14,800 |
| Perfluorocarbons (CClF_3) | 640 | 0.25 | 14,400 |
| Sulfur hexafluoride (SF_6) | 3200 | 0.52 | 22,800 |

In order to prevent climate change the emission of greenhouse gas must be suppressed. The United Nations Framework Convention on Climate Change (UNFCCC) established the Kyoto Protocol in 1997 in order to mitigate the global emission of greenhouse gas [10]. Under the Kyoto protocol, developed countries that ratified the protocol committed to reduce greenhouse gas emissions by at least 5% between 2008-2012 related to the emissions in the base year, 1990 [11].

The contributors to the Kyoto protocol such as the European Union (EU) adopted the goal of reducing 8% of greenhouse gas in 2008-2012 [10, 12]. Track record of greenhouse gas emissions published in the Annual European Union greenhouse gas inventory 1990-2012 report (Figure 1.3) demonstrated the significant emission

reduction since 2009. In 2012, the EU achieved 19.2% lower emission than the base year level ¹ [12].

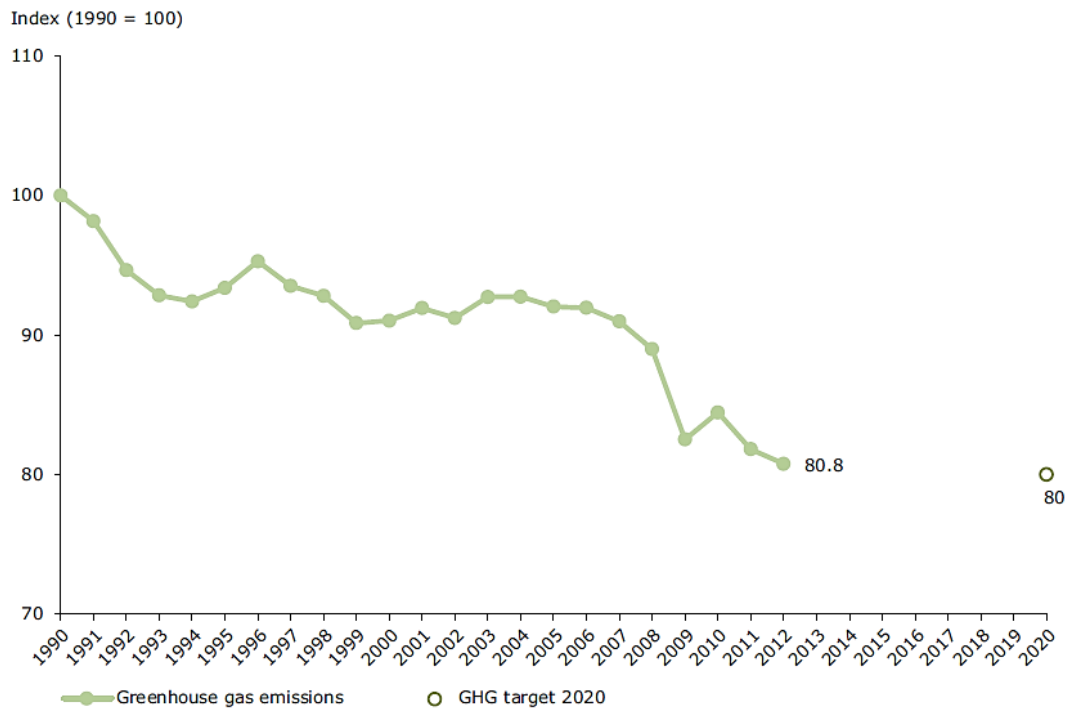


FIGURE 1.3: Greenhouse gases emissions of the European Union in 1990-2012 compared with target for 2008-2012 [12]

1.2 Motivation

While global energy consumption is growing, the climate change and environmental problems are a concern. As shown in Figure 1.1 and 1.2, in 2004 the most abundant of greenhouse gas is CO₂ and 26% of CO₂ is emitted by energy consumption [7]. Unfortunately, CO₂ emission rose to 35% of total greenhouse gas emission in 2010 [13]. The combustion of fossil fuels for electricity and heat is the main source of greenhouse gas emission. Consequently, an alternative electrical system with low CO₂ emission, high efficiency, renewable fuel source, safe and convenient refuelling is required [14–16].

¹Greenhouse gas emission data do not include emissions and removals from Land Use Activities and Land-Use Change and Forestry

1.2.1 Green electricity

Several methods are used to produce the green electricity which is an energy generated from renewable sources such as solar, wind, geothermal, biomass, hydropower and fuel cell with little or no pollution emission, as illustrated in Table 1.2. The renewable energy shares only 22.1% of the global electricity generated in 2011 [17] (Figure 1.4).

TABLE 1.2: Electricity generated from renewable energy sources

| Energy sources | Descriptions | Limitation | Ref. |
|-----------------------|---|--|--------------|
| Solar | Photon from solar radiation is converted into electricity by photovoltaic modules. | Electricity production depends on the locations and season. | [17, 18] |
| Wind | Electricity is generated from mechanical energy by wind turbine systems. | Season and locations affect energy production. | [17, 19, 20] |
| Geothermal | Heat energy in the mantle and core of the earth is transferred to electricity generation. | There is huge investment for setting up a geothermal plant including the problem of earthquakes and landslides. | [21–23] |
| Hydro | Hydropower produces electricity using kinetic energy from water. | The environmental conditions and aquatic life in reservoirs or river systems are disturbed by hydropower plants. | [17, 24, 25] |
| Biomass | The biological wastes including organic matter derived from living organisms are used as raw materials to generate electrical energy. | Huge area for crop is required to meet high energy demand. | [26, 27] |
| Fuel cell | Chemical energy is converted into electrical energy. | Its cost reduction is considered. | [28] |

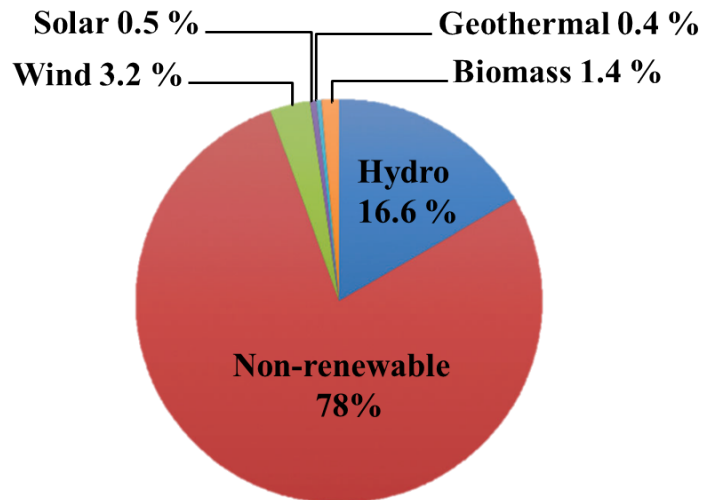


FIGURE 1.4: Share of renewable energy in global electricity production in 2011 (adapted from [17])

1.2.2 Fuel cell for green electricity

Fuel cells are the renewable technology providing high energy conversion efficiency and low air pollution. They are the electrical generators using chemical reaction without any burning of fuel. Furthermore, fuel cells utilise either a liquid or gaseous fuel that give flexibility. They can be applied as the power supply for many scales such as portable and stationary devices, vehicles and aircraft [29].

Fuel cells are useful in a variety of applications because of the different types which provide wide power ranges from micro-fuel cells producing only 2-3 W [30] to large scale multi-megawatt systems [31, 32]. In order to achieve high power output, multiple cells are connected together [33]. Fuel cells can be used for portable power supply, stationary power generation and transportation power supply [33].

1.2.2.1 Portable applications

Portable fuel cells have power ranges of 5-500 W [32]. Main applications of portable fuel cells are categorised into two groups. First focuses on the power generators for outdoor lights such as camping and garden lights. Second is the

power source for electronic devices such as notebooks and mobile phones in lieu of a battery. Fuel cells are favourable in portable applications because of their low operating temperature, lightweight systems and easy refuelling [34–38]. Furthermore, they present a higher power density and longer lifespan than batteries [35, 37, 39].

1.2.2.2 Stationary applications

Fuel cells can be used as stationary power supply for instance as emergency back-up power supply (EPS) in hospitals, telecommunications, bank, and government agencies [40–42] and as combined heat and power (CHP) systems in remote areas or residential dwellings [43]. Large scale central power generation can be expensive to deliver electric power to the consumers; therefore, the decentralized distributed power supply is an alternative solution [32, 44–46]. Fuel cells can serve a demand of residential electric power which requires low power range <10 kW [47]. Japan has distributed fuel cells on the residential CHP system throughout the country [47–49]. The system of CHP is shown in Figure 1.5.

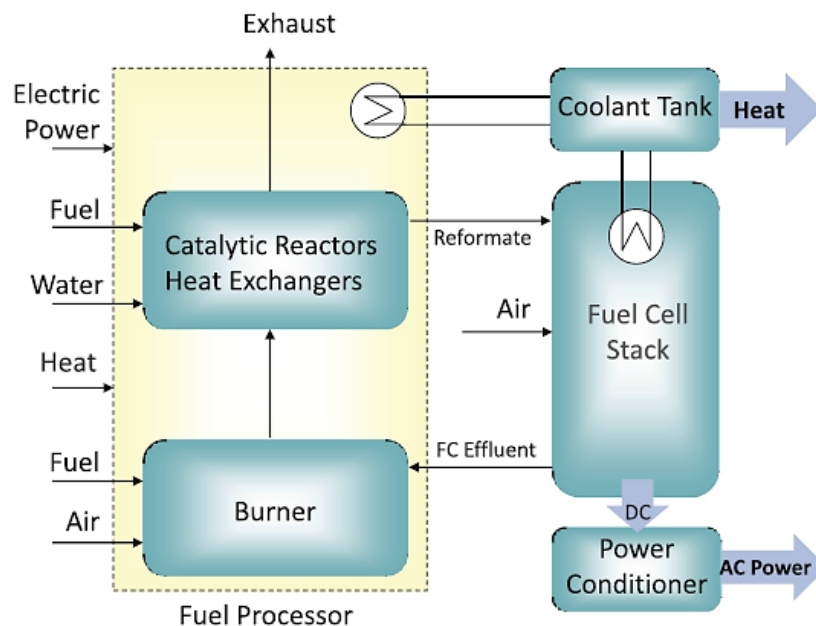


FIGURE 1.5: Schematic of a fuel cell based combined heat and power (CHP) system [46]

The primary fuel for example natural gas is reformed into a hydrogen-rich gas by a fuel processor and then it is electrochemically oxidised in a fuel cell stack to produce electric power and heat [46].

1.2.2.3 Transportation applications

Fuel cells can be used in electric vehicles such as a cars, trucks, and buses [50]. An example of a fuel cell vehicle (FCV) model is given in Figure 1.6 [32]. The FCV composes of hydrogen storage, fuel cell stack, high voltage battery and/or ultracapacitors, power drive unit and electric drive motor. Compressed hydrogen from the hydrogen tank flows to the fuel cell stack to generate electricity. Under the control of power drive unit, the produced electricity powers the electric drive motor to change electrical energy into mechanical energy [51, 52]. The excess electricity is stored in the battery. It is supplied to the drive motor as a supplementary power in high load driving. Honda Motor Co., Ltd. [52] revealed a new model of FCV, Clarity Fuel Cell, in the 44th Tokyo Motor Show on October 28, 2015. The fuel cell stack for this car offers the power output of 100 kW, 134 horsepower, cruising range of more than 700 km and 4 seats using pure hydrogen as a fuel.

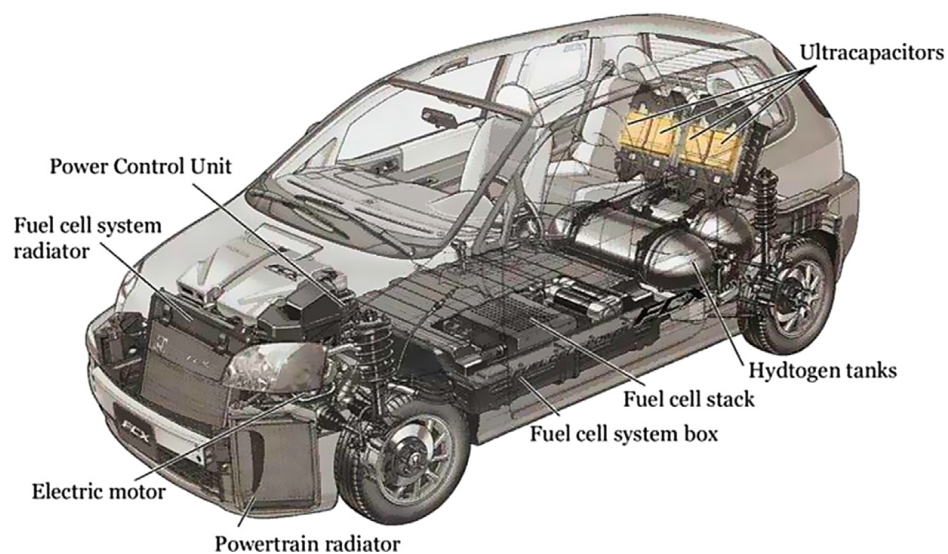


FIGURE 1.6: Model of Fuel cell vehicle based on the Honda 2005 FCX [32]

1.2.3 Fuel cell cost

Although fuel cells are the key technology for generated green electricity, the barriers of their high system cost have been identified. In order to address this issue it is necessary to focus on cost reduction before mass production and extensive commercialization of fuel cells [53, 54]. Summarised the target cost for fuel cell technology in the United States [32] are shown in Table 1.3. Sun [55] demonstrated that a significant fraction of the fuel cell cost comes from the cost of platinum catalyst. "A 50 kW fuel cell with a power density of 700 mW cm^{-2} has approximately 46 g of platinum, costing \$2240." Mudd [56] mentioned that global the productions of platinum and noble metal catalyst are dominated by South Africa and Russia. They supply these metal catalysts for many decades, therefore, the concern in long term availability of metals to meet the future demands must be considered.

1.3 Objective

The aim of improvement in direct methanol fuel cell (DMFC) performance has been implemented in this research. The study focuses on DMFC due to an advantage of using methanol solution as a fuel and a high efficiency of this technology. However, the major technological barrier for DMFC application is a methanol crossover from an anode to a cathode of fuel cell which reduces the power output of the DMFC.

The performance of DMFC can be enhanced using an alternative procedure which incorporates Nafion/inorganic composite layer, a methanol barrier layer, onto the anode side of the membrane electrode assembly (MEA). Two types of inorganic structures, microporous and 2-dimensional structure, are used in order to demonstrate their influence on DMFC performance.

The literature also demonstrates that hydrophilic/hydrophobic properties play a crucial role in methanol prevention. Therefore, the hydrophobic nature of the Nafion/inorganic methanol barrier layer will be studied in this work using contact angle measurement.

In order to achieve additional DMFC improvement, the morphology of MEA will be adjusted by modifying a technique for MEA fabrication.

TABLE 1.3: Summarised the target cost for fuel cell technology in the United States [32]

| Application | Details | Current cost 2011 | Target cost 2020 |
|---------------------------------|---|------------------------------|-----------------------------|
| 80 kW Automotive transportation | Production level of 500,000 units/annum | 49 (\$/kWe) | 30 (\$/kWe) |
| 110 kW Small residential CHP | Production level of 500,000 units/annum | 2,300-4,000 (\$/kWe) | 1,500 (\$/kWe) |
| 100-3,000 kW Medium CHP | Natural gas fuel | 2,500-4,500 (\$/kWe) | 1,000 (\$/kWe) |
| | Biogas fuel | 4,500-6,500 (\$/kWe) | 1,400 (\$/kWe) |
| 10-50 W Small portable | Production level of 25,000 units/annum | 15 (\$/system) | 7 (\$/system) |
| 100-250 W Medium portable | Production level of 10,000 units/annum | 15 (\$/system) | 5 (\$/system) |

1.4 Outline of thesis

Chapter 1 introduces fuel cells and the advantages of this technology.

Chapter 2 provides principles and operating technique of fuel cells especially direct methanol fuel cell (DMFC). This chapter also gives an account of potential loss and methanol crossover problems in DMFC.

Chapter 3 reviews the crucial drawback which obstructs DMFC from a high efficiency in addition to the research and the development method to resolve limitation of DMFC. The effort to diminish methanol permeability from anode to cathode electrode is focused in this study.

Chapter 4 displays two preparation procedures for the standard membrane electrode assemblies (MEAs) as well as the experimental system. In addition, a strategy of modified MEA by incorporating a methanol barrier layer into the anode side is established. Four MEAs including individual Nafion composite layers containing mordenite, zeolite Y, montmorillonite and titanate were formed.

Chapter 5 distributes the operating results of standard and modified MEAs produced by a conventional procedure (procedure I). The performance of standard and modified MEAs have been analysed. Contact angle of methanol barrier layers are measured in order to investigate their hydrophilic/hydrophobic properties which would impact to the MEAs performance.

Chapter 6 examines the additional improvement in DMFC performance by modifying a MEA preparation procedure. The performances of new standard and new modified MEAs produced by a modified procedure (procedure II). The results between the conventional standard made from procedure I and the new standard fabricated from procedure II are compared.

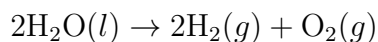
Chapter 7 concludes this study and suggests future work which exhibits proton conductivity and methanol permeability using linear sweep voltammetry and electrochemical impedance spectroscopy.

Chapter 2

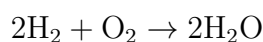
Fuel cell

2.1 History of fuel cell

Since 1800 British scientists Sir Anthony Carlisle and William Nicholson discovered a water electrolysis, a decomposition of water into hydrogen and oxygen using electricity, a reverse of this reaction was further valuable in fuel cell technology [57, 58].



Sir William Robert Grove a lawyer and physician first demonstrated a fuel cell [59] which is originally referred as *gas-battery* at the *British Association Meeting* at Birmingham in 1839, this work was then published in a paper of *Philosophical Magazine* in October 1839 [50, 57]. He used an inverse reaction of electrolysis to produce electricity by the combination of hydrogen and oxygen. His experiment is shown in Figure 2.1. Two platinum electrodes were immersed into sulphuric acid solution. The electrolysis of water into hydrogen and oxygen gas occurred by passing an electrical current. Therefore, the small electric current was produced by the inverse of electrolysis reaction [29].



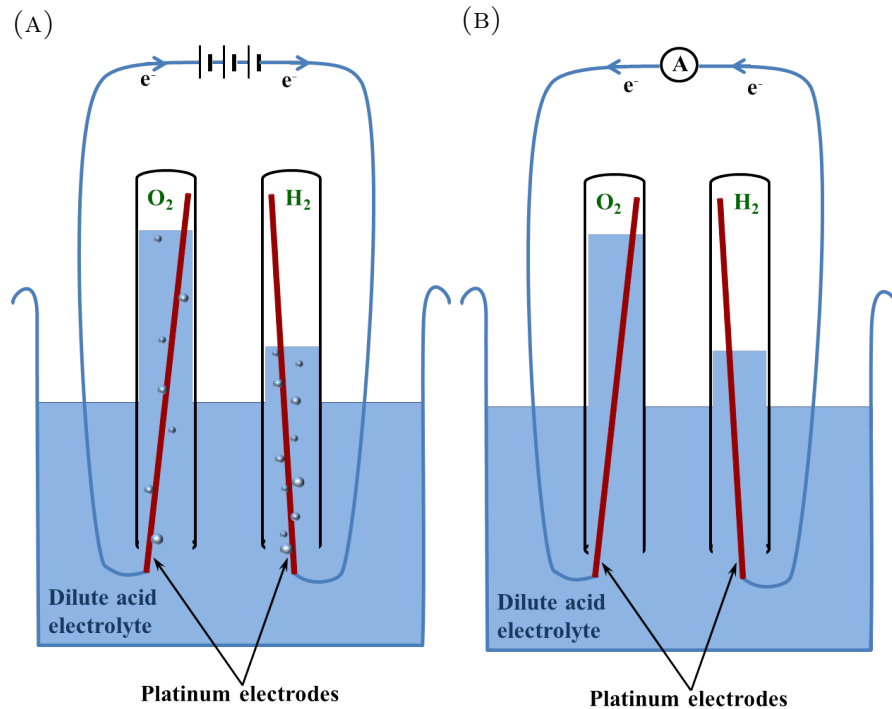


FIGURE 2.1: Basic operation of the first fuel cell (A) Electrolysis of water into hydrogen and oxygen (B) Recombination of hydrogen and oxygen to water (adapted from [29])

Fuel cells were successfully developed to the first fully-operational fuel cell in the 1959 by Francis Thomas Bacon, an English engineer [32]. It was used by NASA in the Gemini spacecraft program in the 1960s. The early fuel cell design had a limited lifetime and its electrolyte membrane quickly degraded [60].

The development of fuel cell technology started since 1967; the improved membrane, Nafion[®], has been developed by DuPont. This membrane was recognized as the key to improving fuel cell performance and it has been used in fuel cells until now. The molecular structure of Nafion is shown in Figure 2.2. It consists of a backbone of fluorine and carbon, which makes it highly hydrophobic and provides thermal and chemical stability; proton and water transport through Nafion is via the hydrophilic sulfonic acid side chains [29, 60].

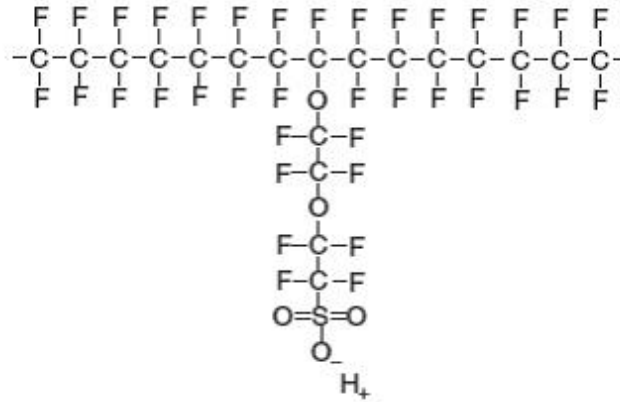


FIGURE 2.2: Molecular structure of Nafion [29]

2.2 Principle of fuel cell

A fuel cell is an energy source that generates electrical energy from a chemical reaction [61]. Main components of fuel cells can be divided into two groups. First is an external circuit which composes of an insulator, a current collector and fuel flow field. Second is a membrane electrode assembly (MEA) where an electrochemical reaction takes place. The MEA consists of anode and cathode electrodes separated by an electrolyte. Two electrodes are also linked through an external electrical circuit. Each electrode is supplied with fuel or oxidant therefore its structure has to be porous materials to serve the purpose of gas or liquid permeability. The MEA not only conducts ions between anode and cathode, but the function of an electrolyte also insulates electron transportation so that the electrons are only delivered through an external circuit [29]. This set up is depicted in Figure 2.3

2.3 Different Types of Fuel Cell

There are different types of fuel cells which provide various challenges. Classification of fuel cells and their advantage and disadvantages are described in Table

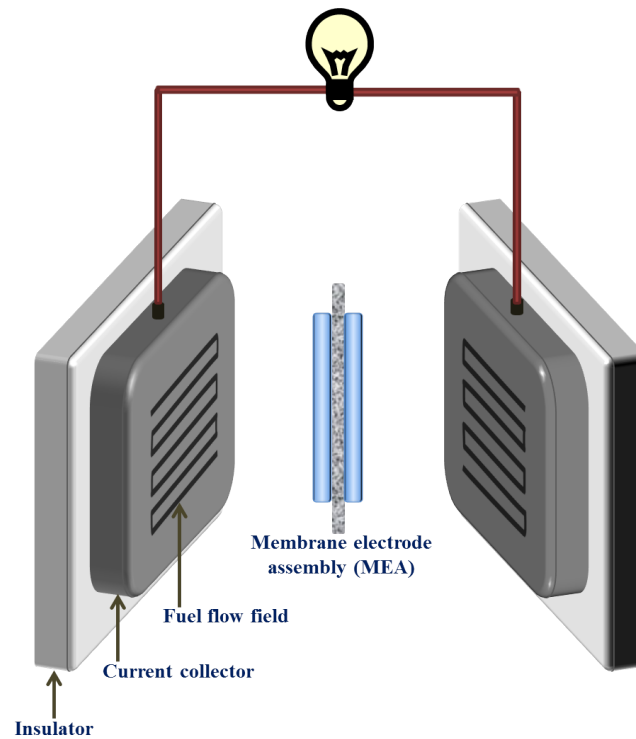


FIGURE 2.3: Fuel cell components

2.1 and 2.1 [29, 62–65]. Although the over all reaction of fuel cells are not exactly different, they are classified to five main types by the characteristic of their electrolytes [44] as:

- Proton Exchange Membrane Fuel Cell (PEMFC)
- Solid oxide fuel cell (SOFC)
- Molten carbonate fuel cell (MCFC)
- Phosphoric acid fuel cell (PAFC)
- Alkaline fuel cell (AFC)

Direct methanol fuel cell (DMFC) is a new technology compared to the main types of fuel cell. It is developed from the proton exchange membrane fuel cell; consequently, it uses polymer membrane as an electrolyte but DMFC supplies liquid methanol as fuel.

TABLE 2.1: Classification of fuel cells

| | SOFC Solid oxide fuel cell | MCFC Molten carbonate fuel cell | PAFC Phosphoric acid fuel cell | PEMFC Polymer electrolyte fuel cell | DMFC Direct methanol fuel cell | AFC Alkaline fuel cell |
|--|---|---|---|---|--|---|
| Operating Temperature (°C) | 800-1000 | ~650 | 160-220 | 30-100 | 30-100 | 50-200 |
| Electrolyte | Ion conducting ceramics | Liquid molten carbonate in LiAlO ₂ | Liquid phosphoric acid in silicon carbide | Proton Conducting Polymer | Proton Conducting Polymer | Potassium hydroxide in asbestos matrix |
| Fuel | H ₂ /CO/CH ₄ | | H ₂ | H ₂ | CH ₃ OH | H ₂ |
| Oxidant | O ₂ /air | CO ₂ /O ₂ /air | O ₂ /air | O ₂ /air | O ₂ /air | O ₂ /air |
| Anode reaction | $2\text{O}^{2-} + 2\text{H}_2$ $\rightarrow 2\text{H}_2\text{O} + 4\text{e}^-$ | $2\text{H}_2 + 2\text{CO}_3^{2-}$ $\rightarrow 2\text{H}_2\text{O} + 2\text{CO}_2 + 4\text{e}^-$ | 2H_2 $\rightarrow 4\text{H}^+ + 4\text{e}^-$ | 2H_2 $\rightarrow 4\text{H}^+ + 4\text{e}^-$ | $\text{CH}_3\text{OH} + \text{H}_2\text{O}$ $\rightarrow \text{CO}_2 + 6\text{H}^+ + 6\text{e}^-$ | $2\text{H}_2 + 4\text{OH}^-$ $\rightarrow 4\text{H}_2\text{O} + 4\text{e}^-$ |
| Cathode reaction | $\text{O}_2 + 4\text{e}^-$ $\rightarrow 2\text{O}^{2-}$ | $\text{O}_2 + 2\text{CO}_2 + 4\text{e}^-$ $\rightarrow 2\text{CO}_3^{2-}$ | $\text{O}_2 + 4\text{e}^- + 4\text{H}^+$ $\rightarrow 2\text{H}_2\text{O}$ | $\text{O}_2 + 4\text{e}^- + 4\text{H}^+$ $\rightarrow 2\text{H}_2\text{O}$ | $\frac{3}{2}\text{O}_2 + 6\text{e}^- + 6\text{H}^+$ $\rightarrow 3\text{H}_2\text{O}$ | $\text{O}_2 + 2\text{H}_2\text{O} + 4\text{e}^-$ $\rightarrow 4\text{OH}^-$ |
| Charge transfer through electrolyte | O ²⁻ | CO ₃ ²⁻ | H ⁺ | H ⁺ | H ⁺ | OH ⁻ |
| Power output | 100 kW–1.7 MW | 100 kW–2 MW | 100 kW–1.3 MW | 2-250 kW | 1-1 kW | 10-100 kW |

TABLE 2.2: Classification of fuel cells

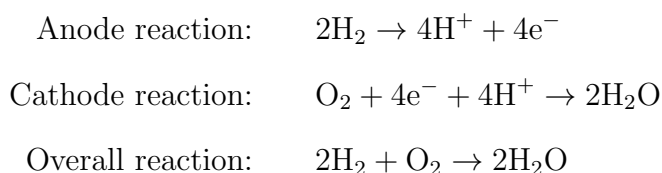
| | SOFC Solid oxide fuel cell | MCFC Molten carbonate fuel cell | PAFC Phosphoric acid fuel cell | PEMFC Polymer electrolyte fuel cell | DMFC Direct methanol fuel cell | AFC Alkaline fuel cell |
|---------------------|---|---|--|---|---|--|
| Application | <ul style="list-style-type: none"> • Stationary power supply • Residential power supply | <ul style="list-style-type: none"> • Stationary power supply | <ul style="list-style-type: none"> • Stationary power supply | <ul style="list-style-type: none"> • Transportation • Portable power supply • Residential power supply | <ul style="list-style-type: none"> • Portable power supply | <ul style="list-style-type: none"> • Space vehicles • Portable power supply |
| Advantage | <ul style="list-style-type: none"> • High electrical efficiencies • Tolerance to impurities in fuel and oxidant • Fuel flexibility | <ul style="list-style-type: none"> • High electrical efficiencies • Tolerance to impurities in fuel and oxidant • Inexpensive catalyst • Fuel flexibility | <ul style="list-style-type: none"> • Tolerance to impurities in fuel and oxidant • Simple water management | <ul style="list-style-type: none"> • Quick start up • Solid electrolyte reduces corrosion | <ul style="list-style-type: none"> • Simple system • Easy fuel storage • High fuel volumetric energy density | <ul style="list-style-type: none"> • Fast cathodic reaction • Inexpensive catalyst |
| Disadvantage | <ul style="list-style-type: none"> • Slow start up • High manufacturing costs | <ul style="list-style-type: none"> • Slow start up • Corrosive electrolyte | <ul style="list-style-type: none"> • Slow start-up • High cost platinum catalyst | <ul style="list-style-type: none"> • High cost platinum catalyst • Low efficiencies | <ul style="list-style-type: none"> • High cost platinum catalyst • Low potential due to poor methanol oxidation • Fuel and water crossover | <ul style="list-style-type: none"> • Sensitive to carbon dioxide • Corrosive electrolyte |

2.3.1 Proton Exchange Membrane Fuel Cell (PEMFC)

Proton Exchange Membrane Fuel Cell (PEMFC) was used by NASA in the Gemini spacecraft, the first manned spacecraft [29]. In 1967, a developed polytetrafluoroethylene membrane of Dupont named Nafion was used as an electrolyte in PEMFC. PEMFC does not suffer from corrosion of electrolyte. For this reason including low operating temperature and high power density, PEMFC is suitable for application in transportation vehicles. However, it carries drawbacks of low efficiency ¹ (40-45%) and expensive platinum catalyst [66].

2.3.1.1 Principles of Operation

The operation of fuel cell can be demonstrated by PEMFC. The oxidation of hydrogen gas takes place at the anode to produce electrons and protons. Electrons are migrated through the external circuit to cathode via a potential gradient between two electrodes while protons are diffused through the electrolyte. Water is formed at the cathode via a combination of protons, electrons flowed from anode and oxygen which is directly supplied to cathode [29, 44, 67, 68]. The electrochemical reaction of PEMFC can be summarised as shown in the equations below and as presented in figure 2.4.



2.3.1.2 Fuel Cell Voltages

Thermodynamic energy, the maximum electric energy produced in fuel cell, is from the change of Gibbs free energy of formation between the products and the

¹The calculation of fuel cell efficiency is given in detail in Section 2.4.2.4, page 61

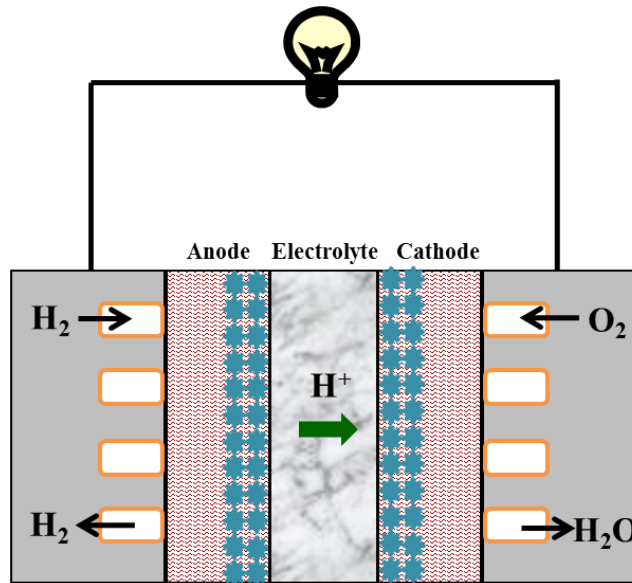


FIGURE 2.4: The system of proton exchange membrane fuel cell (PEMFC)

reactants [29].

$$\text{Ideal electrical work} = \Delta \bar{g}_f = \bar{g}_{f,\text{products}} - \bar{g}_{f,\text{reactants}}$$

where:

\bar{g}_f , Gibbs free energy per mole

$\bar{g}_{f,\text{products}}$, Gibbs free energy per mole of products

$\bar{g}_{f,\text{reactants}}$, Gibbs free energy per mole of reactants

Gibbs free energy of PEMFC has been calculated as:

$$\Delta \bar{g}_f = 2\bar{g}_{f,\text{H}_2\text{O}} - 2\bar{g}_{f,\text{H}_2} - \bar{g}_{f,\text{O}_2} \quad (2.1)$$

Gibbs free energy changes with temperature and state (gas or liquid); thus, the calculation of Gibbs free energy should specify temperature [61]. The PEMFC operating at standard temperature (298 K) has $\Delta \bar{g}_f$ as:

$$\Delta \bar{g}_f^\circ = \bar{g}_{f,\text{H}_2\text{O}}^\circ - \bar{g}_{f,\text{H}_2}^\circ - \frac{1}{2}\bar{g}_{f,\text{O}_2}^\circ$$

$$\begin{aligned}\Delta\bar{g}_f^\circ &= [(2)(-237)] - [0 - 0] \text{ kJ mol}^{-1} \\ &= -546 \text{ kJ mol}^{-1}\end{aligned}$$

The negative value of \bar{g}_f means that energy is released. For the fuel cell, the amount of $\Delta\bar{g}_f$ is converted to its electromotive force (EMF) or reversible open circuit voltage (OCV) [67]. This can be done as follows:

$$\text{Ideal electrical work} = \Delta\bar{g}_f = -nFE$$

Rearranging the equation

$$E = -\frac{\Delta\bar{g}_f}{nF}$$

where:

E , reversible potential of fuel cell

n , number of electrons transferred for each molecule of fuel

F , Faraday constant (charge of a mole of electrons, $96,485 \text{ J V}^{-1} \text{ mol}^{-1}$)

From a Gibbs free energy change of -237 kJ mol^{-1} at 298 K and liquid water product, the highest voltage possible of PEMFC is:

$$\begin{aligned}E^\circ &= -\frac{-546,000 \text{ J mol}^{-1}}{(4)(96,485 \text{ J V}^{-1}\text{mol}^{-1})} \\ &= 1.23\text{V}\end{aligned}$$

2.3.2 Solid oxide fuel cell (SOFC)

Solid oxide fuel cell is a high temperature fuel cell. It operates at 800-1000 °C giving an efficiency of 50-70% [66, 69, 70]. Therefore, a high temperature tolerant electrolyte such as ceramic is required. A ceramic electrolyte, yttrium stabilized zirconia (YSZ), is commonly used in SOFC due to its oxide-ion conductivity of $\sim 0.13 \text{ S cm}^{-2}$. Commercial application of SOFC suffers from a high operating

temperature that makes SOFC unfavourable for portable application and transportation [69]. Nevertheless, SOFC share market with PEMFC for residential power generation [70].

The system of SOFC is shown in Figure 2.5. Fuel for SOFC is hydrocarbon fuels such as methane (CH_4) which require a reforming system to convert the hydrocarbon into hydrogen (H_2) [70, 71]. Oxygen (O_2) molecules at cathode adopt electrons and produce oxide ions O^{2-} . The product ions migrate through an electrolyte to anode and react with fuel. The oxidation-reduction reactions are given as:

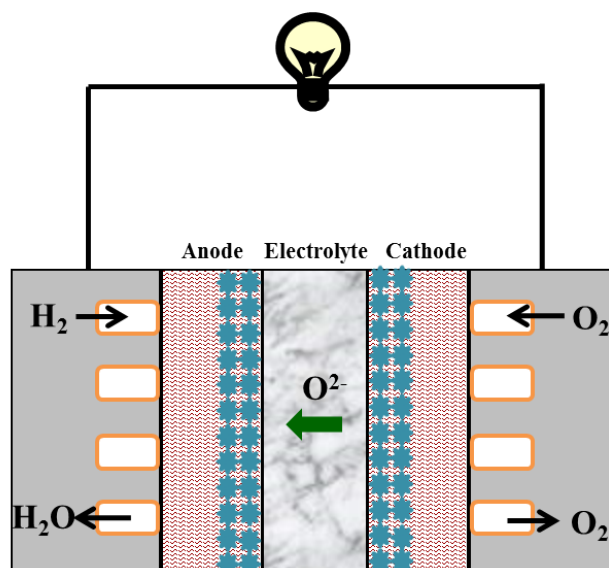
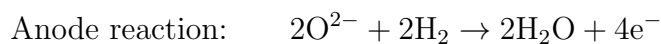
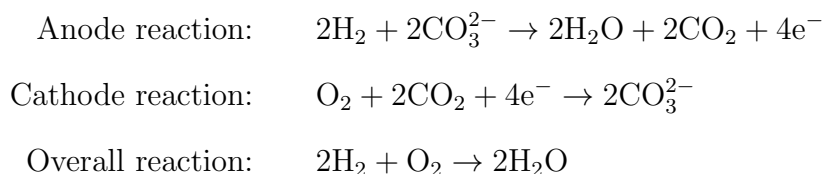


FIGURE 2.5: The system of solid oxide fuel cell (SOFC)

2.3.3 Molten carbonate fuel cell (MCFC)

Similar to SOFC, molten carbonate fuel cell has been grouped into a high temperature fuel cell. The high operating temperature at ~ 650 °C [29, 33] causes 50-60% efficiency without an addition of a precious metal catalyst; nevertheless, MCFC has slow start-up time do to high temperature. The main disadvantage of MCFC is a corrosion from carbonate electrolyte owing to short life-span electrode.

This fuel cell also converts fossil fuels to hydrogen before the oxidation-reduction takes place. Hydrogen reacts with carbonate ion (CO_3^{2-}) which reaches anode by diffusion via an electrolyte to produce water, carbon dioxide (CO_2) and electrons. Carbon dioxide is transferred by recycle system to cathode then it is combined with electrons and oxygen to form carbonate ions. MCFC system is displayed in Figure 2.6. The reactions of MCFC are:



progressive

2.3.4 Phosphoric acid fuel cell (PAFC)

Phosphoric acid fuel cell conducts proton through concentrated phosphoric acid, H_3PO_4 supported in porous matrix of Teflon-silicon carbide. This electrolyte has a higher tolerance to CO_2 impurity in fuel and oxidant compared to alkaline fuel cell [33, 72]. Similar to PEMFC, the platinum catalyst is incorporated into both anode and cathode. An operating temperature of 175-200 °C gives efficiency of 40-45%. PAFC is compatible for stationary power and heat applications with the high power of 100-500 kW [66]. PAFC system is shown in Figure 2.7 and the

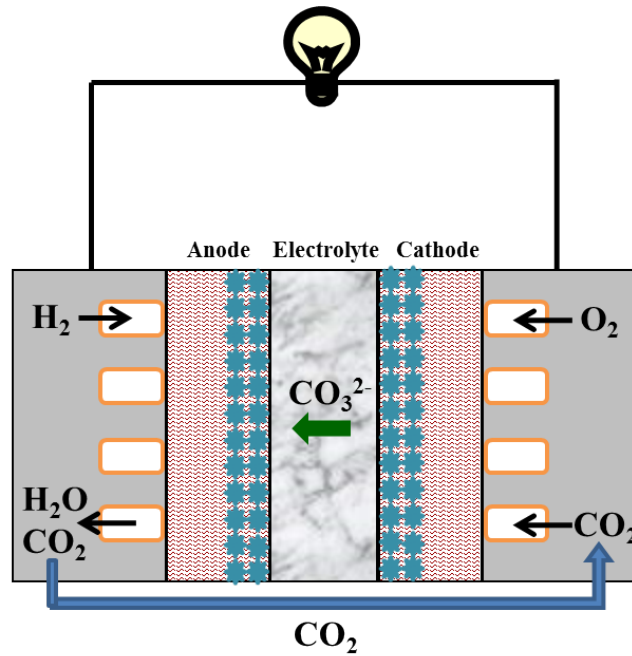
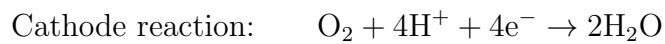
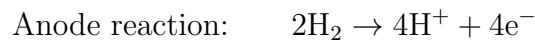


FIGURE 2.6: The system of Molten carbonate fuel cell (MCFC)

reactions are presented as:



2.3.5 Alkaline fuel cell (AFC)

Alkaline fuel cell was used in NASA space program as electrical generators for the space shuttles [33, 73]. Using potassium hydroxide aqueous solution (KOH) as an electrolyte operating $\sim 100^\circ\text{C}$, AFC achieves efficiency of 60-70%. The application of AFC is applying in a portable power supply. The reduction of oxygen at cathode produces hydroxyl ions which then travel to the anode. At the

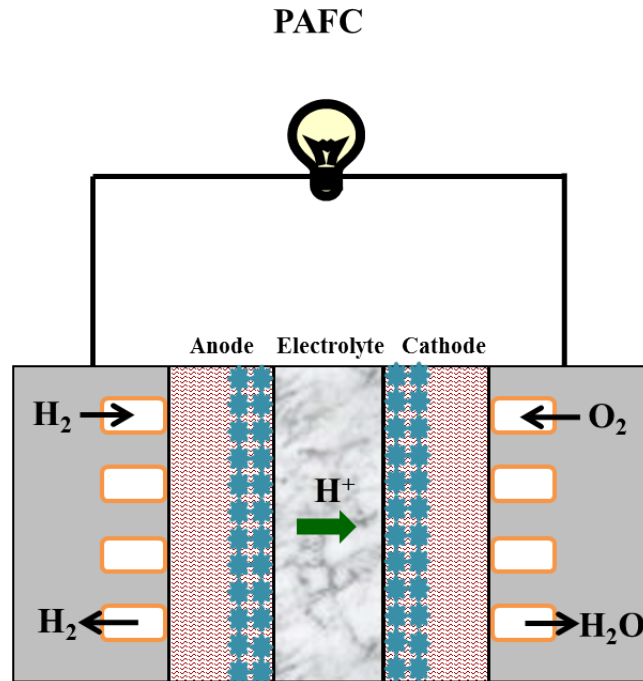
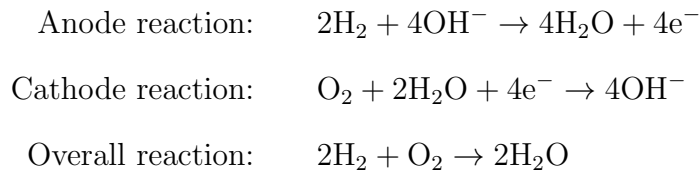


FIGURE 2.7: The system of phosphoric acid fuel cell (PAFC)

anode the molecules of hydrogen fuel react with hydroxy ions and release water. AFC system is shown in Figure 2.8 and the reactions in AFC are presented as:



The advantage of AFC is low cost because the faster oxygen reduction in an alkaline media compared to an acid media allows AFC to use non-noble metal catalyst such as nickel and silver [74]. The main disadvantages of AFC is degradation when exposed to carbon dioxide from fuel or oxidant [33]. In the presence of carbon dioxide, it can block the electrolyte pathway by reacting with hydroxide electrolyte to form carbonate (Equation 2.2). This phenomena reduces electrolyte

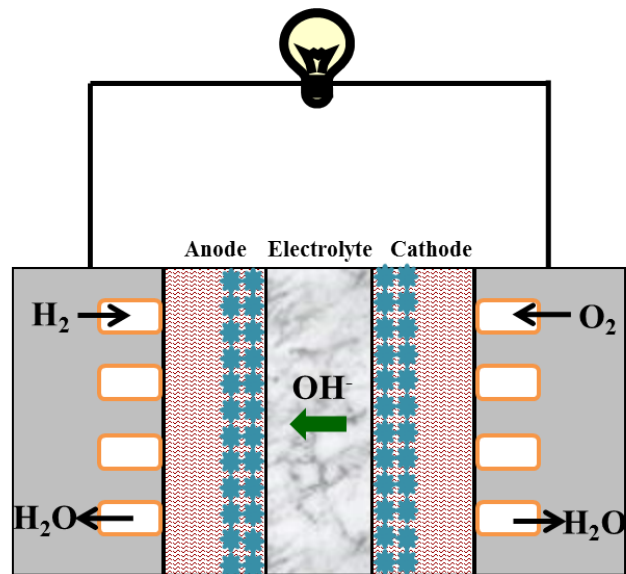
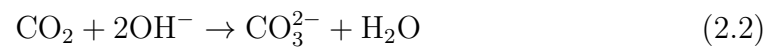


FIGURE 2.8: The system of alkaline fuel cell (AFC)

conductivity and electrode activities [74].



Summary the oxidation-reduction reactions and the charge transfer direction through the electrolytes are given in Figure 2.9.

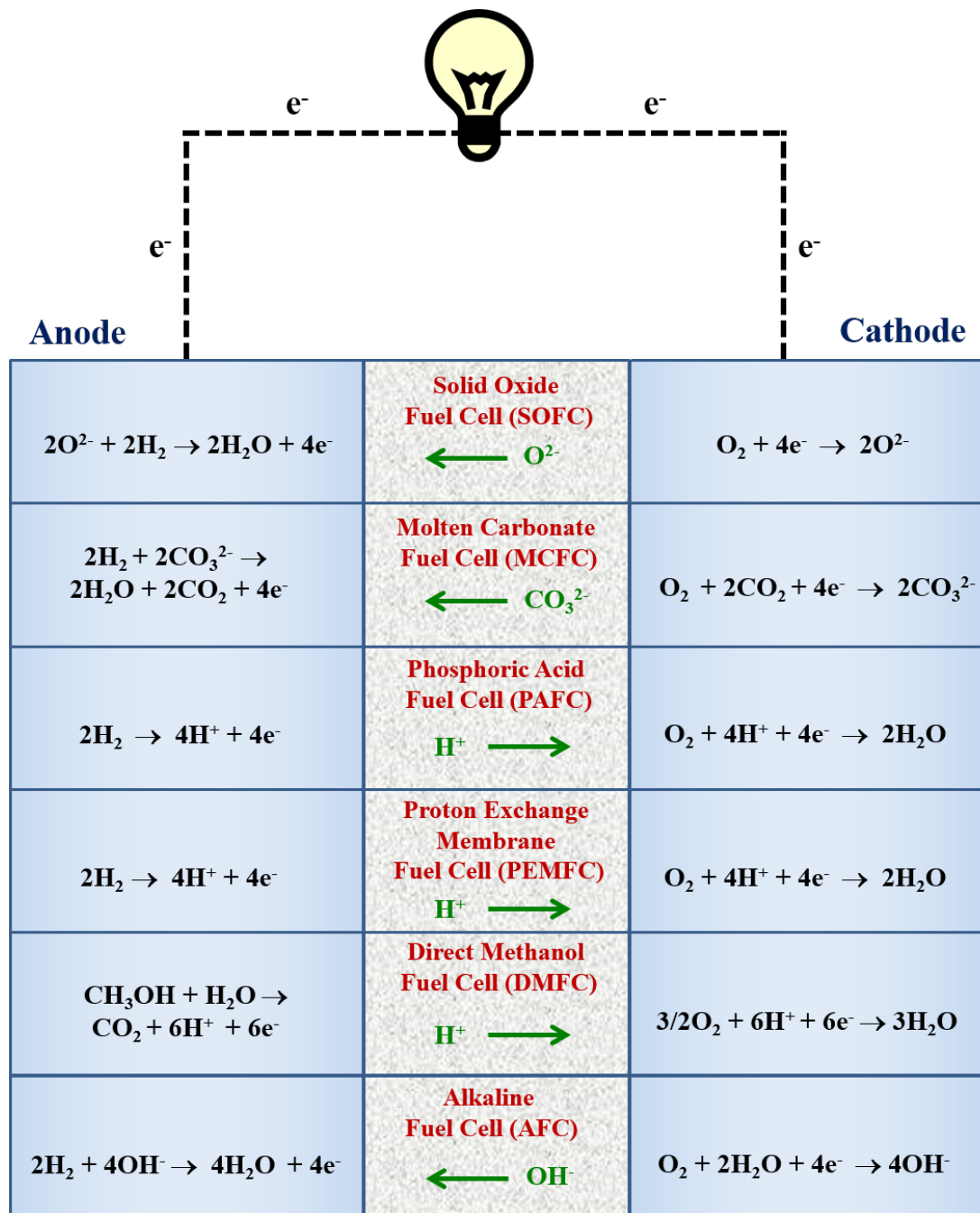


FIGURE 2.9: The oxidation-reduction reactions and the charge transfer direction of fuel cells

2.4 Direct methanol fuel cell (DMFC)

An alternative power source should generate high energy densities. Methanol has larger energy density (4.8 kWh cm^{-3}) than that of hydrogen (0.18 kWh cm^{-3}); therefore, it can provide long operation time for portable and mobile devices [75, 76]. Methanol has high hydrogen-to-carbon ratio (4:1); moreover, it has no carbon-carbon bonds which require breaking during the oxidation reaction [77]. For this reason, methanol is favourable to use as a renewable source for the electrical energy.

Direct methanol fuel cell is a polymer electrolyte membrane fuel cell (PEMFC) [78] which is supplied with liquid methanol fuel. PEMFC gives high power output but it still has many important disadvantages because it uses hydrogen gas as a fuel: the complication of its operation system and the requirement for safe and effective of hydrogen storage. To overcome these problems, DMFC has been developed from PEMFC [37, 60, 62]. DMFC offers several advantages for using liquid as a fuel that makes the DMFC operation system simple than PEMFC. This section gives an overview of fundamental and key components of DMFC.

2.4.1 Electrochemical reaction

The DMFC components are depicted in Figure 2.10. The fuel cell consists of two electrodes, anode and cathode, partitioned by an electrolyte membrane. Each electrode comprises a gas- or solution-permeable layer to allow fuel or oxidant transportation and a porous catalyst layer to service the reacting area for the electrochemical reaction. Electrons and protons are produced at the anode by the oxidation reaction of methanol. Protons permeate through the electrolyte membrane to reach the cathode, where oxygen gas is supplied. To complete the electrochemical reaction, the two electrodes are linked by an external electrical circuit [29, 36, 37, 61, 62]. The excess of electrons at the anode compared to the cathode gives potential difference which drives electron flow through an external

circuit [79] toward the cathode. When protons and electrons reach the cathode, they combine with oxygen to form water.

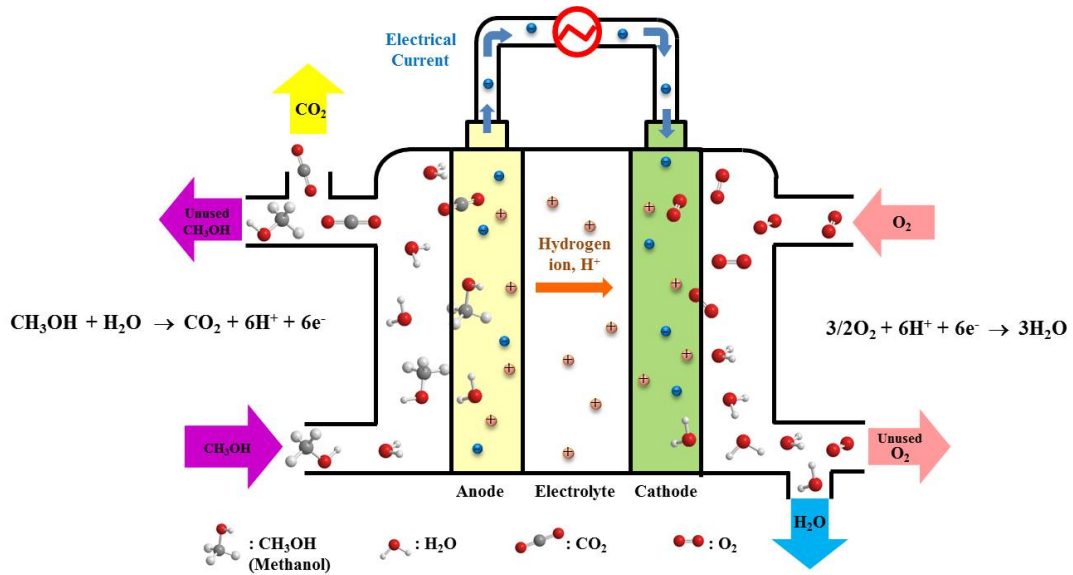
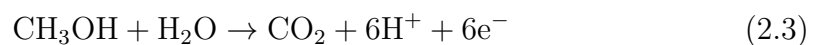


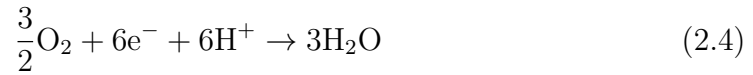
FIGURE 2.10: Components of DMFC

The function of an electrolyte is to conduct protons between anode and cathode, but it should inhibit electrons so that the electrons only transfer through the external circuit. Furthermore, a good electrolyte membrane should prevent the methanol crossover, a crucial problem in DMFC, which causes the fuel loss and reduces DMFC performance [80]. The constraint of methanol permeability is a major challenge in development of DMFC electrolyte membrane. The electrochemical reaction of DMFC can be summarized as [29]: (i) methanol is oxidised at an anode (Equation 2.3) with slow and complex mechanisms which the detail will be illustrated in Section 2.5.1.2, page 71; (ii) a reduction of oxygen takes place at a cathode (Equation 2.4) which the full information will be seen in Section 2.5.1.2, page 73.

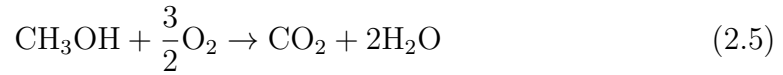
Anode reaction



Cathode reaction



Overall reaction



2.4.2 Thermodynamics

2.4.2.1 Gibbs free energy

The main purpose of a fuel cell is to convert the energy in the chemical bonds of a fuel to electrical energy through an electrochemical reaction. The Gibbs free energy is the key factor for representing the thermodynamics of the reaction.

$$G = H - TS \quad (2.6)$$

with:

G , Gibbs free energy

H , enthalpy

T , temperature (K)

S , entropy, a measure of disorder in a system or reversibility of a process

The output of a fuel cell is demonstrated by the electrical work made available by the system. This is equal to the Gibbs free energy of formation and can be illustrated as the change in Gibbs free energy of formation between the products and the reactants [29, 61, 81].

$$W_{\text{cell}} = \Delta G_{\text{f}} = G_{\text{f, products}} - G_{\text{f, reactants}} \quad (2.7)$$

where:

W_{cell} , work done by the fuel cell

G_{f} , Gibbs free energy of formation

$G_{\text{f, products}}$, Gibbs free energy of formation of products

$G_{\text{f, reactants}}$, Gibbs free energy of formation of reactants

For convenience, the Gibbs free energy of the electrochemical reaction of the DMFC in Equation 2.5 can be presented in terms of Gibbs free energy per mole of chemical species as:

$$\Delta\bar{g}_{\text{f}} = [2\Delta\bar{g}_{\text{f, H}_2\text{O}} + \Delta\bar{g}_{\text{f, CO}_2}] - \left[\frac{3}{2}\Delta\bar{g}_{\text{f, O}_2} + \Delta\bar{g}_{\text{f, CH}_3\text{OH}} \right] \quad (2.8)$$

where:

\bar{g}_{f} , Gibbs free energy per mole of chemical species

2.4.2.2 Reversible potential

If the system is in equilibrium, which implies reversibility in terms of thermodynamics, the electrical work is equivalent to the Gibbs free energy, as shown in Equation 2.7. The electrical work done in the fuel cell is defined by moving the electrons round the external circuit through a potential difference, E . Therefore, the Gibbs free energy represents the maximum amount of energy available to do work; it also relates to the potential, as shown in Equation 2.9. In this state, a fuel cell reaches maximum potential, which is called the reversible potential. The potential of the system is measured in volts [29, 61, 81].

$$\Delta\bar{g}_{\text{f}} = W_{\text{reversible}} = -nFE_{\text{reversible}} \quad (2.9)$$

where:

$E_{\text{reversible}}$, reversible potential of fuel cell

n , number of electrons transferred for each molecule of fuel

F , Faraday constant (charge of a mole of electrons, $96,485 \text{ J V}^{-1} \text{ mol}^{-1}$)

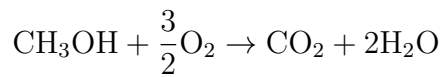
Rearranging the equation,

$$E_{\text{reversible}} = -\frac{\Delta\bar{g}_f}{nF} \quad (2.10)$$

If the system is at standard temperature and pressure (STP)², the reversible potential and the Gibbs free energy per mole at this state are indicated in E° and $\Delta\bar{g}_f^\circ$, respectively.

2.4.2.3 Open circuit voltage

From the overall electrochemical reaction of DMFC in Equation 2.3, a Gibbs free energy change of $-702.35 \text{ kJ mol}^{-1}$ under STP and six electrons have been released from the oxidation of each methanol molecule.



$$\begin{aligned} \Delta\bar{g}_f^\circ &= [2\Delta\bar{g}_{f, \text{H}_2\text{O}}^\circ + \Delta\bar{g}_{f, \text{CO}_2}^\circ] - \left[\frac{3}{2}\Delta\bar{g}_{f, \text{O}_2}^\circ + \Delta\bar{g}_{f, \text{CH}_3\text{OH}}^\circ \right] \\ &= [2(-237.13) + (-394.36)] - \left[\frac{3}{2}(0) + (-166.27) \right] \\ &= -702.35 \text{ kJ mol}^{-1} \end{aligned}$$

Substitute these factors into Equation 2.10:

$$\begin{aligned} E_{\text{reversible}}^\circ &= -\frac{\Delta\bar{g}_f^\circ}{zF} \\ &= \frac{-702.35}{(6)(96,485)} \frac{(\text{J mol}^{-1})}{(\text{J V}^{-1} \text{ mol}^{-1})} \\ &= 1.21 \text{ V} \end{aligned}$$

²Standard temperature and pressure are 298 K and 1 atm, respectively [61].

The reversible potential 1.21 V is the maximum potential of DMFC [79]. It is obtained when there is no electrical energy loss in the cell or no current is drawn from the cell. The potential at this state is also called the open circuit voltage (OCV) [81].

2.4.2.4 Maximum efficiency

The efficiency of the fuel cell, ε , is identified as the useful energy that can produce work compared with the energy produced from a combustion of fuel, change in enthalpy of formation [29, 61, 82, 83].

$$\varepsilon = \frac{\text{Work}}{\Delta \bar{h}_f} \quad (2.11)$$

The maximum electrical energy available to do work is equal to the change in Gibbs free energy.

$$\varepsilon = \frac{\Delta \bar{g}_f}{\Delta \bar{h}_f} \times 100\%$$

where:

ε , efficiency of fuel cell

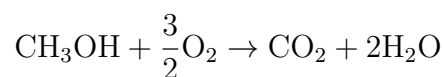
\bar{g}_f , Gibbs free energy per mole of chemical species

\bar{h}_f , enthalpy per mole of chemical species

For fuel cell operating at standard temperature and pressure (STP), the Gibbs free energy and the enthalpy are presented in term of \bar{g}_f° and \bar{h}_f° , respectively.

$$\varepsilon = \frac{\Delta \bar{g}_f^\circ}{\Delta \bar{h}_f^\circ} \times 100\% \quad (2.12)$$

The enthalpy of formation for methanol oxidation is calculated as:



$$\begin{aligned}
\Delta \bar{h}_f^\circ &= [2\Delta \bar{h}_{f, \text{H}_2\text{O}}^\circ + \Delta \bar{h}_{f, \text{CO}_2}^\circ] - \left[\frac{3}{2}\Delta \bar{h}_{f, \text{O}_2}^\circ + \Delta \bar{h}_{f, \text{CH}_3\text{OH}}^\circ \right] \\
&= [2(-285.83) + (-393.51)] - \left[\frac{3}{2}(0) + (-238.86) \right] \\
&= -726.31 \text{ kJ mol}^{-1}
\end{aligned}$$

Substitute the factors into Equation 2.12. The maximum efficiency of DMFC is 96.70%.

$$\begin{aligned}
\varepsilon &= \frac{-702.35}{-726.31} \times 100\% \\
&= 96.70\%
\end{aligned}$$

The efficiency of fuel cell can be compared to the internal combustion engines (ICE) which converts chemical energy into mechanical energy. A combustion of hydrocarbon fuel by increasing a temperature of reaction releases gases. An expansion of gas products turn the pistons to generate mechanical work. The ICE maximum efficiency is illustrated by Carnot efficiency [32, 62, 83], ε , as:

$$\begin{aligned}
\varepsilon_{\text{Carnot}} &= \frac{\text{Work}}{\Delta H} \\
&= \frac{T_1 - T_2}{T_1} \tag{2.13}
\end{aligned}$$

where:

$\varepsilon_{\text{Carnot}}$, Carnot efficiency

Work_{ICE} , reversible work of the internal combustion engines

ΔH , enthalpy of reaction

T_1 , the absolute temperature at the engine inlet (K)

T_2 , the absolute temperature at the engine exit (K)

Considering the fuel cell efficiency from Equation 2.12, there are convenient using

the plain forms of Gibbs free energy and enthalpy to compare with the ICE efficiency.

$$\begin{aligned}\varepsilon &= \frac{Work}{\Delta H} = \frac{\Delta G}{\Delta H} \\ &= \frac{\Delta H - T\Delta S}{\Delta H}\end{aligned}\quad (2.14)$$

where:

T , temperature for the operation of fuel cell(K)

H , enthalpy

S , entropy

$T\Delta S$, heat exchanged with the external environment

From Equation 2.14, the enthalpy which is not converted into electrical energy but transform to heat increase with fuel cell temperature [29]. Equation 2.13 and 2.14 demonstrate that the ICE efficiency increases with the temperature; otherwise, low operation temperature provides the maximum fuel cell efficiency [29, 62] as seen in Figure 2.11.

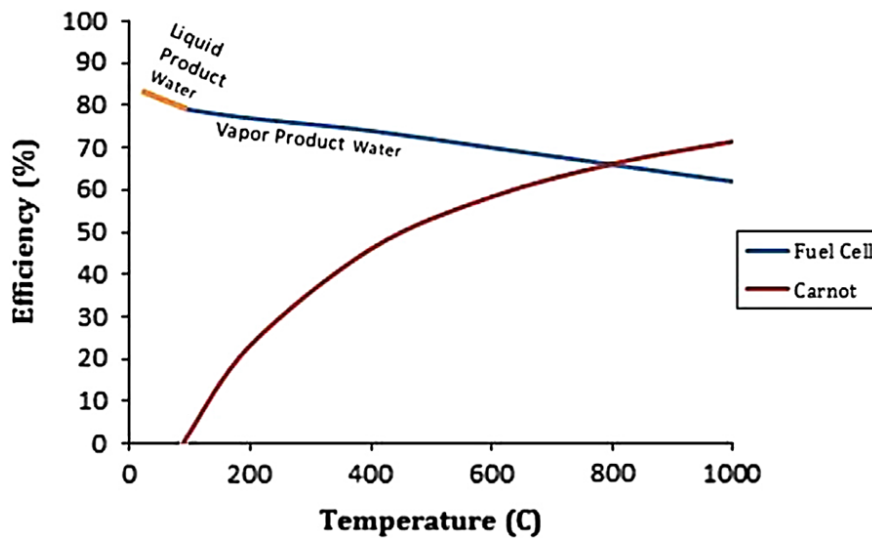


FIGURE 2.11: Comparison of ideal fuel cell efficiency and Carnot efficiency (using temperature of 90 °C) as a function of temperature [32]

2.4.3 Performance

A fuel cell's performance is monitored using a polarization curve of current density plotted as a function of cell voltage. This is commonly called the j - V curve. The current produced in the electrochemical reaction is proportional to the active area of the fuel cell. To compare the performances of differently sized fuel cells, current density (current per unit area) is applied instead of current [61]:

$$j = \frac{i}{A}$$

where:

j , current density (A cm^{-2})

i , current (A)

A , area (cm^2)

The voltage drop in the polarization curve results from the irreversible processes in the fuel cell system [29]. As shown in Figure 2.12, the polarization curve can be divided into three parts to show the causes of cell potential losses.

2.4.3.1 Part I: Activation loss

The initial part of the polarization curve relates to activation loss. The potential drops dramatically when a low current density is applied because of the slow kinetic reaction at the electrode surfaces. The produced voltage is lost to drive the electrochemical reaction in fuel cell [29, 61, 62, 82, 84]. The activation loss is given in the Tafel equation, as follows:

$$\eta_{\text{act}} = \frac{RT}{\alpha nF} \cdot \ln \left(\frac{j}{j_0} \right) \quad (2.15)$$

where:

η_{act} , activation loss

R , gas constant ($8.314 \text{ J mol}^{-1} \text{ K}^{-1}$)

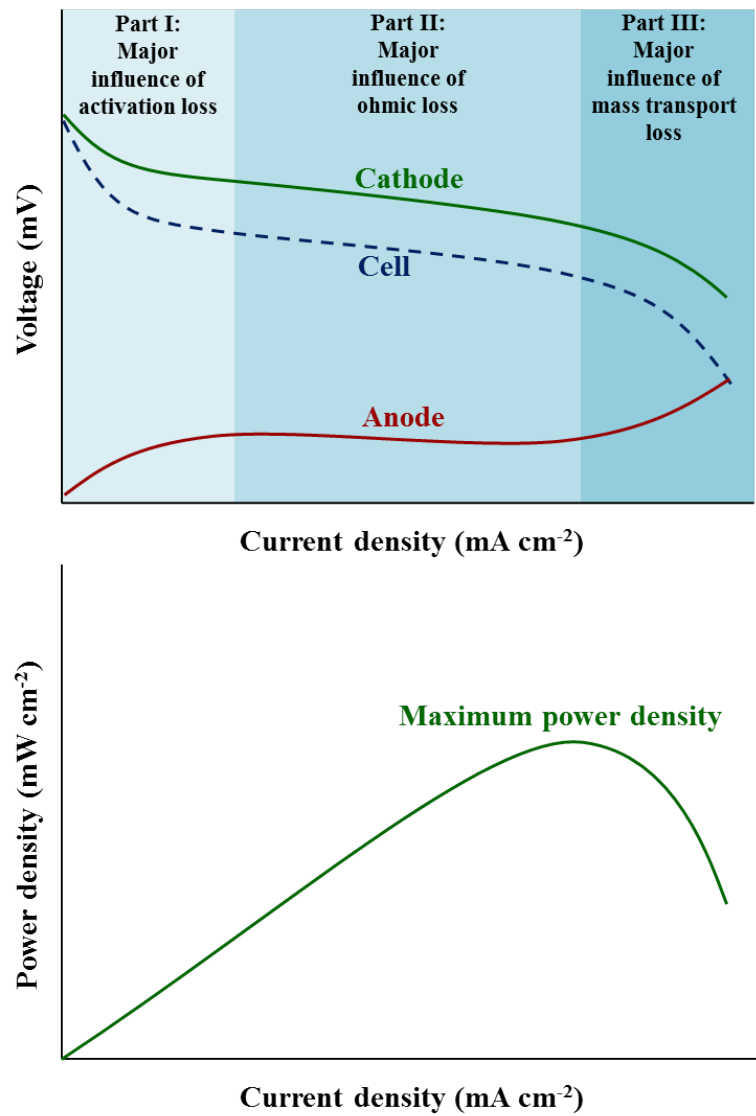


FIGURE 2.12: Polarization curve and power density curve of fuel cell (adapted from [62])

T , temperature (K)

α , charge transfer coefficient

n , number of electrons transferred per mole of reactant

F , Faraday constant ($96,485 \text{ J V}^{-1} \text{ mol}^{-1}$)

j , current density

j_0 , exchange current density

2.4.3.2 Part II: Ohmic loss

The ohmic loss is represented in a slope at middle region of the j - V curve [85, 86]. In complete fuel cell structure, both electron and proton produced from the electrochemical reaction are transferred from anode to cathode side. Charge transport through the MEA result in a ohmic loss due to the intrinsic resistance of electrons transferring through the electrodes and the external circuit. Also included is the resistance of the electrolyte membrane when protons flow through it. This part of the curve is linear and follows Ohm's law [29, 61, 62, 82, 86–88].

$$V = ir \quad (2.16)$$

where:

V , voltage

i , current

r , resistance

2.4.3.3 Part III: Mass transport loss

Mass transport or concentration loss has considerable influence on the final section of the graph. The cell potential drops rapidly, owing to a change in concentration of the reactants at the surface of the electrodes. At high current density, a large amount of reactant is consumed, leading to a low concentrations of reactant near the electrode surface and limiting transportation of fresh reactants to the electrode active sites, yielding a drop of voltage to zero. The current density at zero voltage is called the limiting current density [29, 62, 82].

$$\eta_{\text{conc}} = \frac{RT}{nF} \cdot \ln \frac{j_L}{j_L - j} \quad (2.17)$$

where:

η_{conc} , concentration loss

R , gas constant (8.314 J mol⁻¹ K⁻¹)

T , temperature (K)

n , number of electrons transferred per molecule of reactant

F , Faraday constant (96,485 J V⁻¹ mol⁻¹)

j_L , limiting current density

j , current density

The fuel cell operating potential and potential losses are summarized in Equation 2.18 and Figure 2.13 [61, 89]

$$V = E_{\text{reversible}} - \eta_{\text{act}} - \eta_{\text{ohmic}} - \eta_{\text{conc}} \quad (2.18)$$

where:

V , operating voltage

$E_{\text{reversible}}$, reversible potential

η_{act} , activation loss due to reaction kinetics

η_{ohmic} , ohmic losses from ionic and electronic resistance

η_{conc} , concentration loss due to mass transport

The ideal polarization curve is constant at the OCV (Figure 2.13A), where there is no voltage loss in a fuel cell. Nevertheless, because of the voltage losses (Figure 2.13B) the magnitude of the operating voltage is always less than that of the theoretical voltage throughout the current density range (Figure 2.13C) [61].

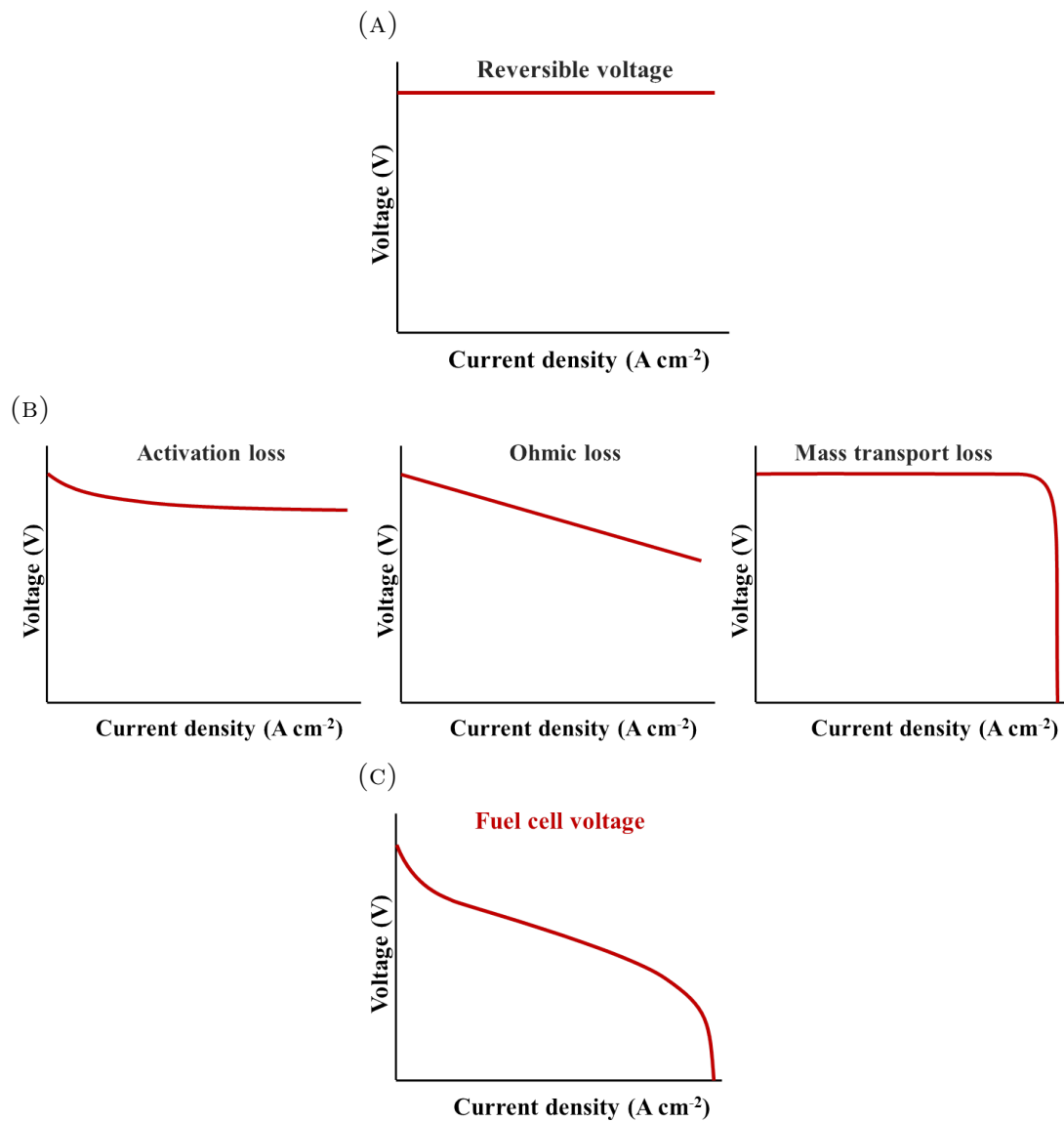


FIGURE 2.13: Influence of voltage losses on the overall fuel cell j - V performance (adapted from [61]) (A) Reversible voltage (B) Voltage losses (C) Fuel cell voltage

2.4.3.4 Methanol crossover

Methanol permeation through a membrane is a major problem limiting the DMFC performance. It not only reduces fuel utilisation at anode, but also diminishes oxidation of oxygen at cathode. Furthermore, the oxidation of methanol at cathode lowers the cathode potential as well as decreasing the cell performance

[80, 86, 87, 90, 91]. Around 40% of supplied methanol permeates from anode to cathode side during the DMFC operation. Crossover of methanol has negative influence on the open circuit voltage (OCV) by reducing the potential ~ 200 mV [61, 92] as seen in Figure 2.14. Methanol crossover rises dramatically with the increase of methanol concentration; hence, the DMFC operating at high methanol concentration could present lower OCV [86].

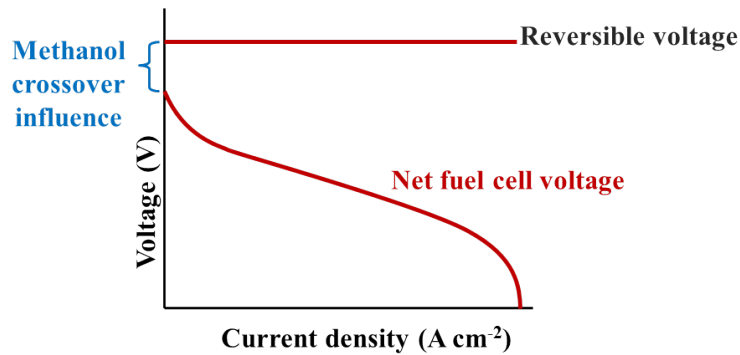


FIGURE 2.14: Influence of methanol crossover on the overall fuel cell j - V performance (adapted from [61])

2.5 Components of a direct methanol fuel cell (DMFC)

2.5.1 Membrane electrode assembly (MEA)

The crucial component of a DMFC is the MEA. The MEA can be divided into three parts: an anode, a proton-conducting membrane and a cathode. Each electrode is composed of four layers of carbon paper, microporous layer, a catalyst layer and a Nafion binding layer.

2.5.1.1 Gas diffusion layer

Porous carbon is generally coated onto a carbon paper or a carbon cloth to be used as the gas diffusion layer. This layer has two functions: to provide a support for the catalyst layer and to distribute methanol over the catalyst layer. Moreover, it conducts the generated electrical current from the catalyst segment to the current collector [93, 94] and removes carbon dioxide (Figure 2.15). It is challenging to develop an electrode with high surface area, good electrical conductivity and suitable porosity to obtain the best output of the fuel cell.

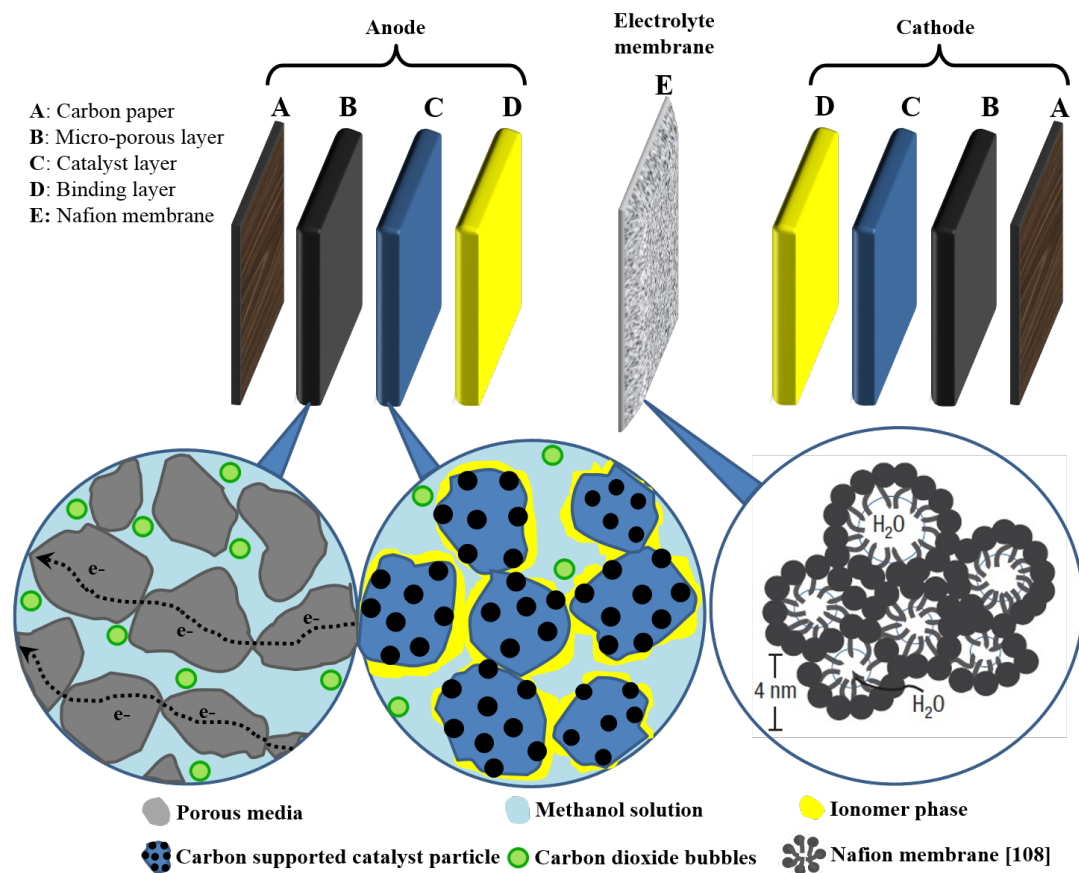


FIGURE 2.15: DMFC membrane electrode assembly (MEA)

2.5.1.2 Catalyst layer

Anode catalyst layer

A methanol molecule reacts with a water molecule at the anode triple phase boundary which consists of: (i) the Pt-Ru particles; (ii) carbon support; (iii) electrolyte region (ionomer), to release six protons, six electrons and a carbon dioxide molecule, as expressed in Equation 2.5, page 58. Electrons are conducted via carbon support to reach anode current collector. Meanwhile, protons are transported through the ionomer phase to the electrolyte membrane [78]. Nafion ionomer is added into catalyst layer in the propose of binding the carbon-supported catalyst particles to provide the proton passageway (Figure 2.15) [95, 96]. The overall oxidation reaction of a primary alcohol can be written as in Equation 2.19 [82]:



The oxidation reaction of methanol has been extensively investigated to improve the knowledge of reaction mechanisms. This reaction includes several steps, with each step producing an intermediate [82]. A scheme of the reactions is depicted in Figure 2.16.

To overcome the low DMFC performance, which is caused by the poor kinetics of the anode reaction, a catalyst is used in the electrodes to reduce an activation energy which is a required energy for proceeding a reaction (Figure 2.17). Platinum (Pt) is chosen as DMFC catalyst for its high stability and its ability to adsorb methanol under acidic conditions [29, 37, 62, 92, 97].

A scheme for methanol adsorption and deprotonation on the Pt catalyst surface is given in Figure 2.18. This scheme shows that CO is formed during the oxidation mechanism and strongly adsorbs to the Pt surface, reducing the number of available active sites of the catalyst [62, 81, 92, 98, 99].

To prevent CO deactivation, Pt-based alloy such as platinum-ruthenium (Pt-Ru) is used. The participation of Ru promotes a bi-functional mechanism [99, 100]:

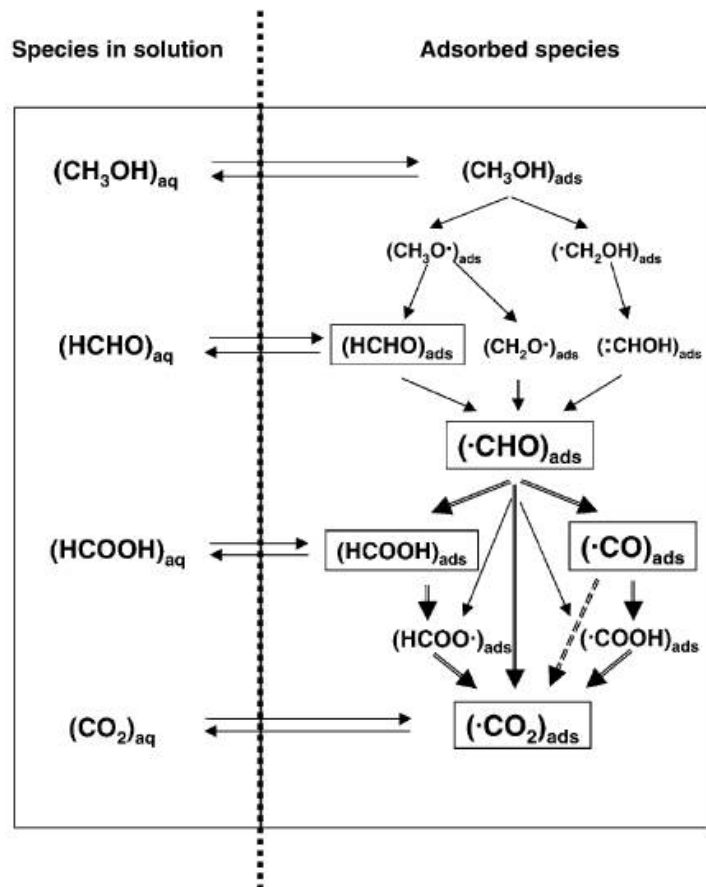
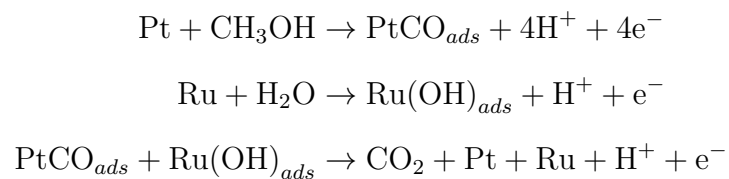
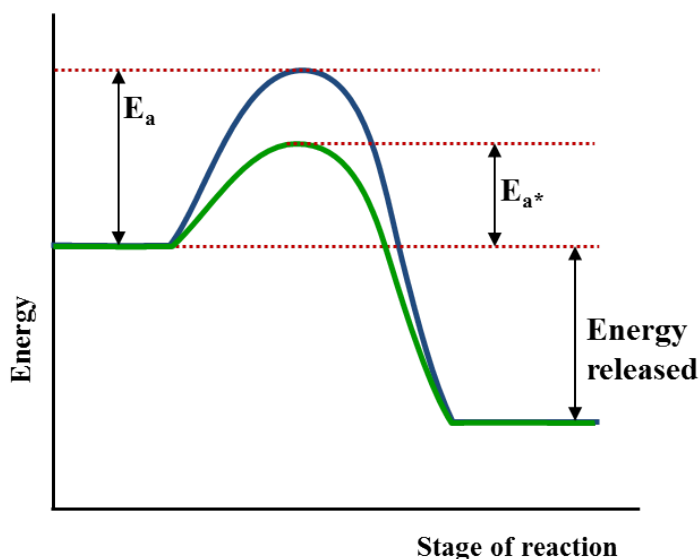


FIGURE 2.16: Reaction mechanism of methanol oxidation on a platinum electrode [82]

Pt adsorbs and dissociates methanol generating the CO while Ru activates water and adsorbs OH which supports the oxidation from CO to CO₂ as seen in Figure 2.19. Due to Ru provides OH adsorption at lower potential (0.35 V) than pure Pt does (0.75 V) [100], the Pt-Ru alloy reduces CO poisoning by the rapid oxidation of CO [98, 100–105]. The mechanisms are:





E_a Activation energy without catalyst

E_{a^*} Activation energy with catalyst

FIGURE 2.17: Activation energy of reaction without and with catalyst

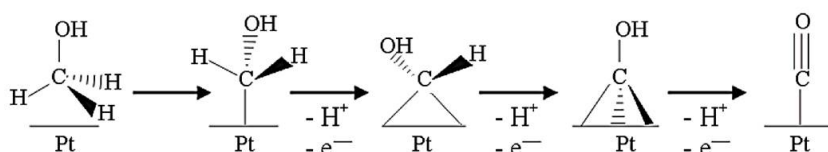


FIGURE 2.18: Scheme of methanol oxidation on Pt surface, showing consecutive stripping of hydrogen atoms [62]

During the electrochemical reaction, methanol should be provided to the catalyst's active site; moreover, electrons generated from a reaction must be taken away from the reaction site. The main requirements of a good catalyst layer are porosity and electrical conductivity; therefore, a catalyst metal is dispersed on a carbon support material [29]. Electronic conductivity is usually achieved by supporting the catalyst particles on carbon [62]. The microstructure of fuel cell catalyst is shown in Figure 2.20.

Cathode catalyst layer

The cathode is supplied with air or oxygen. A Pt catalyst is also used on the

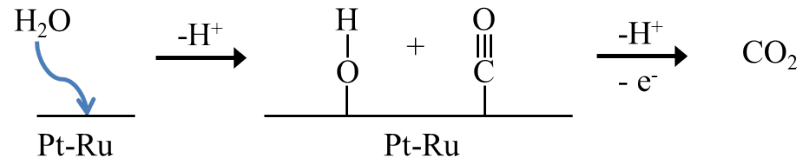


FIGURE 2.19: Scheme of CO oxidation on Pt-Ru catalyst surface (adapted from [106])

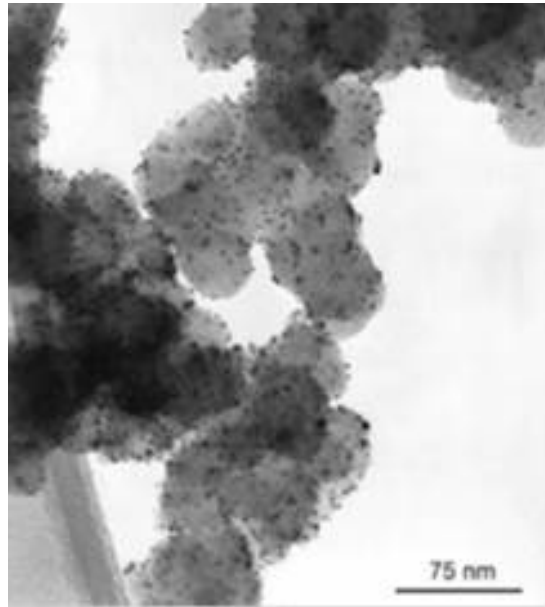
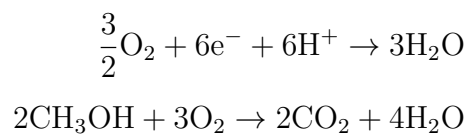


FIGURE 2.20: TEM image showing the microstructure of fuel cell catalysts [29].

cathode, to improve oxygen reduction. Oxygen is reduced on the cathode side; also methanol crossing from the anode to the cathode is oxidized at this electrode, resulting in a mixed potential and reducing the overall cell efficiency [37, 91]. To increase power output and improve opportunities for fuel cell commercialization, one target is to reduce fuel crossover by using an electrolyte which is less fuel permeable while providing good proton conduction.



2.5.1.3 Electrolyte membrane

The anode and cathode are separated by an electrolyte membrane for exchanging protons and preventing methanol transportation from anode to cathode. This membrane must be highly proton conductive, impermeable to methanol, electrically resistive and chemically stable [29, 107]. The commercial Nafion membrane has been intensively used as a standard solid polymer electrolyte in DMFC, owing to its high proton conductivity and excellent chemical stability. The molecular structure of Nafion is presented in Page 43.

Figure 2.21 shows two separate phases of the hydrophobic backbone and hydrophilic sulfonate domain in Nafion morphology [107]. The sulfonate branches are organized into parallel cylinder water channels. These inverted-micelle cylinders are stabilized externally by the backbone segments [108].

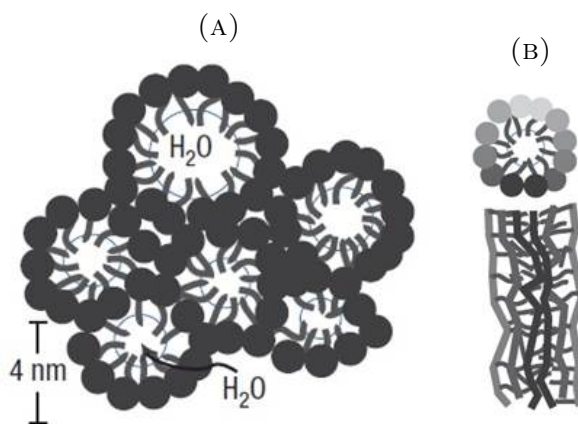


FIGURE 2.21: Parallel water channel morphology of hydrated Nafion (A) Packing of several inverted-micelle cylinders (B) Side view of an inverted-micelle cylinder [108]

A Nafion membrane conducts protons but repels electrons by the negative charge, SO_3^- , of the water channels. Unfortunately, this cation exchange membrane has a limit in that it is proton conductive only in humid conditions [108, 109]. Thus, proton conductivity increases with increasing water content in Nafion [110]. There is 0.0133 S cm^{-1} for Nafion 117 at $30 \text{ }^\circ\text{C}$ and 100% relative humidity [111].

Proton transportation through a Nafion membrane is described by two proposed mechanisms.

2.5.1.4 Proton hopping or the Grotthuss mechanism

The sulfonate ionic domains are swollen when Nafion is immersed in water to provide channels for proton transportation. In the Grotthuss mechanism, a proton produced at the anode bonds to an oxygen atom in a water molecule, forming a hydronium ion, and then one of the hydrogen atoms in this hydronium ion ‘hops’ onto another water molecule [109, 111–114]. This hopping mechanism continues along the water channel, promoting proton migration across the membrane. The hopping mechanism is presented in Figure 2.22(A).

2.5.1.5 Diffusion or vehicular mechanism

In this mechanism, a proton first bonds to a water molecule to form $(\text{H}^+(\text{H}_2\text{O})_x)$. Afterwards, the hydrated proton diffuses through the membrane in response to potential differences [109, 111, 113]. The mechanism is shown in Figure 2.22(B). Water transport through the membrane can also be achieved through two mechanisms. Electro-osmotic drag occurs when protons pull water through the membrane, or water may diffuse along a concentration gradient [111].

Methanol crossover through electrolyte membrane

As the methanol solution is fed to the anode, the methanol also diffuses across the Nafion membrane to the cathode. It combines with water molecules, $(\text{CH}_3\text{OH})_m(\text{H}_2\text{O})_n$, bonds to protons, $\text{H}^+(\text{CH}_3\text{OH})_y$, or associates with itself, $(\text{CH}_3\text{OH})_z$, and then it is oxidized at the cathode region, resulting in a mixed potential and reducing the overall cell efficiency [110]. There is around 40% of feeding methanol fuel crossing over at the membrane, which is effectively wasted fuel [115].

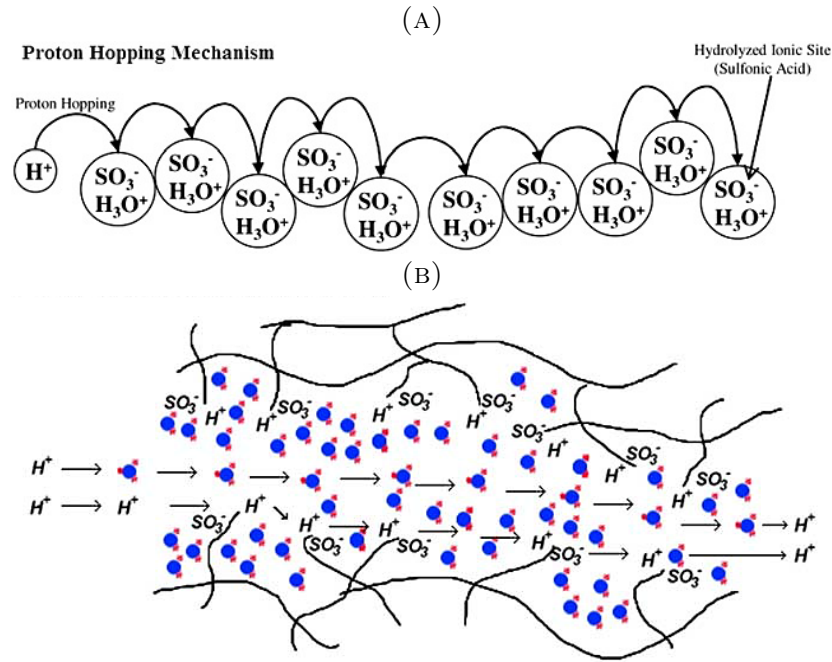
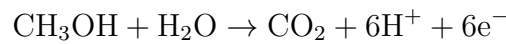


FIGURE 2.22: Proton transportation through Nafion membrane
 (A) Proton hopping or the Grotthuss mechanism [111]
 (B) Diffusion or vehicular mechanism [109]

When methanol reaches the cathode side, it is oxidised as seen in Equation 2.3. The products from methanol oxidation such as organic residues and carbon monoxide can cause blocking of catalyst surface [116].



Moreover, the reaction between methanol and oxygen takes place as follows [116]:



The operation of DMFC at 100 mA cm^{-2} , $80 \text{ }^\circ\text{C}$, 0.5 M methanol concentration and $5 \text{ cm}^2/\text{min}$ methanol flow rate illustrates methanol conversion at 47% with low cell potential at 534 mV [87]. The methanol permeability of Nafion is $1.0106 \text{ cm}^2 \text{ S}^{-1}$.

Chapter 3

Development of the direct methanol fuel cell (DMFC)

As discussed in Section 2.4.3, the theoretical performance of a DMFC cannot be attained because of potential losses in its constituent parts, including those due to the influence of methanol crossover (Figure 3.1).

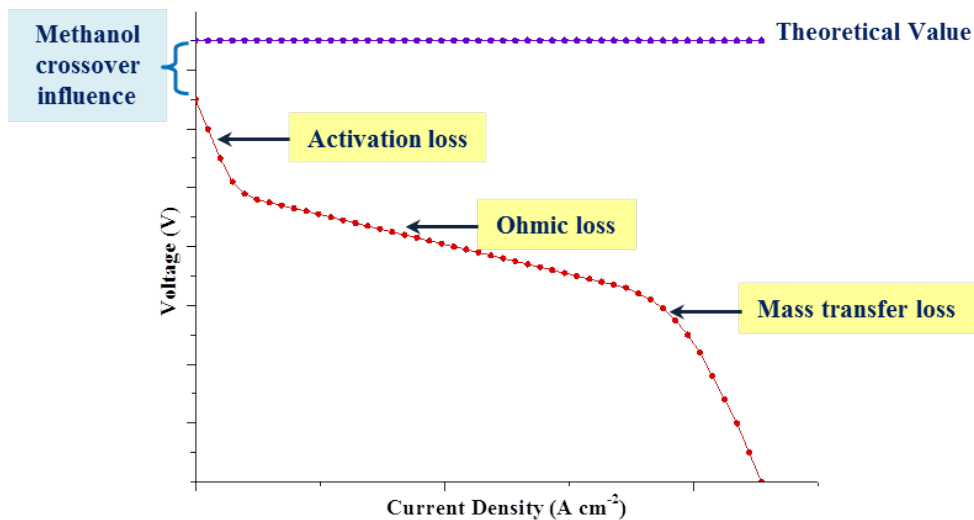


FIGURE 3.1: Polarization curve

The approximate voltage losses determined by Zainoodin *et al.* [94] are summarized in Figure 3.2. There is much research into developing new DMFC materials, to eliminate voltage losses and improve DMFC performance. The development of DMFC components is also discussed in this chapter.

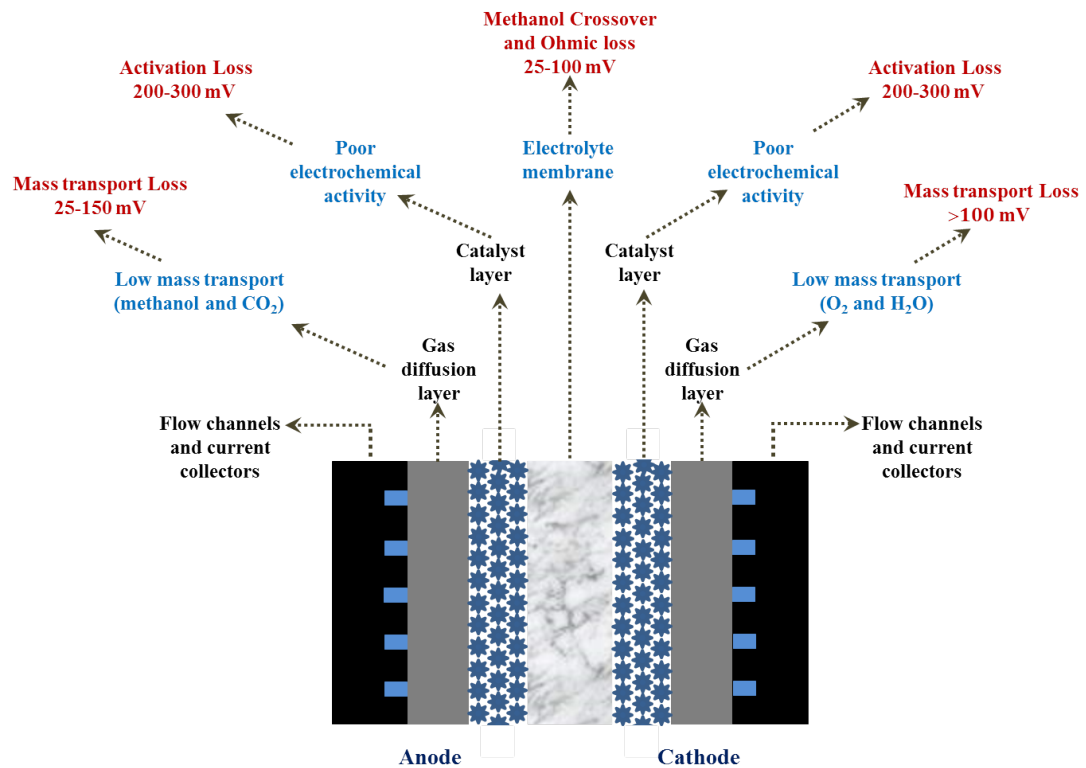


FIGURE 3.2: Potential loss in DMFC

3.1 Development of direct methanol fuel cell to reduce activation loss

In a DMFC, the maximum cell voltage suffers from activation loss, which is caused by low electrochemical activity at both the anode and the cathode. Carbon-supported platinum (Pt/C) is current the best anode catalyst material for DMFCs. However, the major drawbacks of high cost and low durability are a concern [79, 117]. Therefore, many novel Pt structures, alternative catalyst supports and

new catalysts have been developed, to enhance electrochemical activity while reducing catalyst loading.

3.1.1 Improvements in anodic catalyst materials

Rauber *et al.* [118] reported a method to fabricate a three-dimensional Pt nanowire catalyst using hard templates. The network of nanowires provides a continuous three-dimensional porous structure, which promotes easy access of reactants to the catalyst active area and good electron transport; thus, it is suitable for catalysing methanol oxidation. The electrocatalytic activity of the Pt nanowire network was studied in 0.5 M methanol solution and 0.5 M H₂SO₄ at room temperature, and anodic current density peaks of 0.76, 0.39 and 0.24 mA cm⁻² were achieved for Pt nanowire, platinum black and carbon-supported Pt nanoparticles, respectively. The better activity of Pt nanowires, resulting from a reduction of interfaces between the electrocatalysts, as compared with nanoparticles, produced excellent electronic conductivity [79].

Although Pt has acceptable electrocatalytic activity, it still carries drawbacks of high cost and poisoning from intermediate CO formed during the oxidation reaction. It is important to use a Pt-based alloy, such as PtRu [119, 120], PtAu [121], PtPd [122–124], PtCo [125] to decrease Pt loading but increase poisoning tolerance. Wang *et al.* [123] synthesized Pd/Pt core-shell nanowire arrays with very high specific surface areas. The electrochemically active area of Pd/Pt core-shell nanowires in comparison with commercial carbon-supported PtRu (PtRu/C) are 6791 and 349 m² g⁻¹, respectively. The electrocatalytic activity of Pd/Pt core-shell nanowires (22.7 mA cm⁻²) is four times that obtained for PtRu/C (5.4 mA cm⁻²). Palladium can reduce poisoning by removing CO intermediates from the Pt shell. It is an oxophilic metal, thus it is available to promote CO removal by forming active oxygen-containing species (e.g., PdO/PdOx). Long *et al.* [124] also prepared a series of Pt/Pd core-shell bimetallic catalysts, for which the highest current was observed at 1.5×10^{-3} A cm⁻².

3.1.2 Improvements in cathodic catalyst materials

Several non-precious metal catalysts were tested for oxygen reduction at the cathode to maintain the low cost of fuel cell manufacture. In addition, it is known that the diffusion of methanol from the anode to the cathode is the main problem in reducing DMFC potential and improving fuel cell efficiency because of the voltage loss from methanol oxidation at the cathode [126]. The challenge lies in constructing a cathode catalyst that is selective for oxygen reduction in the competition between O_2 and crossover methanol. For example:

Piela *et al.* [127] aimed to produce a high-selectivity catalyst that could maintain current densities over 0.1 A cm^{-2} at cell potentials higher than 0.4 V. The catalyst comprised Co_xO_y/Co particles deposited on a template of pyrolyzed cotetramethoxyphenylporphyrin (CoTMPP). Methanol-oxidation current densities measured at the cathode indicated that CoTMPP catalyst has an activity two or three times lower than Pt catalysts. This makes CoTMPP remarkable as a high-selectivity catalyst in DMFC. Other research investigated Me- N_x -type catalysts but these have lower catalytic activity and are less durable than conventional Pt catalysts [127].

Zhang *et al.* [128] compared the electrocatalytic activity toward oxygen reduction reaction (ORR) of nanoporous PdCu alloys to the commercial Pt supported on carbon (Pt/C). The ORR activity of PdCu alloys were investigated by cyclic voltammetry (CV) method in 0.1 M $HClO_4$ solution with and without 0.1 M methanol. The PdCu alloys with the Pd:Ru ratio of 1:1 enhanced specific activity compared to Pt/C catalyst. This is indicated to methanol-tolerance of the alloy. Furthermore, this PdCu alloy performed 5-fold higher for ORR activity durability than that of Pt/C catalyst.

3.1.3 Improvements in catalyst support materials

One major limitation of a Pt catalyst supported on a carbon carrier is the low effective surface area, leading to its unfavourable utilization and electrocatalytic activity [79, 117]. Currently, commercial preparations of carbon black, such as Vulcan XC-72R (Cabot, $250 \text{ m}^2 \text{ g}^{-1}$), Shawinigan Black (Chevron, $80 \text{ m}^2 \text{ g}^{-1}$), Black Pearl 2000 (Cabot, $1500 \text{ m}^2 \text{ g}^{-1}$), Ketjenblack (AkzoNobel, $1270 \text{ m}^2 \text{ g}^{-1}$) are widely used for the Pt catalyst support. These particles consist of near-spherical graphite of $<50 \text{ nm}$ diameter. However, there is a disadvantage, owing to the structures of these particles. The deep micropores of carbon black trap the catalyst particles, reducing their catalytic activity [129]. In a new approach, the dispersal of Pt nanoparticles is improved with high surface area materials, for example the two-dimensional nanostructures of carbon nanotubes and graphene [79]. Because the high surface area of the catalyst particles facilitate reactant diffusion, enabling interaction between catalyst particles and proton collectors (Nafion ionomer) and removing water from the catalyst layer, it can restrict the activation loss in DMFCs [117, 129].

Many studies have been devoted to the arrangement of Pt nanoparticles on carbon nanotubes, for example, electrodeposition and chemical deposition [130, 131]. Nevertheless, carbon nanotubes have a lack of binding sites for Pt, yielding poor dispersion of metal particles. For this reason, small organic molecules or polymers are introduced as bridging molecules on carbon nanotube surfaces [79, 130]. Li *et al.* [131] combined polyoxometalates as bridging molecules. It can be seen that tri-component support of Pt nanoparticles, polyoxometalate and carbon nanotubes exhibited higher electrocatalytic activity for methanol oxidation than the traditional Pt/carbon black support and the Pt/carbon nanotube system, with mass activities of Pt in the systems of 431, 137 and 96 mA mg^{-1} , respectively.

Another approach has been reported that involves the modification of graphene by nitrogen doping, to prevent the agglomeration of graphene nanosheets; better catalyst performance towards methanol oxidation was observed for this approach.

Delocalized π bonding of the nitrogen-doped support increased the number of anchoring sites for Pt nanoparticles, resulting in uniform dispersion [132]. Platinum dispersion on nitrogen-doped functionalized graphene has superior current density than achieved with non-functionalized graphene [133]. Sun and Kim [132] obtained the highest current density, 13.0 mA cm^{-2} , for Pt/N-functionalized graphene, while the result for Pt/graphene was 6.1 mA cm^{-2} . These results all suggested that functionalized graphene is promising as an effective catalyst support for DMFCs.

Alternative candidates for catalyst support are conducting polymers (CPs). Interest in CPs has increased because the heteroatom (often nitrogen) contained in the main chain of these polymers can provide an anchor site for metal catalyst atoms. Consequently, bridging molecules are not required for CP catalyst support [134]. In addition, they have a high electronic conductivity, of 10^{-6} – 10^3 S cm^{-1} . Li *et al.* [135] dispersed Pt nanoparticles on poly(*m*-phenylenediamine) (PmPD) surfaces. The backbone of PmPD contains a large amount of amino/imino ($\text{NH}_2/\text{C}=\text{NH}$) groups. These functional groups improve oxidation by forming H bonds with methanol and its intermediates, facilitating oxidation from methanol to CO_2 . Results indicate that Pt/PmPD have excellent catalytic activity and satisfactory poisoning tolerance towards methanol oxidation, compared with Pt/glassy carbon electrodes.

3.2 Development of direct methanol fuel cell to reduce ohmic loss

3.2.1 Ohmic loss in Nafion electrolyte membrane

For DMFC, proton transport resistance causes more ohmic loss excess than does electron transport resistance [85, 136]. The electron conductivity of gas diffusion layer ($1000 \text{ } \Omega^{-1} \text{ m}^{-1}$) is much higher than the proton conductivity of Nafion

membrane ($10 \Omega^{-1} \text{ m}^{-1}$) [78]. Consequently, the main sources of ohmic loss are from the intrinsic membrane resistance and the interface contact between the Nafion membrane and the anode and cathode catalyst layers. The ohmic loss due to electron conduction is neglected. Moreover, the water content of the fuel cell also influences proton migration in the membrane. Dry membranes yield high ohmic resistance, which is represented as a large slope in the j - V curve and a low limiting current density. This means that the ohmic loss is linked to the conductivity of the electrolyte membrane [85, 136].

3.3 Development of direct methanol fuel cells to reduce mass transfer loss

The mass transfers involved in DMFCs can be separated into three groups, that is, mass permeating through a membrane, mass transport at the anode and mass removal at the cathode [93].

3.3.1 Mass transport through the membrane

Since the reactants (methanol and water) permeate through the membrane, it minimizes DMFC performance by reducing the cell voltage. Water crossover through the membrane via electro-osmotic drag from protons and diffusion along the water concentration gradient can cause flooding problems at the cathode in addition to swelling of the membrane [93, 137]. The former problem prohibits oxygen reduction at the cathode active site, while the latter issue reduces the durability of the membrane.

3.3.2 Mass transport at the electrodes

At high operating currents, DMFCs consume large amounts of both methanol and oxygen; therefore, the flow-field plate and the microporous carbon layer are essential compartments, delivering fresh reactants to the active catalyst surface. At the same time, waste products must be removed from the active site [85]. Insufficient mass transport constrains the electrochemical reactions, producing a small limiting current density in the fuel cell [85, 90].

When the methanol feed is less than 1 M, the anode performance is limited by the mass transport of methanol to the active catalyst layer. This problem can be solved by increasing the supply of methanol solution from the fuel flow field to the carbon layer. Conversely, to improve the methanol diffusion coefficient by decreasing the diffusion distance, the GDL should be thinner and more porous. Furthermore, carbon dioxide bubbles produced in the catalyst layer should be immediately removed to prevent blocking of methanol from the reaction area [94, 138].

3.3.2.1 Improvements in electrode morphology

The gas diffusion layer (GDL) consists of two layers. First, there is a backing layer, which is normally made of carbon cloth or carbon paper. Second is a microporous layer (MPLs), which is made of hydrophobic polymer and carbon powder [93]. Excellent electronic conductivity and good reactant diffusion properties are required for the GDL [94].

Owing to the dominant role of electrode morphology in the mass transfer loss of a fuel cell, the control of pore structure and thickness for MPLs in the cathode GDL causes the improvement in DMFC performance. Park *et al.* [139] studied the effect of two types of electrode structure, modified cathode MPL and commercial cathode MPL, on fuel cell performance. The modified-MPL exhibited

higher power density of 117 mW cm^{-2} at 0.4 V and $70 \text{ }^\circ\text{C}$. Hence, the combination electrochemical analysis and physicochemical investigations was discussed. Air permeability of MPLs were 31.0 and $21.7 \text{ cm}^3 \text{ cm}^{-2} \text{ s}^{-1}$ for modified-MPL and commercial-MPLs, respectively. The two MEAs had different pore size distributions of 40 nm – $1 \mu\text{m}$ for a commercial-MPLs and 2060 nm for modified-MPL. Smaller pore size in modified-MPL increased the hydraulic pressure in cathode resulting in a low water and methanol crossover flux. This phenomenon would have positive influence on cell performance. This experiment suggested that control of the microporous layer in the cathode had impact on mass transport and also affected to the performance of fuel cell.

Gao *et al.* [140] investigated influences of a carbon-nanotube-based GDL on mass transfer ability. Their results confirmed that a carbon-nanotube-based GDL had better mass transfer ability and more abundant pores (1000 – 3000 nm in diameter) than a commercially produced Toray GDL. There was a remarkable 40% increase in limiting current density (350 mA cm^{-2}) and 27% better power density (76 mW cm^{-2}) for the carbon-nanotube-based GDL over the Toray GDL.

Wang *et al.* [141] improved the hydrophilic character of the anode diffusion layer by nitrated treatment. To investigate the influence of hydrophobicity or hydrophilicity of the diffusion layer on the DMFC performance, three anode microporous layers were prepared: a layer of hydrophobic carbon black with a hydrophobic additive, a layer of hydrophobic carbon with a hydrophilic additive and a layer of hydrophilic nitrate-treated carbon black with a hydrophilic additive. Their power densities were 221 mA cm^{-2} , 240 mA cm^{-2} and 260 mA cm^{-2} , respectively. Therefore, it is favourable to use a hydrophilic anode diffusion layer in DMFCs.

3.3.2.2 Improvements in the reactant flow field

The DMFC reactant flow fields are normally made from graphite plate because of its electrical conduction. To reduce mass transport loss, the reactants and the

products migration to and from the membrane electrode assembly (MEA) should be effective and continuous. The main component to serve this function is the flow field. The different flow channel in DMFC have been studied. The main types of flow field are shown in Figure 3.3 [93]. During the fuel cell operation, product gas bubbles transport in the flow channel. Lu *et al.* [142] suggested that gas bubbles were held on the carbon paper by surface tension before detachment. The bubbles may block mass transfer of MEA. Many researches was found that the serpentine flow field has better CO₂ removal than the parallel flow field [37, 93, 143–146]. From this reasons the serpentine flow channel is used in this research.

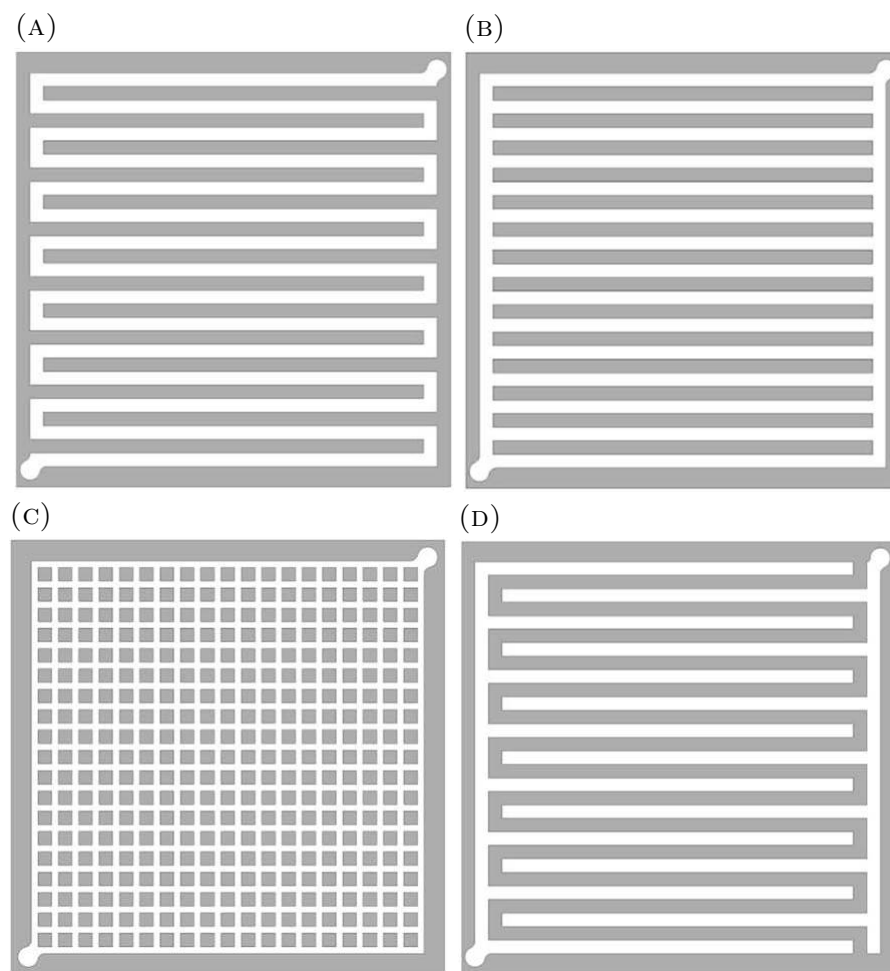


FIGURE 3.3: Different flow fields for direct methanol fuel cell (A) Serpentine (B) Parallel (C) Spot (D) Interdigitated [93]

In addition of the flow channel design, the influence of cathode flow field wettability on the performance of DMFCs was investigated by Schröder *et al.* [147]. It is known that the oxygen reduction at the cathode produces water and that discontinuous removal of water from the cathode channel can block the oxygen supply, leading to a decrease in fuel cell performance. The wettability of the cathode channel walls has an influence on the distribution of water. To prove this, Schröder *et al.* [147] modified the graphite cathode flow fields individually as hydrophobic, hydrophilic or untreated, and measured the contact angles as 26.2°, 126.8° and 115.9°, respectively. It turns out that hydrophilic channels enhance DMFC performance by enabling water removal, thereby preventing oxygen restriction.

3.4 Development of direct methanol fuel cell to reduce methanol crossover

3.4.1 Methanol crossover in Nafion membrane

The most commonly used electrolyte membrane in DMFCs is perfluorosulfonic acid (PFSA) polymer membrane and the most used PFSA is Nafion membrane. The characteristics of Nafion membrane¹ are shown in Table 3.1.

TABLE 3.1: Characteristics of Nafion membranes [60]

| Membrane | Thickness ($\times 10^{-6}\text{m}$) | Methanol crossover rate ($\text{mol s}^{-1} \text{cm}^{-2}$) | Methanol diffusion coefficient ($\text{s}^{-1} \text{cm}^{-2}$) |
|------------|---|--|---|
| Nafion 112 | 51 | 15.3×10^{-8} | 7.8×10^{-7} |
| Nafion 115 | 127 | 9.3×10^{-8} | 11.8×10^{-7} |
| Nafion 117 | 178 | 7.2×10^{-8} | 12.8×10^{-7} |

¹The numbers of Nafion membrane are defined as an equivalent weight (Grams of dry polymer/Mole of HSO_3 groups) and a thickness (in thousandths of an inch) of the membrane e.g. Nafion 117 refers to the membrane which has 1100 equivalent weight and thickness of 0.007 inch.

Although Nafion membranes provide advantages of mechanical strength, chemical stability and high proton conductivity ($\sim 0.1 \text{ S cm}^{-1}$) in the fully hydrated state, they also have drawbacks, such as high methanol permeability, which reduces the open circuit potential by around 0.15–0.20 V [60, 148], a limiting operation temperature of below 100 °C and high cost [149]. Methanol permeability and proton conductivity of Nafion membranes are shown in Table 3.2. Therefore, many studies have been addressed to the problem of searching for alternative membranes to replace Nafion. The required properties of DMFC electrolyte membranes are [137, 150–152]:

- High proton conductivity and low electronic conductivity to support the electrochemical reaction between the two anode and the cathode;
- Reduce methanol crossover to improve performance of cell;
- Good chemical and mechanical stability to restrict membrane degradation during the cell operation;
- Large cohesion, so that two electrodes can be combined as the MEA;
- Low manufacturing cost.

TABLE 3.2: Methanol permeability and proton conductivity of Nafion membranes

| Membrane type | Methanol permeability ($\times 10^{-6} \text{ cm}^2 \text{ s}^{-1}$) | Proton conductivity (mS cm^{-1}) | Conditions | Reference |
|---------------|--|---|-----------------------|-----------|
| Nafion 112 | 1.77 | 93 | 5 M Methanol 25 °C | [148] |
| Nafion 115 | 1.08 | 65 | 5 M Methanol 25 °C | [153] |
| Nafion 117 | 0.891 | 22.14 | 5 M Methanol 25 °C | [154] |

As mentioned in Section 2.5.1.5, page 76, methanol travels together with solvated protons through the ionic channels of the Nafion membrane. Hence, water uptake,

degree of ionic species and connectivity between ion clusters play a crucial role in proton conductivity, methanol permeability and overall membrane performance [155]. The factors relevant to MEA performance are discussed in the next section.

3.4.1.1 Water uptake

Water uptake and membrane swelling are related to the proton conductivity of the membrane [156–158]. This factor can be calculated as the difference between the weight of the dry membrane (W_{dry}) and the weight of the fully hydrated membranes (W_{wet}) as a percentage of the weight of the dry membrane [151]:

$$\text{Water uptake (\%)} = \frac{W_{\text{wet}} - W_{\text{dry}}}{W_{\text{dry}}} \times 100 \quad (3.1)$$

3.4.1.2 Electro-osmotic coefficient of the membrane

The water retention of the electrolyte membrane is represented by the electro-osmotic coefficient, which is defined as the transported water molecules as a fraction of the transported protons (Equation 3.2) [159].

$$\text{Electro-osmotic coefficient} = \frac{\text{Transported water molecules}}{\text{Transported proton ions}} \quad (3.2)$$

Water transport through the polar channels of Nafion membrane can be verified by determining the electro-osmotic coefficient (Equation 3.2). The electro-osmotic coefficient of Nafion is 2.5 $\text{H}_2\text{O}/\text{H}^+$ [159–162]. In consideration of methanol oxidation, 1 mole of oxidized methanol produces 6 moles of protons, and 6 moles of protons transported through the membrane will drag 15 moles of water together. This high water content can result in membrane swelling [150–152, 163]. Moreover, the Nafion membrane repeatedly swells and shrinks during the fuel cell operation. The high changes in membrane width when there is a

large water uptake can cause membrane failure and reduce membrane durability [137].

3.4.1.3 Membrane selectivity

This is the ratio of proton conductivity to methanol permeability [155, 156, 164, 165].

$$\text{Membrane selectivity} = \frac{\text{Proton conductivity}}{\text{Methanol permeability}} \quad (3.3)$$

Nafion has a composite structure with a hydrophobic polymer domain and hydrophilic sulfonic acid channels. It realizes proton conductivity by transporting hydrated protons through hydrophilic channels; however, methanol transport also occurs via these channels, owing to the electro-osmotic drag of methanol and hydrated protons along the diffusion gradient [157, 159]. It has been found that high selectivity between proton and methanol molecule is a satisfiable property of an electrolyte membrane. Hence, the size of hydrophilic channel could be improved to prevent methanol transport but without compromising on proton conduction. Thus, polar clusters of nanosize particles have been constructed, with the purpose of modifying the size and structure of Nafion ionic domains. In addition, the contribution of alternative membrane materials with high proportions of functional groups has attracted attention [137, 152, 155, 159].

3.4.2 Improvements in polymer electrolyte membranes

Many studies have focused on reducing the methanol permeability of electrolyte membrane by using inorganic additives to form a composite membrane, modifying the surface of the Nafion membrane or developing alternative electrolyte membranes [156].

3.4.2.1 Conventional Nafion composite membranes

The selectivity of the Nafion composite membrane can be improved by incorporating inorganic particles into Nafion hydrophilic channels. Although hydrophilic inorganic additives enhance proton conductivity and methanol blocking, they cause swelling of the composite membrane, owing to the interactions of water and the inorganic moiety (ionic, hydrogen bonding and dipole interactions). Meanwhile hydrophobic inorganic doping has the potential of preventing excessive water swelling because the repulsion with water molecules reduces proton transport via water [137, 159]. Compromises in content, good dispersion and hydrophilic or hydrophobic properties of inorganic particles has been attempted, to improve proton transport and methanol permeability but reduce membrane swelling [137, 137, 150–152, 163, 166].

Several studies have reported that the interaction of Nafion side chains with inorganic fillers, $-\text{SO}_3\text{H}\cdots[\text{M}_x\text{O}_y]\cdots\text{H}_3\text{OS}-$, restricts the flexible motion of both the hydrophilic clusters and the hydrophobic backbone of Nafion. This feature prevents excessive water swelling of the electrolyte membrane and thus reduces methanol crossover [137, 150–152, 163].

Nafion/metal oxide (M_xO_y) composite membranes

• Nafion/silica (SiO_2)

Methanol crossover is influenced by the microstructure of the sulfonate channels in Nafion; hence, modified Nafion composite membranes have been formed by distributing such inorganic particles as SiO_2 , TiO_2 , ZrO_2 , Al_2O_3 into the Nafion polymer matrix to modify its morphology.

Along with metal oxides, SiO_2 is often selected as an inorganic filler because it is chemically inert in nanoscale morphologies, provides a large surface area and is easy to use for surface modification [137, 150–152]. Composite membranes composed of Nafion and hydrophobic silica nanoparticles have been employed. Park

et al. [137] introduced 1% hydrophobic surface-treated silica (Fluorosurfactant-silica) into recast Nafion membranes. The silica nanoparticles easily dispersed homogeneously into the Nafion matrix, owing to the similarity in hydrophobic nature between the surface-treated silica and the perfluorinated domains of Nafion. Furthermore, the hydrophobic properties of the fluorosurfactant-silica repelled water molecules, reducing both water swelling and methanol permeability of the Nafion/silica composite membrane with hydrophobic fluorosurfactant-silica compared with recast Nafion membrane and Nafion/silica membrane without fluorosurfactant. The Nafion/surface-treated silica membrane delivered a maximum power density of 138 mW cm^{-2} higher than 103 mW cm^{-2} of the recast Nafion membrane with 1M methanol.

Yuan *et al.* [152] incorporated fluoroalkyl modified SiO_2 ($\text{SiO}_2\text{-F}$) into a Nafion base membrane. The $\text{SiO}_2\text{-F}$ particles could rearrange the water channels in the Nafion. As shown in Figure 3.4, the good dispersion of $\text{SiO}_2\text{-F}$ may result from the affinity between the hydrophobic fluoroalkyl group on the SiO_2 surface and the hydrophobic fluorocarbon backbone of the Nafion. This research gives an example for the reorganization of Nafion morphology.

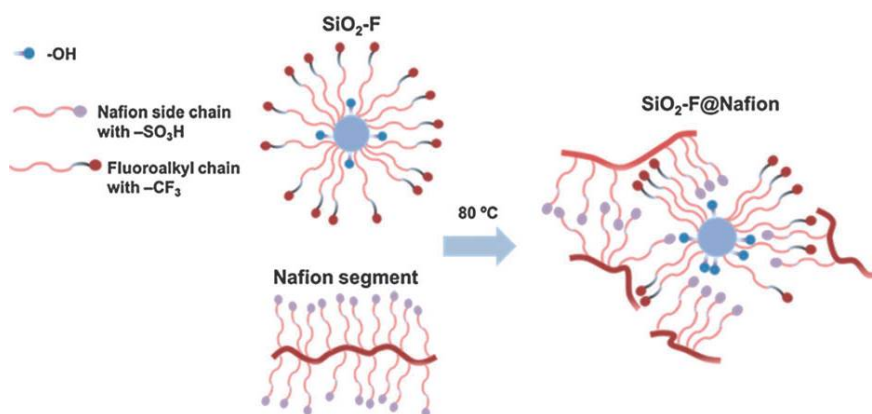


FIGURE 3.4: The affinity between the $\text{SiO}_2\text{-F}$ and the fluorocarbon backbone of Nafion [152]

Feng *et al.* [157] synthesized and then introduced 0.1–0.8 wt% of sulfonated

graphene oxide silica (SiO₂-GO-S) into the Nafion matrix. The composite membranes showed higher water uptake but lower membrane swelling than the recast Nafion membrane. It could be considered that SiO₂-GO-S maintained the membrane structure in a wet condition by suppressing the movement of polymer chains. High water retention in the composite membrane could support both the proton hopping mechanism and vehicle transportation. Moreover, the membrane containing 0.5 wt% SiO₂-GO-S had a large surface and are high connectivity of proton cluster domains. These features enhanced proton conductivity through the membrane. SiO₂-GO-S enlarged the methanol barrier effect by increasing the tortuosity in the ionic channels. An increased SiO₂-GO-S content promoted proton conductivity while reducing methanol permeation, in comparison with the recast Nafion membrane.

Lin *et al.* [156] functionalized SiO₂ with a hydrophilic perfluoroalkylsulfonic acid group. The composite membranes of Nafion/functionalized silica (M-SiO₂-SiO₃H) showed higher proton conductivity than that of pristine Nafion membrane. This could be due to the influence of M-SiO₂-SiO₃H, which was embedded in the Nafion ionic cluster, providing more proton transportation pathways compared with pristine Nafion. These phenomena are depicted in Figure 3.5. The M-SiO₂-SiO₃H filler created an alternative proton hopping route (Figure 3.5A) via the additional -SiO₃H groups on its surfaces. Furthermore, the hydrophilic -SiO₃H groups on the silica surface accelerated the vehicle mechanism, leading to enhanced proton conductivity in the composite membrane. The permeability to methanol was $4.5 \times 10^6 \text{ cm}^2 \text{ S}^{-1}$ by 30% decreased permeability from that of the original Nafion membrane, indicating that there was a longer path for methanol migration when M-SiO₂-SiO₃H particles were distributed in the ion channels of the composite membrane [156, 167]. The additive particles facilitate proton

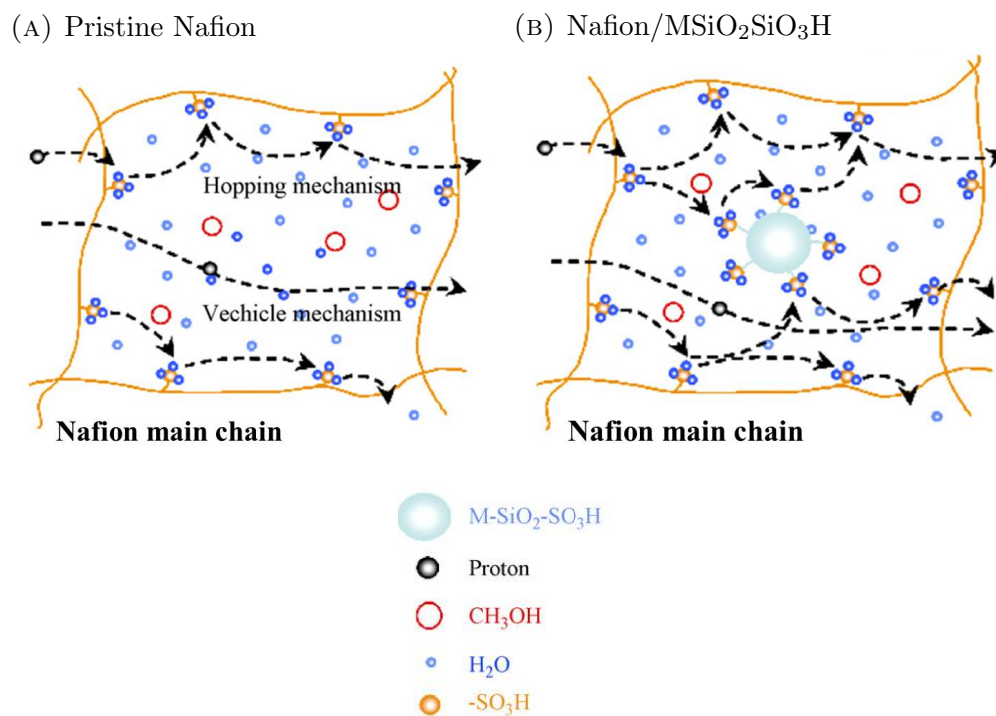


FIGURE 3.5: Proposed proton transport pathways in Nafion/MSiO₂SiO₃H composite membrane [156]

transport by providing additional ionic conduction pathways [157] and increasing water uptake in the composite membrane [111, 168]. Furthermore, dispersed fillers promote tortuosity of the transport channels of the membrane, restricting methanol migration [157, 169]. The comparison performance of Nafion/silica composite membranes are shown in Table 3.3.

TABLE 3.3: DMFC power density of Nafion/silica composite membranes

| Composite membrane | Inorganic particles (°C) | Inorganic mass (%) | Catalyst loading (mg cm ⁻²) | Methanol (M) | Methanol permeability (×10 ⁻⁶ cm ² s ⁻¹) | Proton conductivity (mS cm ⁻¹) | Current density (mA cm ⁻²) | Max. power density (mW cm ⁻²) | Ref. | |
|---------------------------|-------------------------------------|--------------------|---|---------------|--|--|--|---|-------|-------|
| Nafion/hydrophobic silica | SiO ₂ | 1 | 3 | 1 | — | — | 254 (90 °C, 0.4 V) | 103 (90 °C) | [137] | |
| | SiO ₂ -SO ₃ H | 1 | 3 | 1 | — | — | 342 (90 °C, 0.4 V) | 138 (90 °C) | | |
| | | 1 | 3 | 3 | — | — | 538 (90 °C, 0.4 V) | 229 (90 °C) | | |
| | SiO ₂ -GO-S | | 1 | 2 | — | 0.1904 (50 °C) | 10.4 (50 °C) | — | — | [157] |
| | | | 5 | 2 | — | 0.0216 (50 °C) | 34.0 (50 °C) | — | — | |
| | | | 8 | 2 | — | 0.0163 (50 °C) | 48.1 (50 °C) | — | — | |
| GO | 0.5 | 2 | 1 | 0.792 (25 °C) | 0.0400 (25°C) | — | 62 (30 °C) 141 (70 °C) | [170] | | |
| Nafion/hydrophilic silica | Core-shell SiO ₂ | 6 | 2 | 1 | — | — | — | 129.9 (60 °C) | [151] | |

GO, Graphene oxide

Nafion/two-dimensional material composite membranes**• Nafion/montmorillonite (MMT)**

Although metal oxides have the desirable property of reducing methanol cross-over, they have negative influence on proton conductivity. To block methanol migration while maintaining satisfactory proton transport, two-dimensional inorganic conducting materials, such as clay and graphene, are combined with the Nafion matrix [170, 171]. A single structure unit of montmorillonite (MMT) crystal structure is illustrated in Figure 3.6. This class of clay has a three-layered structure. There are two silica tetrahedral sheets partitioned by an octahedral sheet [171, 172]. MMT has a high molecular selectivity and good ion-exchange capability as well as a proton conductivity of around 0.296×10^{-4} S cm⁻¹ [173]. Hence, it is suitable for incorporation with Nafion ionomers to produce a methanol-resistant membrane.

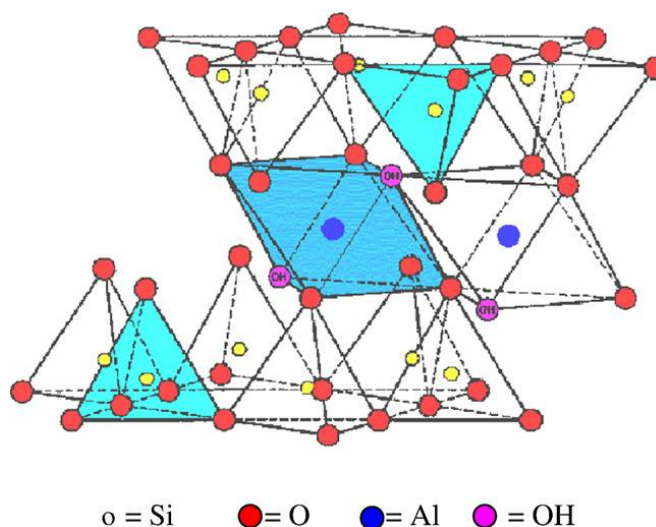


FIGURE 3.6: Crystal structure of montmorillonite [172]

Jung *et al.* [174] produced a Nafion/MMT composite membrane by the direct melt injection technique. Nafion resin and MMT were mechanically mixed and the mixture was formed into a sheet by hot pressing. Unfortunately, the OCV, proton conductivity and methanol permeability of the composite membrane were lower than pure Nafion membrane at the temperature range of 90-110 °C. Silva *et al.* [175] fabricated Nafion/MMT composite membranes using a solvent recast

procedure. These recast membranes showed higher proton conductivity than the samples of Jung; however, they had similar properties to those of commercial Nafion. Mura *et al.* [162] demonstrated an increase water content of Nafion composite membrane containing 1 wt.% MMT with respect to the MMT-free membrane.

The problem of low proton conductivity must be solved before incorporating MMT into the composite membrane; therefore, several modifications, such as treatment with ammonium cations [176], sulfonic acid [177, 178], silylating agent, perfluorinated sulfonic acid, chitosan biopolymer, 2-acrylamido-2-methylpropanesulfonic acid (AMPS) have been designed, to improve the methanol barrier effect and proton transport property of MMT.

Hasani-Sadrabadi *et al.* [169] reported an application of modified MMT with 2-acrylamido-2-methylpropanesulfonic acid (AMPS) on the fuel cell. Three types of modified MMT, AMPS modified-MMT (AMPS-MMT), quaternary ammonium salt modified-MMT (CloisiteTM 15A) as well as unfunctionalized-MMT (Na-MMT), were used as additives in Nafion composite membranes. The intercalation of AMPS molecules in the interlayer spaces of MMT were determined by X-ray diffraction. The crystalline peak, which corresponds to the MMT interlayer distance was shifted in the functionalized MMT. Nevertheless, these peaks disappeared when the functionalized MMT was incorporated into the Nafion matrix. It seems that the exterior layers of the MMT were delaminated because of the intercalation of the Nafion chain into the MMT interlayers. The evidence of this intercalation of perfluorinated polymer into the MMT gallery was also reported elsewhere [115, 167, 174, 178]. All of the composite membranes had lower proton conductivities and also showed less methanol permeability than recast Nafion and Nafion 117. It was indicated that the exfoliated MMT layers diminished proton and methanol transfer by increasing the length of dispersion path; a similar feature is reported by Gosalawit *et al.* [115].

Among the composite membranes, Nafion/AMPS-MMT has lowest methanol

crossover. The significant decrease in permeability of the modified clay sample could be due to its strong interfacial interaction and the obstruction of methanol molecules. The single cell test confirmed that the modified clay gives an advantage in cell performance increasing power density by 122% from 47.06 mW cm⁻² of Nafion 117 to 87.96 mW cm⁻² of Nafion/MMT-AMPS-3 wt%.

Not only does the filler structure affect the conductivity of the composite membrane, the functional groups on the filler surface also influence membrane performance. By grafting an organic sulfone and a perfluorinated sulfone onto a MMT surface, Kim *et al.* [178] demonstrated that the superior proton conductivity of membranes containing perfluorinated sulfonic acid MMT is caused from ‘the strongly-electron withdrawing fluorine atoms increase the acid strength of the terminal sulfonic acid groups’, yielding the large H⁺ exchange capacity of composite membranes.

As reported in the literature, the good distribution of additive particles together with the ionic channel alignment have crucial influence on the transport nature of membranes. To understand the morphology of the composite membrane, the orientation of hydrophilic ionic domains and non-polar polymer matrix have been studied by Alonso *et al.* [155]. In pure Nafion, the perfluorinated polymer matrix was arranged in crystalline domains, whereas the ionic clusters are embedded uniformly throughout the polymer matrix (Figure 3.7A). For Nafion/clay nanocomposite membranes, the two-dimensional structure of clay forced the polymeric aggregates to orient parallel to the membrane surface (Figure 3.7B) resulting in dramatically decreased methanol permeation. This parallel alignment contributed to the formation of a highly tortuous pathway for methanol transport. Alonso *et al.* found that the proton conductivity of the composite membrane reduces with the increase in MMT loading.

It is known that proton conductivity and methanol permeability are related to the size of polar clusters of the membrane as well as the connection of these polar channels. Introducing additives into the membrane polymer matrix reduces the

size of the ion channels, producing the high selectivity of the composite membrane. The reduction in cluster size has been investigated by X-ray diffraction. The peak related to the ionic channel of Nafion shifts towards higher θ in the composite membrane [178]. It can be interpreted from Bragg's law ($d = \lambda/2\sin\theta$) that the cluster size is decreased.

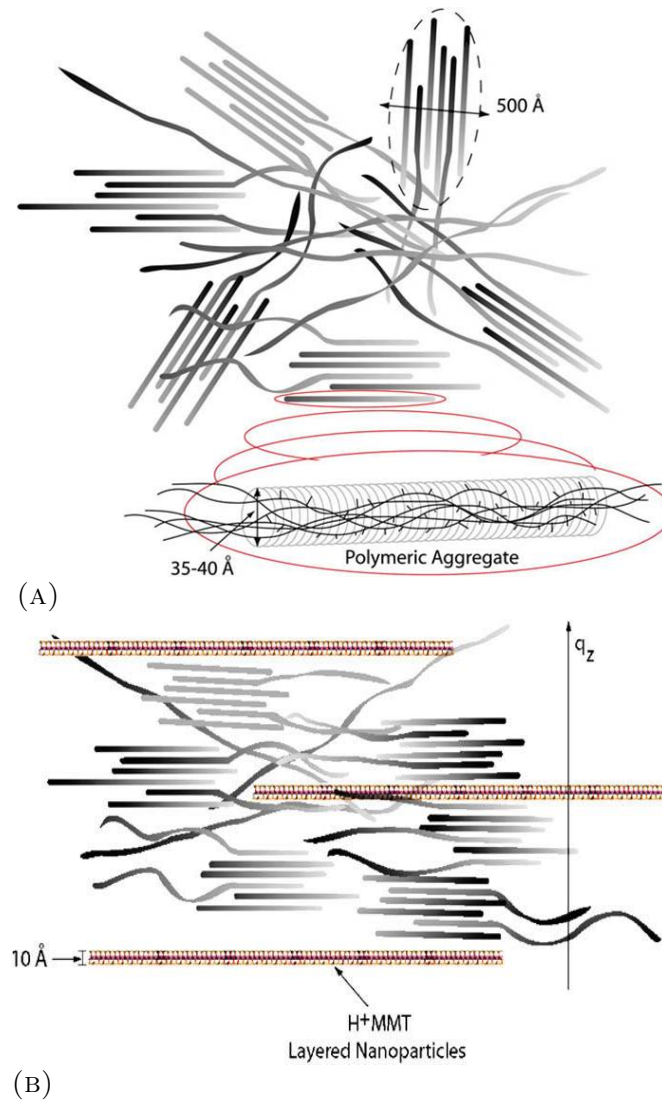


FIGURE 3.7: Orientation of polymeric aggregates in (A) Nafion membrane (B) Nafion/MMT composite membrane [155]

TABLE 3.4: DMFC power density of Nafion/montmorillonite composite membranes

| Composite membrane | Inorganic particles (°C) | Inorganic mass (%) | Catalyst loading (mg cm ⁻²) | Methanol (M) | Methanol permeability (×10 ⁻⁶ cm ² s ⁻¹) | Proton conductivity (mS cm ⁻¹) | Current density (mA cm ⁻²) | Max. power density (mW cm ⁻²) | Ref. |
|-----------------------------|--------------------------|---------------------|---|--------------|--|--|--|---|-------|
| Nafion/MMT | MMT | 3 | 3(A), 5(C) | 2 | — | 76 (110 °C) | 452 (110 °C, 0.4 V) | — | [174] |
| Nafion/MMT-m | MMT-NH ₂ | 3 | 3(A), 5(C) | 2 | — | 77.2 (110 °C) | 440 (110 °C, 0.4 V) | — | [174] |
| Nafion/MMT-HSO ₃ | MMT-HSO ₃ | 5 | 8 | 2 | — | — | 336 (40 °C, 0.2 V) | 67 | [177] |
| Nafion/MMT-chitosan | MMT-NH ₂ | 2 | 4 | 1 | 0.084 (25 °C) | 80 (25 °C) | — | 105 | [179] |
| Nafion/MMT-POPD400-PS | MMT-SO ₃ | 5 | 0.2(A), 0.4(C) | 2 | — | — | 95 (40 °C, 0.2 V) | — | [167] |
| Nafion/MMT-AMPS | MMT-SO ₃ | 3 | 4 | 5 | 0.091 (25 °C) | 81.7 (25 °C) | — | 87.96 | [180] |
| Nafion/MMT-POP | MMT-POP-SO ₃ | 2 (MMT) 27 (POP) | 4 | 1 | 0.17 | 10.8 (25 °C) | 280 (0.2 V) | 90 (0.2 V) | [181] |
| Nafion/MMT-Krytox | MMT-CF ₃ | 2.5 | — | — | 1.2 (25 °C) | 25 (40 °C) | — | — | [115] |
| Nafion/MMT-Krytox | MMT-CF ₃ | 5 | — | — | 0.87 (25 °C) | 0.023 (40 °C) | — | — | [115] |

AMPS, 2-acrylamido-2-methylpropanesulfonic acid; Krytox, carboxylic acid terminated perfluoropolyether; m, dodecylamine-exchanged; POP, poly(2,6-dimethyl-1,4-phenylene oxide; POPD400-PS, poly(oxypropylene)-backboned quaternary ammonium salts

- **Nafion/titanate nanotubes ($X_2Ti_3O_7$)**

Although metal oxides such as SiO_2 , TiO_2 , etc., are well known fillers, they still have the limitation of low proton conductivity, $10^{-4} \text{ S cm}^{-1}$. Alternative materials that have desirable properties of high surface area, high ionic conductivity and hydrophilicity have been studied. Titanate nanotubes, $X_2Ti_3O_7$, are a promising additive for Nafion composite membrane because they serve all these requirements, with a relative high conductivity at 10^{-2} – $10^{-3} \text{ S cm}^{-1}$ [182].

The crystal structure of $Na_2Ti_3O_7$ consists of octahedral TiO_6 building blocks, which share edges to form a one-dimensional tunnel structure. It forms a two-dimensional structure by sharing oxygen atoms at the octahedral vertices, while sodium or hydrogen atoms occupy the interlayer spaces, as shown in Figure 3.8 [183–185].

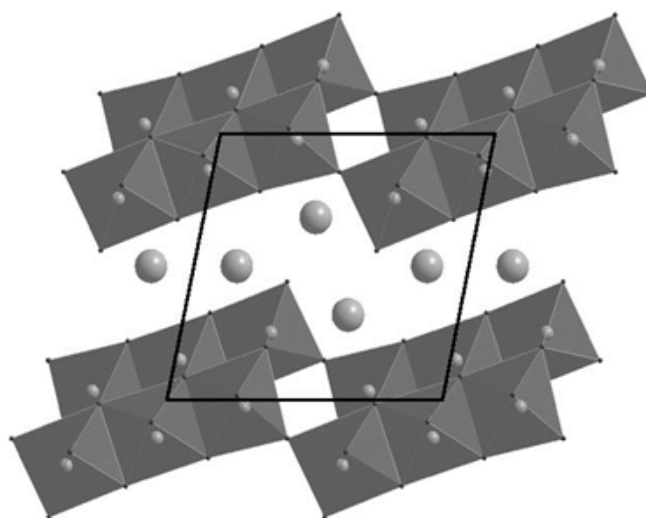


FIGURE 3.8: Crystal structure of titanate ($Na_2Ti_3O_7$) [185]

Titanate nanotubes have been prepared using various strategies. Zhang *et al.* [186] synthesized $H_2Ti_3O_7$ by a single-step reaction. TiO_2 powder was mixed with 10 M NaOH aqueous solution and then the mixture was heated in a Teflon container for 72 hours. The $H_2Ti_3O_7$ plates were formed in 24 hours of reaction and the nanotubes (yield, <90%) were formed after 3 days.

Dong *et al.* [187] prepared a series of samples with various hydrothermal synthesis times. The procedure starts with adding rutile TiO_2 powder to a solution of polyethylene glycol, to promote good dispersion of TiO_2 . This suspension is crushed to form a colloid and then calcined to transform the polyethylene glycol into CO_2 and H_2O . In a second step, the calcined powder is mixed with 10 M NaOH solution and undergoes sonication and ultrasonic treatment followed by autoclaving for 4, 12, 24 or 36 hours. In the final step, a precipitate from the hydrothermal reaction is washed with HCl and distilled water until pH 7 is obtained. From TEM characterization, the sheet structure and some nanotubes are observed at a reaction time of 4 hours. There are coexisting sheet structures and nanotubes until a reaction period of 36 hours, when the nanotubes are completely formed. A cross section of the nanotubes is shown in Figure 3.9.

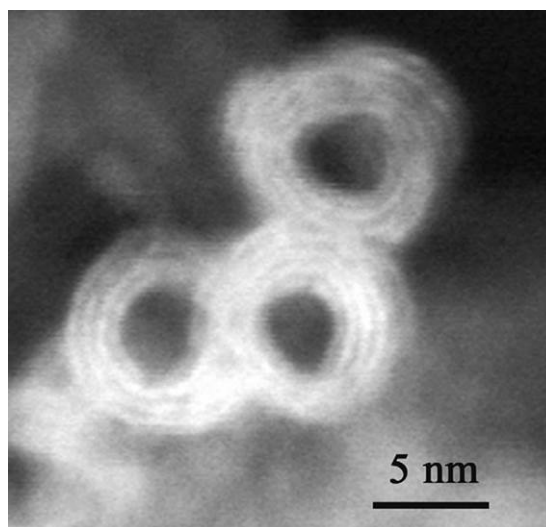


FIGURE 3.9: TEM image of the cross section of $\text{H}_2\text{Ti}_3\text{O}_7$ nanotubes [187]

The hydrothermal treatment of anatase TiO_2 with NaOH to prepare sodium titanate, $\text{Na}_2\text{Ti}_3\text{O}_7$, was reported by Wei *et al.* [188]. A composite membrane of Nafion/ $\text{Na}_2\text{Ti}_3\text{O}_7$ with a titanate content of 1–10 wt% was formed and tested. The proton conductivity and methanol permeability of the membrane reduced with $\text{Na}_2\text{Ti}_3\text{O}_7$ content increase. Considering selectivity, 5% $\text{Na}_2\text{Ti}_3\text{O}_7$ was the optimum content. Compared with the result from Nafion 112 membrane, the

composite membrane presented a higher water uptake but a lower proton conductivity and methanol diffusivity [189]. The performances of the composite membrane are superior to those of Nafion 112 and close to Nafion 117 at high temperature [190].

Rhee *et al.* [191] functionalized the surface of titanate with organic sulfonic acid (HSO_3^-). $\text{TiOSO}_4 \cdot x\text{H}_2\text{SO}_4 \cdot x\text{H}_2\text{O}$ and NH_4OH were used as precursors to form ammonium titanate ($(\text{NH}_4)_2\text{Ti}_3\text{O}_7$) via hydrothermal treatment followed by treatment with 0.5 M H_2SO_4 to change ammonium titanate into hydrogen titanate ($\text{H}_2\text{Ti}_3\text{O}_7$). The final step was taken by refluxing $\text{H}_2\text{Ti}_3\text{O}_7$ with functionality precursors – 1,3-propane sulfone (1,3-PS) and 3-mercaptopropyltrimethoxy silane (3-MPTMS) – resulting in HSO_3 -titanate (1,3-PS) and HSO_3 -titanate (3-MPTMS). The maximum power density of Nafion-based membrane composed of 3 wt% HSO_3 -titanate (1,3-PS) and HSO_3 -titanate (3-MPTMS) exceeded those of pure Nafion 115 membrane and Nafion/unmodified TiO_2 composite membrane. These results are displayed in Table 3.5.

The superior performance can be explained by the reduction in size of the ion transport channel in the composite membrane, which decreased methanol permeability by 38% relative to pure Nafion membrane. The smaller cluster size was observed via a single X-ray diffraction peak responsible for channel size in Nafion matrix shifting to a higher value of 2θ in the composite membrane. In addition, like MMT, titanate has a layer structure that is easily delaminated in the Nafion matrix, hence the separated layer increased the tortuosity of the pathway for the methanol molecules and hindered methanol passage.

- **Nafion/graphene**

Graphene oxide (GO) has desirable characteristics, such as excellent mechanical strength, thermal stability, and is rich in oxygen-containing functional groups. Furthermore, GO is inherently amphiphilic, consisting of largely hydrophobic basal planes and hydrophilic edges [157, 170]. It has been proposed to incorporate

graphene oxide into Nafion composite membranes, to enhance proton conductivity.

Choi *et al.* [170] also used the amphiphilic property of GO to enhance the performance of a Nafion base membrane. The hydrophobic basal planes and hydrophilic functional groups of GO interact and modify the microstructures of both polar ionic channels and non-polar backbones of Nafion, reducing the size of the ionic channels. This feature slightly decreased proton conductivity; however, it also reduced methanol crossover of the composite membrane compared with pristine Nafion membrane.

TABLE 3.5: DMFC power density of Nafion/titanate composite membranes

| Composite membrane | Inorganic particles (°C) | Inorganic mass (%) | Catalyst loading (mg cm ⁻²) | Methanol (M) | Methanol permeability (×10 ⁻⁶ cm ² s ⁻¹) | Proton conductivity (mS cm ⁻¹) | Current density (mA cm ⁻²) | Max. power density (mW cm ⁻²) | Ref. |
|---|----------------------------|--------------------|---|--------------|--|--|--|---|-----------|
| Nafion/titanate | Titanate | 5 | 4 | 2 | 0.174 | — | — | — | [188–190] |
| Nafion/titanate-SO ₃ H (1,3-PS) | Titanate-SO ₃ H | 3 | 8 | 2 | — | — | 318 (27 °C, 0.2 V) | 73 (40 °C) | [191] |
| Nafion/titanate-SO ₃ H (3-MPTMS) | Titanate-SO ₃ H | 3 | 8 | 2 | — | — | 284 (27 °C, 0.2V) | 63.8 (40 °C) | [191] |

1,3-PS, 1,3-propane sultone;
3-MPTMS , 3-mercaptopropyltrimethoxy silane

Nafion/porous material composite membranes

• Nafion/mordenite

Mordenite (MOR) is composed of a (SiO_4^{4-}) and (AlO_4^{5-}) framework (Figure 3.10). The microporous structure of MOR materials provides the advantage of high molecular selectivity including ion conduction. MOR has desirable properties of decreasing methanol transport from anode to cathode while conducting protons [192].

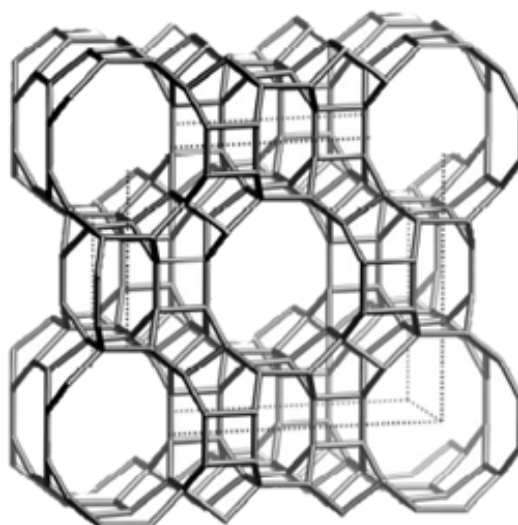


FIGURE 3.10: Crystal structure of mordenite (MOR) [193]

Nafion/functionalized mordenite composite membranes have been prepared by Yoonoo *et al.* [194, 195]. This research showed that a composite membrane obtained by functionalizing H-mordenite with γ -glycidoxypropyltrimethoxysilane (GMPTS) had a superior maximum power density over that of a recast Nafion membrane. The composite containing 5 wt% mordenite-GMPTS achieved a maximum power density of 40.7 mW cm^{-2} at 1 M methanol and $70 \text{ }^\circ\text{C}$, while the recast membrane delivered 37.9 mW cm^{-2} . However, Yoonoo *et al.* noted that mordenite settled out of the bulk solution when the mix solution of mordenite and Nafion was left to stand for a long time before the recasting.

Conclusions for conventional Nafion composite membrane

- The incorporation of additives in a perfluorosulfonic acid membrane enhances the membrane performance; methanol permeability is reduced by providing a long diffusion path for methanol molecules.
- Additional hydrophilic sites, such as $-\text{SO}_3$, $-\text{NH}_2$, or $-\text{OH}$, supplied by the functionalized filler promote hydrogen bonding with water molecules, increasing water uptake in the composite membrane and proton conductivity.

3.4.2.2 Alternative membranes

To resolve problems caused by methanol crossover, electrolyte membranes based on sulfonated aromatic polymers, such as poly(etheretherketone) (PEEK), polysulfone (PSF) and polybenzimidazole (PBI) have been designed. Aromatic polymers are considered to good candidates for use in electrolyte membranes because they have low methanol crossover, satisfactory proton conductivity and stability in fuel cell operation conditions, and they can be functionalized [196–198]. Therefore, composites of aromatic polymer membranes using similar additives as those used to modify Nafion membranes have been investigated.

Poly(etheretherketone) (PEEK) hybrid membranes

The hydrophilic channels of PEEK are narrow and more branched. In addition, there is less interconnection, resulting in lower water uptake (21.25%) and less membrane swelling (9.33%) than Nafion (water uptake, 30.8%; swelling ratio, 14.87%). Therefore, the proton conductivity of PEEK is less than that of Nafion because it relies on water content in the membrane [173]. Mohtar *et al.* [173] found that the composite of PEEK with silicotungstic acid (STA) surface-modified MMT (PEEK/STA-MMT membrane) gives an enhancement in proton conductivity over pristine PEEK and Nafion. STA can donate or accept protons

from water molecules; hence, it facilitates the proton hopping mechanism in the composite membrane. The vehicle mechanism is also enhanced, owing to the hygroscopic nature of STA, which provides a high water content, leading to high proton diffusion through water molecules.

In terms of methanol permeability, PEEK/STA-MMT membranes give better results than pure PEEK membranes. The MMT additive has an impact on the microstructure of the hydrophilic channels and obstructs connections between these channels, further blocking methanol diffusion pathways. Moreover, the narrow ionic clusters of PEEK also reduce methanol migration.

Sulfonated polysulfone (SPSF) hybrid membranes

Lufrano *et al.* [196, 197] combined sulfonated polysulfone (SPSF) with acidic silica to find a good compromise between the desirable and undesirable properties of the composite membrane (Table 3.6). Although the composite membrane of SPSF and acidic silica (SPSF-SiO₂-S) exhibited low proton conductivity, it produced the highest maximum power density, at 23 mW cm⁻², compared with values of 21 and 16 mW cm⁻² obtained from composite SPSF, unmodified-silica (SPSF-SiO₂) and pristine SPSF, respectively. Considering methanol crossover, SPSF-SiO₂-S has the lowest crossover current, at 8 mA cm⁻², which was 33% better than SPSF-SiO₂ and 43% worse than SPSF.

TABLE 3.6: DMFC power density of SPSF/filler composite membranes

| Composite membrane | Inorganic particles (°C) | Inorganic mass (%) | Catalyst loading (mg cm ⁻²) | Methanol (M) | Methanol permeability (×10 ⁻⁶ cm ² s ⁻¹) | Proton conductivity (mS cm ⁻¹) | Current density (mA cm ⁻²) | Max. power density (mW cm ⁻²) | Ref. |
|-----------------------------|--------------------------|--------------------|---|--------------|--|--|--|---|-------|
| PEEK | — | — | — | — | 0.642 (25 °C) | 2.29 (25 °C) | — | — | [173] |
| PEEK/MMT | MMT | 1 | — | — | 0.441 (25 °C) | 1.97 (25 °C) | — | — | [173] |
| PEEK/MMT-STA | MMT-STA | 1 (MMT) | — | — | 0.35 (25 °C) | 3.76 (25 °C) | — | — | [173] |
| | | 0.3 (STA) | — | — | — | — | — | — | — |
| | | 1 (MMT) | — | — | 0.394 (25 °C) | 6.08 (25 °C) | — | — | [173] |
| 0.5 (STA) | — | — | — | — | — | — | — | — | |
| SPSF | SPSF | 10 | 2.5 | 1 | 14.5 | 36 (30 °C) | — | 16 (30 °C) | — |
| SPSF/SiO ₂ | SPSF-SiO ₂ | 10 | 2.5 | 1 | 12 | 20 (30 °C) | — | 21 (30 °C) | — |
| SPSF/SiO ₂ -acid | SPSF-SiO ₂ -S | 10 | 2.5 | 1 | 8 | 27 (30 °C) | — | 23 (30 °C) | [197] |

MMT, montmorillonite;
 PEEK, poly(etheretherketone),
 SPSF, sulfonated polysulfone,
 STA, silicotungstic acid

3.4.2.3 Multilayered membranes

The adsorption of polyanions and polycations can be utilized to construct polyelectrolyte multilayer membranes in a layer-by-layer (LBL) self-assembly method. Two opposite charges are deposited on a support surface by an electrostatic interaction via a solution dipping technique [199]. Jiang and Tang [148] produced polyelectrolyte multilayer on Nafion 112 surfaces. It was found that the proton conductivity of multilayer membranes were in the range of 68-91 mS cm⁻¹ slightly lower than 93 mS cm⁻¹ slightly of pure Nafion 112. This could be described as the less favourable complexation of protons by methanol compared to water in multilayer membranes. Methanol permeability was related to the structure of multilayer membranes. The polyanions with small linear monomeric blocks would promote interdiffusion during the self-assembly process because of their low steric hindrance. This feature produces a high density multilayer (Figure 3.11A), which presents lower methanol permeability (1.01×10^{-6} cm² s⁻¹) than multilayers produced using polyanions with large monomeric blocks (1.34×10^{-6} cm² s⁻¹) (Figure 3.11B). Nevertheless, the effect of polyanions/polycations multilayer on the methanol permeability is not clear.

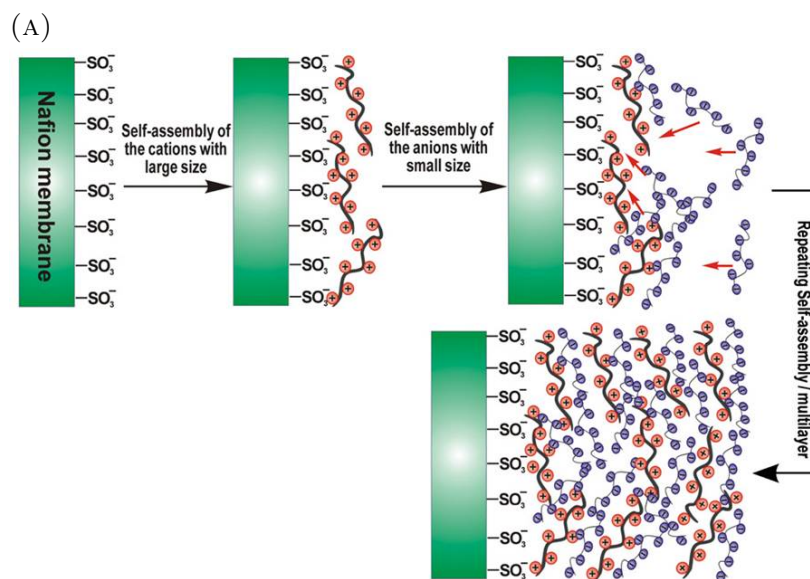


FIGURE 3.11: Adsorption of polyanions and polycations on Nafion with (A) small sized monomeric block, (B) large sized monomeric block [148]

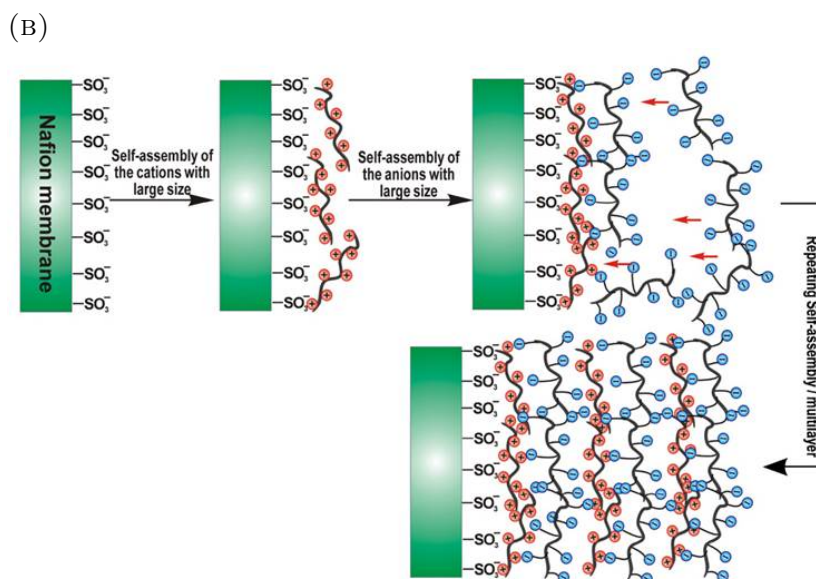


FIGURE 3.11 (cont.): Adsorption of polyanions and polycations on Nafion with (A) small sized monomeric block, (B) large sized monomeric block [148]

3.4.3 Incorporating methanol barrier layers into MEAs

3.4.3.1 Introduction to methanol barrier layer

Previous studies [194] improved DMFC performance by producing Nafion composite membranes with silane surface modified mordenite. However, a problem with inorganic particles is that they aggregate at the bottom edge of the recast membrane due to gravity driven setting, as shown in Figure 3.12.

This research has been extended by applying a Nafion/inorganic composite layer onto the anode electrode instead of using the composite membrane [106]. The additional layer acts as a methanol barrier, which reduces methanol migration through the membrane. Dawson [106] fabricated novel (MEAs) containing Nafion/-mordenite and Nafion/silane functionalized mordenite as a methanol barrier layer. This technique can prevent large agglomeration of inorganic additives (Figure 3.13). A MEA with 13.67 wt% silane functionalized mordenite presented the best performance, with 42% increase in the power density compared with an

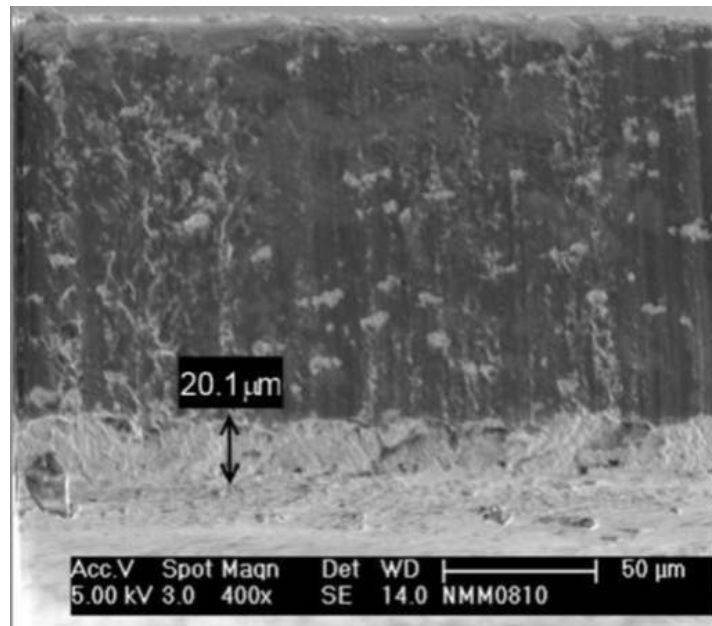


FIGURE 3.12: Cross-section of Nafion/5 wt% mordenite composite membrane [194]

MEA without a barrier layer. These results suggest that this procedure can be used to ensure methanol blocking, for an improved performance of DMFCs.

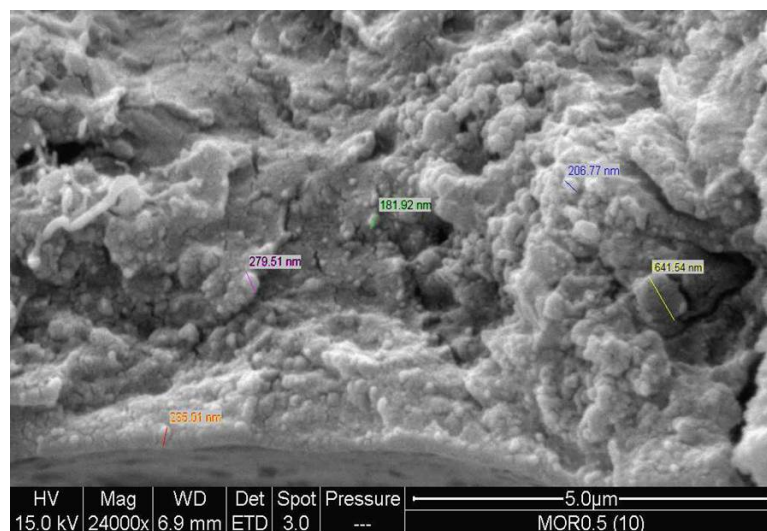


FIGURE 3.13: Cross-section of Nafion/functionalized mordenite barrier layer [106]

Summary

To improve DMFC performance, the potential losses which are activation loss,

ohmic loss, mass transport loss and methanol crossover should be reduced. The critical loss in DMFC is from methanol crossover; therefore, producing membranes which decrease methanol migration but remain reasonable proton conductivity is still a major challenge for the development of DMFC. A large number of experiments focus on modified Nafion membrane due to its high ionic conductivity. The literature explores the methanol resistance of Nafion/inorganic composite membranes; moreover, it has found that the crystal structure of inorganic filler plays an important role in proton conductivity and methanol permeability of the membranes.

Chapter 4

Fabrication of membrane electrode assembly (MEA) and experimental system

4.1 Standard membrane electrode assembly fabrication

The MEA without an additional methanol barrier layer was produced as a reference. This is called the standard MEA; it consists of three main components, a polymer electrolyte membrane and two electrodes, an anode and a cathode. A spray-coating method was used to fabricate the MEA throughout this project. Using a procedure from [106, 194], the process of MEA fabrication is described in Figure 4.1 and the arrangement of MEA layers is shown in Figure 4.2. This procedure can be divided into two parts: electrode fabrication and membrane treatment.

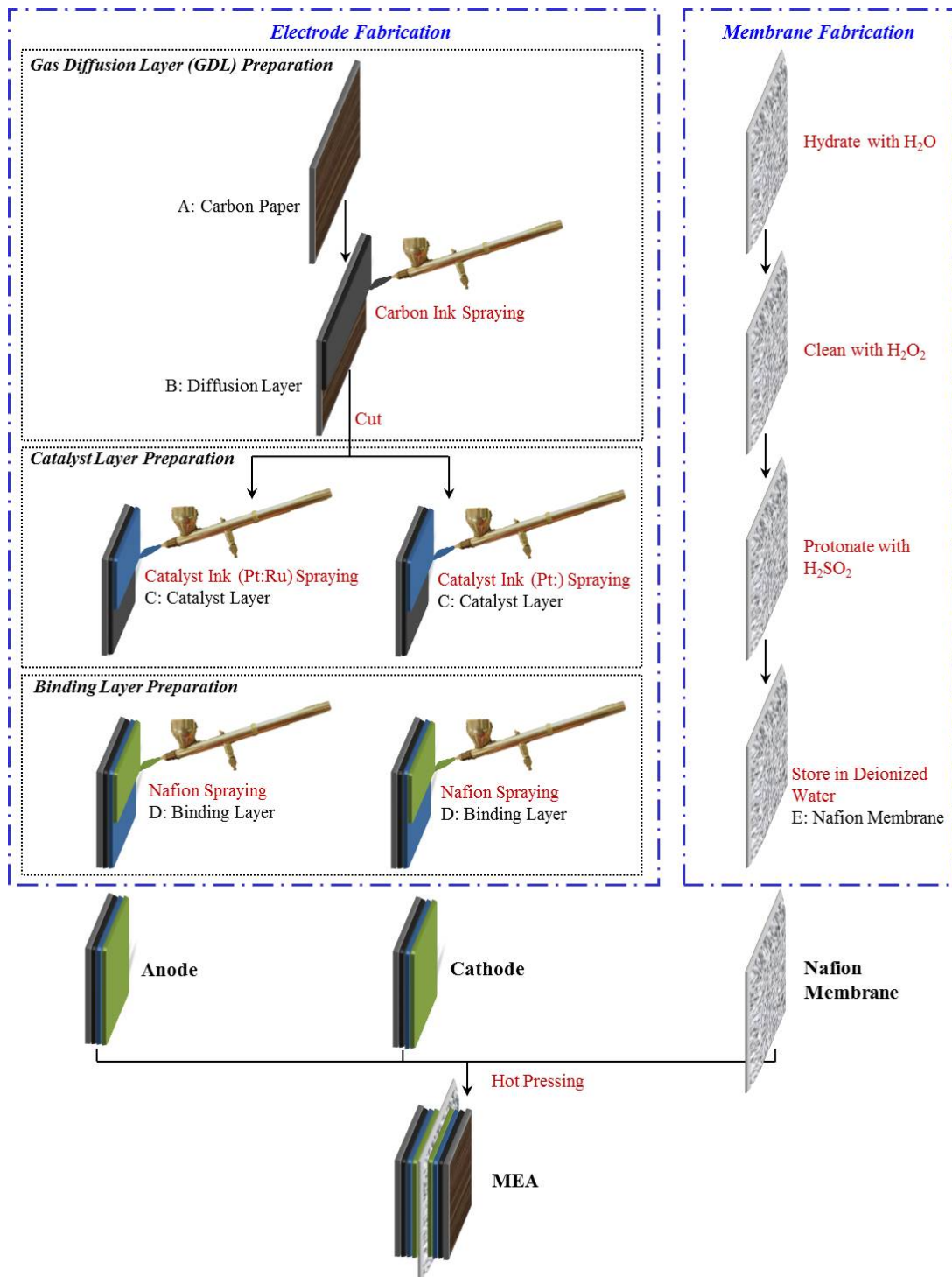


FIGURE 4.1: Standard MEA fabrication

For the electrode fabrication, each electrode is composed of three layers, a gas diffusion layer (GDL), a catalyst layer and a Nafion binding layer. The GDL is formed by spraying carbon ink onto carbon paper ($4.5\text{ cm} \times 9.0\text{ cm}$), which is used as the electrode support. The GDL is cut into two pieces ($4.5\text{ cm} \times 4.5\text{ cm}$). Next, the two different compositions of catalyst ink are prepared and applied onto each GDL to form the catalyst layer. The last layer is a Nafion solution, which is coated over the catalyst surfaces to bind the two electrodes to the membrane.

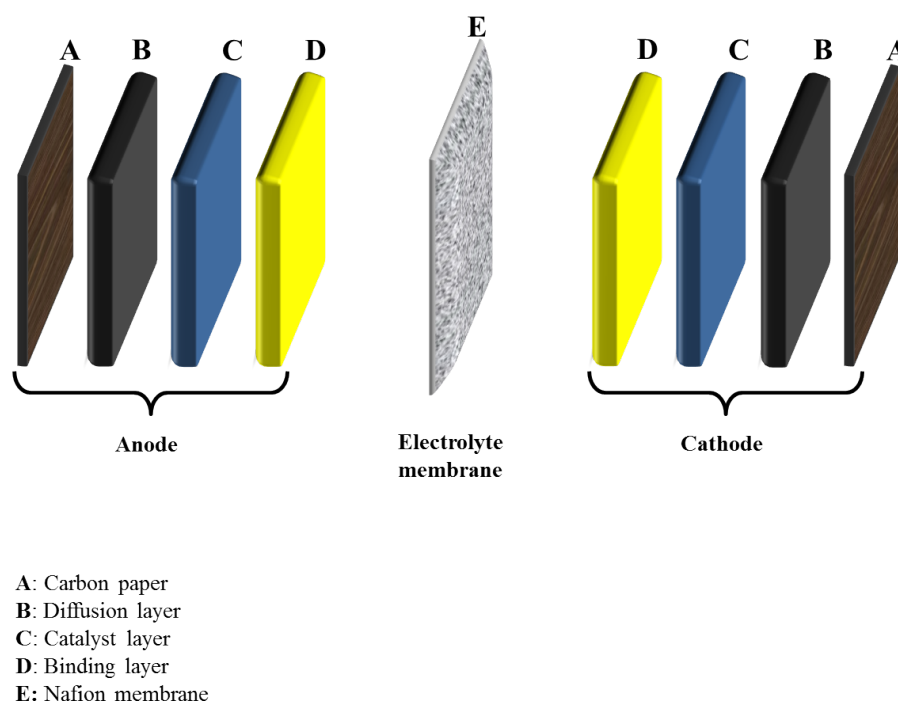


FIGURE 4.2: Standard MEA layers

For the membrane preparation, the Nafion polymer membrane is cleaned and protonated before use. Finally, the Nafion membrane is sandwiched between the two electrodes and hot pressed together.

4.1.1 Gas diffusion layer (GDL)

4.1.1.1 Carbon ink preparation

Using a standard method from [194] explained herein, the gas diffusion layer is made from a carbon ink, a dispersion of porous carbon in isopropanol (IPA), coated on carbon paper. The appropriate proportions of carbon ink are calculated to ensure that 60 cm³ IPA produces a homogeneous ink coating [194, 200]. A surface density of 1.0 mg cm⁻² for the diffusion layer contributes the best DMFC performance by providing the optimum thickness that balances between reactant dispersion and mass transport resistance [200].

To enhance mass transport within the diffusion layer, 10 wt% of polytetrafluoroethylene (PTFE) is included in the carbon ink. The PTFE forms hydrophobic channels, providing a pathway for carbon dioxide to leave the anode [138]. The amount of PTFE is calculated as:

$$\left(\frac{\text{PTFE}}{\text{PTFE} + \text{Carbon black}} \right) \times 100 = 10\% \quad (4.1)$$

The compositions of carbon ink are shown in Table 4.1. A waste factor of 4 is used, to allow for material loss while spraying the ink onto the electrode. This means that the volume of ink required is four times the target volume. The quantity of carbon ink components suitable for producing two GDLs (4.5 × 9.0 cm) are shown in Figure 4.3.

The carbon ink is prepared by mixing 60.0 mg of PTFE (60 wt% PTFE dispersion water, Aldrich) in 5.0 cm³ of IPA (Aldrich) in an ultrasonic bath for 10 minutes, after which the suspension is added to 324.0 mg of carbon black (Ketjen black carbon, EC-300J, Akzo Nobel) and the mixture is continuously mixed in an ultrasonic bath for 30 minutes. Another 2.0 cm³ of IPA is then added, followed by sonication for 30 minutes. The processes of adding IPA and sonication are

TABLE 4.1: Composition of carbon ink for producing two GDLs

| Material | Specification | Quantity | Quantity including waste factor (4) |
|------------------------------------|--------------------------|-------------------|-------------------------------------|
| Ketjen carbon black | 1.0 mg cm^{-2} | 81.0 mg | 324.0 mg |
| PTFE solution (60 wt% solution) | 10 wt% PTFE | 15.0 mg | 60.0 mg |
| IPA | 99.5% purity | 15 cm^3 | 60 cm^3 |

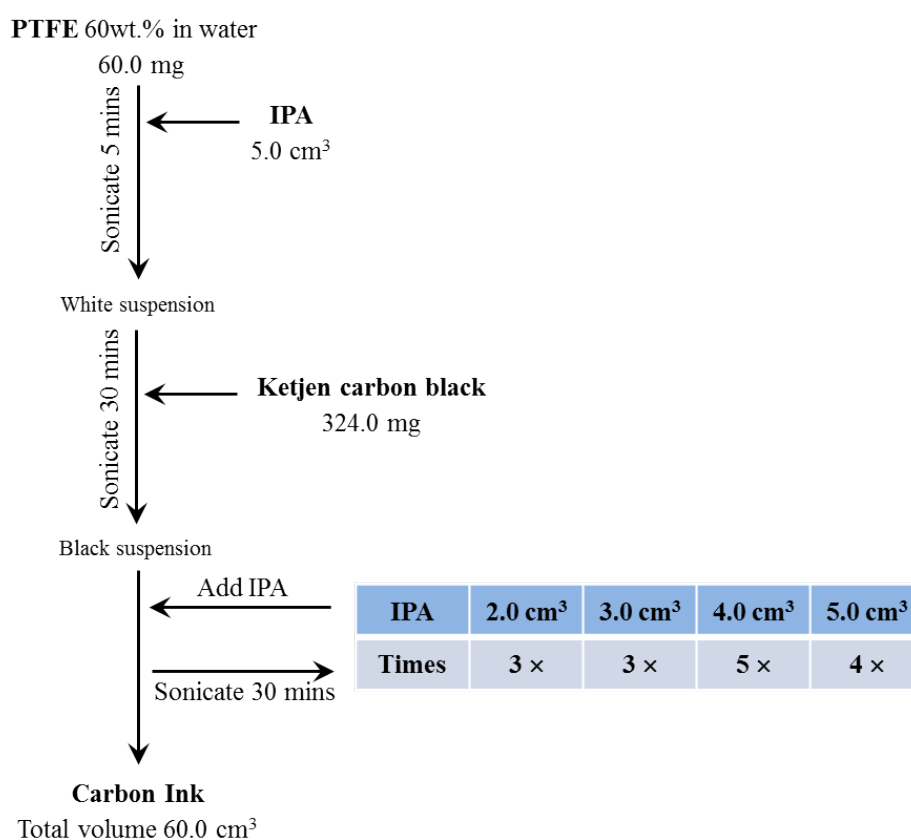


FIGURE 4.3: Carbon ink preparation

repeated until a total volume of 60.0 cm^3 of carbon ink is obtained.

4.1.1.2 Spraying the gas diffusion layer

A dual action airbrush (Badger 100LG, double action) is controlled manually during the spraying process using N_2 at a pressure of 1 bar. The procedure is as

follows:

1. A carbon support paper (Toray TGPH-090, 20 wt% wet proofing, thickness, 0.26 mm; density, 0.49 g cm^{-3} , from E-TEK) of area $4.5 \text{ cm} \times 9.0 \text{ cm}$ for the fabrication of two $4.5 \text{ cm} \times 4.5 \text{ cm}$ MEAs. The mass of this paper is recorded.
2. The carbon paper is attached to a hot plate and cleaned by spraying 3 cm^3 of IPA while heating at $60 \text{ }^\circ\text{C}$ to evaporate the solvent.
3. A first portion of 6 cm^3 of carbon ink is applied to the carbon paper.
4. The paper is dried in an oven at $120 \text{ }^\circ\text{C}$ for 10 minutes and weighed.
5. To avoid congestion with carbon ink, the spray gun is cleaned with 6 cm^3 of IPA before applying additional carbon ink.
6. The additional carbon ink is sprayed and dried. These steps are repeated until a target mass of 45.0 mg (1.0 mg cm^{-2}) of dry carbon black is achieved.

To complete GDL fabrication, a sintering process is carried out using a programmable furnace [106, 194]. The temperature is raised from room temperature to $360 \text{ }^\circ\text{C}$ over a period of 2.5 hours and then maintained at $360 \text{ }^\circ\text{C}$ for 1 hour. Finally, the temperature is reduced to room temperature. The temperature control is plotted in Figure 4.4. The sintered GDL is cut into two pieces. Each piece has an area of $4.5 \text{ cm} \times 4.5 \text{ cm}$.

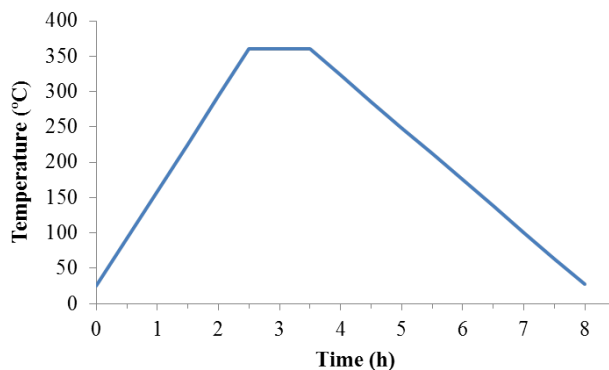


FIGURE 4.4: Temperature control for sintering process [106]

4.1.2 Catalyst layer (procedure I)

The electrode catalyst inks are prepared with different compositions. The anode ink is made from a Pt:Ru catalyst but the cathode ink uses a Pt catalyst. The method for preparing the catalyst ink is here called **procedure I**.

4.1.2.1 Anode catalyst ink preparation

The anode catalyst ink comprises Pt:Ru particles supported on carbon (with a Pt:Ru:C mass ratio of 40:20:40), with acetone as a dispersion medium. In addition, Nafion solution is combined in the catalyst ink to produce the proton transfer pathways from the catalyst layer to the electrolyte membrane. Equation 4.2 describes the method for calculating the % of Nafion solution [194, 200].

$$\left(\frac{\text{Nafion}}{\text{Nafion} + \text{Catalyst} + \text{Catalyst support}} \right) \times 100 = 15\% \quad (4.2)$$

The procedure for preparing the anode catalyst ink is outlined in Figure 4.5. To produce the catalyst ink, Nafion solution (20 wt% Nafion solution, Ion Power DE2021) is mixed with 16 cm³ of acetone (Aldrich) under sonication for 5 minutes. Next, the Pt:Ru catalyst (60% Pt:Ru alloy on Vulcan XC-72, E-TEK) is added

to the mixture under sonication for 60 minutes. The required mass of anode catalyst ink for preparing two electrodes is shown in Table 4.2.

TABLE 4.2: Composition of anode catalyst ink for producing two electrodes

| Material | Specification | Quantity | Quantity including waste factor (4) |
|--|----------------------------|-------------------|-------------------------------------|
| Pt:Ru catalyst (Pt:Ru:C = 40:20:40) | 1.0 mg Pt cm ⁻² | 101.3 mg | 405.0 mg |
| Nafion solution (20 wt% solution) | 15 wt% Nafion | 89.3 mg | 357.3 mg |
| Acetone | 99.8% purity | 4 cm ³ | 16 cm ³ |

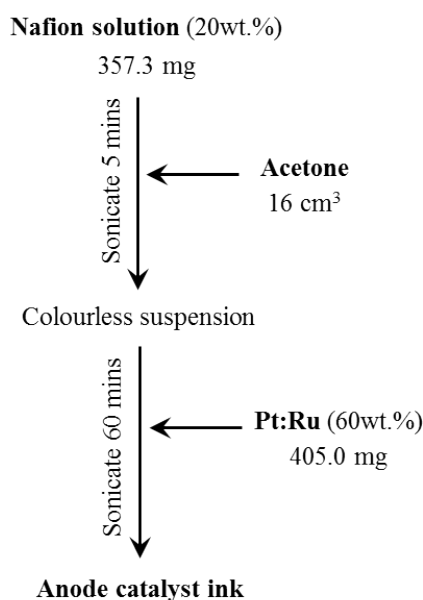


FIGURE 4.5: Anode catalyst ink preparation

4.1.2.2 Cathode catalyst ink preparation

The cathode ink is also composed of a combination of Nafion solution and acetone but Pt catalyst (60 wt% Pt on Vulcan XC-72, E-TEK) is used instead of the Pt:Ru. A quantity of 15 wt% Nafion is also used in the cathode ink.

Figure 4.6 outlines the preparation of the cathode ink, which begins by mixing 16 cm³ of acetone with Nafion solution and sonicating for 5 minutes. The mixture is then added to the required weight of Pt catalyst followed by sonication for 60 minutes to disperse the Pt particles. For the best activity, the catalyst ink should be used immediately. The cathode catalyst constituents for preparing two electrodes are detailed in Table 4.3.

TABLE 4.3: Composition of cathode catalyst ink for producing two electrodes

| Material | Specification | Quantity | Quantity including waste factor (4) |
|--------------------------------------|----------------------------|-------------------|-------------------------------------|
| Pt catalyst (Pt:C = 60:40) | 1.0 mg Pt cm ⁻² | 67.5 mg | 270.0 mg |
| Nafion solution (20 wt% solution) | 15 wt% Nafion | 59.6 mg | 238.3 mg |
| Acetone | 99.8% purity | 4 cm ³ | 16 cm ³ |

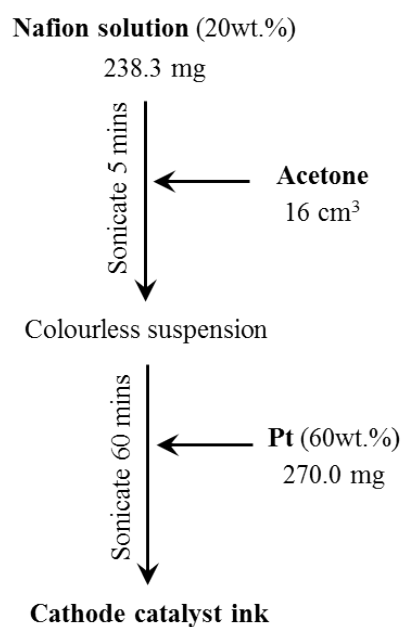


FIGURE 4.6: Cathode catalyst ink preparation

4.1.2.3 Spraying the catalyst layer

1. The catalyst ink is applied to the GDL in a similar manner to the diffusion layer. Before spraying the catalyst ink, each sintered GDL is weighed and then its surface is cleaned with 3 cm³ of acetone.
2. An initial 3 cm³ of catalyst ink is loaded into the airbrush and sprayed on the GDL.
3. The electrode with catalyst cloth is placed in an oven at 120 °C for 10 minutes to evaporate the acetone.
4. To measure the deposited catalyst layer, the electrode mass electrode is recorded again. Subtracting the mass of the uncoated GDL from this mass gives the mass of the catalyst layer.
5. Additional catalyst ink is sprayed and dried until the target mass is reached. Both electrodes have similar target catalyst surface densities, that is 1 mg Pt cm⁻², and the area of each electrode is 4.5 × 4.5 cm. The dry masses of the catalyst layers were 59.6 ± 3 mg for the anode and 39.7 ± 2 mg for the cathode.

4.1.3 Binding layer

To achieve excellent adhesion between the electrodes and a Nafion membrane, a binding layer of surface density 1.2 mg cm⁻² has to be applied over the surface of each electrodes.

Nafion 20 wt% solution is weighed and then mixed with 16 cm³ of acetone under sonication for 30 minutes. The preparation method is outlined in Figure 4.7 and the compositions are listed in Table 4.4.

4.1.3.1 Spraying the binding layer

1. The anode and cathode are weighed.

TABLE 4.4: Composition of binding ink for producing two electrodes

| Material | Specification | Quantity | Quantity including waste factor (4) |
|-----------------------------------|--------------------------------|-------------------|-------------------------------------|
| Nafion solution (20 wt% solution) | 1.2 mg Nafion cm ⁻² | 243.0 mg | 972.0 mg |
| Acetone | 99.8% purity | 4 cm ³ | 16 cm ³ |

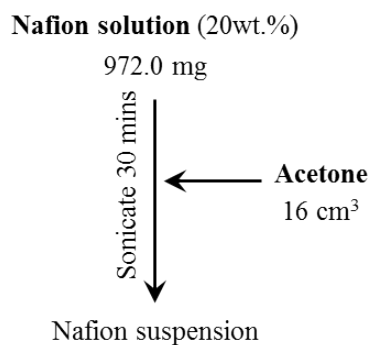


FIGURE 4.7: Binding ink preparation

2. An air brush is filled with 3 cm³ of acetone, which is sprayed over each electrode surface.
3. The Nafion suspension is then applied to each electrode.
4. The electrodes are dried at 120 °C for 10 minutes
5. Supplementary Nafion suspension is added until the target mass of 24.3 ± 2 mg (1.2 mg cm⁻²) of dry Nafion is achieved.

4.1.4 Membrane treatment

A Nafion 117 membrane (thickness, 183 μm; density, 1.98 g/cm³; DuPont) is used in this research. It is treated before fabricating into MEAs. The process is outlined in Figure 4.8.

1. The polymer membrane is cut to an area of 6.0 cm × 6.0 cm.

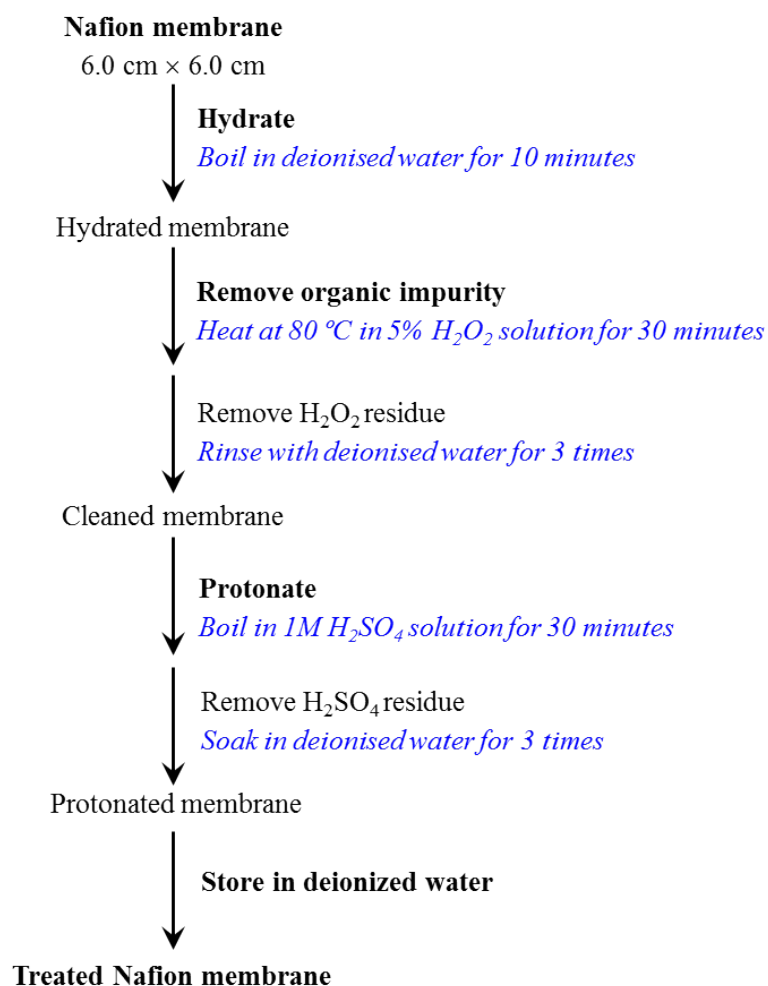


FIGURE 4.8: Membrane treatment

2. The membrane sheet is boiled in deionized water for 10 minutes to hydrate.
3. The membrane is then heated in 5% hydrogen peroxide solution (H₂O₂, Aldrich) at 80 °C for 30 to remove organic impurities, after which it is cleaned three times with deionized water.
4. To protonate the membrane, a step of boiling in a 1 M sulfuric acid solution (H₂SO₄, Aldrich) for 30 minutes is required. Afterwards, the membrane is washed three times in deionized water for 10 minutes each time.
5. The membranes are stored in deionized water until needed.

4.1.5 Hot pressing

The anode and cathode and a membrane sheet are pressed together to form a completed MEA.

1. The Nafion membrane is taken from the deionized water and dried with filter paper.
2. Two stainless steel backing plates are covered with aluminium foil to avoid the membrane sticking to the plates.
3. The anode is placed on a metal plate with the catalyst layer face up followed by the membrane sheet. The cathode is placed on the top of membrane with the catalyst layer face down. A second metal plate is put over the cathode and then the whole assembly is wrapped in aluminium foil.
4. The assembly is placed in a hydraulic press for 3 minutes under a pressure of 3 bar at 135 °C. Afterwards, the press is cooled from 135 °C to 60 °C in 27 minutes, while the pressure is maintained.
5. The completed MEA is removed from the press and allowed to cool room temperature.
6. Since the hot-pressing dries out the Nafion membrane, it is important to hydrate the MEA with deionized water overnight at room temperature before operating the MEA.

4.2 DMFC experimental system

The experimental system is composed of five main parts: the methanol reservoir, the air supplier, the temperature controller, the electrical circuit and the DMFC assembly. The experimental system is illustrated in Figure 4.9.

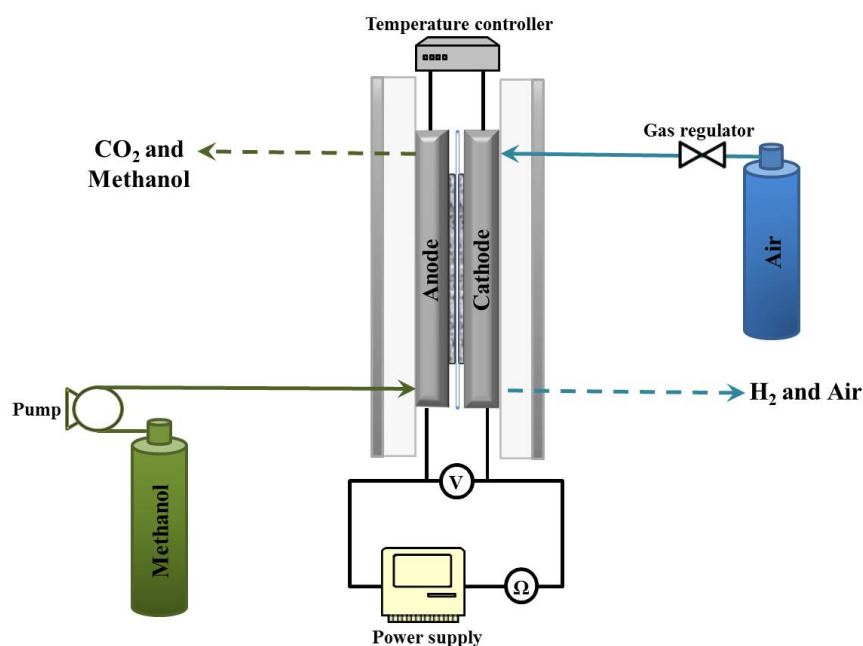


FIGURE 4.9: DMFC experimental system

On the anode side, methanol fuel from the storage tank is delivered by a peristaltic pump through the anode inlet of the DMFC assembly and then to the flow field over the anode side. Unreacted methanol solution, water and carbon dioxide gas leave the cell at the anode outlet.

Air is supplied from a gas cylinder into the DMFC assembly at the cathode inlet and flows through the cathode flow field. The flow rate of gas is controlled by a flowmeter. The excess air stream and the product of the cathode reaction, water, are released from the cell at the cathode outlet.

A voltmeter is connected across the anode and the cathode to measure the overall voltage of the fuel cell. A power supply is also connected to the fuel cell to control and vary the magnitude of the electrical current during the fuel cell operation process.

4.2.1 DMFC operation

The method for measuring MEA performance can be separated into two steps which are a MEA condition and a MEA operation.

In order to obtain a high performance, the fabricated MEA was generally conducted via the condition step [201–203]. The condition method in this research was adapted from [106, 194] as:

- The single fuel cell was flowed with deionised water for 12 hours to fully hydrate the Nafion membrane.
- Methanol solution (1 M) was delivered to the anode side at the flow rate of $5 \text{ cm}^3 \text{ min}^{-1}$ while air was supplied to the cathode at the flow rate of $1000 \text{ cm}^3 \text{ min}^{-1}$.
- An actual cell temperature was maintained at $70 \text{ }^\circ\text{C}$.
- During the condition step, the polarization (j-V) curves were measured in a galvanostatic mode by increasing current at 0.20 A interval and observing the related voltage. The current was applied until the magnitude of voltage was reduced to zero. The conditioning process was carried out many times until the j-V curves were stable. This research presented a suitable MEA condition at five times running.

After the condition step, the MEA performance was also investigated via the j-V curve using similar current interval. However, the performance has been operated by changing cell temperature and methanol concentration. Methanol fuel was changed at 1 M, 2 M and 4 M and cell temperature was varied from 30 to $80 \text{ }^\circ\text{C}$ for individual methanol concentration. An open circuit voltage was measured without any current loading at 30 minutes after methanol and air were fed into the cell in order to stabilize the cell. It should be noted that the condition step was applied every time when the methanol concentration was changed. The power density can be calculated by multiplying the current density with the related voltage.

4.2.2 DMFC assembly

The MEA is put in a specially constructed DMFC assembly, which was built in-house [194]. It is sandwiched between two graphite plates, which act as the current collector and the flow channel of the fuel and oxidant. A heater plate is attached to the back of each graphite block; this is also connected to a temperature controller to measure and maintain the cell temperature. PTFE insulator plates are located next to the heating elements to prevent heat loss from the assembly. Each insulator plate forms a cavity to align the heater plate and graphite block firmly. An aluminium plate is placed at either end of the assembled cell. The purpose of these metal plates is to protect the soft PTFE material from damage when all components are fixed together. As seen from Figure 4.10, the assembly is completed by the tightening of nuts and washers.

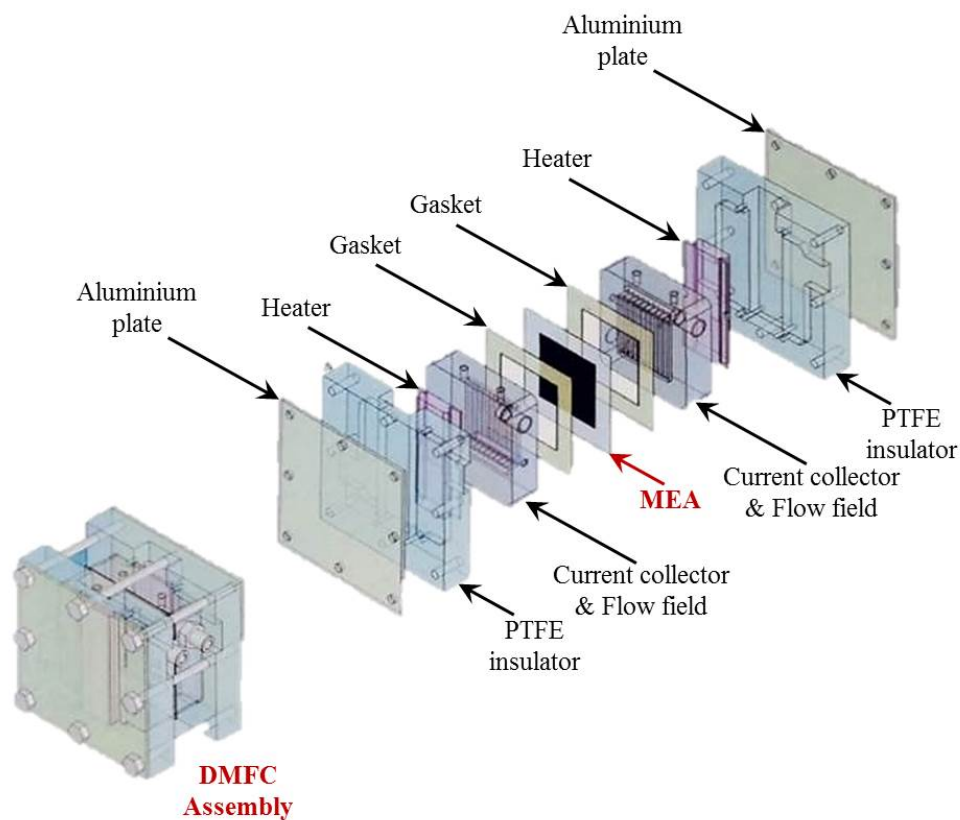
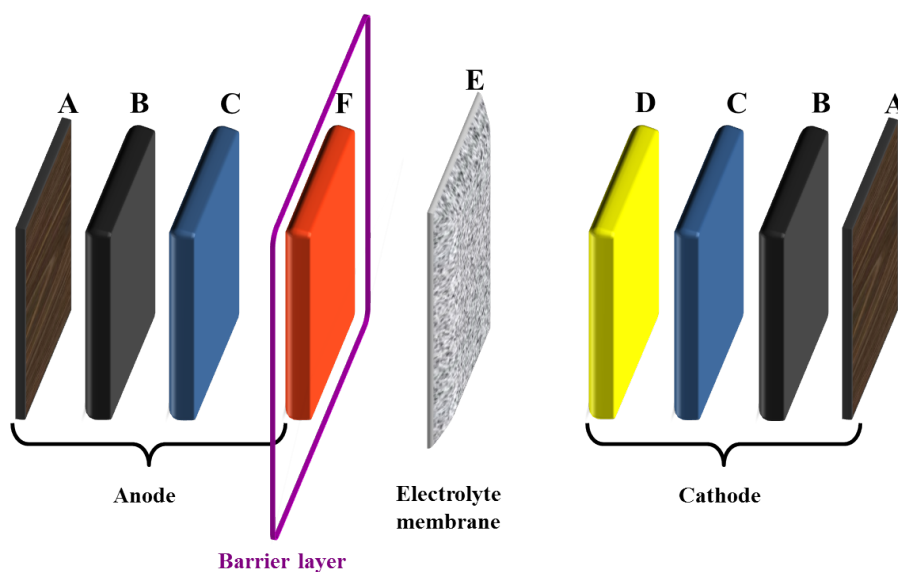


FIGURE 4.10: DMFC assembly [194]

4.3 Fabrication of modified MEAs (procedure I)

4.3.1 Modified MEA using methanol barrier layer

With the purpose of preventing methanol transport through the electrolyte membrane, the methanol barrier layer is best located between the anode and the membrane, as shown in Figure 4.11. The MEA combined with the methanol barrier layer is called the modified MEA. The fabrication procedure of the modified MEA is similar to that of the standard MEA, except that the Nafion binding layer (D) on the anode side is replaced by a Nafion/inorganic composite layer (F).



- A: Carbon paper
- B: Micro-porous layer
- C: Catalyst layer
- D: Binding layer
- E: Nafion membrane
- F: Methanol barrier layer

FIGURE 4.11: Standard MEA fabrication

4.3.2 Methanol barrier layer preparation

The methanol barrier layer is a composite of Nafion and inorganic material. The DMFC performances carried out by this group [106, 194, 200] indicated that the composite layer containing 0.5 wt% of inorganic particles related to the weight of Nafion 117 membrane presented the best performance; hence this amount of the barrier layer is applied to the anode side of the MEA. The inorganic mass incorporated in the barrier layer is expressed as:

$$\left(\frac{\text{Inorganic particles weight}}{\text{Inorganic particles weight} + \text{Nafion membrane weight}} \right) \times 100 = 0.5\% \quad (4.3)$$

Furthermore, the quantity of inorganic particle relative to the total amount of the barrier layer can be calculated from:

$$\left(\frac{\text{Inorganic particles weight}}{\text{Inorganic particles weight} + \text{weight of Nafion in the composite layer}} \right) \times 100 = 13.21\% \quad (4.4)$$

To investigate the appropriate material for improving DMFC performance, four modified MEAs containing different methanol barrier layers were formed. These are summarized in Table 4.5. A commercial Mordenite powder (MOR) and Zeolite Y (ZY) was obtained from Zeolyst International. Montmorillonite K10 (MMT) was from Sigma-Aldrich. Titanate (TN) was synthesised by a hydrothermal method.

TABLE 4.5: Modified MEAs

| MEA label | Inorganic material | Inorganic wt% (Equation 4.3) | Inorganic wt% (Equation 4.4) |
|-----------|--------------------|------------------------------|------------------------------|
| 0.50% MOR | Mordenite | 0.50 | 13.12 |
| 0.50% ZY | Zeolite Y | 0.50 | 13.12 |
| 0.50% MMT | Montmorillonite | 0.50 | 13.12 |
| 0.50% TN | Sodium titanate | 0.50 | 13.12 |

There are two steps in producing the Nafion/inorganic composite. First, the inorganic suspension is prepared. Then the Nafion/inorganic composite is produced.

4.3.2.1 Inorganic suspension

The composition of the inorganic suspension is detailed in Table 4.6 and the preparation method is outlined in Figure 4.12. Because the Nafion/inorganic composite layer comprises only a very little amount of inorganic powder, it is difficult to weigh this substance accurately. Ten times the required mass of inorganic suspension is prepared. A portion of 37.0 mg inorganic powder is weighed and dispersed in 10 cm³ of acetone. The suspension is placed in an ultrasonic bath for 15 minutes, then mixed with a magnetic stirrer for 15 minutes. These two steps of sonication and stirring are repeated for a total of 2 hours for the excellent dispersion of inorganic particles. This procedure is developed by this group [106].

TABLE 4.6: Composition of inorganic suspension

| Material | Specification | Quantity | Quantity including waste factor (10) |
|--------------------|---------------|-------------------|--------------------------------------|
| Inorganic particle | 0.5 wt% | 3.7 mg | 37.0 mg |
| Acetone | 99.8% purity | 1 cm ³ | 10 cm ³ |

4.3.2.2 Nafion/inorganic composite

To make the Nafion/inorganic composite layer, 3.7 mg of the inorganic substance and 1.2 mg cm⁻² of Nafion is required at the electrode surface. The ingredients of the Nafion/inorganic composite are listed in Table 4.7.

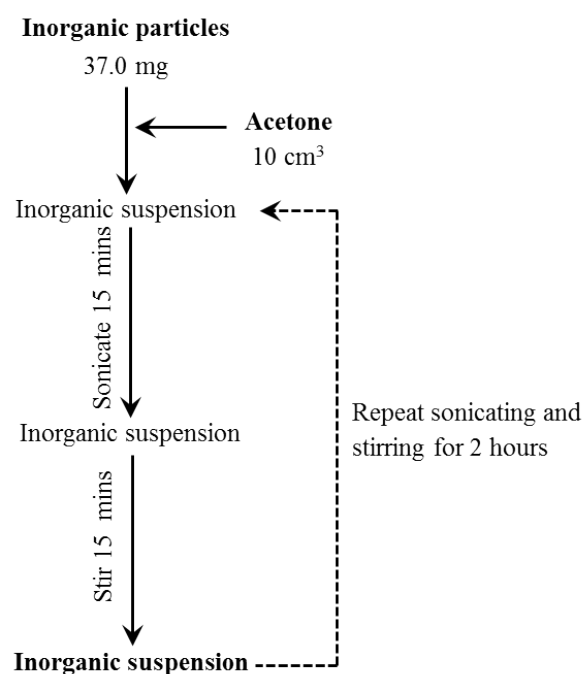


FIGURE 4.12: Inorganic suspension preparation

TABLE 4.7: Composition of Nafion/inorganic composite

| Material | Specification | Quantity | Quantity including waste factor (4) |
|--------------------------------------|--------------------------------|-------------------|-------------------------------------|
| Nafion solution (20 wt% solution) | 1.2 mg Nafion cm ⁻² | 121.5 mg | 486.0 mg |
| Inorganic suspension | 3.7 mg | 1 cm ³ | 4 cm ³ |
| Acetone | 99.8% purity | 4 cm ³ | 16 cm ³ |

Including the waste factor of 4, therefore, 486.0 mg of 20 wt% Nafion solution is mixed with 16 cm³ of acetone and then 4 cm³ of inorganic suspension is added to the mixture. To achieve a well dispersed mixture, the two steps of 15 minutes stirring and another 15 minutes sonication are repeated for a total of 2 hours. The preparation method is illustrated in Figure 4.13.

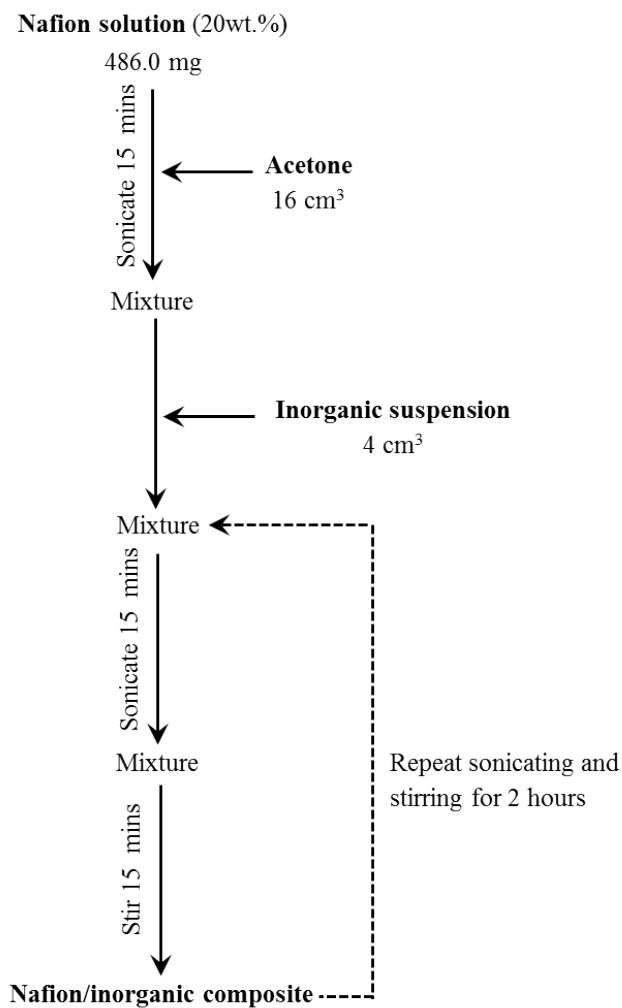


FIGURE 4.13: Nafion/inorganic composite preparation

4.3.3 Incorporating the methanol barrier layer onto the anode

The barrier layer is a modification of the binding layer; consequently, it is incorporated onto the anode instead of the binding layer.

1. The gas diffusion layer is constructed and the catalyst coating applied, as for the standard MEA preparation.

2. The mass of the anode is recorded, then it is cleaned by spraying 3.0 cm³ of acetone.
3. A first portion of 1.5 cm³ of the Nafion/inorganic composite is applied to the anode.
4. The solvent is evaporated by heating at 120 °C for 10 minutes and the anode is weighed.
5. To avoid blockage with the Nafion/inorganic composite, the spray gun is cleaned with 6 cm³ of acetone.
6. The additional composite ink is sprayed and dried. These steps are repeated until a target mass of 28.0 ± 2 mg of dry Nafion/inorganic composite layer is achieved.

4.4 Fabrication of new modified membrane electrode assemblies (procedure II)

An improved procedure for catalyst ink preparation was developed, by reducing the concentration of ink. This method is named **procedure II**. In addition, the E-TEK catalyst supplier closed, catalysts were obtained from Premetek instead. However, the catalysts from both companies had similar specifications, that is, 60 wt% Pt:Ru alloy on Vulcan XC-72 for the anode catalyst and 60 wt% Pt on Vulcan XC-72 for the cathode catalyst.

4.4.1 New standard MEA fabrication

4.4.1.1 New anode catalyst ink preparation

The compositions of new anode ink are depicted in Table 4.8 and the preparation method is presented in Figure 4.14.

TABLE 4.8: Composition of new anode catalyst ink for producing one electrode

| Material | Specification | Quantity | Quantity including waste factor (4) |
|--|----------------------------|-------------------|-------------------------------------|
| Pt:Ru catalyst (Pt:Ru:C = 40:20:40) | 1.0 mg Pt cm ⁻² | 50.6 mg | 202.4 mg |
| Nafion solution (20 wt% solution) | 15 wt% Nafion | 44.7 mg | 178.8 mg |
| Acetone | 99.8% purity | 4 cm ³ | 16 cm ³ |

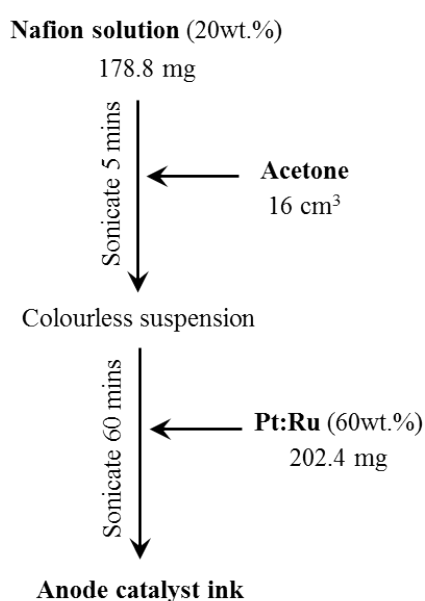


FIGURE 4.14: Preparation of new anode catalyst ink

4.4.1.2 New cathode catalyst ink preparation

The required masses of the new cathode catalyst ink are shown in Table 4.9 and the preparation method is presented in Figure 4.15.

TABLE 4.9: Compositions of new cathode catalyst ink for producing one electrode

| Material | Specification | Quantity | Quantity including waste factor (4) |
|--------------------------------------|----------------------------|-------------------|-------------------------------------|
| Pt catalyst (Pt:C = 60:40) | 1.0 mg Pt cm ⁻² | 33.8 mg | 135.2 mg |
| Nafion solution (20 wt% solution) | 15 wt% Nafion | 29.8 mg | 119.2 mg |
| Acetone | 99.8% purity | 4 cm ³ | 16 cm ³ |

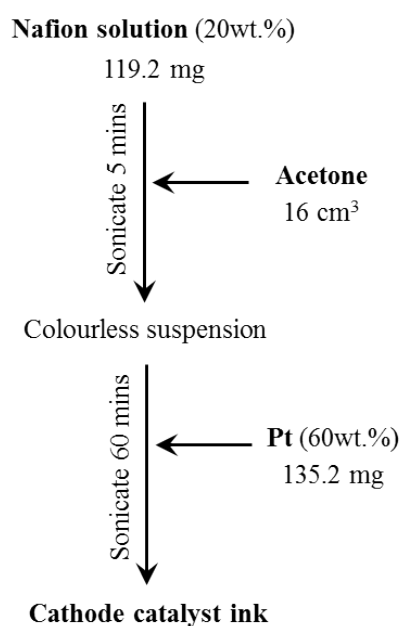


FIGURE 4.15: New cathode catalyst ink preparation

4.4.2 New modified MEAs

Because of the convenience of coating the catalyst ink onto the electrode, the improved catalyst preparation method was used to produce the new modified MEAs. Of the four inorganic materials (mordenite, zeolite Y, montmorillonite and sodium titanate) reviewed, the Nafion/montmorillonite composite was selected for incorporation as the methanol barrier layers. The new modified MEAs

with these inorganic components were produced to achieve the best DMFC performance. These are summarized in Table 4.10.

TABLE 4.10: New modified MEAs incorporating Nafion/montmorillonite (MMT) composite or Nafion/sodium titanate (TN) composite as the methanol barrier layer

| Inorganic wt% (Equation 4.3) | Inorganic wt% (Equation 4.4) | Nafion/MMT label |
|---------------------------------|---------------------------------|---------------------|
| 0.25 | 7.04 | 0.25% MMT |
| 0.50 | 13.21 | 0.50% MMT |
| 1.00 | 23.37 | 1.00% MMT |

Summary

Two procedures for preparing the MEAs are described in this chapter. The procedure I is a standard method developed by this group. This method aims to enhance the DMFCs power output by incorporating the methanol barrier layer into the MEAs. Meanwhile the procedure II is first used in this research to improve the performance of MEAs by adjust the morphology of MEAs in addition of introducing the methanol barrier layer into the MEAs.

Chapter 5

Results and discussion I:

Performance of standard and modified membrane electrode assemblies

5.1 Standard membrane electrode assembly operation

These experiments have been carried out to study the effect of temperature and methanol concentration on the standard MEA to achieve the optimum conditions of the fuel cell performance. In these tests, a 4.5×4.5 cm standard MEA, labelled STD1, was fabricated and tested under the conditions listed in Table 5.1.

TABLE 5.1: Parameters of DMFC operation for STD1

| Parameter | Value |
|---|--|
| Anode catalyst E-TEK 60% Pt:Ru on Vulcan XC72 | 1 mg Pt cm ⁻² |
| Cathode catalyst E-TEK 60% Pt on Vulcan XC72 | 1 mg Pt cm ⁻² |
| Methanol concentration | 1, 2, 4 M |
| Methanol flow rate | 5 cm ³ min ⁻¹ |
| Air flow rate | 1000 cm ³ min ⁻¹ |
| Cell temperature | 30–80 °C |

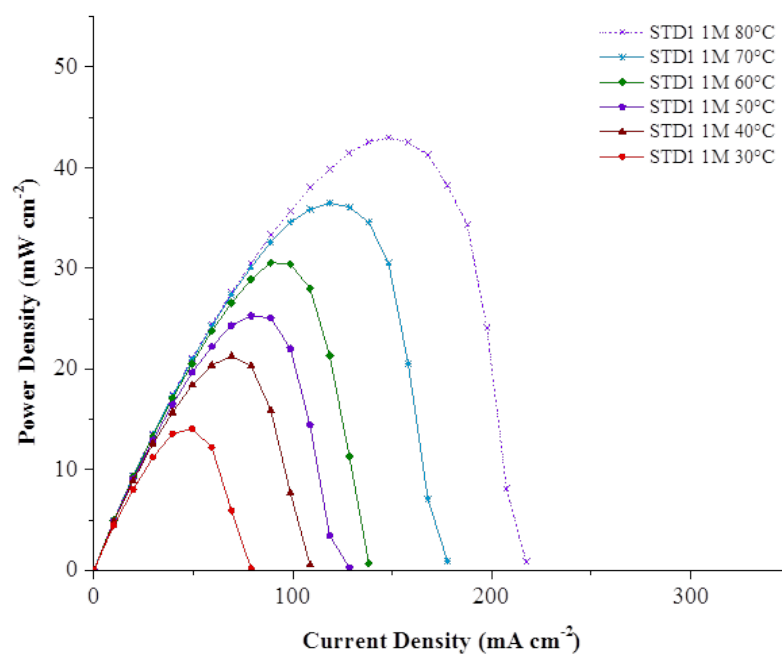
5.1.1 Influence of cell temperature on performance of STD1 using 1 M methanol solution

Polarization and power density curves are shown in Figure 5.1. It can be seen that the maximum power density and the limiting current density noticeably increase with cell temperature. This feature is generally present in the DMFC system because the raised cell temperature improves the electrochemical kinetics at both electrodes. This means that the activation loss is reduced. Moreover, membrane resistance decreases with increasing temperature, reducing ohmic loss. However, high operating temperatures also give the disadvantages, at low current densities, of extending membrane diffusivity and increasing electro-osmotic drag, leading to methanol transport through the membrane. At high current densities, methanol consumption is greater, reducing methanol concentration at the anode, thereby providing low methanol crossover to the cathode [86, 204, 205].

The main conclusions to be drawn from this experiment are as follows:

- Magnitudes of OCV are comparable. They increase with increasing temperature, from 584 mV at 30 °C to 599 mV at 80 °C. This trend shows that the improvement in electrochemical activity has more influence than the effect from the methanol crossover.

(A) Polarization curve



(B) Power density curve

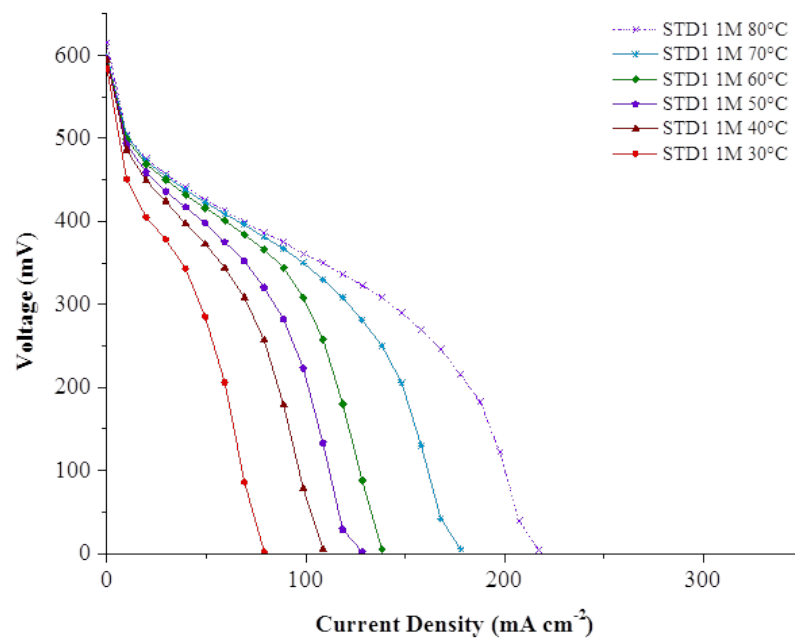


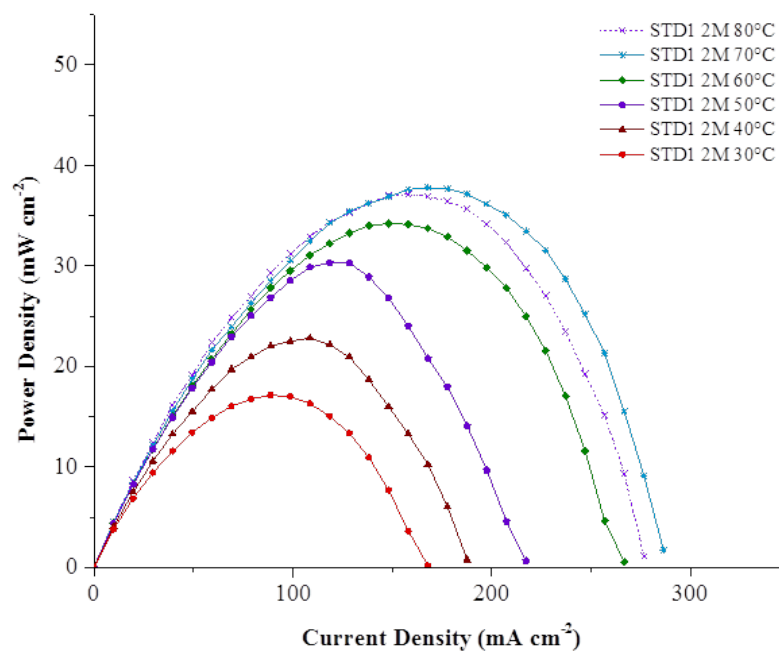
FIGURE 5.1: Performance of STD1 at 1 M methanol

- Limiting current densities increase with increasing temperature, from 79.01 mA cm⁻² at 30 °C to 217.28 mA cm⁻² at 80 °C.
- Mass transport loss dominates at high current densities for every performance plot. This is observed by the rapid drop in voltage at high current densities.
- Polarization and power density curves of STD1 are consistent in value and characteristic with standard MEAs previously prepared in this research group using the same procedure [106, 194, 200].

5.1.2 Influence of methanol concentration on performance of STD1 using 2 M and 4 M methanol solution

Experiments with higher methanol feed concentrations were carried out to study the effect on cell performance and to investigate the phenomenon of methanol crossover. While the other operating parameters remained the same, the methanol concentration was increased to 2 M and 4 M. The results are presented in Figures 5.2 and 5.3.

(A) Power density curve



(B) Polarization curve

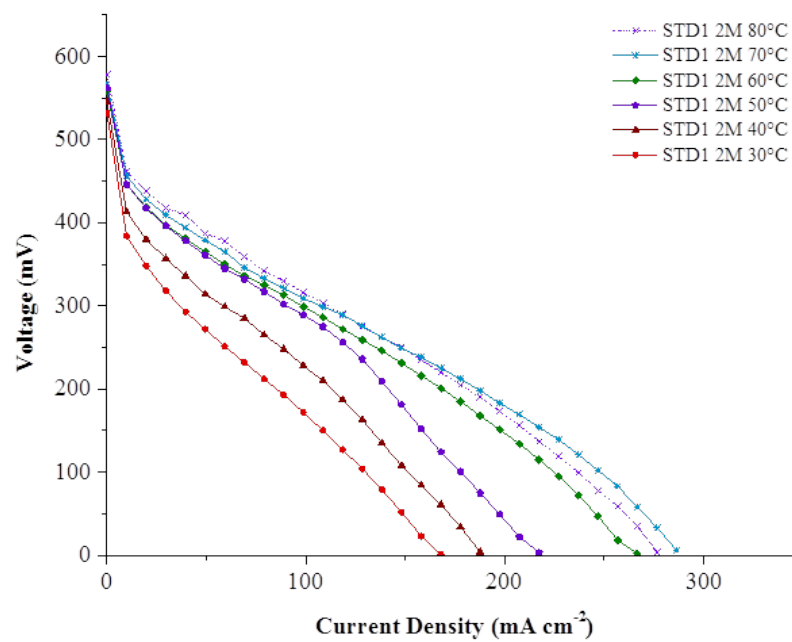
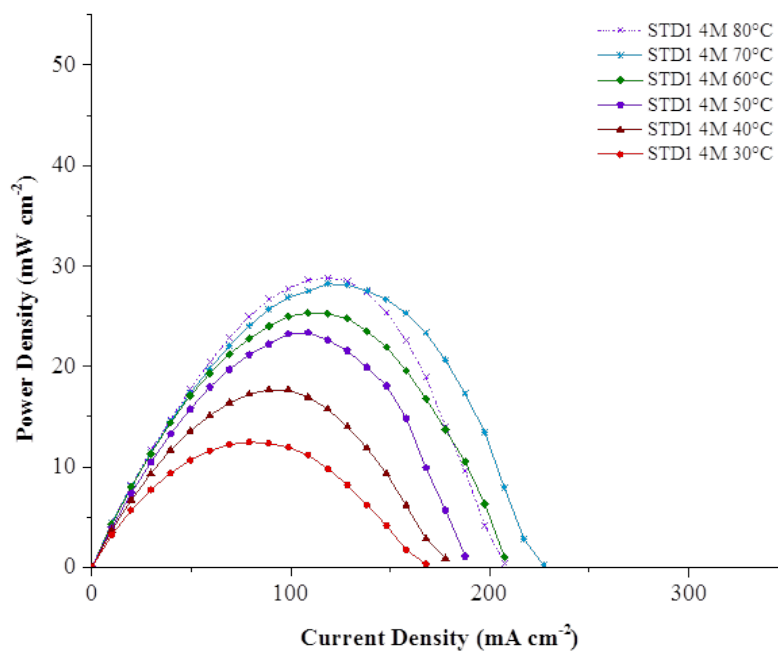


FIGURE 5.2: Performance of STD1 at 2 M methanol

(A) Power density curve



(B) Polarization curve

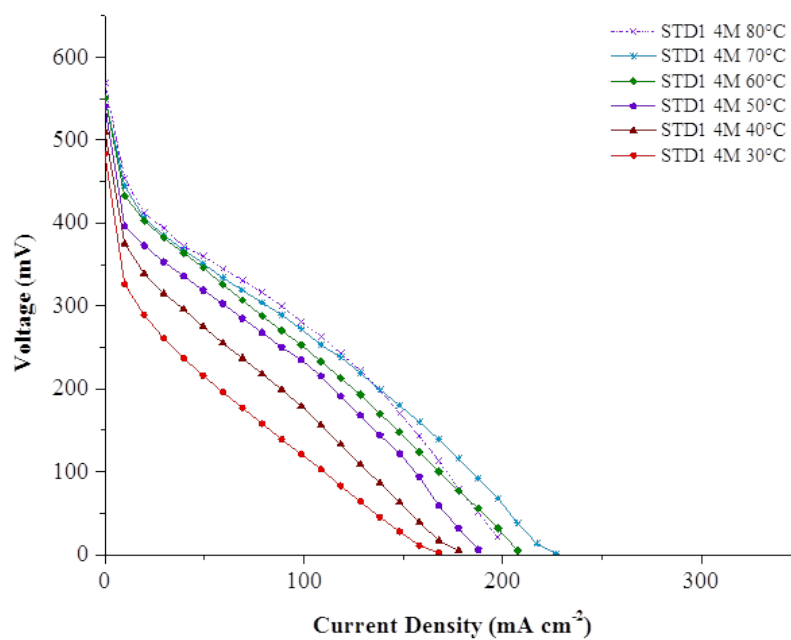


FIGURE 5.3: Performance of STD1 at 4 M methanol

As seen in Figure 5.4, at higher methanol concentrations, maximum power density rises with cell temperature. Comparing the three concentrations, 1 M gives the best power density (42.96 mW cm^{-2}) at $80 \text{ }^\circ\text{C}$ but at $30\text{--}70 \text{ }^\circ\text{C}$ the maximum power densities for 2 M are greater than those at 1 M. Nevertheless, the peak power density for 2 M drops at $80 \text{ }^\circ\text{C}$ because of an increase in methanol diffusion. It is clear that 2 M gives superior limiting current densities over 1 M, owing to better mass transfer at high methanol concentrations. Maximum power densities dropped for 4 M at all temperatures. This can be explained by the effect of methanol crossover, which is more influential at higher concentrations, in good agreement with the literature [86, 204].

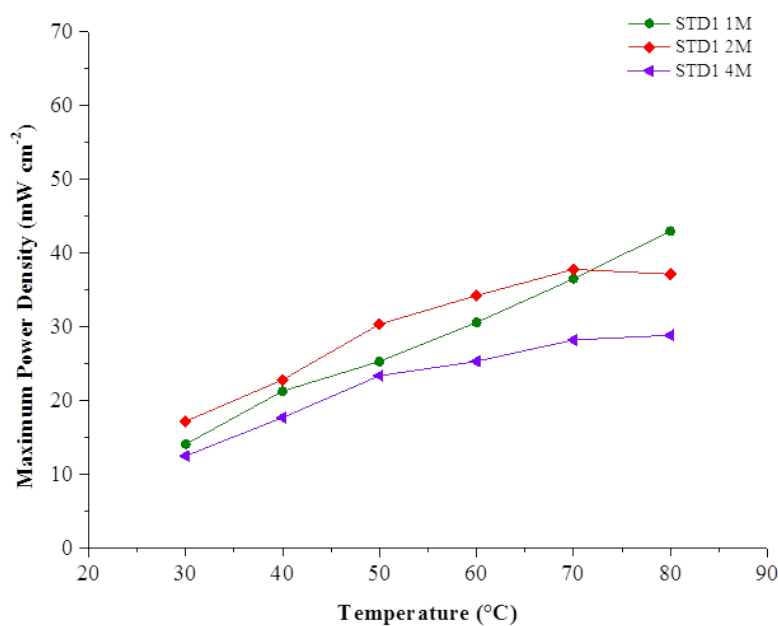


FIGURE 5.4: STD1 maximum power density at methanol concentrations of 1 M, 2 M and 4 M

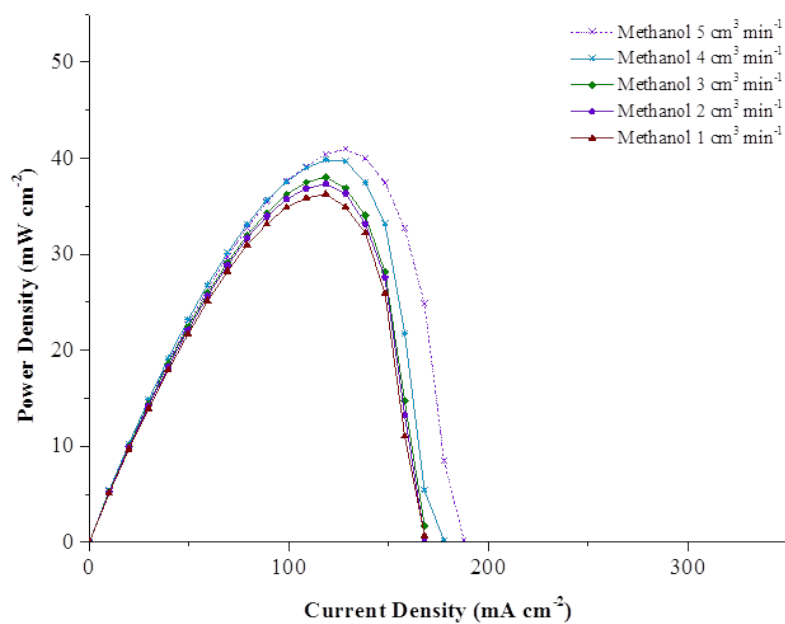
5.1.3 Influence of methanol and oxygen flow rate on STD1 performance using 1M methanol solution

To optimize the methanol and air flow rates, a set of experiments was carried out with methanol flow rates of 1–5 cm³ min⁻¹ and air flow rates of 400–2000 cm³ min⁻¹. The concentration of methanol was 1 M and the cell temperature was maintained at 70 °C.

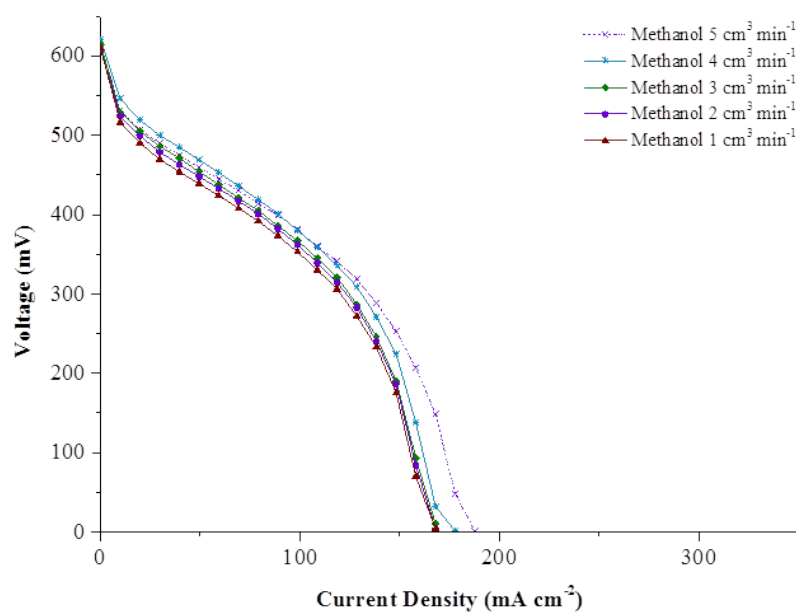
Figure 5.5 shows that increasing methanol flow rate slightly improves fuel cell performance. Our group found (data not shown) that cell performance was not improved for flow rates higher than 5 cm³ min⁻¹, hence a methanol flow rate of 5 cm³ min⁻¹ is used in the rest of this research.

It can be seen in Figure 5.6 that changing air flow rate has very little effect on performance. Nevertheless, low air flow rates reduce the access of oxygen to the cathode and cause higher mass transport limitations [90].

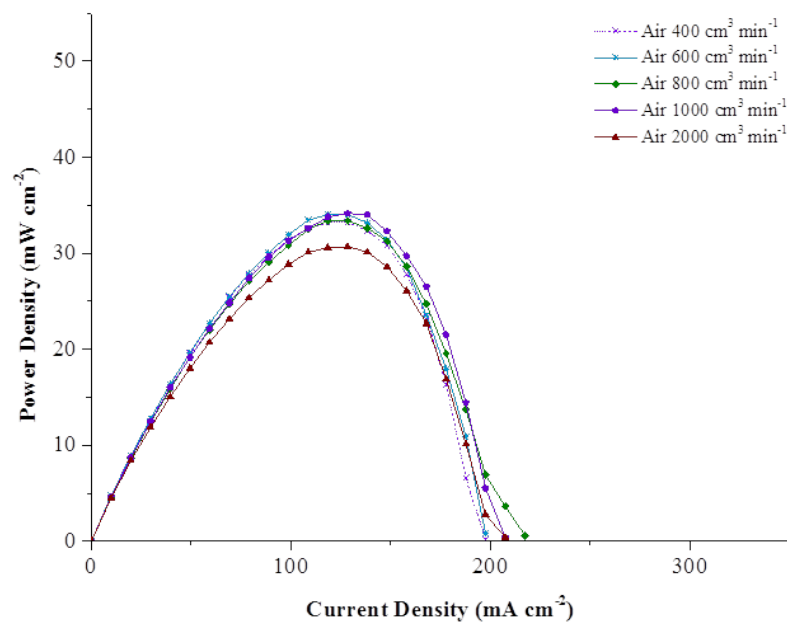
(A) Power density curve



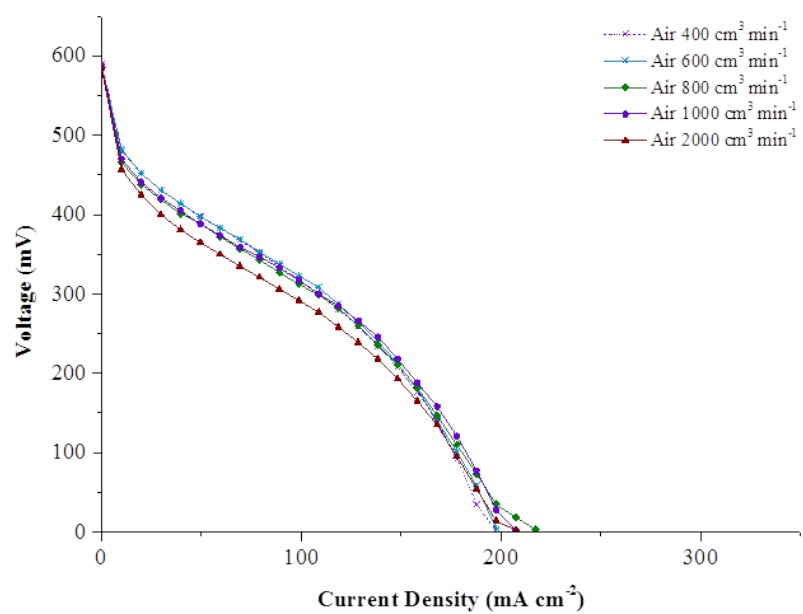
(B) Polarization curve

FIGURE 5.5: Performance of STD1 at different methanol flow rates (1–5 cm³ min⁻¹)

(A) Power density curve



(B) Polarization curve

FIGURE 5.6: Performance of STD1 at different air flow rates (400–2000 cm³ min⁻¹)

5.1.4 Influence of catalyst loading

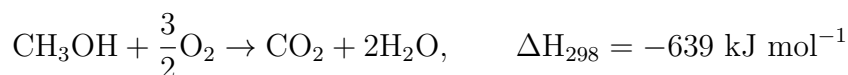
To commercialize DMFCs, it is important to reduce the amount of high cost Pt catalyst used. A lower catalyst loading, with 0.5 mg Pt cm⁻² was used on both electrodes to investigate the effect of the catalyst. This MEA is labelled STD2. Operating conditions are listed in Table 5.2 and the results of this experiment are shown in Appendix A, Figures A.1 - A.3, Page 234.

TABLE 5.2: Parameters of DMFC operation for STD2

| Parameter | Value |
|---|--|
| Anode catalyst E-TEK 60% Pt:Ru on Vulcan XC72 | 0.5 mg Pt cm ⁻² |
| Cathode catalyst E-TEK 60% Pt on Vulcan XC72 | 0.5 mg Pt cm ⁻² |
| Methanol concentration | 1, 2, 4 M |
| Methanol flow rate | 5 cm ² min ⁻¹ |
| Air flow rate | 1000 cm ² min ⁻¹ |
| Cell temperature | 30–80 °C |

The trend of cell performance in STD2 is similar to that in STD1; the power densities shift upward over the whole temperature range when the methanol concentration is increased from 1 M to 2 M. However, the power densities decrease as the methanol concentration is increased further, to 4 M.

It is important to note when operated STD2 at low current density, the cell temperature is unstable due to the oxidation of permeated methanol in a present of oxygen releasing heat as shown in Equation 2.20, Page 77 which is recalled as:



Therefore, the unstable temperature attributes to the fluctuation in performance curves of STD2. In contrast, methanol crossover linearly declines with the rise in cell current. The heating because of Equation 2.20 tends to zero at high current density [205].

There is a significant decrease in the cell performances with a reduction of catalyst loading. As seen in Figure 5.7, STD2 presents lower power densities than STD1 over all methanol concentrations.

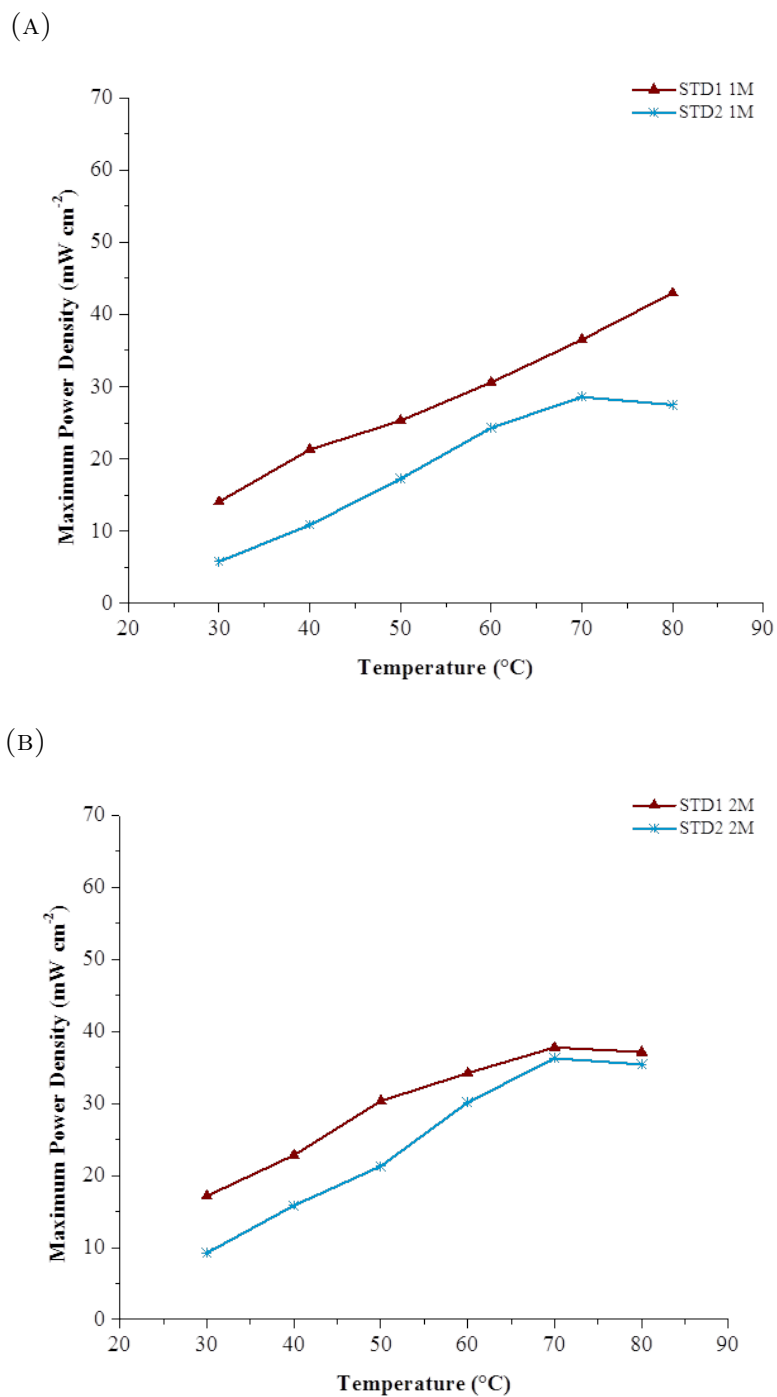


FIGURE 5.7: Comparison of maximum power densities of STD1 and STD2 at (A) 1 M methanol (B) 2 M methanol (C) 4 M methanol

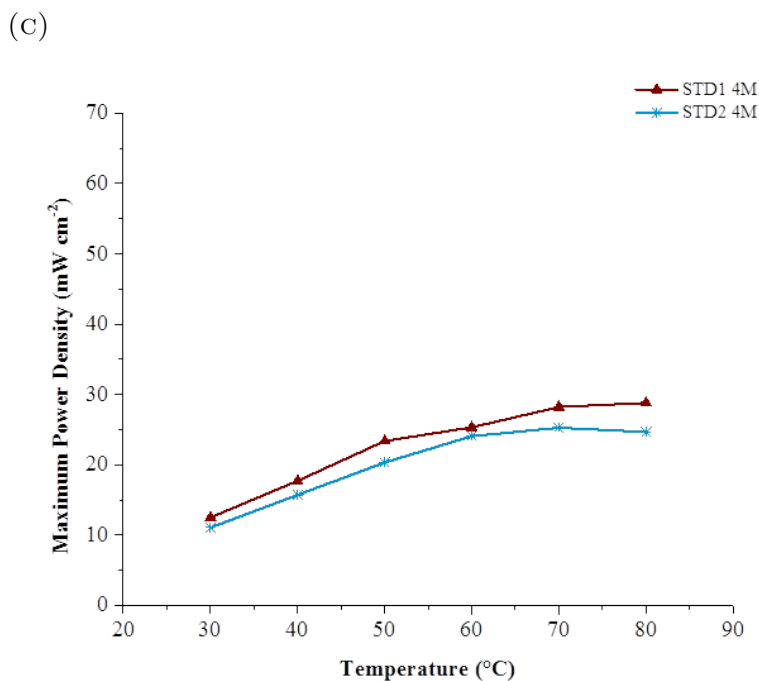


FIGURE 5.7 (cont.): Comparison of maximum power densities of STD1 and STD2 at (A) 1 M methanol (B) 2 M methanol (C) 4 M methanol

5.1.5 Summary of optimum conditions for MEA operation

Catalyst loading

By comparing STD1 and STD2 MEAs, it can be concluded that a better performance for this DMFC system is obtained using 1 mg Pt cm^{-2} .

Methanol concentration

Methanol concentrations of 1 M, 2 M and 4 M are used to investigate the MEA performance.

Methanol flow rate

A methanol feed of $5 \text{ cm}^3 \text{ min}^{-1}$ was selected because it provide the best power density. This flow rate supports a suitable methanol stoichiometry for the oxidation reaction and removal of CO_2 from the flow field channels.

Air flow rate

An air flow rate of $1000 \text{ cm}^3 \text{ min}^{-1}$ will be set for the remaining experiments to ensure that water flooding at the cathode is prevented.

5.2 Modified MEAs Operations

Methanol crossover is a critical problem of the DMFC. It has an influence on the reduction of the fuel cell efficiency and the lower OCV value. This research focuses on the modified MEAs by incorporating a methanol barrier layer onto the anode electrode for the purpose of significantly eliminating methanol permeability and achieving improved DMFC performance.

The methanol barrier layer is made up of Nafion/inorganic composite material. The location of the methanol barrier layer is shown in Figure 5.8. At the location of this layer between catalyst layer and Nafion membrane, this layer may be prevent methanol transportation from anode to cathode.

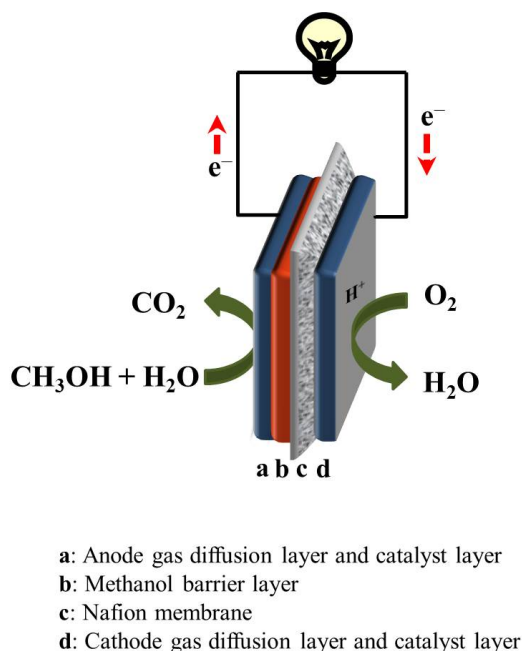


FIGURE 5.8: The modified MEA by incorporating a methanol barrier layer onto the anode electrode

Previous work found that 0.50 wt% of inorganic material to the weight of the Nafion membrane presented the best DMFC performance [106]. Hence this amount of mordenite, zeolite Y, montmorillonite and sodium titanate ($\text{Na}_2\text{Ti}_3\text{O}_7$) are applied on the anode side of four modified MEAs which are labelled as illustrated in Table 5.3. Mordenite, zeolite Y, montmorillonite are the commercial grade but titanate is synthesised by hydrothermal method.

5.2.1 Preparation of titanate

TiO_2 0.25 g (Analytical grade, Aldrich) was mixed with 20 mL of 10 M NaOH aqueous solution (Analytical grade, Aldrich). After stirring at room temperature for an hour, the mixture was transferred to a Teflon-lined autoclave and then heated at 150 C for 24, 48, 72 and 96 hours. The reaction was cooled to the room temperature under natural condition. The precipitate was filtered and washed with deionised water.

A synthesised sodium titanate was analysed through X-ray diffraction (XRD) crystallography. The XRD patterns are presented in Figure 5.9. Comparing XRD patterns of samples against the literature, it can be observed that intensity and located peaks of sample corresponding to those of monoclinic sodium titanate nanotubes ($\text{Na}_2\text{Ti}_3\text{O}_7$) (JCPDS No. 00-031-1329) [206, 207]. SEM image in Figure 5.10 present morphology of synthesis titanate.

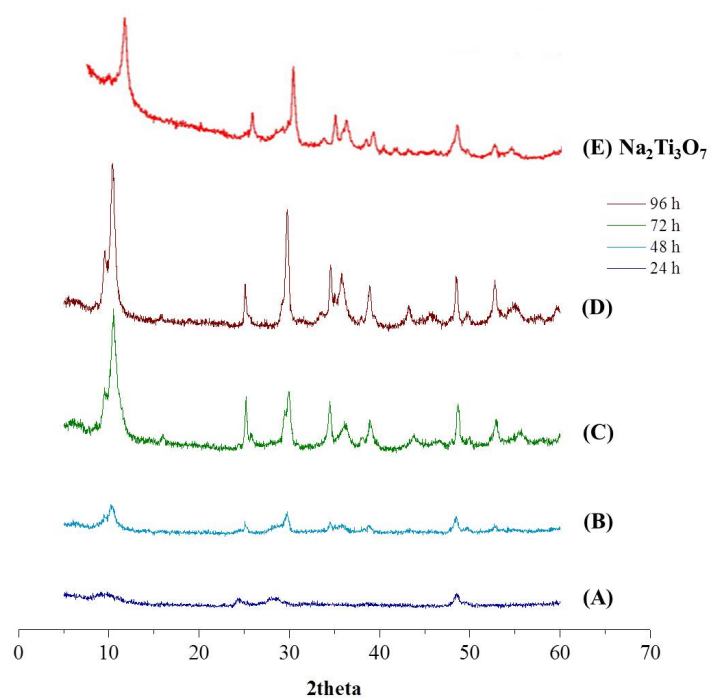


FIGURE 5.9: XRD patterns of titanate with different hydrothermal periods at (A) 24 hours (B) 48 hours (C) 72 hours (D) 96 hours and $\text{Na}_2\text{Ti}_3\text{O}_7$ [206]

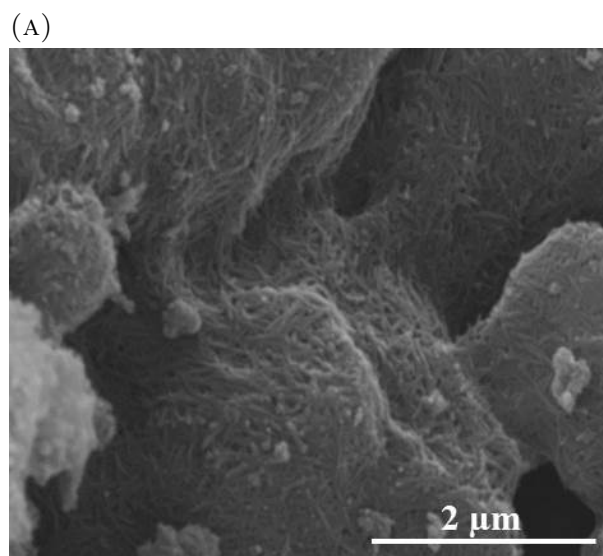


FIGURE 5.10: SEM image of titanate with different hydrothermal periods at (A) 24 hours (B) 48 hours (C) 72 hours (D) 96 hours

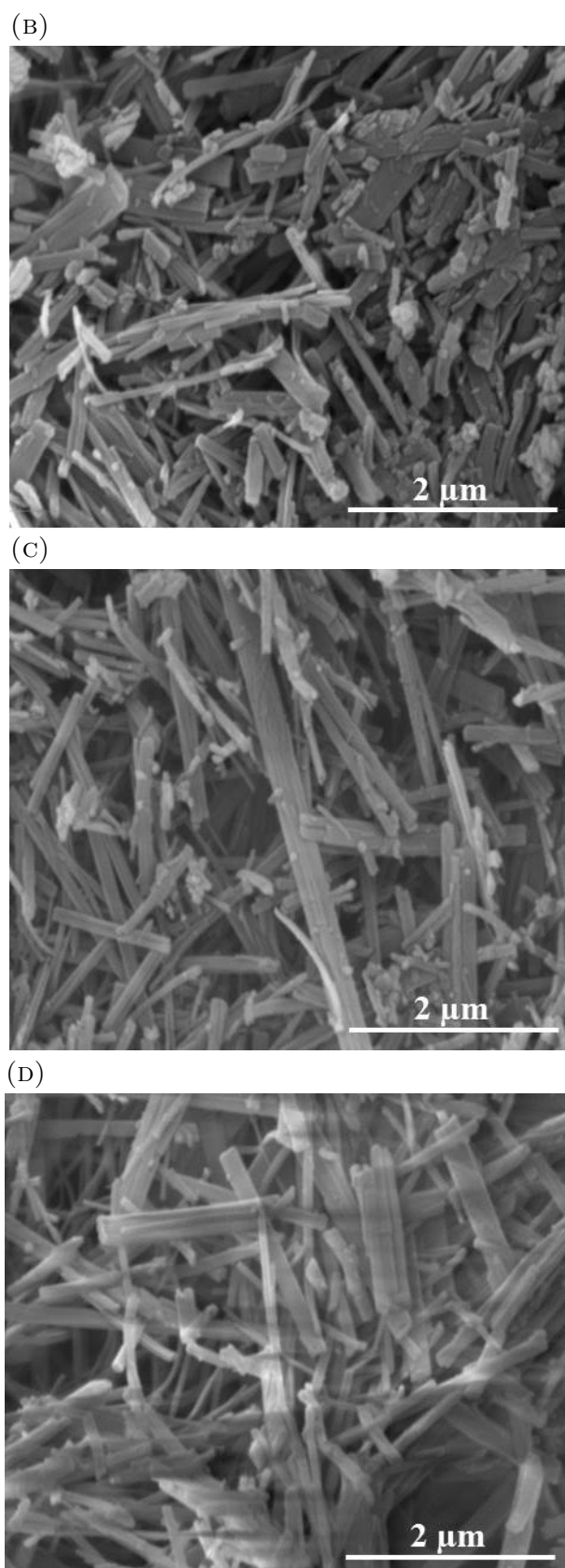
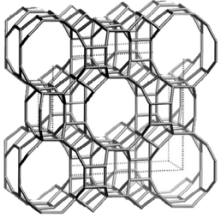
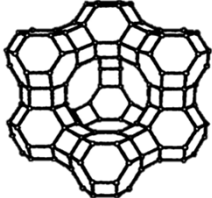
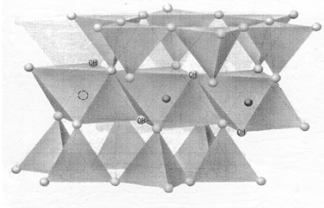
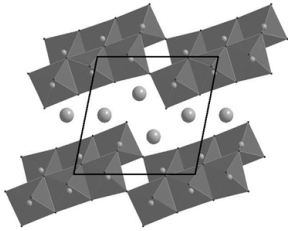


FIGURE 5.10 (cont.): SEM image of titanate with different hydrothermal periods at (A) 24 hours (B) 48 hours (C) 72 hours (D) 96 hours

TABLE 5.3: Modified MEAs

| Materials | Crystal Structures | wt.% of Materials | Label |
|-----------------|---|-------------------|-----------|
| Mordenite |  [193] | 0.50 | 0.50% MOR |
| Zeolite Y |  [208] | 0.50 | 0.50% ZY |
| Montmorillonite |  [172] | 0.50 | 0.50% MMT |
| Titanate |  [185] | 0.50 | 0.50% TN |

5.2.2 The Comparison Performance of the STD1 and the modified MEAs with 1 M Methanol

The performance of modified MEAs are displayed by the polarization and power density curves, as shown in Appendix A, Figure A.12 - A.15, Page 252.

The comparison of maximum power density between the STD1 and the modified MEAs with a 1 M methanol are presented in Figure. The maximum power density of the 0.50% MOR and the 0.50% MMT outperform the STD1 over the entire temperature. At 80 °C, they offer the best power densities 5.52% and 9.63% better than that value of the STD1 (42.96 mW cm⁻²). Not only the power densities

have been improved but the limiting current densities of the modified MEAs also significantly exceed the STD1. This feature could be due to the methanol barrier layer which impedes methanol transportation from anode to cathode. With low methanol crossover, a high methanol concentration in catalyst layer improve the oxidation reaction and reduces the mass transfer loss at anode. However, the barrier layer can repel both methanol and protons hence it could be obstruct proton conductive resulting the lower performance as presented in the curves of 0.50% ZY and the 0.50% TN.

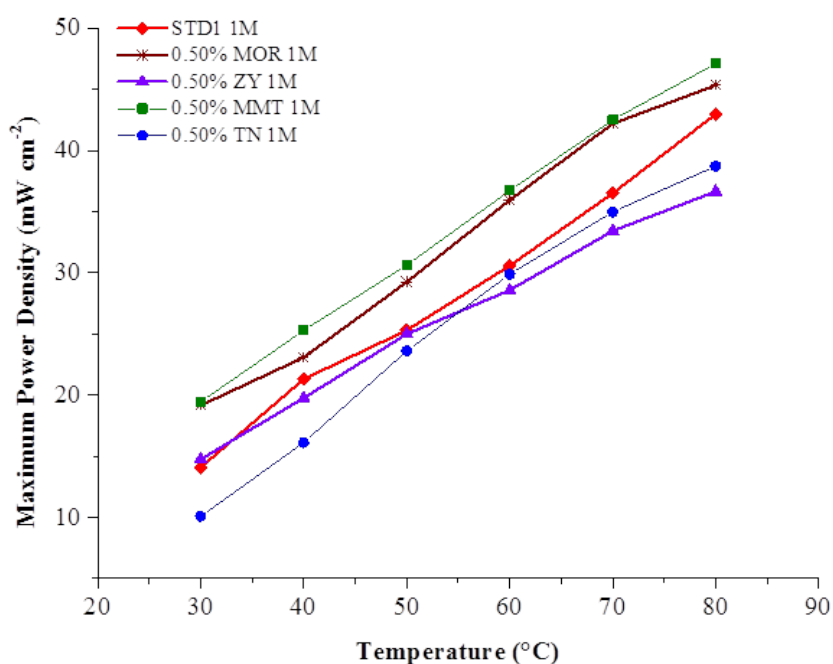


FIGURE 5.11: Comparison of maximum power densities of STD1, 0.50% MOR, 0.50% ZY, 0.50% MMT and 0.50% TN at 1 M methanol

5.2.3 The Comparison Performance of the STD1 and the modified MEAs with 2 M Methanol

The performances of modified MEAs can be seen in Appendix A, Figure A.18 - A.19, Page 258. The results at a 2 M methanol feed show an interesting phenomenon. The maximum power densities of 0.50% TN are slightly lower than

those obtained from STD1 at the low temperature (30-50 °C) as shown in Figure 5.12. On the other hand, at the high temperature (60-80 °C) the performances of 0.50% TN are found to be higher than those of STD1. The curve of the 0.50% MMT exhibits superior power densities than STD1 at all temperatures. The best improvement 26.60% and 19.76% are obtained at 80 °C from the 0.50% TN and the 0.50% MMT, respectively when compared with STD1 (37.14 mW cm^{-2}). This occurs because the STD1 has higher methanol flux through the membrane with the increased methanol concentration [86] giving the power density drop in comparison with the 0.50% TN and the 0.50% MMT. It appear that the barrier layer achieves the goal to suppress methanol transportation. For the 0.50% MOR and the 0.50% ZY, they show the comparable performance with STD1.

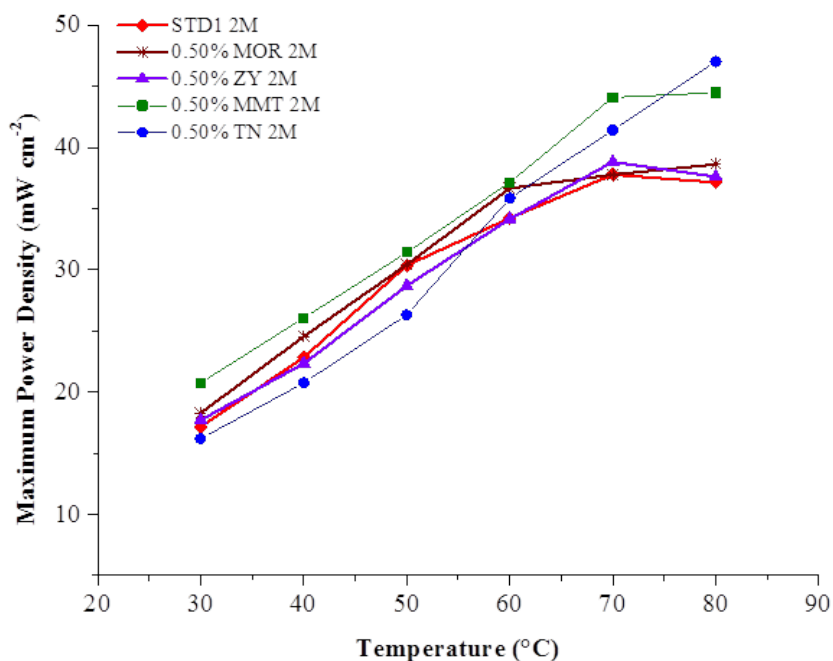


FIGURE 5.12: Comparison of maximum power densities of STD1, 0.50% MOR, 0.50% ZY, 0.50% MMT and 0.50% TN at 2 M methanol

5.2.4 The Comparison Performance of the STD1 and the modified MEAs with 4 M Methanol

The performances of modified MEAs can be seen in Appendix A, Figure A.22 - A.23. The results exhibit lower performance related to the output of 1 M and 2 M. This indicated to the high methanol crossover. In terms of power density, the maximum value of all MEAs significantly drop when methanol feed is changed to 4 M. This is an effect of the higher methanol concentration leading to more methanol permeability via the electrolyte membrane. The performance can be categorised into two groups by the characteristic of the maximum power density curve. The first group are STD1, 0.50% MMT and 0.50% TN in which maximum power densities are improved proportionally with the temperature. The second group consists of 0.50% MOR and 0.50% ZY. Their maximum power densities noticeably fall at high temperature 70-80 °C. There are 28.40% and 66.26% lower power density than STD1.

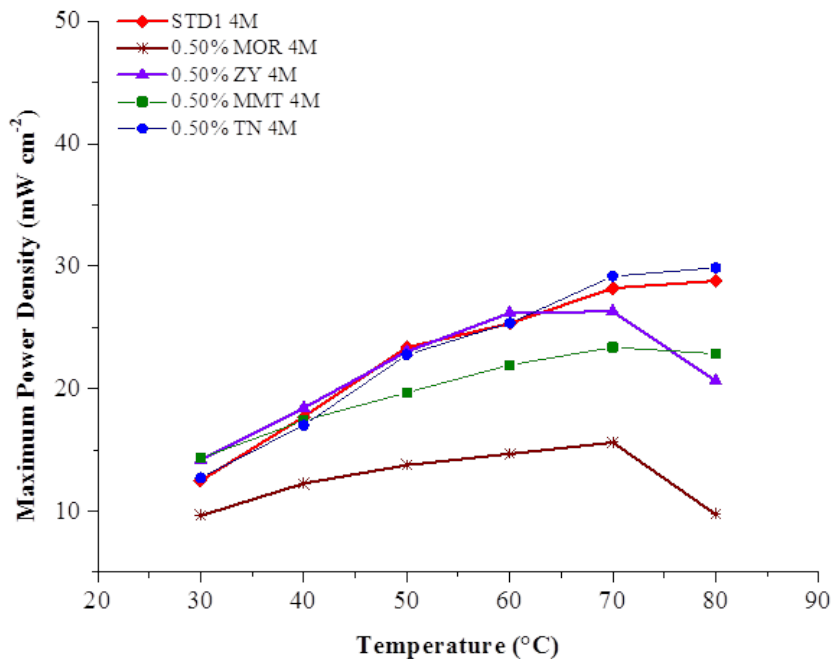


FIGURE 5.13: Comparison of maximum power densities of STD1, 0.50% MOR, 0.50% ZY, 0.50% MMT and 0.50% TN at 4 M methanol

5.2.5 Contact Angle Measurement

From the literature [141, 152, 209], hydrophilicity/hydrophobicity of electrode and membrane have an impact on the methanol transportation. As a methanol barrier layer is applied onto the anode to prevent methanol migration, the contact angle of each barrier layer as well as the pristine Nafion layer were determined. Water, 1 M and 2 M methanol are dropped on the surface of Nafion/inorganic composite layer. Contact angles are measured using KRUSS DSA 100 drop size analyser at 23 °C on three different areas of each electrode then the average value was calculated. Three series of contact angle measurement are summarised in Figure 5.14 and the details are presented in Appendix B, Figure B.1 - B.3, Page 281.

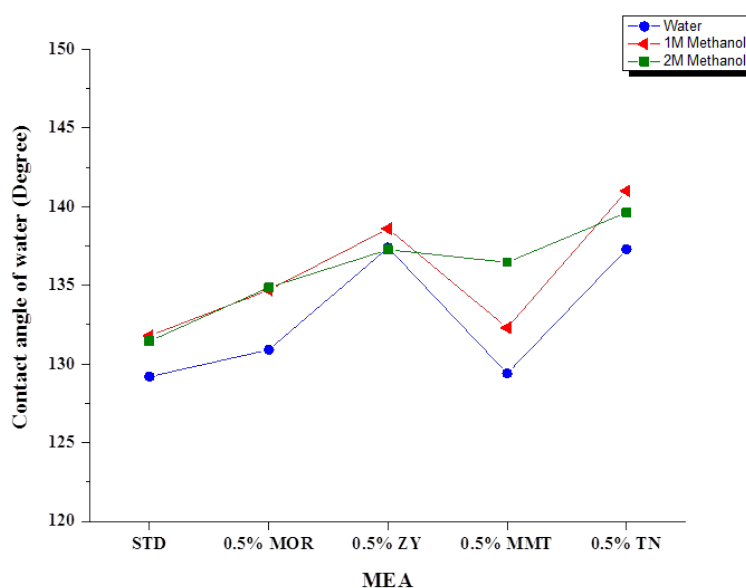


FIGURE 5.14: Comparison contact angle of water, 1 M and 2 M methanol

All layers contribute large contact angle with methanol solution than water (Figure 5.14) which implied that the layers would repel methanol over water. In addition, the composite layers provide larger angle with methanol than those of

pure Nafion layer. That means the composite layers have more organophobic character¹ than a bare Nafion layer.

As shown in Figure 5.15 and 5.16, 0.5% TN conducts higher contact angle than other barrier layers both in methanol solution and water. The higher contact angle, the lower maximum power density. It would imply that, although the barrier layer serves a function of methanol barrier layer, it also prevents water transportation. This appearance would reduce a performance of 0.5% TN as seen in the lowest maximum power density relative to other modified MEA.

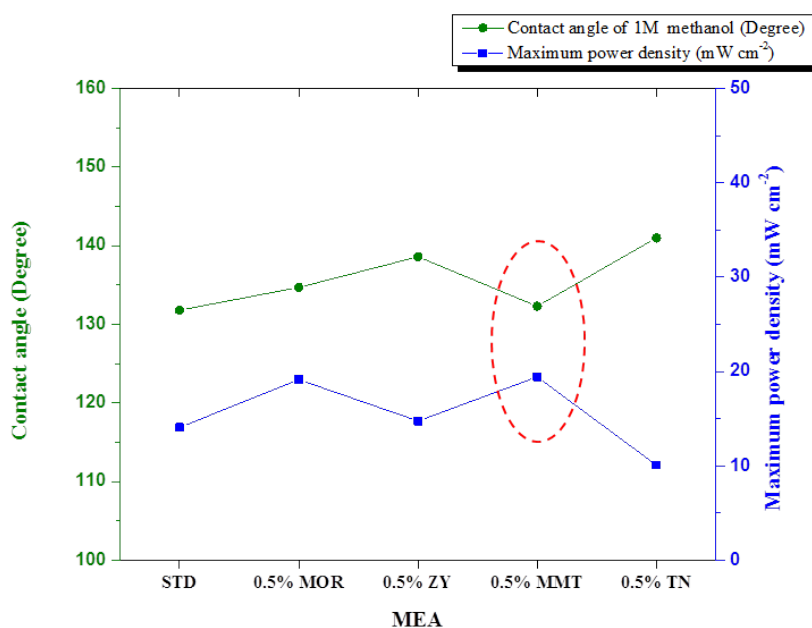


FIGURE 5.15: Relation of contact angle and maximum power density at 1 M methanol

Considering the contact angles of 0.5% MMT which presents an interesting phenomenon. It has a lower contact angle than 0.5% TN but bigger than STD that indicates moderate relative hydrophobic property. It could influence the best performance of this MEA. From the experiment, a reduction of methanol crossover could be control by organophilic/organophobic property of the composite barrier layer.

¹It is resistant to organic compounds.

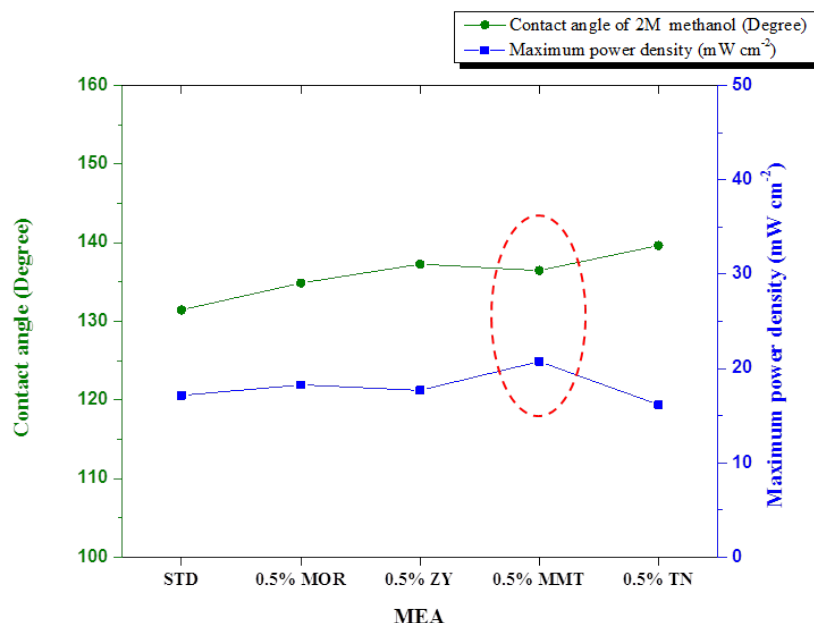


FIGURE 5.16: Relation of contact angle and maximum power density at 2 M methanol

5.2.6 Summary

The materials suitable for Improving DMFC Performance

Two types of inorganic materials which are microporous materials and (MOR and ZY) 2-dimensional material (MMT and TN) have been incorporated into a methanol barrier layer. The best improvement in maximum power densities of the modified MEAs relative to STD1 are presented in Table 5.4. Superior performances are enhanced from 2-dimensional material, MMT and TN. Therefore, further investigation of MMT content in the barrier layer will be carried out.

TABLE 5.4: The best improvement in maximum power densities of the modified MEAs relative to STD1

| Sample | 0.5% MOR | 0.5% ZY | 0.5% MMT | 0.5% TN |
|--|--------------------|--------------------|--------------------|--------------------|
| % Improvement in maximum power densities | 5.52 | 2.73 | 19.74 | 26.58 |
| Operation conditions | 1M methanol, 80 °C | 1M methanol, 70 °C | 2M methanol, 80 °C | 2M methanol, 80 °C |

The potential of organophobic property of the methanol barrier layers to DMFC Performance

The higher organophobic property contributes to the larger contact angle between methanol barrier layer and methanol droplet. The contact angles of barrier layers featuring with microporous material (0.5% ZY) and 2-dimensional material (0.5% MMT) exist an interested characteristic.

Results in Table 5.5 indicate that organophobic property impacts on MEA performances yielding higher maximum power density of 0.5% ZY and 0.5% MMT related to STD. Although both barrier layers offer almost similar angles, there are different maximum power densities observed from the MEAs incorporating with them.

It seems that not only the organophobic property of methanol barrier layer influences on the MEA performance, but also the structure of additive materials introduced into the barrier layer. With comparable organophobic property, an advantage of 2-dimensional structure MMT could increase the power density over that of microporous structure ZY.

TABLE 5.5: Contact angles measured from the barrier layers featuring with 0.5% ZY and 0.5% MMT at 2M methanol

| Sample | Contact angle (Degree) | Maximum power density (mW cm ⁻²) |
|----------|------------------------|--|
| STD | 131.5 | 14.07 |
| 0.5% ZY | 137.3 | 17.70 |
| 0.5% MMT | 136.5 | 20.75 |

Chapter 6

Results and discussion II: Performances of new standard and new modified MEAs

6.1 New standard MEA operation

Although the DMFC performances have been enhanced by incorporating the methanol barrier layer into membrane electrode assemblies (MEA), the maximum power densities of modified MEAs are moderate; hence, further improvement in power output has been targeted.

There are several strategies to increase DMFC and PEMFC performances: i) control hydrophilic/hydrophobic properties of the microporous and/or catalyst layers [95, 141, 146, 210–212]; ii) adjust pore size of catalyst layer [213]; iii) develop MEA fabrication methods [214–216]. Aricò et al. [217] mentioned that an interface of catalyst particles and ionomer phase in a catalyst layer depended on size of carbon-supported catalyst and Nafion micelles. The agglomeration of Nafion micelles reduced the three-phase reaction sites and limited the network for electron and proton transport which resulted in ohmic loss inside the catalyst

layer. Wang et al. [218] illustrated that the small aggregation size of ionomer and catalyst particles contributed to a better contact between them representing a higher electrode performance compared to that of large agglomeration size.

It has been seen that a good distribution of ionomer and catalyst particles inside the catalyst layer strongly influences the performance of MEAs. An approach for producing low concentration catalyst ink which provides a good dispersion of particles in catalyst ink and thus relates to good particle utilisation inside the catalyst layer was carried out.

A new-standard MEA, named STD3, was fabricated using **procedure II**. The concentrations of new anode and cathode catalyst inks halved the preparation time of the catalyst ink, compared with (**procedure I** (Section 4.1.2, 121)). Apart from the concentrations of anode and cathode catalysts, the other processes for the MEA fabrication in Procedure I and II were the same.

A new standard MEA called STD3 has been produced by the catalyst perpetration **procedure II** and tested with the conditions in Table 6.1. Its performances are compared to the results of STD1 which is formed with the catalyst perpetration **procedure I**. Although the concentration of catalyst inks are changed, the catalyst quantity accumulating on each electrode of STD3 and STD1 is similar at 1 mg Pt cm^{-2} .

TABLE 6.1: The parameters of STD3 operation

| Parameters | Units |
|--|--------------------------------------|
| Anode catalyst ETEK 60% Pt:Ru on Vulcan XC72 | 1 mg Pt cm^{-2} |
| Cathode catalyst ETEK 60% Pt on Vulcan XC72 | 1 mg Pt cm^{-2} |
| Methanol concentration | 1, 2, 3, 4 M |
| Methanol flow rate | $5 \text{ cm}^2 \text{ min}^{-1}$ |
| Air flow rate | $1000 \text{ cm}^2 \text{ min}^{-1}$ |
| Cell temperature | 30–80 °C |

6.1.1 Influence of methanol concentration on the performance of STD3 using 1M, 2M and 4M methanol solution

The performance curves of STD3 are shown in Appendix A, Figure A.4 - A.6, Page 238. It can be observed that the maximum of each power density peaks elevate and shift to higher current density when the operating temperature is increased. There is the general trend for DMFC performance. The maximum power densities of STD3 at different methanol concentrations are given in Figure 6.1. The higher performances at 2M methanol concentration outperform those of other concentrations.

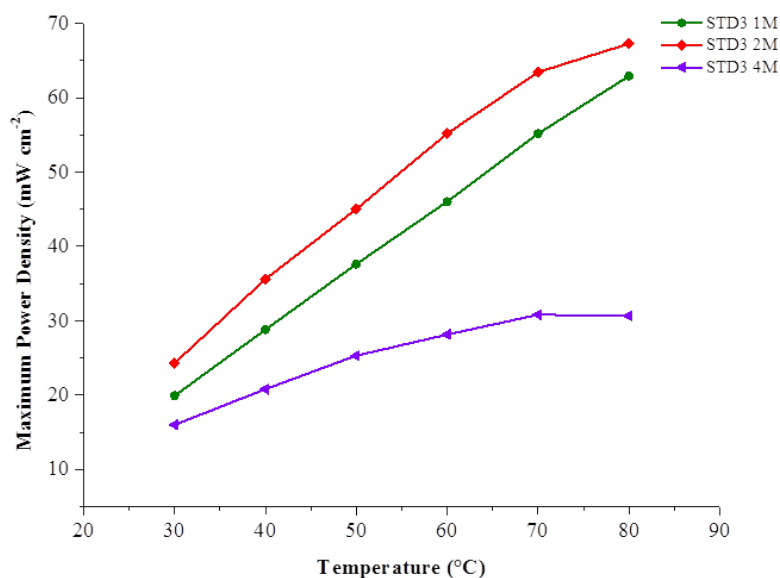


FIGURE 6.1: Comparison of STD3 maximum power densities at methanol concentrations of 1-4 M

The high performance at 2 M methanol indicates to an optimum methanol concentration suitable for an electrochemical stoichiometry of this operation system. When the cell performs at 2 M, a methanol content at the anode catalyst area is compatible with a demand from an electrochemical reaction. That causes low methanol concentration in an anode side leading low methanol distribution to a

cathode compartment [86, 90]. Consequently, a limitation of methanol crossover in 2 M operation is illustrated by the high open circuit voltage (OCV) as shown in Figure 6.2.

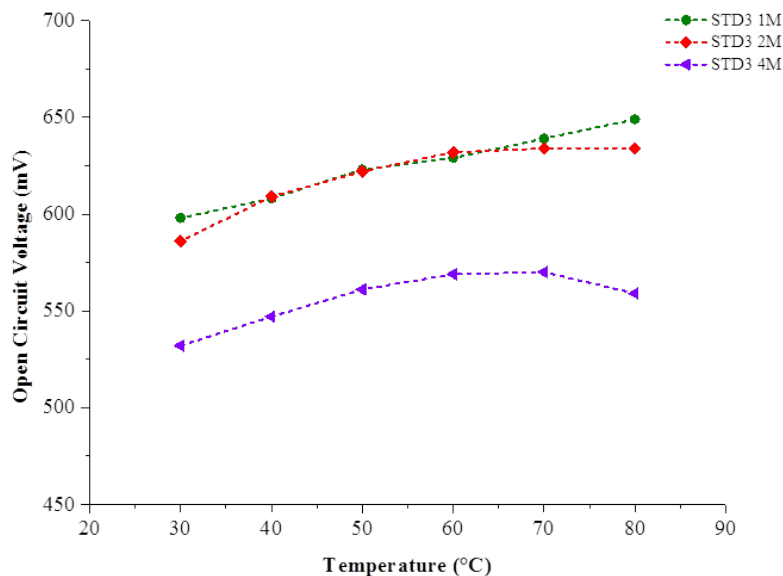


FIGURE 6.2: Comparison of STD3 open circuit voltages at methanol concentrations of 1-4 M

As seen in this graph, although 1M methanol concentration also provides high OCVs due to a reduction of methanol permeation, it is not as high. From this reason, 1 M concentration present lower maximum power densities than 2 M methanol system. At 4 M methanol concentration, severe methanol permeation to the cathode electrode leads to very low cell performance and OCVs. It has been concluded that high methanol concentration intensively influence a methanol crossover phenomena [90]. From this graph, the low methanol molarity (1 M and 2 M) are the optimum operating condition and the high methanol concentration as 4M is appropriated to investigate the methanol permeation. Therefore, other experiments will carry out with these methanol concentrations.

The order of limiting current densities of STD3 at different methanol solution can be seen in Figure 6.3. A similar trend to the maximum power densities is observed that STD3 also shows the best limiting current densities at 2 M methanol solution.

The limiting current densities are higher at increased temperature because of a great diffusion of reactants to the active surface area.

Methanol and air flow rate adjustment also present the same trend of STD1 which displays the suitable methanol flow rate at $5 \text{ cm}^3 \text{ min}^{-1}$ and $1000 \text{ cm}^3 \text{ min}^{-1}$ for air flow rate. The experimental results of reactants flow rate are shown in Appendix AA.

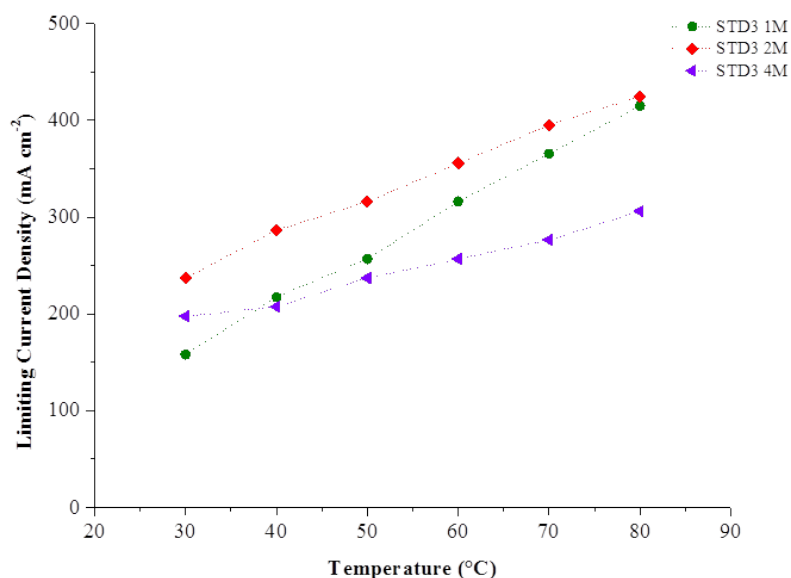


FIGURE 6.3: The comparison of STD3 limiting current densities at methanol concentrations of 1-4 M

6.1.2 The consistency of MEA fabricating by procedure II

One more standard MEA which called STD4 is produced by the similar method of STD3 to confirm the consistency of the catalyst perpetration **procedure II**. The results presented in Figure 6.4 prove that the catalyst perpetration **procedure II** appropriate for using as the MEA fabrication method instead of the **procedure I**.

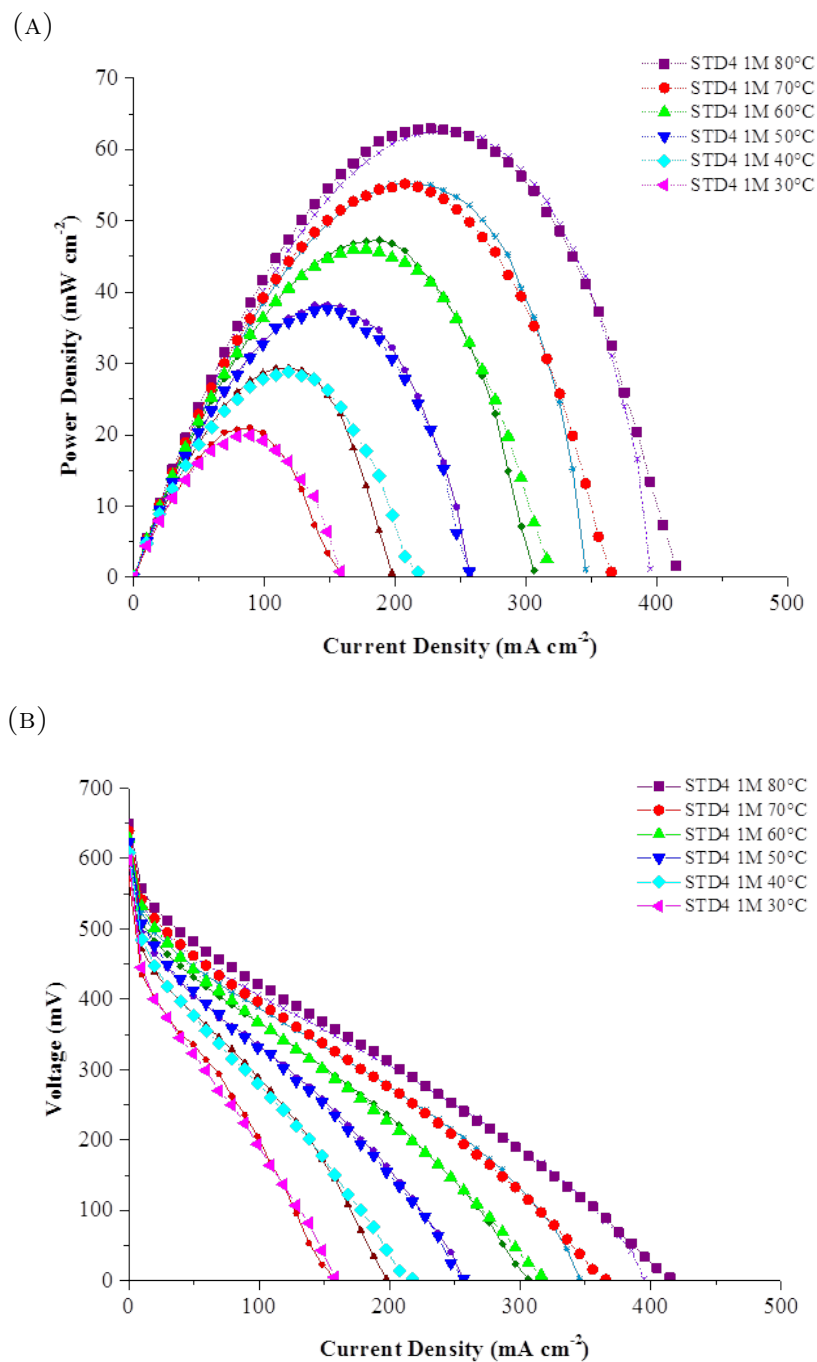


FIGURE 6.4: Reproducibility of MEA fabricating by procedure II: the performance of STD4 and STD3 at 1 M methanol concentration (A) The Power density curves (B) The polarisation curves

6.1.3 The performance of new-standard MEA (STD3) in comparison with conventional-standard MEA (STD1)

The OCV, maximum power density and limiting current density obtained from STD3 are compared to STD1 to confirm that the improved procedure for catalyst ink (**procedure II**) will be a promising category for preparing the catalyst ink.

See Figure 6.5. Apart from high supplied methanol at 4 M, STD3 presents superior performances than those of STD1. The maximum power densities comparing at 1 M methanol concentration and 80 °C show that STD3 (62.92 mW cm^{-2}) achieves 46.46% improvement than STD1 (42.96 mW cm^{-2}) while the most improvement observing at 2 M methanol and 80 °C is 81.15% with the maximum power density of 67.23 mW cm^{-2} and 37.14 mW cm^{-2} for STD3 and STD1, respectively. The rise in power density of STD3 due to the active electrochemical reactions both on anode and cathode sites.

(A)

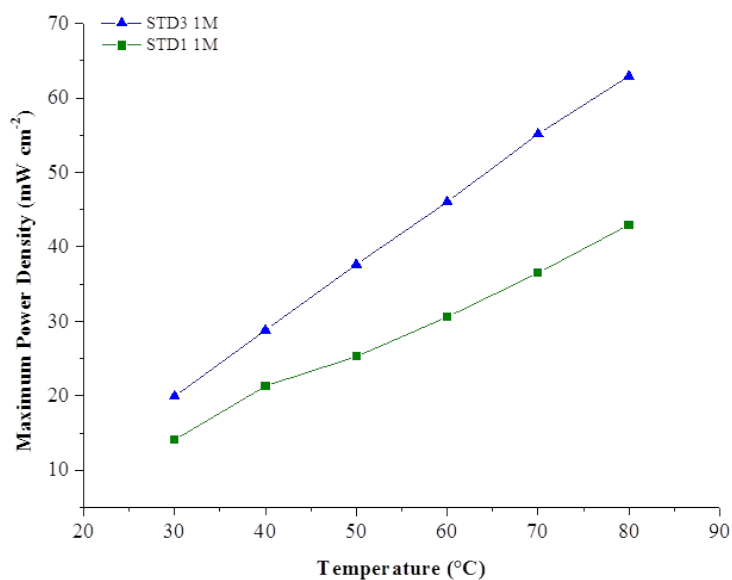
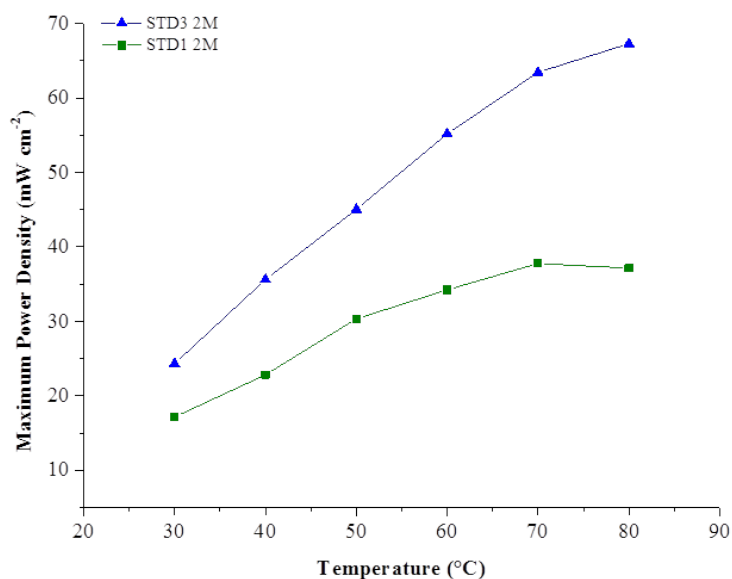


FIGURE 6.5: Maximum power density of STD1 and STD3 at (A) 1 M (B) 2 M (c) 4 M methanol concentrations

(B)



(C)

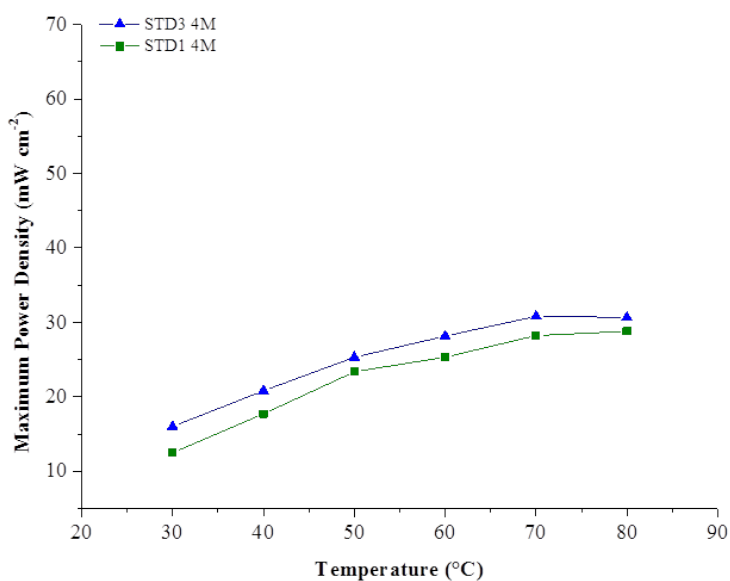


FIGURE 6.5 (cont.): Maximum power density comparison of STD1 and STD3 at (A) 1 M (B) 2 M (c) 4 M methanol concentrations

Although STD3 gives the high performance at 1 M and 2 M, it presents the low magnitude of maximum power density at 4 M methanol concentration which indicating the influence of methanol crossover overcome the advantage of active electrochemical reaction [86]. In the application, the DMFC are designed to

operate at the power density maximum [61].

According to the summarised voltage losses in Equation 2.18, page 67, the experimental cell voltage (V) corresponding to the thermodynamically predicted voltage ($E_{reversible}$) subtract with the voltage losses (η) [61, 89]. Therefore, the overall cell performance is investigated by the j-V curve which is a plot of voltage output with the corresponding current density [61].

$$V = E_{reversible} - \eta_{act} - \eta_{ohmic} - \eta_{conc} - \eta_{methanol}$$

The results at the same experimental conditions (2 M methanol molarity and 80 °C) have been selected to describe the achievement in STD3 performance over STD1. This is confirmed in Figure 6.6 that STD3 offers 81.15% improvement in maximum power density than STD1.

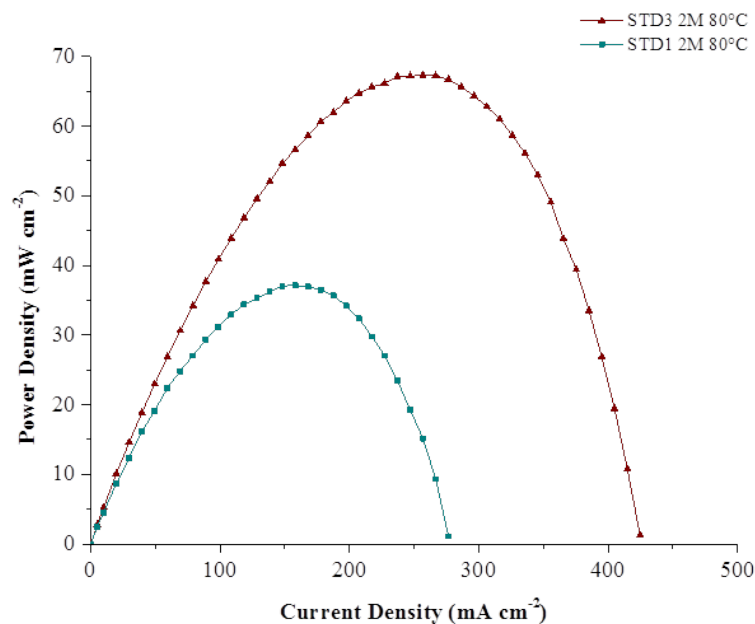


FIGURE 6.6: Power density curve of STD1 and STD3 at 2 M methanol concentration and 80 °C

Comparison in term of open circuit voltage and activation loss

It can be seen in Figure 6.7 that the OCV of STD3 (634 mV) is higher than that of STD1 (578 mV). An increase in OCV corresponds to a reduced methanol crossover in STD3. The methanol crossover is decreased due to the active electrochemical reaction in STD3 consumes more methanol resulting in lower methanol concentration in the anode catalyst site [86]. This feature diminishes methanol diffusion from anode to cathode [86, 87, 91].

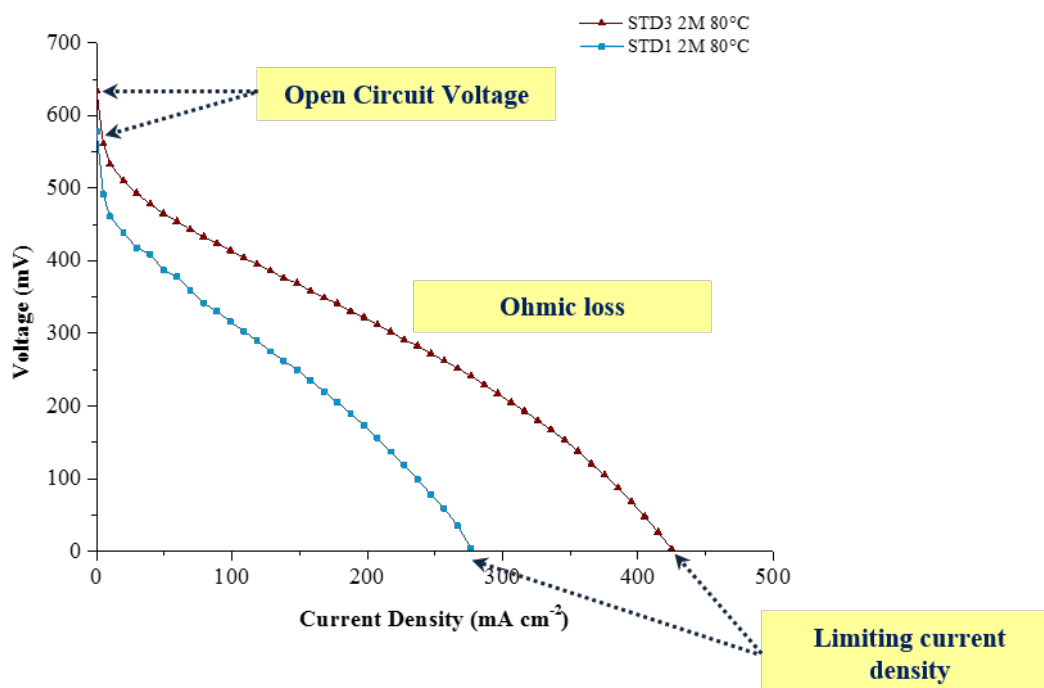


FIGURE 6.7: Polarization curve of STD1 and STD3 at 2 M methanol concentration and 80 °C

Figure 6.8 gives a comparison between OCV of STD3 and STD1. From the graphs, STD3 provides the higher value of OCV than STD1 at 1 M and 2 M methanol concentration. It is implied that, STD3 has less methanol crossover than STD1 [29, 61, 86].

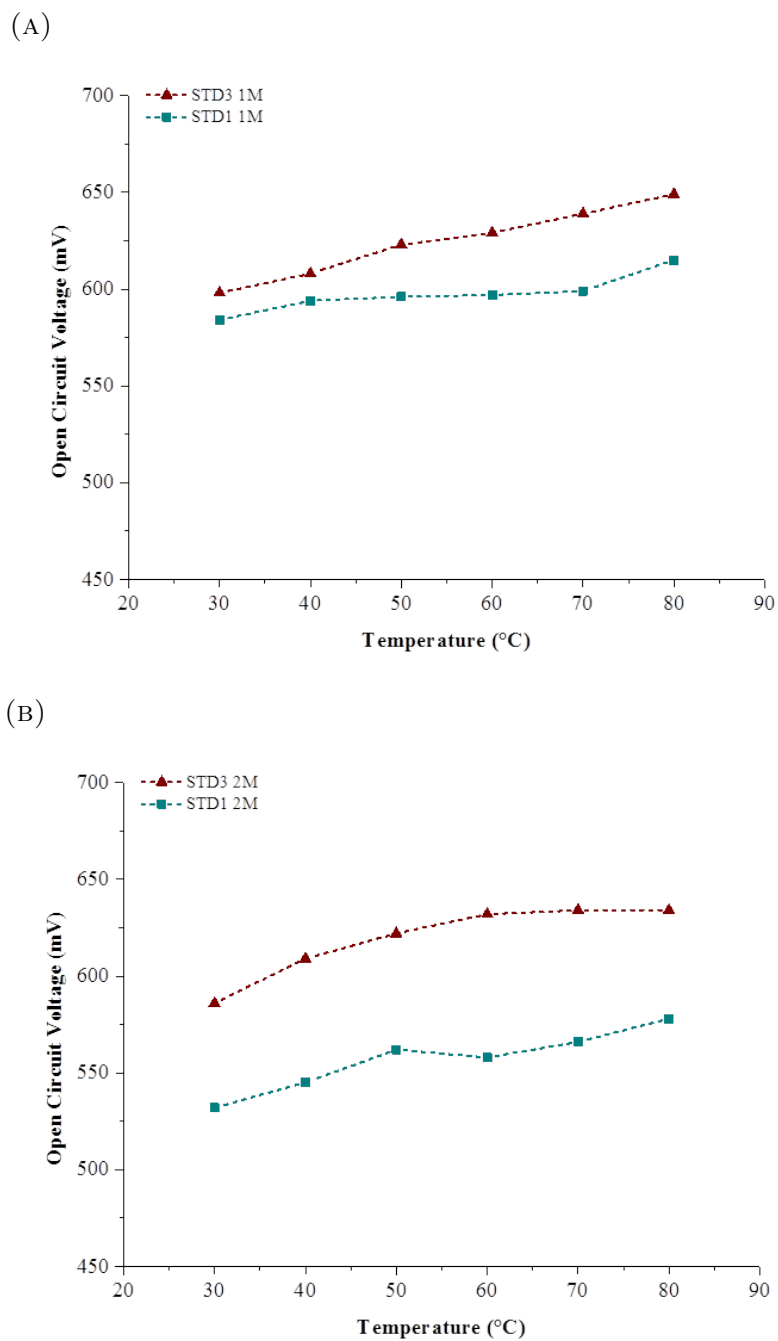


FIGURE 6.8: The OCV comparison of STD1 and STD3 at (A) 1 M (B) 2 M (c) 4 M methanol concentrations

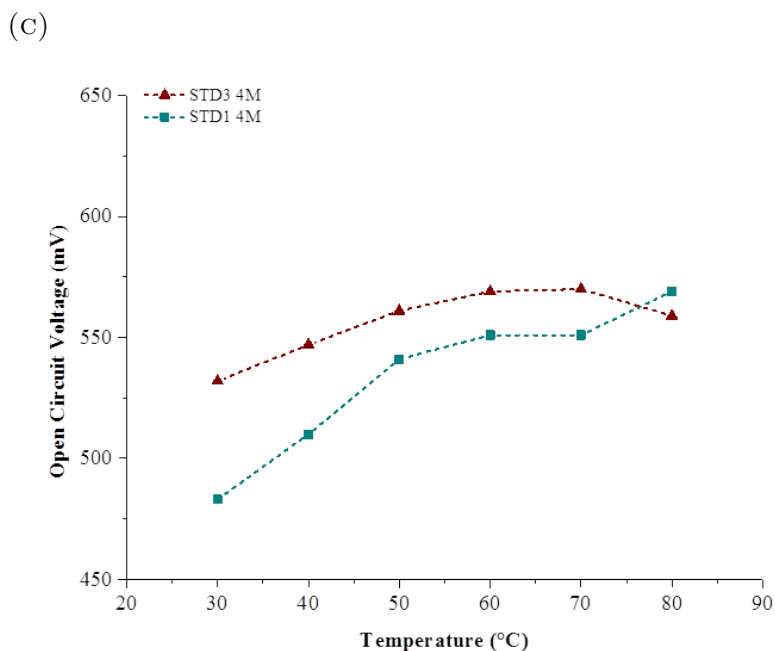


FIGURE 6.8 (cont.): Open circuit voltages of STD1 compared to STD3 at (A) 1 M (B) 2 M (c) 4 M methanol concentrations

Comparison in term of Limiting current density

As discussed in section 2.4.3.3, the cell voltage fall to zero at high current density which results from the limiting mass transport. The current density at this point is called limiting current density. During the electrochemical reaction, reactants are supplied to the catalyst area, meanwhile, the products are removed from this area. It is important to maintain methanol utilisation in the active site; however, the high current density the active oxidation reaction would be which depletes large methanol amount. This appearance declines in cell voltage because fresh reactant could not distribute to the catalyst layer [61, 82, 86].

The experimental results in Figure 6.7 present the limiting current density of STD3 ($424.69 \text{ mA cm}^{-2}$) which is higher 53.57% than that of STD1 ($276.54 \text{ mA cm}^{-2}$). According to the STD3 exhibits less mass transport resistance compared to STD1, it is indicated that STD3 has excellent methanol dispersion in the catalyst layer than STD1. This phenomenon is also observed over the range 1-4 M of methanol as shown in Figure 6.9.

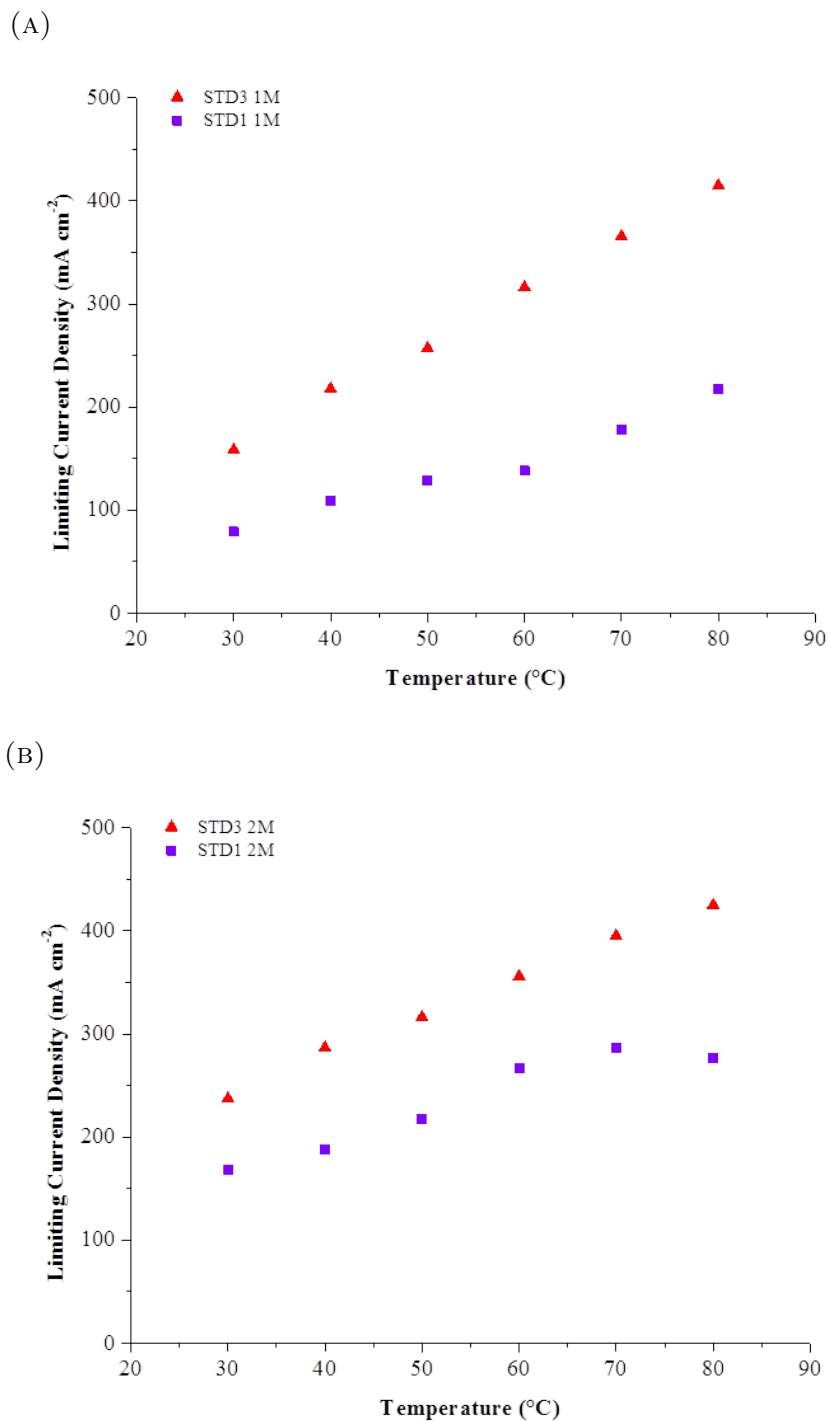


FIGURE 6.9: Limiting current density comparison of STD1 and STD3 at (A) 1 M (B) 2 M (c) 4 M methanol concentrations

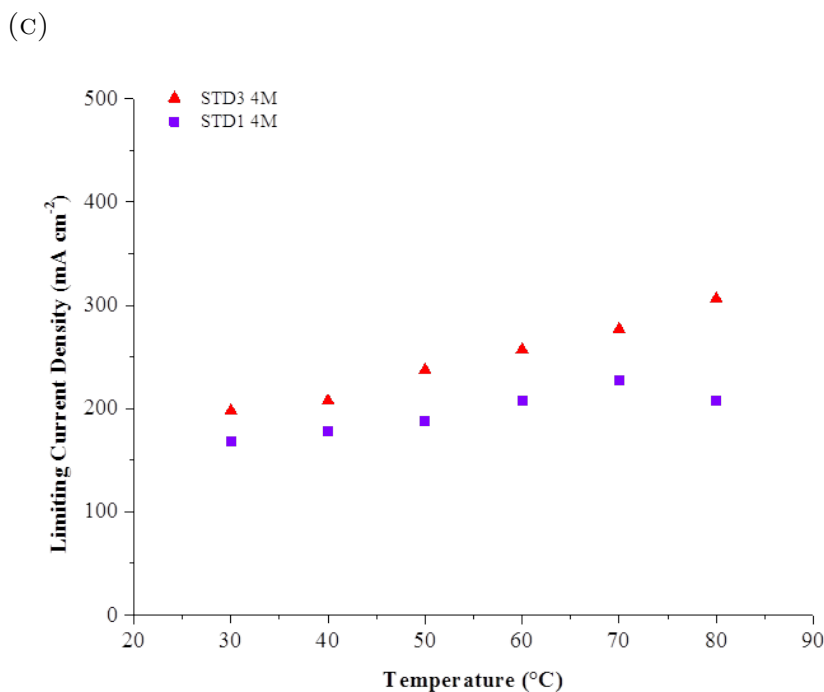


FIGURE 6.9 (cont.): Limiting current density of STD1 compared to STD3 at (A) 1 M (B) 2 M (c) 4 M methanol concentrations

Comparison in term of ohmic loss

The ohmic loss is represented in a large slope at middle region of the j - V curve [85, 86]. As illustrated in Figure 6.7, the rise in current density gives the large voltage drop of STD1 than STD3. This feature could be due to the less ionic resistance in catalyst layers of STD3 comparing with STD1.

It can be concluded from the experiments of STD1 and STD3 that the cell performance is related to the concentration of the catalyst ink. The MEA preparation **procedure II** can improve MEA performance compared to the catalyst ink in the **procedure I**. The low concentration of catalyst ink gives an advantage with a good dispersion of catalyst particles. In other words, it provides a utilisation of catalyst layer and prevents an agglomeration of catalyst particles when depositing catalyst ink onto the electrode.

An excellent dispersion of ionomer and catalyst particles lives advantages in STD3 performance. First, an increase of triple phase boundaries (TPBs: carbon support

particles, catalyst particles and Nafion ionomer) which is the reaction sites in the MEA as seen in Figure 6.10. The large number of TBP's reduce mass-transfer

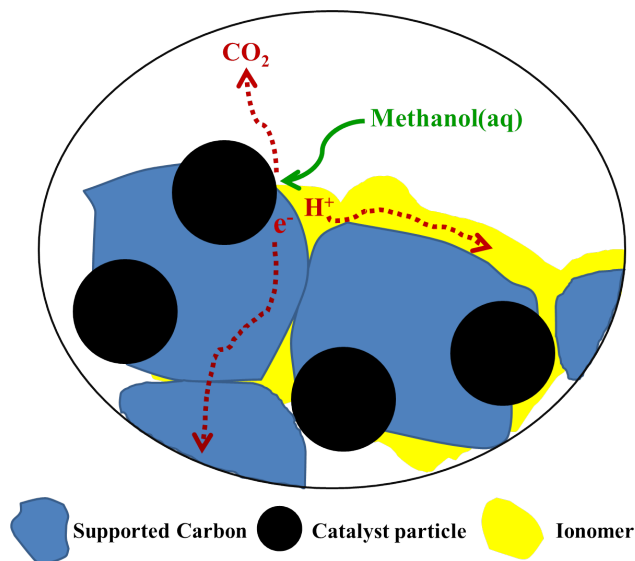


FIGURE 6.10: Triple phase boundaries inside the catalyst layer

limitation by facilitating the diffusion of methanol to catalyst active sites and the release of CO_2 product. This phenomenon provides the active electrochemical reaction both in anode and cathode of STD3.

Second is the decline in ohmic loss. At TBP's, both electrons and protons produced from the electrochemical reaction are transferred from the anode reaction sites to the cathode active areas. Charge transport through the MEA results in a voltage loss due to the intrinsic resistance of the electrode, the electrolyte membrane and the external circuit [29, 61, 86–88]. The good distribution of ionomer and catalyst particles inside both anode and cathode catalyst layers accelerate electrons and protons migration leading to the reduction of ohmic resistance in the electrode.

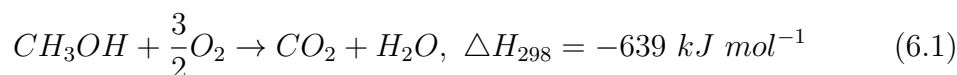
6.1.4 Effect of the different catalyst preparation over the different catalyst manufacturing

Procedure II gives superior performance for a new-standard MEA (STD3) over the conventional-standard MEA (STD1). Two different factors have changed between the fabrication of STD1 and STD3. The first factor is catalyst manufacture and the second is the catalyst ink concentration. To confirm that the concentration of catalyst ink has an effect on the MEA performance, another standard MEA named STD5¹ is produced using the procedure from STD1 but the material from STD3. The condition of MEAs fabrication are described in Table 6.2. The results are shown in Appendix A, Figure A.9 - A.11, Page 244.

TABLE 6.2: The parameters of STD1, STD3 and STD5 fabrication

| Parameters | STD1 | STD3 | STD5 |
|--------------------------------|--------------------------|---------------------------|--------------------------|
| Catalyst manufacture Procedure | <i>E-TEK I</i> | <i>Premetex II</i> | <i>Premetex I</i> |
| Anode catalyst | 60% Pt:Ru on Vulcan XC72 | 60% Pt:Ru on Vulcan XC72 | 60% Pt:Ru on Vulcan XC72 |
| Cathode catalyst | 60% Pt on Vulcan XC72 | 60% Pt on Vulcan XC72 | 60% Pt on Vulcan XC72 |
| Anode catalyst quantity | 1 mg Pt cm ⁻² | 1 mg Pt cm ⁻² | 1 mg Pt cm ⁻² |
| Cathode catalyst quantity | 1 mg Pt cm ⁻² | 1 mg Pt cm ⁻² | 1 mg Pt cm ⁻² |

STD5 presents the fluctuation performance curves because the cell voltages are not in steady-state value during the operation time. For DMFC operation, the crossover methanol is oxidised with oxygen at the cathode side and released heat as shown in Equation 6.1 [205]. The produced heat in this reaction rises the cell temperature and disturbs the electrochemical kinetic equilibrium yielding the fluctuated cell voltage.



¹This MEA was test in the collaborative laboratory

The power density curves of STD5 are much lower than STD3. They are almost similar to those results from STD1. This evident confirms that the concentration of catalyst ink has more influence on the MEA performance than the catalyst manufacture.

6.2 New modified MEAs operations

From the conclusion of chapter 5, the 2-dimensional inorganic material offer enhanced methanol barrier layer properties. In addition the experiments in this chapter point out a suitable procedure for preparing the high performance MEAs. Consequently, new MEAs were fabricated by a procedure II featuring with Nafion/montmorillonite and Nafion/titanate barrier layer. The series of experiments were conducted in order to determine the optimum inorganic content in a composite layer. This quantity should inhibit methanol crossover meanwhile minimizes effect on proton passage. Inorganic loading² are summarized in Table 6.3

TABLE 6.3: the new modified MEAs containing Nafion/inorganic barrier layer (a) is wt% inorganic relative to Nafion 117 membrane (b) is wt% inorganic relative to total weight of the barrier layer

| Inorganic additive | Inorganic loading wt.% (a) | Inorganic loading wt.% (b) | Label |
|--------------------|----------------------------|----------------------------|-----------|
| Na montmorillonite | 0.25 | 7.01 | 0.25% MMT |
| | 0.50 | 13.12 | 0.50% MMT |
| | 1.00 | 23.19 | 1.00% MMT |

²

(a) wt% inorganic relative to Nafion 117 membrane

$$\left(\frac{\text{Inorganic particles weight}}{\text{Inorganic particles weight} + \text{Nafion membrane weight}} \right) \times 100 = 0.5\%$$

(b) wt% inorganic relative to total weight of the barrier layer

$$\left(\frac{\text{Inorganic particles weight}}{\text{Inorganic particles weight} + \text{weight of Nafion in the composite layer}} \right) \times 100 = 13.21\%$$

6.2.1 Performance of new modified MEAs containing Nafion/-montmorillonite barrier layer at 1 M methanol concentration

Four MEAs containing Nafion/montmorillonite barrier layer on an anode electrode with different loading of MMT were fabricated. They are denoted as 0.25% MMT, 0.50% MMT, 0.75% MMT and 1.00% MMT. Power densities curves and polarisation curves of MMT contained MEAs are shown in Appendix A, Figure A.24-A.26, Page 268-270.

6.2.1.1 Open circuit voltage

The elevated temperatures promote electrochemical reactions on both cathode and anode sides which decrease activation loss in cell performance. It results in the increased open circuit voltages with the higher temperature [86, 219]. At 50-80 °C, OCVs obtaining from STD3, 0.25% MMT and 0.50% MMT are high and almost identical. However, the OCVs of 0.50% MMT significantly drop at 30-40 °C. The measured OCVs of 1.00% MMT are lower than other MEAs. The small OCVs especially at low operating temperature could be an effect from high MMT content in methanol barrier layer. Large MMT amount could inhibits methanol and proton (hydrate proton) transport through a barrier layer which reduce an sufficiency reactant for a reduction reaction on cathode side. At high temperature an electro-osmotic drag of methanol and water is increased from active oxidation-reduction kinetics [82, 140]. There manner may give benefit to the barrier layer to balance between methanol permeability and proton conductivity. From this reason the higher OCVs of 0.50% MMT are observed at elevated temperature.

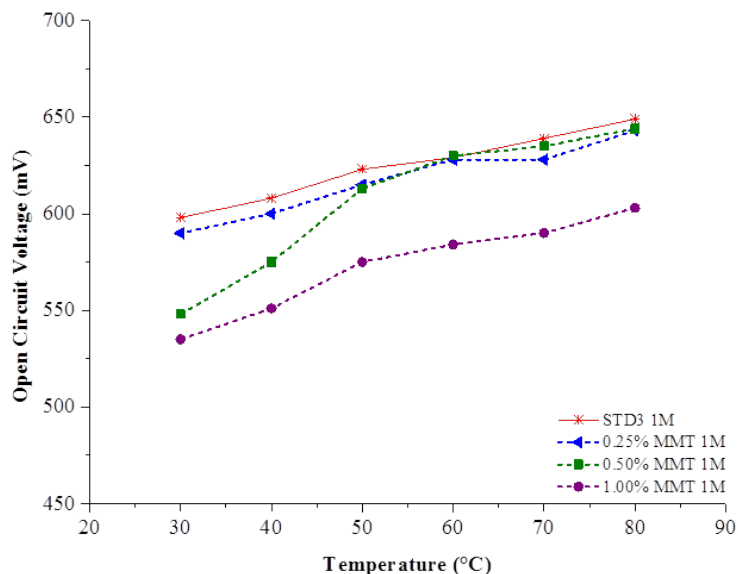


FIGURE 6.11: Open circuit voltage of STD3 compared to 0.25% MMT, 0.50% MMT and 1.00% MMT at 1 M methanol

6.2.1.2 Power density

The power densities of MMT contained MEAs increase with temperature [86, 87]; however, its decrease with inorganic loading. The rise in temperature not only gives an advantage on active kinetic in anode and cathode sides, but also causes disadvantages of high methanol crossover, more water transport from anode to cathode owing a water flooding in cathode side which leads to a concentration loss. Thus, performance of MEAs with increased temperature is a combination between positive effect and negative effects [204].

As seen in Figure 6.12, MEA incorporating with 0.25 wt% of MMT exhibits the best power densities over the entire temperature. Improvement in maximum power density of 0.25% MMT respected to STD3 are shown in Table 6.4. The highest power density of 0.25% MMT and STD3 are 64.27 and 62.92 mW cm^{-2} at 80 °C, respectively. Considering percentage improvement at low operating temperature (30 °C), there is much enhancement in power density of 0.25% MMT from STD3 because a barrier layer restrict methanol migration from anode to

cathode. Thus, a retention of methanol in an anode active area contributes to affective reaction and high power density. In contrast, methanol permeation through the layer is dominant at high temperature. The lack of methanol fuel in anode side reduce the percentage improvement of 0.25% MMT at 70-80 °C.

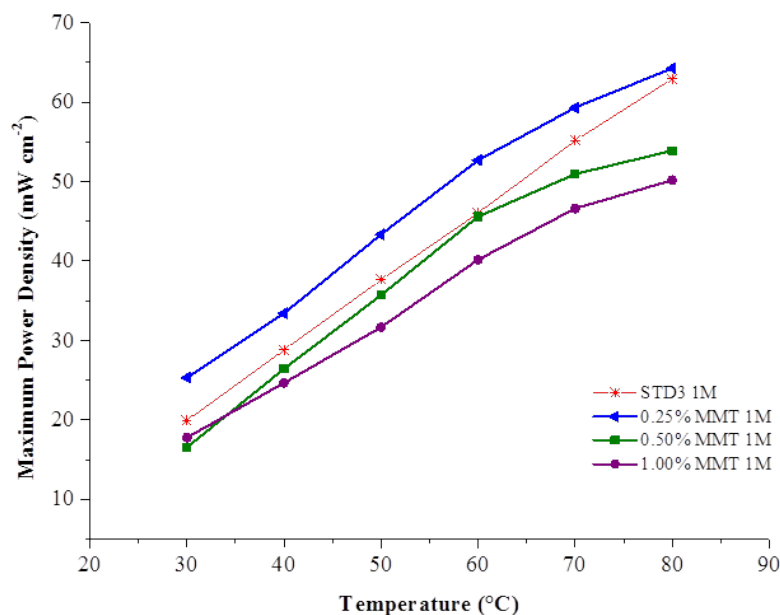


FIGURE 6.12: Power densities of STD3 compared to 0.25% MMT, 0.50% MMT and 1.00% MMT at 1 M methanol

TABLE 6.4: Improvement in maximum power density of 0.25% MMT relative to STD3

| Temperature (°C) | 30 | 40 | 50 | 60 | 70 | 80 |
|-----------------------------------|-------|-------|-------|-------|------|------|
| % Improvement of 0.25% MMT | 27.09 | 16.01 | 15.20 | 14.46 | 7.52 | 2.14 |

At high inorganic content of 0.50% MMT and 1.00% MMT, their performance are lower than 0.25% MMT and STD3. Relative reduction in maximum power density of 0.50% MMT and 1.00% MMT compared to STD3 are list in Table 6.5. The remarkable low maximum power density at large inorganic content may be caused by the MEAs suffering from low proton conductivity. Barrier layer with dense inorganic particles could reduce water transport which equivalently

decreases proton conducting. Moreover, it may enlarges an ohmic loss by increasing contact resistance between the layer and membrane [136]. The highest power density of 0.50% MMT and 1.00% MMT are 53.89 and 50.17 mW cm⁻² at 80 °C, respectively.

TABLE 6.5: Reduction in maximum power density of 0.50% MMT and 1.00% MMT relative to STD3

| Temperature (°C) | 30 | 40 | 50 | 60 | 70 | 80 |
|---------------------------------|-------|-------|-------|-------|-------|-------|
| % Reduction of 0.50% MMT | 16.97 | 8.23 | 5.12 | 0.96 | 7.63 | 14.36 |
| % Reduction of 1.00% MMT | 14.79 | 71.43 | 86.40 | 97.91 | 86.18 | 77.18 |

6.2.1.3 Limiting current density

Limiting current density is affected by mass transport of reactant from fuel flow channel to active site of catalyst [90]. As mentioned previously 0.25% MMT can minimize mass transport loss by constraint methanol diffusion through the layer and maintain methanol quantity in anode electrode leading outperform limiting current densities over other MEAs (Figure 6.13). The 0.50% MMT present better results than STD3 at 30-50 °C but there is a reverse order at 70-80 °C. At 60 °C a limiting current density of 0.50% MMT and STD3 are equivalent. The limiting current density of 1.00% MMT are lowest as expected. Large inorganic content rise mass transport loss due to large interfacial resistance which is indicated by a sharp slope of 1.00% MMT polarization curves at high current density. The most limiting current densities of 0.25% MMT, 0.50% MMT and 1.00% MMT are 454.32, 375.31 and 335.81 mA cm⁻² at 80 °C, respectively.

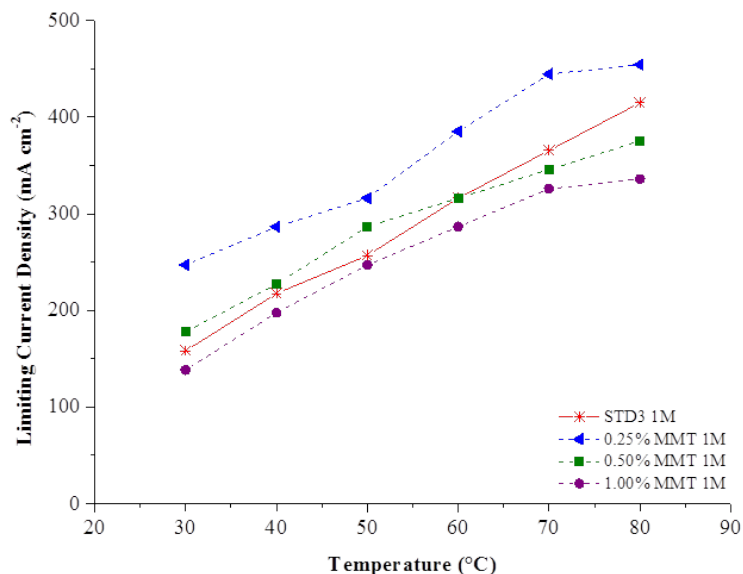


FIGURE 6.13: Limiting current densities of STD3 compared to 0.25% MMT, 0.50% MMT and 1.00% MMT at 1M methanol

6.2.2 Performance of new modified MEAs containing Nafion/-montmorillonite barrier layer at 2 M methanol concentration

Performance of STD3 and the MMT contained MEAs are shown in Appendix A, Figure A.27-A.29, Page 271-273. The performances at 2M methanol concentration exceed those of 1M methanol both in maximum power density and limiting current density.

6.2.2.1 Open circuit voltage

At 2 M methanol, STD3 and the MMT contained MEAs display similar value and pattern of those OCVs at 1 M methanol. There are minor difference which OCVs of 1.00% MMT at 70-80 °C increase as high as other MEAs.

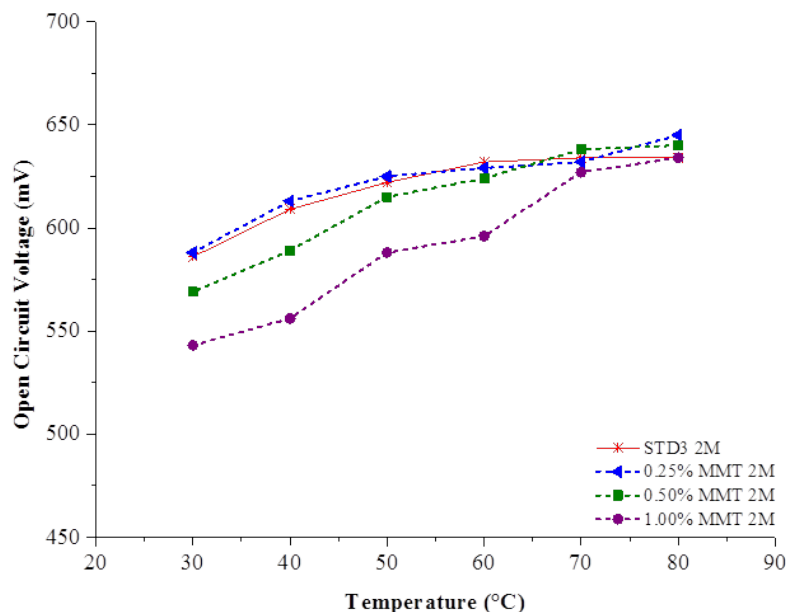


FIGURE 6.14: Open circuit voltage of STD3 compared to 0.25% MMT, 0.50% MMT and 1.00% MMT at 2 M methanol

6.2.2.2 Power density

There is an interesting phenomenon due to an almost comparable maximum power densities of STD3, 0.25% MMT and 0.50% MMT. This manner demonstrate that 2 M methanol is an optimum condition of this MEAs series. Nevertheless, significantly lower power densities at 1.00% MMT remain. The highest power density of 0.25% MMT, 0.50% MMT, 1.00% MMT and STD3 are 69.14, 63.94, 50.48 and 67.23 mW cm^{-2} at 80 °C, respectively. Relative improvement of 0.25% MMT and relative reduction of 0.50% MMT and 1.00% MMT compared to STD3 are shown in Table 6.6 and 6.7, respectively.

TABLE 6.6: Improvement in maximum power density of 0.25% MMT relative to STD3

| Temperature (°C) | 30 | 40 | 50 | 60 | 70 | 80 |
|----------------------------|-------|------|------|----|------|------|
| % Improvement of 0.25% MMT | 13.42 | 5.88 | 4.21 | 0 | 2.96 | 2.76 |

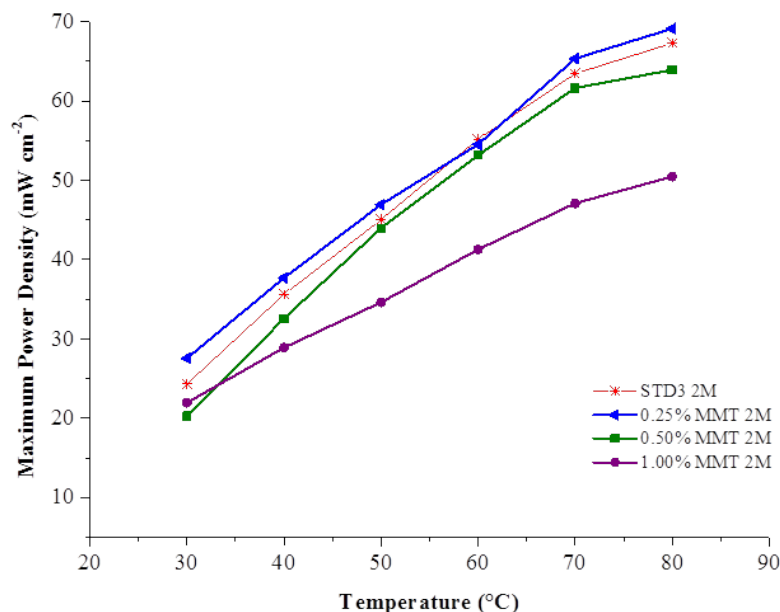


FIGURE 6.15: Maximum power densities of STD3 compared to 0.25% MMT, 0.50% MMT and 1.00% MMT at 2 M methanol

TABLE 6.7: Reduction in maximum power density of 0.50% MMT and 1.00% MMT relative to STD3

| Temperature (°C) | 30 | 40 | 50 | 60 | 70 | 80 |
|--------------------------|-------|-------|-------|-------|-------|-------|
| % Reduction of 0.50% MMT | 16.58 | 8.49 | 2.37 | 3.69 | 2.88 | 4.96 |
| % Reduction of 1.00% MMT | 9.67 | 18.84 | 23.16 | 25.20 | 25.77 | 24.97 |

6.2.2.3 Limiting current density

Due to the limiting current density being influenced by mass transport resistance, that means it is proportional to methanol concentration [90]. Hence, limiting current densities of 0.50% MMT significantly enhance in 2 M methanol solution. Limiting current densities of 0.25% MMT are slightly higher than those of STD3 at 70-80 °C could be due to these performances reach a maximum efficiency of the cell assembly.

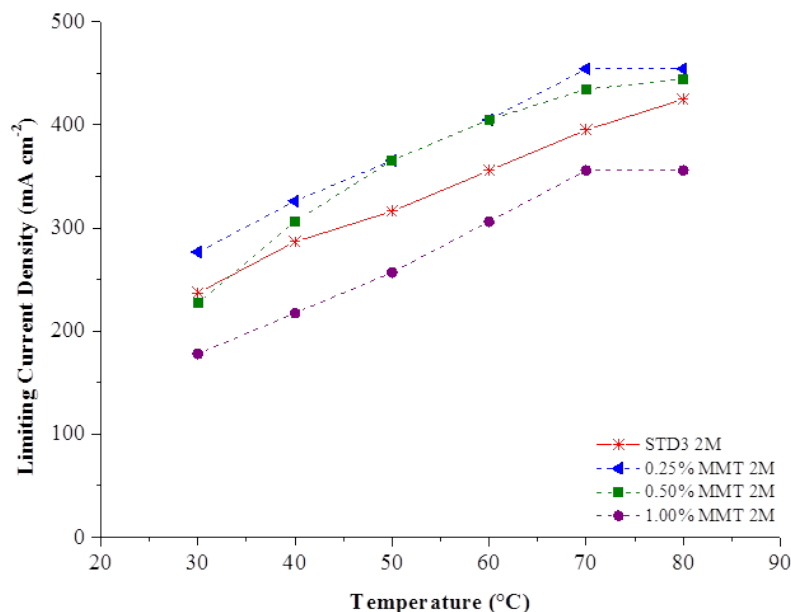


FIGURE 6.16: Limiting current densities of STD3 compared to 0.25% MMT, 0.50% MMT and 1.00% MMT at 2 M methanol

6.2.3 Performance of new modified MEAs containing Nafion/-montmorillonite barrier layer at 4 M methanol concentration

Figure A.30-A.32 in Appendix A, Page 274-276, exhibit performance of STD3 and the MMT contained MEAs at 4 M methanol solution.

High methanol concentration dramatically decreases cell voltages and OCVs because of high methanol permeation [137].

6.2.3.1 Open circuit voltage

Although the order of OCVs is similar to 1M and 2M methanol supply, the values are very low. The OCVs of STD3 are equivalent to those of 0.25% MMT while 0.50% MMT displays slightly less values. 1.00% MMT gives constant and

noticeably low OCVs at around 500 mV. There is an effect from high methanol crossover.

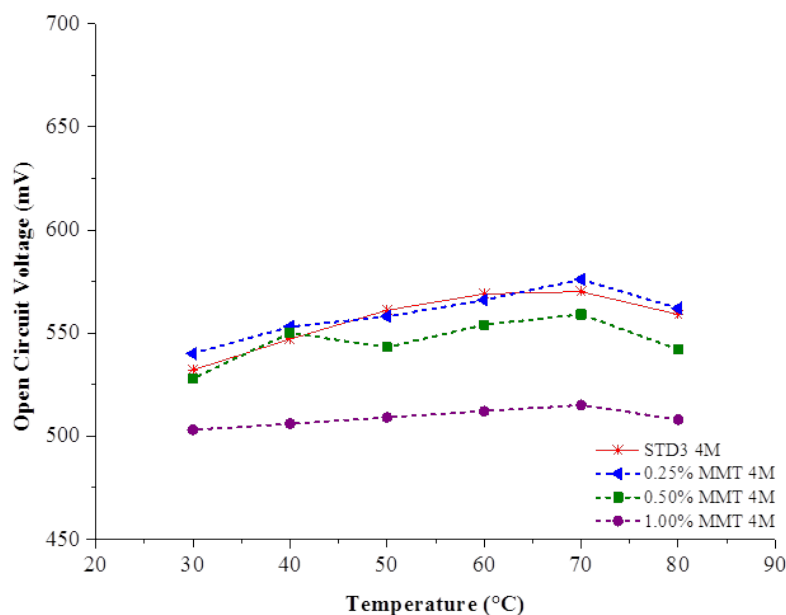


FIGURE 6.17: Open circuit voltage of STD3 compared to 0.25% MMT, 0.50% MMT and 1.00% MMT at 4 M methanol

6.2.3.2 Power density

The advantage of incorporating methanol barrier layer into the MEAs becomes dominant when the MEAs is operated with 4 M methanol concentration. Power densities of 0.25% MMT and 0.50% MMT are obviously better than those of STD3 over the entire temperature. 0.25% MMT and 0.50% MMT have comparable highest power densities but at different temperatures. The most value obtained from 0.25% MMT is 39.82 mW cm^{-2} at $80 \text{ }^\circ\text{C}$ while that of 0.50% MMT is 39.64 mW cm^{-2} at $70 \text{ }^\circ\text{C}$. It would be notice that at $80 \text{ }^\circ\text{C}$ power densities of all MMT contained MEAs outperform that of STD3. The maximum power density of 0.25% MMT, 0.50% MMT, 1.00% MMT and STD3 are 39.82, 33.75, 31.80 and 30.66 mW cm^{-2} , respectively. Relative improvement of 0.25% MMT and

0.50% MMT and relative reduction of 1.00% MMT with respected to STD3 are shown in Table 6.8 and 6.9, respectively. It is note that the maximum power density of 1.00% MMT at 80 °C is slightly higher than that of STD3.

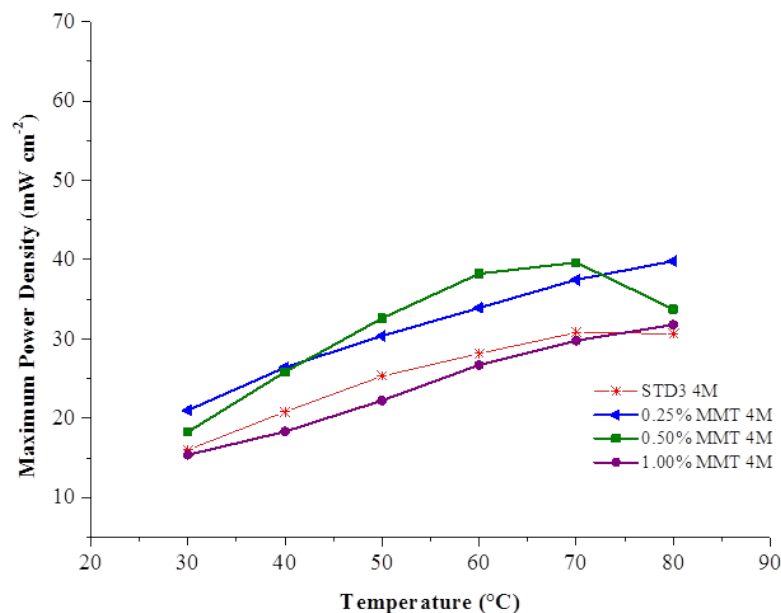


FIGURE 6.18: Maximum power densities of STD3 compared to 0.25% MMT, 0.50% MMT and 1.00% MMT at 4 M methanol

TABLE 6.8: Improvement in maximum power density of 0.25% MMT relative to STD3

| Temperature (°C) | 30 | 40 | 50 | 60 | 70 | 80 |
|-----------------------------------|-------|-------|-------|-------|-------|-------|
| % Improvement of 0.25% MMT | 31.11 | 26.97 | 20.02 | 20.49 | 21.54 | 29.90 |
| % Improvement of 0.50% MMT | 14.20 | 24.22 | 28.81 | 35.79 | 28.65 | 10.08 |

TABLE 6.9: Reduction in maximum power density of 0.50% MMT and 1.00% MMT relative to STD3

| Temperature (°C) | 30 | 40 | 50 | 60 | 70 | 80 |
|---------------------------------|------|-------|-------|------|------|---------|
| % Reduction of 1.00% MMT | 3.89 | 11.97 | 12.18 | 5.12 | 3.37 | improve |

6.2.3.3 Limiting current density

Mass transfer loss in 0.25% MMT and 0.50% MMT have been improved by the barrier layer. It is indicated by their higher limiting current density in comparing with STD3; meanwhile, a large inorganic content of 1.00% MMT gives disadvantage to mass transport. The limiting current densities of 1.00% MMT are approximately 18% lower than STD3 over temperature range.

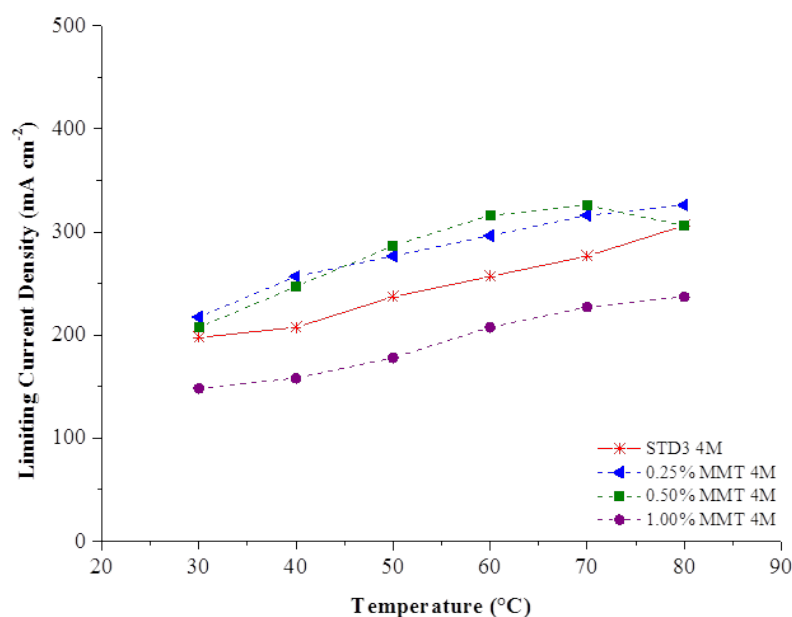


FIGURE 6.19: Maximum power densities of STD3 compared to 0.25% MMT, 0.50% MMT and 1.00% MMT at 4 M methanol

6.3 Summary

New MEA fabrication for the improvement of DMFC performance

The improvement of DMFC performance has been achieved. A new procedure (Procedure II) for MEA preparation was developed by reducing the concentration

of the catalyst ink. Five standard MEAs were produced in this research in order to investigate the procedure for MEA fabrication.

- STD1 and STD2 were fabricated by similar procedure (procedure I), with the same catalyst manufacturer. The slightly lower power densities of STD2 because it contains lower catalyst weight compared to STD1, $0.5 \text{ mg Pt cm}^{-2}$ and 1 mg Pt cm^{-2} , respectively.
- STD1 and STD3 were prepared using different procedure (procedure I and II, respectively) as well as different catalyst manufacturer. Although they have comparable catalyst weight, 1 mg Pt cm^{-2} , STD3 presents dramatically higher performances than those of STD1. Therefore, the different in catalyst ink preparation takes an account to the MEA performance. However, the effect of catalyst manufacturer was not negligible.

Consequently, one more standard MEA (STD5) was produced to demonstrate the catalyst ink preparation influence on the MEA performance with slightly effect from the catalyst manufacturer. The details of catalyst manufacturer and MEA preparation procedures are summarized in Table 6.10.

TABLE 6.10: Parameters for standard MEA fabrication

| Parameters | STD1 | STD2 | STD3 | STD4 | STD5 |
|--|---------------|--------------------------------------|--|--|----------------------------|
| Catalyst manufacturer | E-TEK | E-TEK | Premetex | Premetex | Premetex |
| Procedure | I | I | II | II | I |
| Catalyst weight (mg Pt cm^{-2}) | 1.0 | 0.5 | 1.0 | 1.0 | 1.0 |
| Approach | Reference MEA | Reduce Pt loading from the reference | Improve performance from the reference | Consistency of the improvement procedure | Confirm suitable procedure |

The standard MEAs fabricated by procedure II exhibit the highest enhancement

of power density by 81.15% compared to the MEAs prepared by conventional procedure (Procedure I). Therefore, the new procedure was used for the new modified MEAs incorporated with the methanol barrier layers.

Methanol barrier layer for the improvement of DMFC performance

Nafion/montmorillonite (MMT) composite layer was introduced into the new modified MEA by 0.25wt.%, 0.50wt.% and 1.00wt.% related to the weight of Nafion 117 membrane. The best MMT content for Nafion/MMT barrier layer is 0.25wt.%. Performances of 0.25% MMT exceed the standard MEA (STD3) at 1 M, 2 M and 4 M methanol concentration. The barrier layer containing large MMT content (0.5% MMT and 1.0% MMT) contribute to the reduction of MEA performances which would be explained by a constraint of mass transport through a barrier layer.

Chapter 7

Conclusions and suggestions for future work

7.1 Conclusions

This research focuses on the enhancement of direct methanol fuel cell (DMFC) performance. The method for improving the performance can be divided into two strategies: (I) reducing methanol fuel crossover, a critical problem of DMFC, by incorporating a Nafion/inorganic composite layer into the membrane electrode assemblies (MEA) in order to restrain methanol passage from anode to cathode side; (II) modifying the catalyst morphology inside the MEA.

The influence of inorganic morphologies on DMFC performance have been demonstrated using two different inorganic types. The microporous materials, mordenite (MOR) and zeolite Y (ZY), and the 2-dimensional materials, montmorillonite (MMT) and titanate (TN), were used as the inorganic additive in the methanol barrier layer. It can be concluded from the experiment that 2-dimensional materials enhanced DMFC performances excess those of microporous materials. Therefore, the study of Nafion/MMT barrier layer was carried on.

7.1.1 Methanol barrier layer for the improvement of DMFC performance

The experimental results demonstrated that methanol barrier layer achieved the goal of limiting methanol permeation inside the MEA. It has been proved by the better performances of modified MEAs both in power densities and limiting current densities over those of the standard MEA. Comparison the MEA performances in this research with other from the literature exhibited an appropriated result, as seen in Table 7.1.

The MEA with 0.25wt% MMT dispersing in methanol barrier layer was selected as the optimum sample for a performance discussion. The maximum power density (65.33 mW cm^{-2}) of 0.25% MMT presented three times reduction than the value 171.3 mW cm^{-2} of Nafion/2wt% chitosan-MMT [179] but it obtained four times less catalyst content. Considering at low temperature, despite carrying eight time decrease in catalyst content 0.25wt% MMT exhibited maximum power density of 33.41 mW cm^{-2} which is half of 67 mW cm^{-2} maximum power density from Nafion/5wt% HSO₃-MMT [177]. An equivalent power density with less catalyst loading provided a benefit of MEA reduction cost.

In the present research, the barrier layer containing different MMT weights contributed to various power densities of MEAs. The depletion of MEA performance when the MMT contents are higher than 0.25wt% could be due to an aggregation of MMT. The aggregation decreased an intercalation of Nafion matrix into the interlayer of MMT which also declined a tortuosity factor. Therefore, MMT aggregate may attribute the increase in methanol crossover [220] owning lower power densities.

TABLE 7.1: Comparison the performances of DMFCs incorporated with montmorillonite

| Inorganic additive | Method | Catalyst loading (mg cm ⁻²) | Maximum Power density (mW cm ⁻²) | Operation condition | Ref. |
|-----------------------------------|------------------------|--|---|---------------------|---------------|
| Nafion/0.25wt% MMT | methanol barrier layer | 1 | 33.41 | 2M methanol, 40 °C | This research |
| Nafion/0.25wt% MMT | methanol barrier layer | 1 | 65.33 | 2M methanol, 70 °C | This research |
| Nafion/0.50wt% MMT | methanol barrier layer | 1 | 61.63 | 2M methanol, 70 °C | This research |
| Nafion/0.10wt% MMT | methanol barrier layer | 1 | 47.10 | 2M methanol, 70 °C | This research |
| Nafion/5wt% HSO ₃ -MMT | composite membrane | 8 | 67 | 2M methanol, 40 °C | [177] |
| Nafion/5wt% HSO ₃ -MMT | composite membrane | 4 | 90 | 1M methanol, 70 °C | [181] |
| Nafion/5wt% HSO ₃ -MMT | composite membrane | 4 | 108 | 5M methanol, 70 °C | [181] |
| Nafion/2wt% chitosan-MMT | composite membrane | 4 | 105 | 1M methanol, 70 °C | [179] |
| Nafion/2wt% chitosan-MMT | composite membrane | 4 | 171.3 | 1M methanol, 70 °C | [179] |
| Chitosan/2wt% MMT | composite membrane | 5 | 49.7 | 5M methanol, 70 °C | [220] |

In order to inhibit methanol permeation, the combination of a tortuosity factor and an organophobic property of individual methanol barrier layer should be considered.

7.1.1.1 Tortuosity factor

See Figure 7.2, tortuosity factor (τ) determines from the ratio of the actual distance to the shortest distance that molecule travels through a layer [176, 221, 222]. The calculation of τ is illustrated in Equation 7.1.

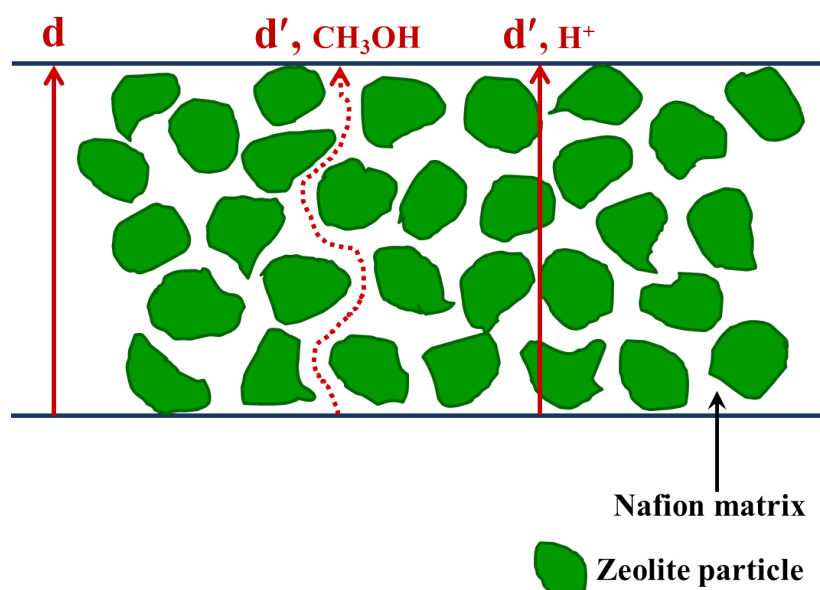


FIGURE 7.1: Migration of proton and methanol molecule through the composite layer (adapted from [111])

$$\tau = \frac{d'}{d} = 1 + \frac{L}{2W} \Phi_s \quad (7.1)$$

Where:

τ , tortuosity factor

d' , actual distance that a penetrant must travel

d , the shortest distance that a penetrant would have travelled in the absence of inorganic layer

L , length of inorganic layer

W , width of inorganic layer

Φ_s , volume fraction of the sheets

Microporous materials such as zeolite provide advantage of selective pore size. Zeolite particles dispersed in the composite layer allowing proton passage through but impermeant methanol [111]. As shown in Figure 7.1, the Nafion/zeolite composite layer inhibited methanol permeation via the increased tortuosity factor of methanol.

However, the results showed that MEAs containing 2-dimensional material presented better performances than those of microporous materials as well as a standard MEA. The best improvement in power density of 19.74% and 26.58% higher than standard power density were obtained from the MEA featuring with Nafion/MMT layer and Nafion/TN layer, respectively. This feature can be described by high length-to-width ratio (L/W) of 2-dimensional materials which contributed a longer diffusive path for methanol causing better methanol barrier related to microporous materials [176].

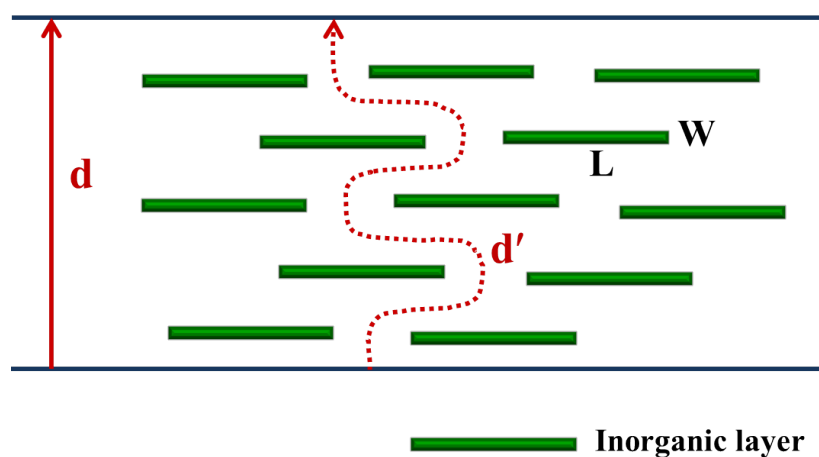


FIGURE 7.2: Description of tortuosity factor (adapted from [176])

7.1.1.2 Organophobic character

Contact angle increases with the organophobic character of the solid surface which is the surface of an anode electrode in this study.

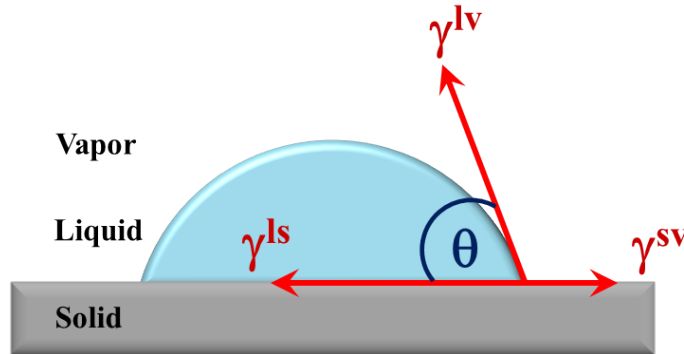


FIGURE 7.3: Determination of contact angle at the interface between water droplet and solid surface

$$\gamma^{sv} = \gamma^{sl} + \gamma^{lv} \cos \theta \quad (7.2)$$

Where:

γ^{sv} , the solid-vapor surface tension

γ^{sl} , solid-liquid interfacial surface tension

γ^{lv} , liquidvapor surface tension

θ , contact angle ($0^\circ < \theta < 180^\circ$)

Organophobic property of the methanol barrier layers was investigated using a contact angle measurement. The composite layers contributed larger contact angles with methanol solution than the pure Nafion layer. Therefore, these layers repelled methanol and prevented the methanol transportation between electrodes. Considering the relation of contact angles and DMFC performances, the Nafion/titanate layer presented the largest angle with methanol compared to other layers. This layer could not only prevent methanol but also repel water. Hence the lowest performance was observed due to the reduction of proton transport via water migration. While a medium angle value of Nafion/montmorillonite

related to the best performance. Consequently, the performance of DMFC could be control by organophilic/organophobic properties of the barrier layer.

7.1.2 Modification of the catalyst morphology for the improvement of DMFC performance

7.1.2.1 Procedure for the membrane electrode assembly preparation

An additional improvement in DMFC performance can be achieved by modifying the catalyst ink preparation procedure (procedure II). The dilution of catalyst ink concentration promoted large number of triple phase boundaries due to the reduction of catalyst agglomeration. From this strategy, a new standard MEA was produced by the new procedure presented 81.15% higher in power density (67.23 mW cm^{-2} from STD3) compared to the value from conventional standard (37.14 mW cm^{-2} form STD1). Over all, the optimum DMFC operating conditions of this research were 2 M methanol concentration and temperature of 80 °C.

7.1.2.2 Optimum Inorganic loading in the methanol barrier layer

Among the MEAs featuring with Nafion/0.25 wt% montmorillonite, Nafion/0.50-wt% montmorillonite and Nafion/1.00 wt% montmorillonite composite layer, the MEAs containing 0.25 wt% montmorillonite illustrated the best performance in power density and limiting current density. The improvement of 27.09% in power density had been obtained at operating condition of 1 M methanol concentration and 30 °C. It should be highlight that the enhancement at low temperature is important for DMFC application in mobile devices such as mobile phone or notebook.

7.2 Future Work

Due to the success for using methanol barrier layer to improve DMFC performance, the understanding of this technique should be extended with different choices of inorganic materials.

Graphene oxide is an appropriate candidate because of its 2-dimensional structure (Figure 7.4) including its outstanding thermal and mechanical properties. Moreover, pure graphene oxide is an electronic insulator [223] which is one of the requirement properties of the electrolyte membrane.

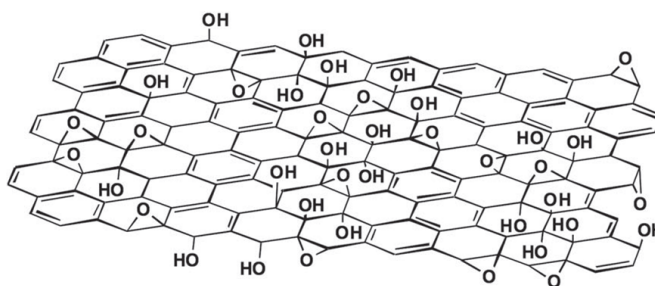


FIGURE 7.4: Structure of Graphene oxide [224]

Although, the aim to produce DMFC membrane via an incorporation of graphene oxide and Nafion have been approached from many researches, an achievement of high DMFC performance could not be accomplished. Two methods were used to produce the electrolyte membrane. First is recasting technique, casting the mixture of graphene oxide and Nafion matrix to form a polymer composite membrane. Second is a dual layer laminated method, printing the colloidal solution of graphene oxide on to a Nafion membrane. The performances of MEAs fabricated by both methods have been investigated and exhibited in Table 7.2.

As seen in the Table, their maximum power densities are lower than those of MMT composite membrane in Table 7.1. Therefore, the application of barrier layer technique on graphene oxide may contribute to superior DMFC performance.

TABLE 7.2: Performances of DMFCs incorporated with graphene oxide

| Inorganic additive | Method | Catalyst loading (mg cm ⁻²) | Maximum Power density (mW cm ⁻²) | Operation condition | Ref. |
|--------------------|-------------------------------|--|---|---------------------|-------|
| Nafion/0.50wt% MMT | composite membrane | 2 | 62 (O ₂) | 1M methanol, 30 °C | [170] |
| Nafion/0.50wt% MMT | composite membrane | 2 | 141 (O ₂) | 1M methanol, 70 °C | [170] |
| Nafion/1.50wt% MMT | dual layer laminated membrane | 3 | 55) | 6M methanol, 50 °C | [223] |
| Nafion/1.50wt% MMT | dual layer laminated membrane | 3 | 32 | 8M methanol, 50 °C | [223] |
| Nafion/0.05wt% MMT | composite membrane | 2 | 42.9 | 1M methanol | [225] |
| Nafion/0.05wt% MMT | composite membrane | 2 | 34.6 | 5M methanol | [225] |

In addition, graphene oxide has an organophobic behavior from hydroxyl, carboxylic and epoxy groups and the organophilic character from sp^2 graphite. To extend an understanding in a relation between organophobic character and DMFC performance, the contact angle measurement must be examined.

The MEAs performance have strongly influenced by proton conductivity and the methanol Permeability. The MEA should prevent methanol crossover with low suppression of proton transport. Nevertheless, this research could not carry out the characterisation for proton conductivity and methanol permeability because of the limited laboratory access to impedance spectroscopy (EIS) . The brief of the methods are shown in next section.

7.2.1 Characterisation of proton conductivity

Proton transportation through a membrane has crucial influence on a MEA performance. The membrane with effective proton transfer contributes to the sufficient supplying reactant for oxygen reduction on cathode side leading to high performance of a MEA. From this reason, proton conductivity of a MEA has been investigated using an electrochemical impedance spectroscopy method. This technique determines a resistance of MEA under an operation condition [61, 196].

7.2.2 Characterisation of methanol permeability

Methanol passage through a membrane has critical effect on DMFC performance. There are several factors determine methanol transport rate such as the hydration of membrane, the characteristic of membrane, the water activity at both anode and cathode side and the electroosmotic drag from protonic current density. Consequently, certainty amount of methanol permeability should be measured under the operating condition of DMFC by a voltammetric technique [226–229].

Bibliography

- [1] N. Mimura. Sea-level rise caused by climate change and its implications for society. *Proceedings of the Japan Academy Series B-Physical and Biological Sciences*, 89(7):281–301, 2013.
- [2] A. Johnson, L. Marrack, and S. Dolan. Threats to Coastal Archaeological Sites and the Effects of Future Climate Change: Impacts of the 2011 Tsunami and an Assessment of Future Sea-Level Rise at Hnaunau, Hawaii. *The Journal of Island and Coastal Archaeology*, 10(2):232–252, 2015.
- [3] S. Yi, W. Sun, K. Heki, and A. Qian. An increase in the rate of global mean sea level rise since 2010. *Geophysical Research Letters*, 42:3998–4006, 2015.
- [4] L. Treut, R. Somerville, U. Cubasch, Y. Ding, C. Mauritzen, A. Mokssit, T. Peterson, M. Prather, D. Qin, M. Manning, Z. Chen, M. Marquis, K. B. Averyt, M. Tignor, U. Kingdom, T. P. Le Treut, H., R. Somerville, U. Cubasch, Y. Ding, C. Mauritzen, A. Mokssit, and M. Prather. Historical Overview of Climate Change Science. In *2007: Historical Overview of Climate Change. In: Climate Change 2007: The Physical Science Basis. Contribution of Working Group I to the Fourth Assessment Report of the Intergovernmental Panel on Climate Change*, chapter 1, pages 93–127. Cambridge University Press, Cambridge, United Kingdom and New York, NY, USA, 2007.
- [5] I. Arto and E. Dietzenbacher. Drivers of the growth in global greenhouse gas emissions. *Environmental science & technology*, 48:5388–94, 2014.

- [6] A. Baede. Annex II: Glossary in IPCC Fourth Assess. Report. In Alfons P. M. Baede, editor, *the Intergovernmental Panel on Climate Change*, chapter Annex, pages 76–89. the Intergovernmental Panel on Climate Change Assessment, 2008.
- [7] United state environmental protection agency (EPA). Global Greenhouse Gas Emissions Data, 2004.
- [8] D. Betowski, C. Bevington, and T. C. Allison. Estimation of Radiative Efficiency of Chemicals with Potentially Significant Global Warming Potential. *Environmental Science & Technology*, 50:790–797, 2016.
- [9] K. A. Solomon, S., D. Qin, M. Manning, Z. Chen, M. Marquis, M. T. (eds.), and H. Miller. *Climate Change 2007: Working Group I: The Physical Science Basis: Contribution of Working Group I to the Fourth Assessment Report of the Intergovernmental Panel on Climate Chang*. Cambridge University Press, Cambridge, United Kingdom and New York, USA, 2007.
- [10] L. C. Lau, K. T. Lee, and A. R. Mohamed. Global warming mitigation and renewable energy policy development from the Kyoto Protocol to the Copenhagen Accord - A comment. *Renewable and Sustainable Energy Reviews*, 16(7):5280–5284, 2012.
- [11] United Nations Framework Convention on Climate Change (UNFCCC). Status of Ratification of the Kyoto Protocol, 2015.
- [12] European Environment Agency (EEA). Annual European Union greenhouse gas inventory 19902012 and inventory report 2014, 2014.
- [13] T. Bruckner, I. A. Bashmakov, Y. Mulugetta, H. Chum, A. de la Vega Navarro, J. Edmonds, A. Faaij, B. Fungtammasan, A. Garg, E. Hertwich, D. Honnery, D. Infield, M. Kainuma, and S. Khennas. Energy Systems. In Working Group III Technical Support Unit, editor, *2014: Energy Systems. In: Climate Change 2014: Mitigation of Climate Change. Contribution of Working Group III to the Fifth Assessment Report of the Intergovernmental*

- Panel on Climate Change*, chapter Chapter 7, pages 511–598. Cambridge University Press, Cambridge, United Kingdom and New York, NY, USA, 1 edition, 2014.
- [14] J. H. Williams, A. Debenedictis, R. Ghanadan, A. Mahone, J. Moore, W. R. M. Iii, S. Price, and M. S. Torn. 2050 : The Pivotal Role of Electricity. *Science (New York, N.Y.)*, 335(April):53–60, 2012.
- [15] D. J. Arent, A. Wise, and R. Gelman. The status and prospects of renewable energy for combating global warming. *Energy Economics*, 33(4):584–593, 2011.
- [16] U. B. Demirci. How green are the chemicals used as liquid fuels in direct liquid-feed fuel cells? *Environment international*, 35(3):626–31, 2009.
- [17] K. G. Reddy, T. G. Deepak, G. S. Anjusree, S. Thomas, S. Vadukumpully, K. R. V. Subramanian, S. V. Nair, and A. S. Nair. On global energy scenario, dye-sensitized solar cells and the promise of nanotechnology. *Physical Chemistry Chemical Physics*, 16:6838, 2014.
- [18] D. J. C. Mackay. Solar energy in the context of energy use , energy transportation and energy storage Solar energy in the context of energy use , energy transportation and energy storage. *Philosophical Transactions of the Royal Society A*, 371, 2013.
- [19] M. Cheng and Y. Zhu. The state of the art of wind energy conversion systems and technologies : A review. *Energy Conversion and Management*, 88:332–347, 2014.
- [20] K. Dai, A. Bergot, C. Liang, W. Xiang, and Z. Huang. Environmental issues associated with wind energy -A review. *Renewable Energy*, 75:911–921, 2015.
- [21] A. Purkus and V. Barth. Geothermal power production in future electricity markets-A scenario analysis for Germany. *Energy Policy*, 39(1):349–357, 2011.

- [22] R. Shortall, B. Davidsdottir, and G. Axelsson. Energy for Sustainable Development Development of a sustainability assessment framework for geothermal energy projects. *Energy for Sustainable Development*, 27:28–45, 2015.
- [23] S. Malafeh and B. Sharp. Role of royalties in sustainable geothermal energy development. *Energy Policy*, 85:235–242, 2015.
- [24] L. Gaudard and F. Romerio. Reprint of "The future of hydropower in Europe: Interconnecting climate, markets and policies". *Environmental Science and Policy*, 43:5–14, 2014.
- [25] J. Zhang, L. Xu, B. Yu, and X. Li. Environmentally feasible potential for hydropower development regarding environmental constraints. *Energy Policy*, 73:552–562, 2014.
- [26] R. Verma and S. Suthar. Utility of Duckweeds as Source of Biomass Energy: a Review. *Bioenergy Research*, 8(4):1589–1597, 2015.
- [27] N. Apergis and C. Tsoumas. Integration properties of disaggregated solar, geothermal and biomass energy consumption in the U.S. *Energy Policy*, 39(9):5474–5479, 2011.
- [28] F. Blaabjerg and D. M. Ionel. Renewable Energy Devices and Systems State-of-the-Art Technology, Research and Development, Challenges and Future Trends. *Electric Power Components and Systems*, 43(12):1319–1328, 2015.
- [29] J. Larminie and A. Dicks. *Fuel Cell Systems Explained*. John Wiley & Sons Ltd., England, 2nd edition, 2003.
- [30] C. D'Urso, V. Baglio, V. Antonucci, a. S. Aric, S. Specchia, U. a. Icardi, G. Saracco, C. Spinella, and G. D'Arrigo. Development of a planar μ DMFC operating at room temperature. *International Journal of Hydrogen Energy*, 36(13):8088–8093, 2011.

- [31] M. Bischoff and G. Huppmann. Operating experience with a 250 kWel molten carbonate fuel cell (MCFC) power plant. *Journal of Power Sources*, 105(2):216–221, 2002.
- [32] O. Z. Sharaf and M. F. Orhan. An overview of fuel cell technology: Fundamentals and applications. *Renewable and Sustainable Energy Reviews*, 32:810–853, 2014.
- [33] S. Giddey, S. P. S. Badwal, a. Kulkarni, and C. Munnings. A comprehensive review of direct carbon fuel cell technology. *Progress in Energy and Combustion Science*, 38(3):360–399, 2012.
- [34] C. Dyer. Fuel cells for portable applications. *Journal of Power Sources*, 106(1-2):31–34, 2002.
- [35] R. Rashidi, I. Dincer, G. F. Naterer, and P. Berg. Performance evaluation of direct methanol fuel cells for portable applications. *Journal of Power Sources*, 187(2):509–516, 2009.
- [36] S. K. Kamarudin, W. R. W. Daud, S. L. Ho, and U. A. Hasran. Overview on the challenges and developments of micro-direct methanol fuel cells (DMFC). *Journal of Power Sources*, 163(2):743–754, 2007.
- [37] S. K. Kamarudin, F. Achmad, and W. R. W. Daud. Overview on the application of direct methanol fuel cell (DMFC) for portable electronic devices. *International Journal of Hydrogen Energy*, 34(16):6902–6916, 2009.
- [38] J. H. Wee. Which type of fuel cell is more competitive for portable application : Direct methanol fuel cells or direct borohydride fuel cells? *Journal of Power Sources*, 161:1–10, 2006.
- [39] M. Broussely and G. Archdale. Li-ion batteries and portable power source prospects for the next 5 10 years. *Journal of Power Sources*, 136:386–394, 2004.

- [40] Y. Zhan, Y. Guo, J. Zhu, and H. Wang. Intelligent uninterruptible power supply system with back-up fuel cell/battery hybrid power source. *Journal of Power Sources*, 179(2):745–753, 2008.
- [41] E. Varkaraki, N. Lymberopoulos, and a. Zachariou. Hydrogen based emergency back-up system for telecommunication applications. *Journal of Power Sources*, 118(1-2):14–22, 2003.
- [42] A. Moreno-Munoz, J. J. G. de la Rosa, J. M. Flores-Arias, F. J. Bellido-Outerino, and A. Gil-de Castro. Energy efficiency criteria in uninterruptible power supply selection. *Applied Energy*, 88(4):1312–1321, 2011.
- [43] M. Hosseini, I. Dincer, and M. a. Rosen. Hybrid solar-fuel cell combined heat and power systems for residential applications: Energy and exergy analyses. *Journal of Power Sources*, 221:372–380, 2013.
- [44] S. Mekhilef, R. Saidur, and A. Safari. Comparative study of different fuel cell technologies. *Renewable and Sustainable Energy Reviews*, 16(1):981–989, 2012.
- [45] X. Zhang, S. H. Chan, H. K. Ho, S.-C. Tan, M. Li, G. Li, J. Li, and Z. Feng. Towards a smart energy network: The roles of fuel/electrolysis cells and technological perspectives. *International Journal of Hydrogen Energy*, 40(21):6866–6919, 2015.
- [46] S. Ahmed, D. D. Papadidas, and R. K. Ahluwalia. Configuring a fuel cell based residential combined heat and power system. *Journal of Power Sources*, 242:884–894, 2013.
- [47] H. R. Ellamla, I. Staffell, P. Bujlo, B. G. Pollet, and S. Pasupathi. Current status of fuel cell based combined heat and power systems for residential sector. *Journal of Power Sources*, 293:312–328, 2015.
- [48] G. Upreti, D. L. Greene, K. G. Duleep, and R. Sawhney. Fuel cells for non-automotive uses: Status and prospects. *International Journal of Hydrogen Energy*, 37(8):6339–6348, 2012.

- [49] H. Aki, Y. Taniguchi, I. Tamura, A. Kegasa, H. Hayakawa, Y. Ishikawa, S. Yamamoto, and I. Sugimoto. Fuel cells and energy networks of electricity, heat, and hydrogen: A demonstration in hydrogen-fueled apartments. *International Journal of Hydrogen Energy*, 37(2):1204–1213, 2012.
- [50] J. Andújar and F. Segura. Fuel cells: History and updating. A walk along two centuries. *Renewable and Sustainable Energy Reviews*, 13(9):2309–2322, 2009.
- [51] American Honda Motor Co. Inc. How FCX Clarity FCEV Works, 2015.
- [52] Honda Motor Co. Ltd. Honda Exhibits World Premiere of CLARITY FUEL CELL, Planned Production Model of its All-new Fuel Cell Vehicle, at 44th Tokyo Motor Show 2015, 2015.
- [53] T. Elmer, M. Worall, S. Wu, and S. B. Riffat. Fuel cell technology for domestic built environment applications : State of-the-art review. *Renewable and Sustainable Energy Reviews*, 42:913–931, 2015.
- [54] A. Aslani and K.-F. V. Wong. Analysis of renewable energy development to power generation in the United States. *Renewable Energy*, 63:153–161, 2014.
- [55] Y. Sun, M. Delucchi, and J. Ogden. The impact of widespread deployment of fuel cell vehicles on platinum demand and price. *International Journal of Hydrogen Energy*, 36(17):11116–11127, 2011.
- [56] G. M. Mudd. Key trends in the resource sustainability of platinum group elements. *Ore Geology Reviews*, 46:106–117, 2012.
- [57] A. Gray. Sir William Robert Grove. *Nature*, 54:393–394, 1896.
- [58] R. Meldola. Faraday and Schonbein. *Nature*, 61:337–340, 1900.
- [59] A. Appleby. From Sir William Grove to today: fuel cells and the future. *Journal of Power Sources*, 29(1-2):3–11, 1990.

- [60] H. Ahmad, S. K. Kamarudin, U. a. Hasran, and W. R. W. Daud. Overview of hybrid membranes for direct-methanol fuel-cell applications. *International Journal of Hydrogen Energy*, 35(5):2160–2175, 2010.
- [61] F. B. O’Hayre, R. Cha, S-W and Colella, S and Prinz. *Fuel cell fundamentals*. Hoboken, N.J. : John Wiley & Sons, Hoboken, N.J., 2006.
- [62] L. Carrette, K. A. Friedrich, and U. Stimming. Fuel Cells Fundamentals and Applications. *Fuel Cells*, 1(1):5–39, 2001.
- [63] S. Hardman, A. Chandan, and R. Steinberger-Wilckens. Fuel Cell Added Value for Early Market Applications. *The European Fuel Cell Forum*, 287:297–306, 2015.
- [64] H. P. Corp, S. Law, W. Ostwald, T. Gas, F. Cell, S. Explained, S. Edition, M. K. Mahapatra, P. Singh, F. Cell, S. Explained, S. Edition, and U. Schr. *Fuel Cells*. Elsevier Ltd., 2 edition, 2014.
- [65] G. Acres and K. Acres. Recent advances in fuel cell technology and its applications. *Journal of Power Sources*, 100(1-2):60–66, November 2001.
- [66] A. Kirubakaran, S. Jain, and R. Nema. A review on fuel cell technologies and power electronic interface. *Renewable and Sustainable Energy Reviews*, 13(9):2430–2440, 2009.
- [67] K. Jiao and X. Li. Water transport in polymer electrolyte membrane fuel cells. *Progress in Energy and Combustion Science*, 37(3):221–291, 2011.
- [68] Y. Wang, K. S. Chen, J. Mishler, S. C. Cho, and X. C. Adroher. A review of polymer electrolyte membrane fuel cells: Technology, applications, and needs on fundamental research. *Applied Energy*, 88(4):981–1007, 2011.
- [69] N. Mahato, A. Banerjee, A. Gupta, S. Omar, and K. Balani. Progress in Material Selection for Solid Oxide Fuel Cell Technology: A Review. *Progress in Materials Science*, 72:141–337, 2015.

- [70] A. Choudhury, H. Chandra, and a. Arora. Application of solid oxide fuel cell technology for power generation - A review. *Renewable and Sustainable Energy Reviews*, 20:430–442, 2013.
- [71] N. Q. Minh. Solid oxide fuel cell technology - Features and applications. *Solid State Ionics*, 174(1-4):271–277, 2004.
- [72] N. Sammes, R. Bove, and K. Stahl. Phosphoric acid fuel cells: Fundamentals and applications. *Current Opinion in Solid State and Materials Science*, 8(5):372–378, 2004.
- [73] G. Cacciola, V. Antonucci, and S. Freni. Technology up date and new strategies on fuel cells. *Journal of Power Sources*, 100:67–79, 2001.
- [74] F. Bidault, D. J. L. Brett, P. H. Middleton, and N. P. Brandon. Review of gas diffusion cathodes for alkaline fuel cells. *Journal of Power Sources*, 187(1):39–48, 2009.
- [75] A. S. Aricò, V. Baglio, and V. Antonucci. Direct Methanol Fuel Cells : History , Status and Perspectives. In H. L. Zhang and JiuJun, editors, *Electrocatalysis of direct methanol fuel cell*, chapter 1, pages 1–70. WILEY-VCH Verlag GmbH & Co. KGaA, Weinheim, 2009.
- [76] J. Y. Park, J. H. Lee, S. K. Kang, J. H. Sauk, and I. Song. Mass balance research for high electrochemical performance direct methanol fuel cells with reduced methanol crossover at various operating conditions. *Journal of Power Sources*, 178(1):181–187, 2008.
- [77] B. Lindström and L. J. Pettersson. Catalytic oxidation of liquid methanol as a heat source for an automotive reformer. *Chemical Engineering and Technology*, 26(4):473–478, 2003.
- [78] H. Bahrami and A. Faghri. Review and advances of direct methanol fuel cells: Part II: Modeling and numerical simulation. *Journal of Power Sources*, 230:303–320, 2013.

- [79] J. N. Tiwari, R. N. Tiwari, G. Singh, and K. S. Kim. Recent progress in the development of anode and cathode catalysts for direct methanol fuel cells. *Nano Energy*, 2(5):553–578, 2013.
- [80] Z. Jusys and R. J. Behm. Simultaneous oxygen reduction and methanol oxidation on a carbon-supported Pt catalyst and mixed potential formation-revisited. *Electrochimica Acta*, 49(22-23 SPEC. ISS.):3891–3900, 2004.
- [81] G. Hoogers. *Fuel Cell Components and Their Impact on Performance*. CRC Press, London, 2003.
- [82] C. Lamy, D. J. Jones, C. Coutanceau, P. Brault, S. Martemianov, and Y. Bultel. Do not forget the electrochemical characteristics of the membrane electrode assembly when designing a Proton Exchange Membrane Fuel Cell stack. *Electrochimica Acta*, 56(28):10406–10423, 2011.
- [83] U. Lucia. Overview on fuel cells. *Renewable and Sustainable Energy Reviews*, 30:164–169, 2014.
- [84] K. Kordesch. *Fuel cells and their applications / Karl Kordesch, Gunter Simader*. Weinheim, Weinheim, 1996.
- [85] V. Antonucci, A. Di Blasi, V. Baglio, R. Ornelas, F. Matteucci, J. Ledesma-Garcia, L. G. Arriaga, and a. S. Aricò. High temperature operation of a composite membrane-based solid polymer electrolyte water electrolyser. *Electrochimica Acta*, 53(24):7350–7356, 2008.
- [86] S. H. Seo and C. S. Lee. A study on the overall efficiency of direct methanol fuel cell by methanol crossover current. *Applied Energy*, 87(8):2597–2604, 2010.
- [87] B. Gurau and E. S. Smotkin. Methanol crossover in direct methanol fuel cells: a link between power and energy density. *Journal of Power Sources*, 112(2):339–352, 2002.

- [88] A. Omosabi and R. S. Besser. Electron beam patterned Nafion membranes for DMFC applications. *Journal of Power Sources*, 228:151–158, 2013.
- [89] S. M. Rezaei Niya and M. Hoorfar. Process modeling of the ohmic loss in proton exchange membrane fuel cells. *Electrochimica Acta*, 120:193–203, 2014.
- [90] K. Scott, W. Taama, P. Argyropoulos, and K. Sundmacher. The impact of mass transport and methanol crossover on the direct methanol fuel cell. *Journal of Power Sources*, 83(1-2):204–216, 1999.
- [91] J. Han and H. Liu. Real time measurements of methanol crossover in a DMFC. *Journal of Power Sources*, 164(1):166–173, January 2007.
- [92] S. Wasmus and A. Kuver. Methanol oxidation and direct methanol fuel cells: a selective review. *Journal of Electroanalytical Chemistry*, 461(1-2):14–31, 1999.
- [93] T. S. Zhao, C. Xu, R. Chen, and W. W. Yang. Mass transport phenomena in direct methanol fuel cells. *Progress in Energy and Combustion Science*, 35(3):275–292, 2009.
- [94] A. M. Zainoodin, S. K. Kamarudin, and W. R. W. Daud. Electrode in direct methanol fuel cells. *International Journal of Hydrogen Energy*, 35(10):4606–4621, 2010.
- [95] A. Li, M. Han, S. H. Chan, and N.-t. Nguyen. Effects of hydrophobicity of the cathode catalyst layer on the performance of a PEM fuel cell. *Electrochimica Acta*, 55(8):2706–2711, 2010.
- [96] M. S. Wilson and S. Gottesfeld. Thin-film catalyst layers for polymer electrolyte fuel cell electrodes. *Journal of Applied Electrochemistry*, 22(1):1–7, 1992.
- [97] A. Hamnett. Mechanism and electrocatalysis in the direct methanol fuel cell. *Catalysis Today*, 38(4):445–457, 1997.

- [98] Y. Tong, H. S. Kim, P. K. Babu, P. Waszczuk, A. Wieckowski, and E. Oldfield. An NMR Investigation of CO Tolerance in a Pt / Ru Fuel Cell Catalyst. *Energy*, 124(3):1–6, 2002.
- [99] C. Lamy, A. Lima, V. LeRhun, F. Delime, C. Coutanceau, and J. M. Léger. Recent advances in the development of direct alcohol fuel cells (DAFC). *Journal of Power Sources*, 105(2):283–296, 2002.
- [100] S. M. M. Watanabe. PART II. ENHANCEMENT OF THE OXIDATION OF METHANOL ON PLATINUM BY RUTHENIUM AD-ATOMS. *Electroanalytical Chemistry and Interracial Electrochemistry*, 60:267–273, 1975.
- [101] H. Liu, C. Song, L. Zhang, J. Zhang, H. Wang, and D. P. Wilkinson. A review of anode catalysis in the direct methanol fuel cell. *Journal of Power Sources*, 155(2):95–110, 2006.
- [102] T. Ralph and M. P. Hogarth. Catalysis for Low Temperature Fuel Cells. *Platinum Metals Rev.*, 46(3):117–135, 2002.
- [103] D. R. Rolison, P. L. Hagans, K. E. Swider, and J. W. Long. Role of Hydrous Ruthenium Oxide in Pt - Ru Direct Methanol Fuel Cell Anode Electrocatalysts : The Importance of Mixed Electron / Proton Conductivity. *Langmuir*, 15(22):774–779, 1999.
- [104] S. Y. Huang and C. T. Yeh. Promotion of the electrocatalytic activity of a bimetallic platinum-ruthenium catalyst by repetitive redox treatments for direct methanol fuel cell. *Journal of Power Sources*, 195(9):2638–2643, 2010.
- [105] A. Velázquez-Palenzuela, F. Centellas, J. A. Garrido, C. Arias, R. M. Rodríguez, E. Brillas, and P. L. Cabot. Kinetic analysis of carbon monoxide and methanol oxidation on high performance carbon-supported Pt-Ru electrocatalyst for direct methanol fuel cells. *Journal of Power Sources*, 196(7):3503–3512, 2011.

- [106] C. P. Dawson. *Materials for Direct Methanol Fuel Cells : Inhibition of Methanol Crossover using Novel Membrane Electrode Assemblies A thesis submitted to the University of Manchester for the Degree of Doctor of Philosophy in the Faculty of Engineering and Physical Scie.* PhD thesis, The University of Manchester, 2011.
- [107] W. Y. Hsu, T. D. Gierke, and D. T. HSU, W. Y. and Gierke. Ion transport and clustering in nafion perfluorinated membranes. *Journal of Membrane Science*, 13(3):307–326, 1983.
- [108] K. Schmidt-Rohr and Q. Chen. Parallel cylindrical water nanochannels in Nafion fuel-cell membranes. *Nature Materials*, 7(1):75–83, 2008.
- [109] W. J. Hogarth, J. Diniz da Costa, and G. Lu. Solid acid membranes for high temperature (140 C) proton exchange membrane fuel cells. *Journal of Power Sources*, 142(1-2):223–237, 2005.
- [110] N. Deluca and Y. Elabd. Polymer electrolyte membranes for the direct methanol fuel cell: a review. *Journal of Polymer Science Part B: Polymer Physics*, 44(December 2005):2201–2225, 2006.
- [111] S. Peighambardoust, S. Rowshanzamir, and M. Amjadi. Review of the proton exchange membranes for fuel cell applications. *International Journal of Hydrogen Energy*, 35(17):9349–9384, 2010.
- [112] S. Cukierman. Et tu, Grotthuss! and other unfinished stories. *Biochimica et biophysica acta*, 1757(8):876–85, 2006.
- [113] B. S. Pivovar. An overview of electro-osmosis in fuel cell polymer electrolytes. *Polymer*, 47(11):4194–4202, 2006.
- [114] N. Agmon. The Grotthuss mechanism. *Chemical Physics Letters*, 244:456–462, 1995.
- [115] R. Gosalawit, S. Chirachanchai, S. Shishatskiy, and S. P. Nunes. Krytox-MontmorilloniteNafion nanocomposite membrane for effective methanol

- crossover reduction in DMFCs. *Solid State Ionics*, 178(29-30):1627–1635, 2007.
- [116] V. A. Paganin, E. Sitta, T. Iwasita, and W. Vielstich. Methanol crossover effect on the cathode potential of a direct PEM fuel cell. *Journal of Applied Electrochemistry*, 35(12):1239–1243, 2005.
- [117] S. Basri, S. K. Kamarudin, W. R. W. Daud, and Z. Yaakub. Nanocatalyst for direct methanol fuel cell (DMFC). *International Journal of Hydrogen Energy*, 35(15):7957–7970, 2010.
- [118] M. Rauber, I. Alber, S. Müller, R. Neumann, O. Picht, C. Roth, A. Schoökel, M. E. Toimil-Molaes, and W. Ensinger. Highly-ordered supportless three-dimensional nanowire networks with tunable complexity and interwire connectivity for device integration. *Nano Letters*, 11(6):2304–2310, 2011.
- [119] W. Tokarz, G. Lota, E. Frackowiak, A. Czerwiski, and P. Piela. Fuel cell testing of Pt-Ru catalysts supported on differently prepared and pretreated carbon nanotubes. *Electrochimica Acta*, 98:94–103, 2013.
- [120] J. Salgado, V. Paganin, E. Gonzalez, M. Montemor, I. Tacchini, A. Ansón, M. Salvador, P. Ferreira, F. Figueiredo, and M. Ferreira. Characterization and performance evaluation of PtRu electrocatalysts supported on different carbon materials for direct methanol fuel cells. *International Journal of Hydrogen Energy*, 38(2):910–920, 2013.
- [121] I. S. Park, K. S. Lee, Y. H. Cho, H. Y. Park, and Y. E. Sung. Methanol electro-oxidation on carbon-supported and Pt-modified Au nanoparticles. *Catalysis Today*, 132(1-4):127–131, 2008.
- [122] F. Kadirgan, S. Beyhan, and T. Atilan. Preparation and characterization of nano-sized Pt-Pd/C catalysts and comparison of their electro-activity toward methanol and ethanol oxidation. *International Journal of Hydrogen Energy*, 34(10):4312–4320, 2009.

- [123] H. Wang, C. Xu, F. Cheng, M. Zhang, S. Wang, and S. P. Jiang. Pd/Pt core-shell nanowire arrays as highly effective electrocatalysts for methanol electrooxidation in direct methanol fuel cells. *Electrochemistry Communications*, 10(10):1575–1578, 2008.
- [124] N. V. Long, T. D. Hien, T. Asaka, M. Ohtaki, and M. Nogami. Synthesis and characterization of Pt-Pd alloy and core-shell bimetallic nanoparticles for direct methanol fuel cells (DMFCs): Enhanced electrocatalytic properties of well-shaped core-shell morphologies and nanostructures. *International Journal of Hydrogen Energy*, 36(14):8478–8491, 2011.
- [125] J. Zeng and J. Y. Lee. Effects of preparation conditions on performance of carbon-supported nanosize Pt-Co catalysts for methanol electro-oxidation under acidic conditions. *Journal of Power Sources*, 140(2):268–273, 2005.
- [126] N. Karim and S. Kamarudin. An overview on non-platinum cathode catalysts for direct methanol fuel cell. *Applied Energy*, 103:212–220, 2013.
- [127] B. Piela, T. S. Olson, P. Atanassov, and P. Zelenay. Highly methanol-tolerant non-precious metal cathode catalysts for direct methanol fuel cell. *Electrochimica Acta*, 55(26):7615–7621, 2010.
- [128] H. Zhang, Q. Hao, H. Geng, and C. Xu. Nanoporous PdCu alloys as highly active and methanol-tolerant oxygen reduction electrocatalysts. *International Journal of Hydrogen Energy*, 38(24):10029–10038, 2013.
- [129] S. Sharma and B. G. Pollet. Support materials for PEMFC and DMFC electrocatalysts A review. *Journal of Power Sources*, 208(0):96–119, 2012.
- [130] T. Maiyalagan. Silicotungstic acid stabilized Pt-Ru nanoparticles supported on carbon nanofibers electrodes for methanol oxidation. *International Journal of Hydrogen Energy*, 34(7):2874–2879, 2009.

- [131] S. Li, X. Yu, G. Zhang, Y. Ma, J. Yao, and P. De Oliveira. Green synthesis of a Pt nanoparticle/polyoxometalate/carbon nanotube tri-component hybrid and its activity in the electrocatalysis of methanol oxidation. *Carbon*, 49(6):1906–1911, 2011.
- [132] Q. Sun and S. Kim. Synthesis of nitrogen-doped graphene supported Pt nanoparticles catalysts and their catalytic activity for fuel cells. *Electrochimica Acta*, 153:566–573, 2015.
- [133] X. Zhang, W. Yuan, J. Duan, Y. Zhang, and X. Liu. Graphene nanosheets modified by nitrogen-doped carbon layer to support Pt nanoparticles for direct methanol fuel cell. *Microelectronic Engineering*, 141:234–237, 2015.
- [134] K. Dutta, S. Das, D. Rana, and P. P. Kundu. Enhancements of Catalyst Distribution and Functioning Upon Utilization of Conducting Polymers as Supporting Matrices in DMFCs: A Review. *Polymer Reviews*, 55(1):1–56, 2015.
- [135] W. Li, H. Wu, J. Chen, H. Xue, and Y. Kong. Synthesis of size-controllable Pt nanoparticles decorated-poly(m-phenylenediamine) and its high catalytic activity for methanol oxidation. *Synthetic Metals*, 185-186:56–60, 2013.
- [136] S. J. Seo, J. J. Woo, S. H. Yun, H. J. Lee, J. S. Park, T. Xu, T.-H. Yang, J. Lee, and S.-H. Moon. Analyses of interfacial resistances in a membrane-electrode assembly for a proton exchange membrane fuel cell using symmetrical impedance spectroscopy. *Physical chemistry chemical physics : PCCP*, 12:15291–15300, 2010.
- [137] C. H. Park, H. K. Kim, C. H. Lee, H. B. Park, and Y. M. Lee. Nafion® nanocomposite membranes: Effect of fluorosurfactants on hydrophobic silica nanoparticle dispersion and direct methanol fuel cell performance. *Journal of Power Sources*, 194(2):646–654, 2009.

- [138] J. Nordlund, A. Roessler, and G. Lindbergh. The influence of electrode morphology on the performance of a DMFC anode. *Journal of Applied Electrochemistry*, 32:259–265, 2002.
- [139] J. Y. Park, H. T. Kim, E. S. Lee, I. H. Son, and S. Han. Effect of the porous carbon layer in the cathode gas diffusion media on direct methanol fuel cell performances. *International Journal of Hydrogen Energy*, 34(19):8257–8262, 2009.
- [140] Y. Gao, G. Q. Sun, S. L. Wang, and S. Zhu. Carbon nanotubes based gas diffusion layers in direct methanol fuel cells. *Energy*, 35(3):1455–1459, 2010.
- [141] Y. Wang, L. Zheng, G. Han, L. Lu, M. Wang, J. Li, and X. Wang. A novel multi-porous and hydrophilic anode diffusion layer for DMFC. *International Journal of Hydrogen Energy*, 39(33):19132–19139, 2014.
- [142] G. Q. Lu and C. Y. Wang. Electrochemical and flow characterization of a direct methanol fuel cell. *Journal of Power Sources*, 134(1):33–40, 2004.
- [143] C. Wong, T. Zhao, Q. Ye, and J. Liu. Experimental investigations of the anode flow field of a micro direct methanol fuel cell. *Journal of Power Sources*, 155(2):291–296, 2006.
- [144] H. Yang and T. S. Zhao. Effect of anode flow field design on the performance of liquid feed direct methanol fuel cells. *Electrochimica Acta*, 50(16-17):3243–3252, 2005.
- [145] S. Basri and S. K. Kamarudin. Process system engineering in direct methanol fuel cell. *International Journal of Hydrogen Energy*, 36(10):6219–6236, 2011.
- [146] C. Xu and T. S. Zhao. A new flow field design for polymer electrolyte-based fuel cells. *Electrochemistry Communications*, 9(3):497–503, 2007.

- [147] A. Schröder, K. Wippermann, G. Zehl, and D. Stolten. The influence of cathode flow field surface properties on the local and time-dependent performance of direct methanol fuel cells. *Electrochemistry Communications*, 12(10):1318–1321, 2010.
- [148] S. P. Jiang and H. Tang. Methanol crossover reduction by Nafion modification via layer-by-layer self-assembly techniques. *Colloids and Surfaces A: Physicochemical and Engineering Aspects*, 407:49–57, 2012.
- [149] H. S. Thiam, W. R. W. Daud, S. K. Kamarudin, A. B. Mohammad, A. A. H. Kadhum, K. S. Loh, and E. H. Majlan. Overview on nanostructured membrane in fuel cell applications. *International Journal of Hydrogen Energy*, 36(4):3187–3205, 2011.
- [150] V. Di Noto, M. Bettiol, F. Bassetto, N. Boaretto, E. Negro, S. Lavina, and F. Bertasi. Hybrid inorganic-organic nanocomposite polymer electrolytes based on Nafion and fluorinated TiO₂ for PEMFCs. *International Journal of Hydrogen Energy*, 37(7):6169–6181, April 2012.
- [151] J. H. Kim, S. K. Kim, K. Nam, and D. W. Kim. Composite proton conducting membranes based on Nafion and sulfonated SiO₂ nanoparticles. *Journal of Membrane Science*, 415-416:696–701, 2012.
- [152] D. Yuan, Z. Liu, S. W. Tay, X. Fan, X. Zhang, and C. He. An amphiphilic-like fluoroalkyl modified SiO₂ nanoparticle@Nafion proton exchange membrane with excellent fuel cell performance. *Chemical communications*, 49(83):9639–41, 2013.
- [153] Y. Fang, T. Wang, R. Miao, L. Tang, and X. Wang. Modification of Nafion membranes with ternary composite materials for direct methanol fuel cells. *Electrochimica Acta*, 55(7):2404–2408, 2010.
- [154] H. Ahmad, S. K. Kamarudin, U. a. Hasran, and W. R. W. Daud. A novel hybrid Nafion-PBI-ZP membrane for direct methanol fuel cells. *International Journal of Hydrogen Energy*, 36(22):14668–14677, 2011.

- [155] R. Herrera Alonso, L. Estevez, H. Lian, A. Kellarakis, and E. P. Giannelis. Nafionclay nanocomposite membranes: Morphology and properties. *Polymer*, 50(11):2402–2410, 2009.
- [156] Y. F. Lin, C. Y. Yen, C. C. M. Ma, S. H. Liao, C. H. Lee, Y. H. Hsiao, and H. P. Lin. High proton-conducting Nafion/-SO₃H functionalized mesoporous silica composite membranes. *Journal of Power Sources*, 171(2):388–395, 2007.
- [157] K. Feng, B. Tang, and P. Wu. Sulfonated graphene oxidesilica for highly selective Nafion-based proton exchange membranes. *J. Mater. Chem. A*, 2(38):16083–16092, 2014.
- [158] D. S. Hwang, C. H. Park, S. C. Yi, and Y. M. Lee. Optimal catalyst layer structure of polymer electrolyte membrane fuel cell. *International Journal of Hydrogen Energy*, 36(16):9876–9885, 2011.
- [159] B. P. Tripathi and V. K. Shahi. Organic-inorganic nanocomposite polymer electrolyte membranes for fuel cell applications. *Progress in Polymer Science*, 36(7):945–979, July 2011.
- [160] T. a. Zawodzinski. Water Uptake by and Transport Through Nafion 117 Membranes. *Journal of The Electrochemical Society*, 140(4):1041, 1993.
- [161] T. A. Zawodzinski, J. Davey, J. Valerio, and S. Gottesfeld. The water content dependence of electro-osmotic drag in proton-conducting polymer electrolytes. *Electrochimica Acta*, 40(3):297–302, 1995.
- [162] F. Mura, R. F. Silva, and A. Pozio. Study on the conductivity of re-cast Nafion/montmorillonite and Nafion/TiO₂ composite membranes. *Electrochimica Acta*, 52(19):5824–5828, 2007.
- [163] V. Di Noto, S. Lavina, E. Negro, M. Vittadello, F. Conti, M. Piga, and G. Pace. Hybrid inorganic-organic proton conducting membranes based on Nafion and 5 wt% of MxOy (M = Ti, Zr, Hf, Ta and W). Part II:

- Relaxation phenomena and conductivity mechanism. *Journal of Power Sources*, 187(1):57–66, 2009.
- [164] S. Y. So, Y. T. Hong, S. C. Kim, and S.-Y. Y. Lee. Control of water-channel structure and state of water in sulfonated poly(arylene ether sulfone)/diethoxydimethylsilane in situ hybridized proton conductors and its influence on transport properties for DMFC membranes. *Journal of Membrane Science*, 346(1):131–135, 2010.
- [165] X. Li, E. P. L. Roberts, and S. M. Holmes. Evaluation of composite membranes for direct methanol fuel cells. *Journal of Power Sources*, 154(1):115–123, 2006.
- [166] L. Ghassemzadeh, G. Pace, V. Di Noto, and K. Müller. Effect of SiO₂ on the dynamics of proton conducting [Nafion/(SiO₂)X] composite membranes: a solid-state ¹⁹F NMR study. *Physical chemistry chemical physics : PCCP*, 13(20):9327–9334, 2011.
- [167] Y. F. F. Lin, C. Y. Y. Yen, C. H. H. Hung, Y. H. H. Hsiao, and C.-C. M. C. M. Ma. A novel composite membranes based on sulfonated montmorillonite modified Nafion for DMFCs. *Journal of Power Sources*, 168(1):162–166, May 2007.
- [168] S. Slade, J. Smith, S. Campbell, T. Ralph, C. Ponce de León, and F. Walsh. Characterisation of a re-cast composite Nafion 1100 series of proton exchange membranes incorporating inert inorganic oxide particles. *Electrochimica Acta*, 55(22):6818–6829, 2010.
- [169] M. M. Hasani-Sadrabadi, E. Dashtimoghadam, N. Mokarram, F. S. Majedi, and K. I. Jacob. Triple-layer proton exchange membranes based on chitosan biopolymer with reduced methanol crossover for high-performance direct methanol fuel cells application. *Polymer*, 53(13):2643–2651, 2012.

- [170] B. G. Choi, Y. S. Huh, Y. C. Park, D. H. Jung, W. H. Hong, and H. Park. Enhanced transport properties in polymer electrolyte composite membranes with graphene oxide sheets. *Carbon*, 50(15):5395–5402, 2012.
- [171] D. R. Paul and L. M. Robeson. Polymer nanotechnology: Nanocomposites. *Polymer*, 49(15):3187–3204, 2008.
- [172] K. G. Bhattacharyya and S. S. Gupta. Adsorption of a few heavy metals on natural and modified kaolinite and montmorillonite: A review. *Advances in Colloid and Interface Science*, 140(2):114–131, 2008.
- [173] S. S. Mohtar, a. F. Ismail, and T. Matsuura. Preparation and characterization of SPEEK/MMT-STA composite membrane for DMFC application. *Journal of Membrane Science*, 371(1-2):10–19, 2011.
- [174] D. H. Jung, S. Y. Cho, D. H. Peck, D. R. Shin, and J. S. Kim. Preparation and performance of a Nafion/montmorillonite nanocomposite membrane for direct methanol fuel cell. *Journal of Power Sources*, 118(1-2):205–211, May 2003.
- [175] R. F. Silva, S. Passerini, and A. Pozio. Solution-cast Nafion/montmorillonite composite membrane with low methanol permeability. *Electrochimica Acta*, 50(13):2639–2645, 2005.
- [176] J. M. Thomassin, C. Pagnoulle, D. Bizzari, G. Caldarella, A. Germain, and R. Jérôme. Improvement of the barrier properties of Nafion (R) by fluoro-modified montmorillonite. *Solid State Ionics*, 177(13-14):1137–1144, 2006.
- [177] C. H. Rhee, H. K. Kim, H. Chang, and J. S. Lee. Nafion/sulfonated montmorillonite composite: A new concept electrolyte membrane for direct methanol fuel cells. *Chemistry of Materials*, 17(7):1691–1697, April 2005.

- [178] Y. Kim, J. S. Lee, C. H. Rhee, H. K. Kim, and H. Chang. Montmorillonite functionalized with perfluorinated sulfonic acid for proton-conducting organic-inorganic composite membranes. *Journal of Power Sources*, 162(1):180–185, 2006.
- [179] M. M. Hasani-Sadrabadi, E. Dashtimoghadam, F. S. Majedi, K. Kabiri, M. Solati-Hashjin, and H. Moaddel. Novel nanocomposite proton exchange membranes based on Nafion and AMPS-modified montmorillonite for fuel cell applications. *Journal of Membrane Science*, 365(12):286–293, 2010.
- [180] M. M. Hasani-Sadrabadi, E. Dashtimoghadam, F. S. Majedi, K. Kabiri, N. Mokarram, M. Solati-Hashjin, and H. Moaddel. Novel high-performance nanohybrid polyelectrolyte membranes based on bio-functionalized montmorillonite for fuel cell applications. *Chemical communications*, 46(35):6500–6502, 2010.
- [181] M. M. Hasani-Sadrabadi, S. H. Emami, and H. Moaddel. Preparation and characterization of nanocomposite membranes made of poly(2,6-dimethyl-1,4-phenylene oxide) and montmorillonite for direct methanol fuel cells. *Journal of Power Sources*, 183(2):551–556, 2008.
- [182] B. Matos, R. Isidoro, E. Santiago, A. Tavares, A. Ferlauto, R. Muccillo, and F. Fonseca. Nafiontitanate nanotubes composites prepared by in situ crystallization and casting for direct ethanol fuel cells. *International Journal of Hydrogen Energy*, 40(4):1859–1867, 2015.
- [183] S. Andersson and a. D. Wadsley. The Crystal Structure of $\text{Na}_2\text{Ti}_3\text{O}_7$. *Acta Cryst.*, 14(12):1245–1249, December 1961.
- [184] Y. V. Kolen'ko, K. a. Kovnir, A. I. Gavrilo, A. V. Garshev, J. Frantti, O. I. Lebedev, B. R. Churagulov, G. Van Tendeloo, and M. Yoshimura. Hydrothermal synthesis and characterization of nanorods of various titanates and titanium dioxide. *The journal of physical chemistry. B*, 110(9):4030–8, 2006.

- [185] O. V. Yakubovich and V. V. Kireev. Refinement of the Crystal Structure of $\text{Na}_2\text{Ti}_3\text{O}_7$. *Crystallography Reports*, 48:24–28, 2003.
- [186] S. Zhang, L.-M. L.-M. Peng, Q. Chen, G. H. Du, G. Dawson, and W. Z. Zhou. Formation mechanism of $\text{H}_2\text{Ti}_3\text{O}_7$ nanotubes. *Physical review letters*, 91(25):256103, 2003.
- [187] P. Dong, Y. Wang, B. Liu, L. Guo, Y. Huang, and S. Yin. Effect of hydrothermal reaction time on morphology and photocatalytic activity of $\text{H}_2\text{Ti}_3\text{O}_7$ nanotubes obtained via a rapid synthesis route. *Applied Surface Science*, 258(18):7052–7058, 2012.
- [188] Y. Wei, L. Shen, F. Wang, W.-D. D. Yang, H. Zhu, Z. Wang, and K. Han. Synthesis and characterization of novel nanocomposite membrane of sodium titanate/Nafion. *Materials Letters*, 65(11):1684–1687, 2011.
- [189] Y. Wei, L. Shen, Z. Wang, W.-D. D. Yang, H. Zhu, and H. Liu. A novel membrane for DMFC - $\text{Na}_2\text{Ti}_3\text{O}_7$ nanotubes/Nafion composite membrane. *International Journal of Hydrogen Energy*, 36(8):5088–5095, 2011.
- [190] Y. Wei, S. Matar, L. Shen, X. Zhang, Z. Guo, H. Zhu, and H. Liu. A novel membrane for DMFC $\text{Na}_2\text{Ti}_3\text{O}_7$ Nanotubes/Nafion composite membrane: Performances studies. *International Journal of Hydrogen Energy*, 37(2):1857–1864, 2012.
- [191] C. H. Rhee, Y. Kim, J. S. Lee, H. K. Kim, H. Chang, C. Houn, Y. Kim, J. Sung, H. Kyung, H. Chang, C. H. Rhee, Y. Kim, J. S. Lee, H. K. Kim, and H. Chang. Nanocomposite membranes of surface-sulfonated titanate and Nafion for direct methanol fuel cells. *Journal of Power Sources*, 159(2):1015–1024, 2006.
- [192] K. L. Yeung and W. Han. Zeolites and mesoporous materials in fuel cell applications. *Catalysis Today*, 236:182–205, 2014.

- [193] C. Baerlocher, L. McCusker, and D. Olson. *MOR-Framework type data*. the structure Commission of the international Zeolite Association, sixth edition, 2007.
- [194] C. Yoonoo and D. Holmes. *Development of Nafion-Mordenite Composite Membranes for Direct Methanol Fuel Cell Application*. PhD thesis, The University of Manchester, Manchester, 2010.
- [195] C. Yoonoo, C. P. Dawson, E. P. L. Roberts, and S. M. Holmes. Nafion/mordenite composite membranes for improved direct methanol fuel cell performance. *Journal of Membrane Science*, 369(1):367–374, 2011.
- [196] F. Lufrano, V. Baglio, O. Di Blasi, P. Staiti, V. Antonucci, and a. S. Aricò. Solid polymer electrolyte based on sulfonated polysulfone membranes and acidic silica for direct methanol fuel cells. *Solid State Ionics*, 216:90–94, 2012.
- [197] F. Lufrano, V. Baglio, O. Di Blasi, P. Staiti, V. Antonucci, and a. S. Aricò. Design of efficient methanol impermeable membranes for fuel cell applications. *Physical Chemistry Chemical Physics*, 14(8):2718, 2012.
- [198] F. Lufrano, V. Baglio, P. Staiti, V. Antonucci, and A. S. Arico'. Performance analysis of polymer electrolyte membranes for direct methanol fuel cells. *Journal of Power Sources*, 243:519–534, 2013.
- [199] Y. Xiang, S. Lu, and S. P. Jiang. Layer-by-layer self-assembly in the development of electrochemical energy conversion and storage devices from fuel cells to supercapacitors. *Chemical Society Reviews*, 41(21):7291, 2012.
- [200] S. Danu. *DEVELOPMNT OF COMPOSITE BINDING LAYER FOR DIRECT METHANOL FUEL* School of Chemical Engineering and Analytical Science. PhD thesis, The University of Manchester, 2010.
- [201] M. Inoue, T. Iwasaki, K. Sayama, and M. Umeda. Effect of conditioning method on direct methanol fuel cell performance. *Journal of Power Sources*, 195(18):5986–5989, 2010.

- [202] S. H. Seo and C. S. Lee. Effect of Operating Parameters on the Direct Methanol Fuel Cell Using Air or Oxygen As an Oxidant Gas. *Energy & Fuels*, 22(2):1212–1219, 2008.
- [203] J. Zhang, G. Yin, Z. Wang, and Y. Shao. Effects of MEA preparation on the performance of a direct methanol fuel cell. *Journal of Power Sources*, 160(2):1035–1040, 2006.
- [204] J. Ge and H. Liu. Experimental studies of a direct methanol fuel cell. *Journal of Power Sources*, 142(12):56–69, 2005.
- [205] A. A. Kulikovskiy. Heat transport in the membrane-electrode assembly of a direct methanol fuel cell: Exact solutions. *Electrochimica Acta*, 53(3):1353–1359, 2007.
- [206] Y. J. Zhang, W. Yan, Y. P. Wu, and Z. H. Wang. Synthesis of TiO₂ nanotubes coupled with CdS nanoparticles and production of hydrogen by photocatalytic water decomposition. *Materials Letters*, 62(23):3846–3848, 2008.
- [207] Z. Zhang, J. B. M. Goodall, S. Brown, L. Karlsson, R. J. H. Clark, J. L. Hutchison, I. U. Rehman, and J. a. Darr. Continuous hydrothermal synthesis of extensive 2D sodium titanate (Na₂Ti₃O₇) nano-sheets. *Dalton transactions (Cambridge, England : 2003)*, 39(3):711–4, 2010.
- [208] A. N. Fitch, H. Jovic, and A. Renouprez. Localization of benzene in sodium-Y-zeolite by powder neutron diffraction. *The Journal of Physical Chemistry*, 90(7):1311–1318, 1986.
- [209] N. Jung, Y.-H. Cho, M. Ahn, J. W. Lim, Y. S. Kang, D. Y. Chung, J. Kim, Y.-H. Cho, and Y.-E. Sung. Methanol-tolerant cathode electrode structure composed of heterogeneous composites to overcome methanol crossover effects for direct methanol fuel cell. *International Journal of Hydrogen Energy*, 36(24):15731–15738, 2011.

- [210] M. Ahn, Y. H. Cho, Y. H. Cho, J. Kim, N. Jung, and Y. E. Sung. Influence of hydrophilicity in micro-porous layer for polymer electrolyte membrane fuel cells. *Electrochimica Acta*, 56(5):2450–2457, 2011.
- [211] X. H. Yan, T. S. Zhao, G. Zhao, L. An, and X. L. Zhou. A hydrophilic-hydrophobic dual-layer microporous layer enabling the improved water management of direct methanol fuel cells operating with neat methanol. *Journal of Power Sources*, 294:232–238, 2015.
- [212] Y. Kang, M. Ren, T. Yuan, Y. Qiao, Z. Zou, and H. Yang. Effect of Nafion aggregation in the anode catalytic layer on the performance of a direct formic acid fuel cell. *Journal of Power Sources*, 195(9):2649–2652, 2010.
- [213] J. H. Kim, H. Y. Ha, I. H. Oh, S. A. Hong, and H. I. Lee. Influence of the solvent in anode catalyst ink on the performance of a direct methanol fuel cell. *Journal of Power Sources*, 135(1-2):29–35, 2004.
- [214] H. S. Park, Y. H. Cho, Y. H. Cho, C. R. Jung, J. H. Jang, and Y. E. Sung. Performance enhancement of PEMFC through temperature control in catalyst layer fabrication. *Electrochimica Acta*, 53(2):763–767, 2007.
- [215] A. Lindermeir, G. Rosenthal, U. Kunz, and U. Hoffmann. Improvement of MEAs for Direct-Methanol Fuel Cells by Tuned Layer Preparation and Coating Technology. *Fuel Cells*, 4(1-2):78–85, 2004.
- [216] H. Tang, S. Wang, M. Pan, S. P. Jiang, and Y. Ruan. Performance of direct methanol fuel cells prepared by hot-pressed MEA and catalyst-coated membrane (CCM). *Electrochimica Acta*, 52(11):3714–3718, 2007.
- [217] A. S. Aricò, P. Cret, P. L. Antonucci, J. Cho, H. Kim, and V. Antonucci. Optimization of operating parameters of a direct methanol fuel cell and physico-chemical investigation of catalyselectrolyte interface. *Electrochimica Acta*, 43(24):3719–3729, 1998.

- [218] S. Wang, G. Sun, Z. Wu, and Q. Xin. Effect of Nafion ionomer aggregation on the structure of the cathode catalyst layer of a DMFC. *Journal of Power Sources*, 165(1):128–133, 2007.
- [219] R. Jiang, C. Rong, and D. Chu. Determination of energy efficiency for a direct methanol fuel cell stack by a fuel circulation method. *Journal of Power Sources*, 126(1-2):119–124, 2004.
- [220] S. E. Shakeri, S. R. Ghaffarian, M. Tohidian, G. Bahlakeh, and S. Taranejoo. Polyelectrolyte Nanocomposite Membranes, Based on Chitosan-phosphotungstic Acid Complex and Montmorillonite for Fuel Cells Applications. *Journal of Macromolecular Science, Part B*, 52(9):1226–1241, 2013.
- [221] F. Tye. Tortuosity. *Journal of Power Sources*, 9(2):89–100, 1983.
- [222] R. K. Bharadwaj. Modeling the barrier properties of polymer-layered silicate nanocomposites. *Macromolecules*, 34(26):9189–9192, 2001.
- [223] C. Lin and Y. Lu. Highly ordered graphene oxide paper laminated with a Nafion membrane for direct methanol fuel cells. *Journal of Power Sources*, 237:187–194, 2013.
- [224] Y. Zhu, S. Murali, W. Cai, X. Li, J. W. Suk, J. R. Potts, and R. S. Ruoff. Graphene and graphene oxide: Synthesis, properties, and applications. *Advanced Materials*, 22(35):3906–3924, 2010.
- [225] H.-C. Chien, L.-D. Tsai, C.-P. Huangb, C.-y. Kang, J.-N. Lin, and C. Feng-Chih. Sulfonated Graphene Oxide/Nafion Composite Membranes for High-Performance Direct Methanol Fuel Cells. *Int. J. Hydrogen Energy*, 38:13792–13801, 2013.
- [226] X. Ren, T. E. Springer, and S. Gottesfeld. Water and Methanol Uptakes in Nafion Membranes and Membrane Effects on Direct Methanol Cell Performance. *Journal of The Electrochemical Society*, 147(1):92, 2000.

-
- [227] X. Ren, T. E. Springer, T. A. Zawodzinski, and S. Gottesfeld. Methanol Transport Through Nafion Membranes. Electro-osmotic Drag Effects on Potential Step Measurements. *Journal of The Electrochemical Society*, 147(2):466–474, 2000.
- [228] S. Hikita, K. Yamane, and Y. Nakajima. Measurement of methanol crossover in direct methanol fuel cell. *JSAE Review*, 22(2):151–156, 2001.
- [229] M. N. A. Mohd Norddin, A. F. Ismail, D. Rana, T. Matsuura, A. Mustafa, and A. Tabe-Mohammadi. Characterization and performance of proton exchange membranes for direct methanol fuel cell: Blending of sulfonated poly(ether ether ketone) with charged surface modifying macromolecule. *Journal of Membrane Science*, 323(2):404–413, 2008.

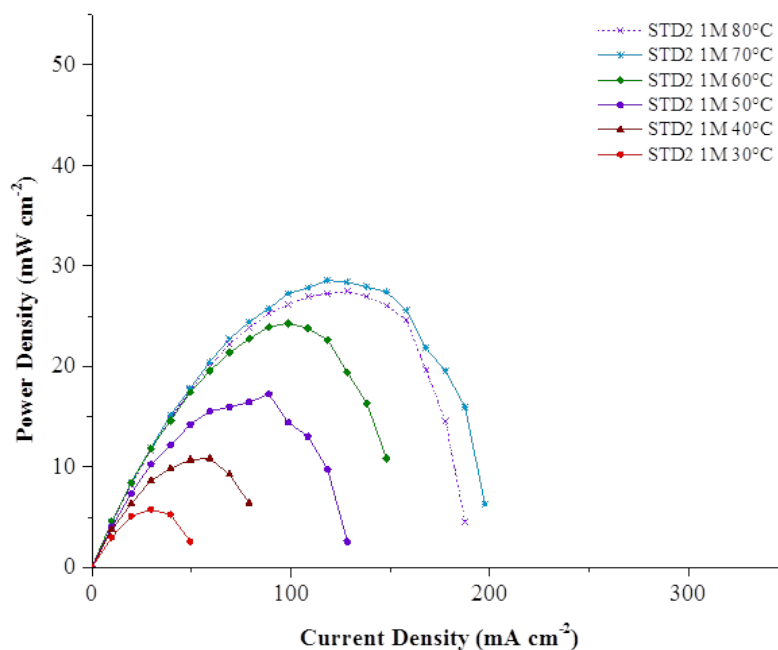
Appendix A

Performances of the membrane electrode assemblies

A.1 Experimental results of the standard membrane electrode assemblies

A.1.1 Polarization and power density curves of the standard 2 (STD2) using 1M, 2M and 4M methanol concentration

(A) Power density curve



(B) Polarization curve

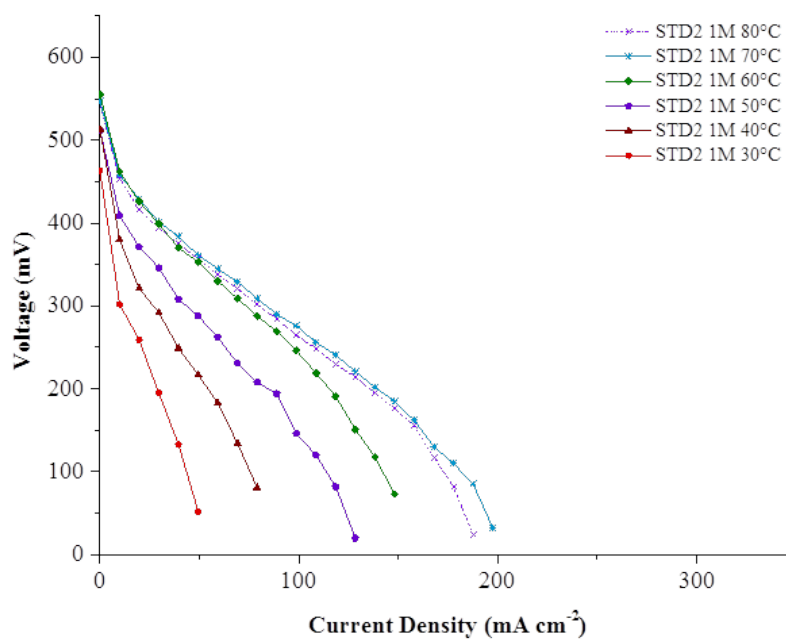
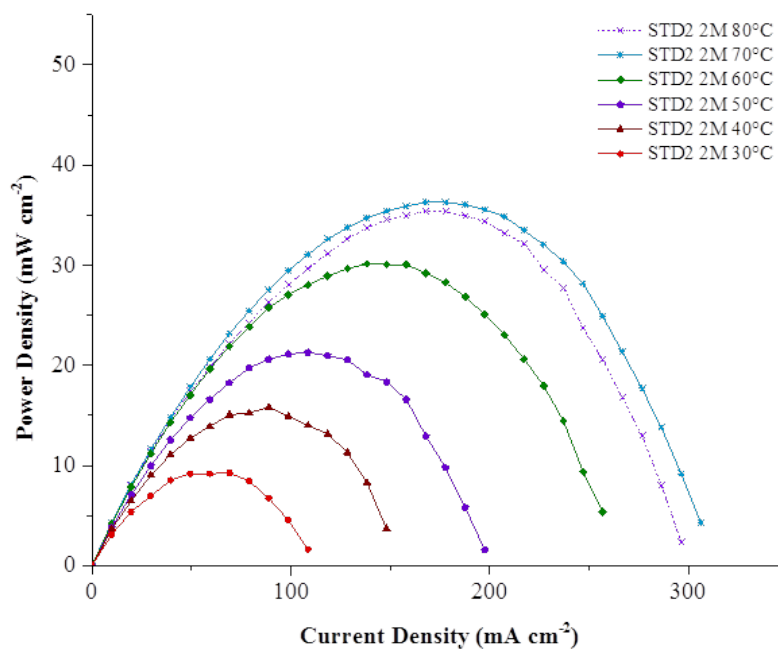


FIGURE A.1: Performance of STD2 at 30–80 °C and 1 M methanol

(A) Power density curve



(B) Polarization curve

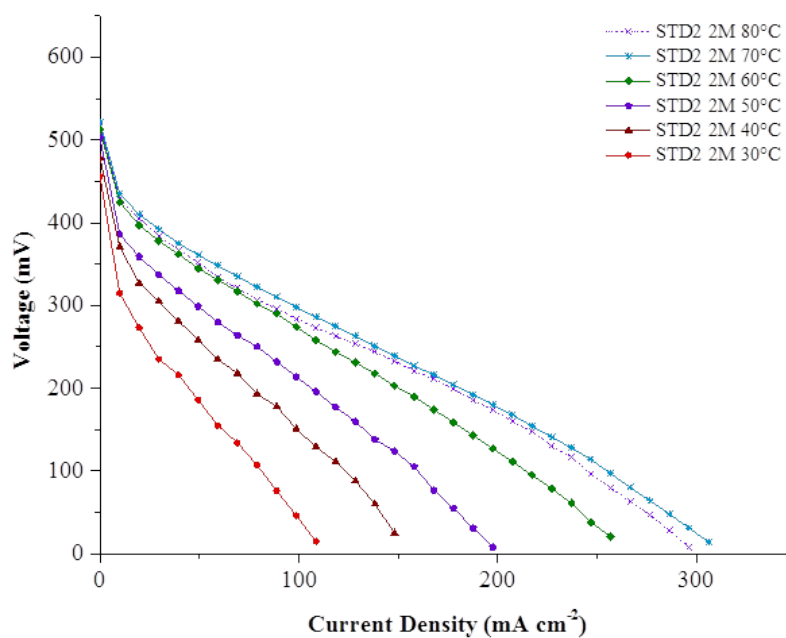
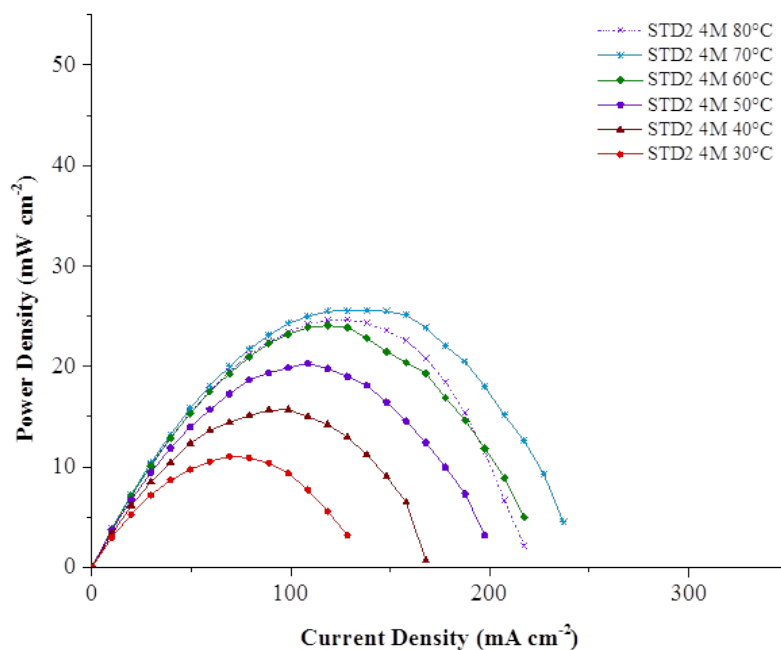


FIGURE A.2: Performance of STD2 at 30–80 °C and 2 M methanol

(A) Power density curve



(B) Polarization curve

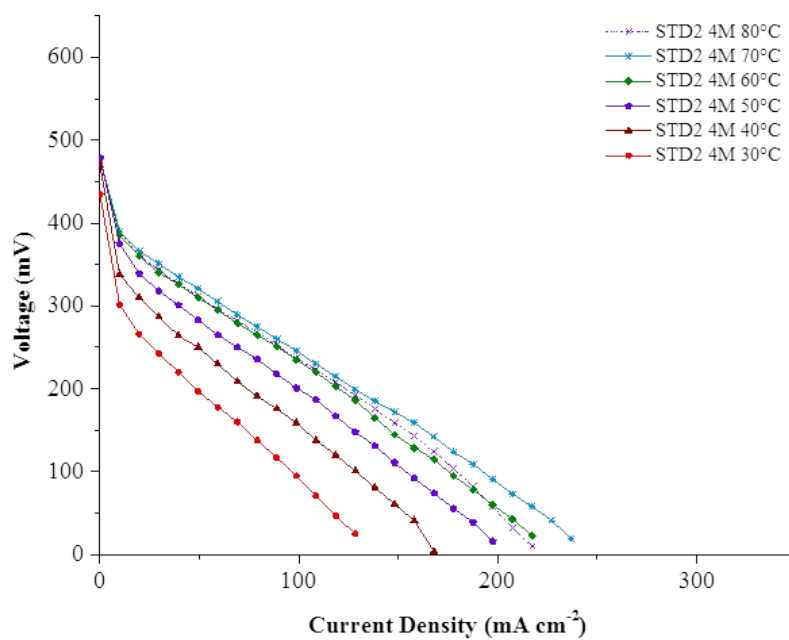


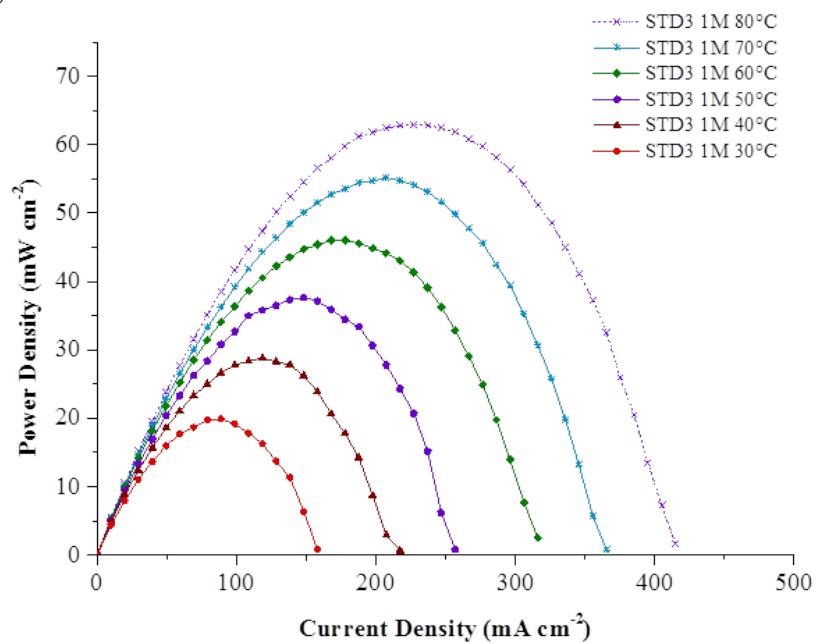
FIGURE A.3: Performance of STD2 at 30–80 °C and 4 M methanol

A.1.2 Polarization and power density curves of the the standard 3 (STD3) using 1M, 2M and 4M methanol concentration

It is important to note that the axis scale of performance curves in this chapter are different from those graphs in chapter 5. The different are:

- The power density scale of graphs in chapter 5 is 0-50 mW cm⁻² while the scale in chapter 6 is 0-70 mW cm⁻².
- The current density scale of graphs in chapter 5 is 0-350 mA cm⁻² while the scale in chapter 6 is 0-500 mA cm⁻².

(A) Polarization curve



(B) Power density curve

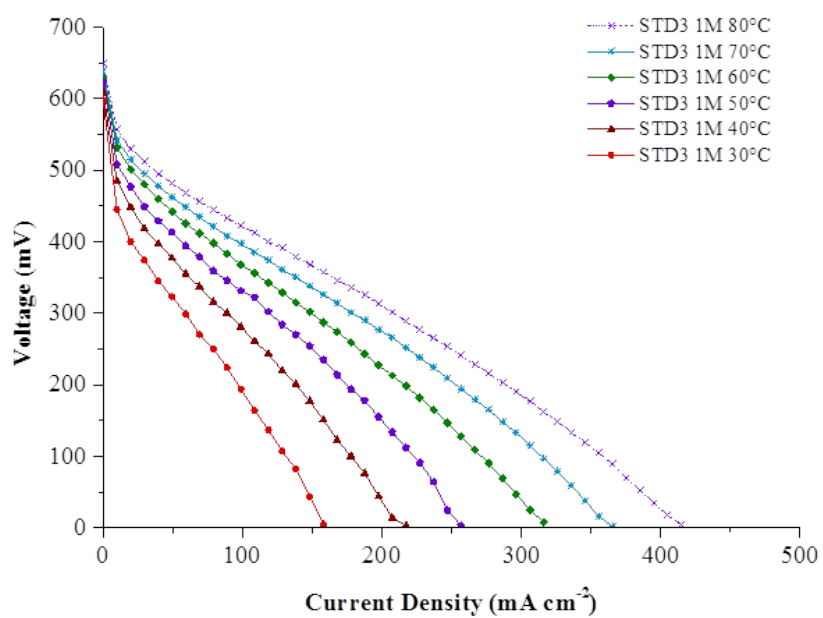
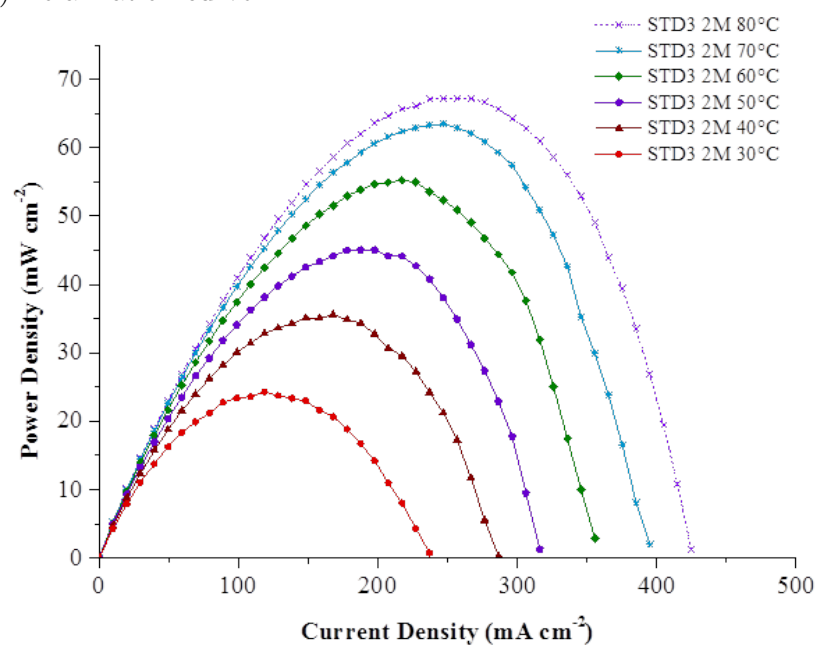


FIGURE A.4: Performance of STD3 at 1 M methanol

(A) Polarization curve



(B) Power density curve

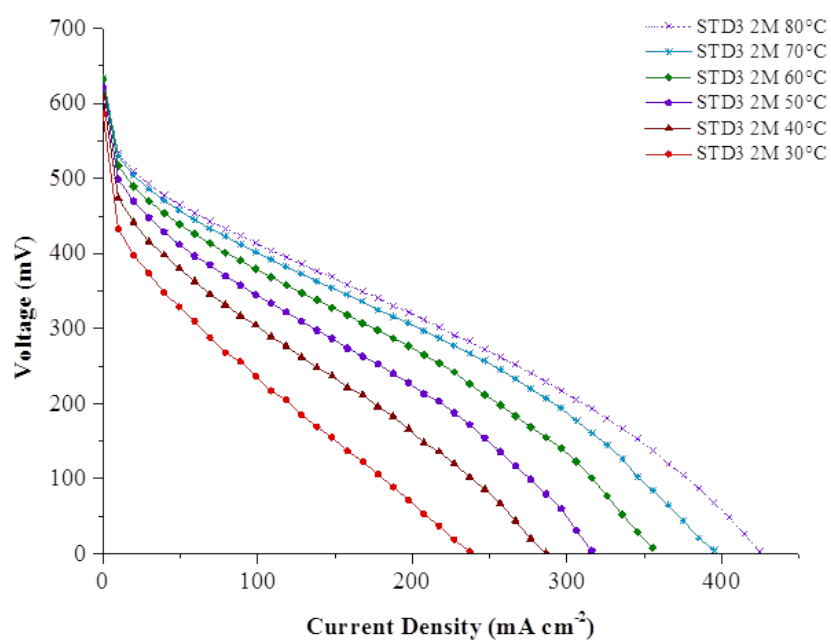
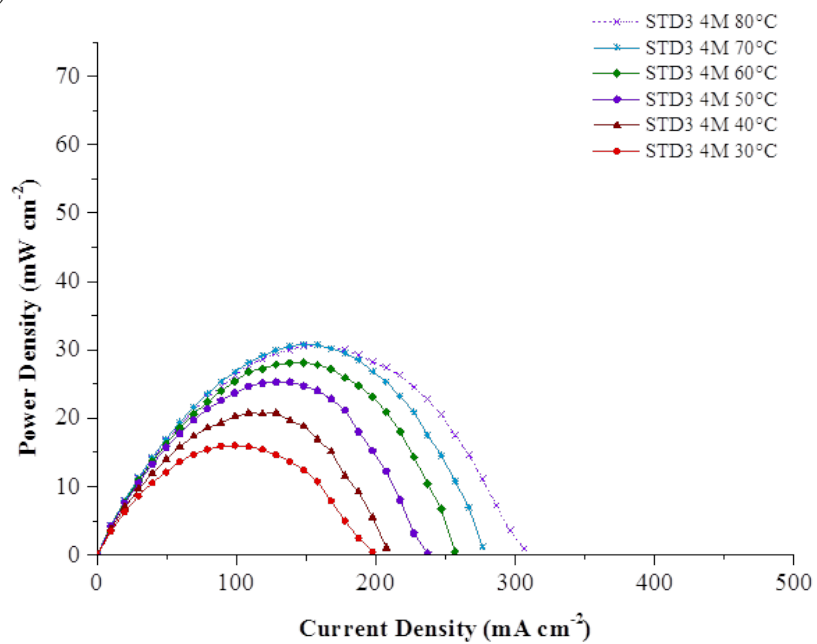


FIGURE A.5: Performance of STD3 at 30–80 °C and 2 M methanol

(A) Polarization curve



(B) Power density curve

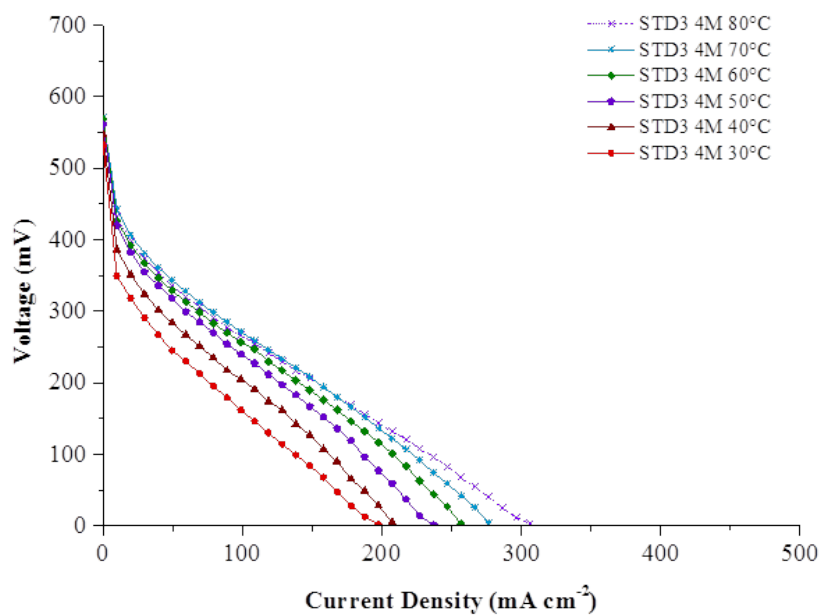


FIGURE A.6: Performance of STD3 at 30–80 °C and 4 M methanol

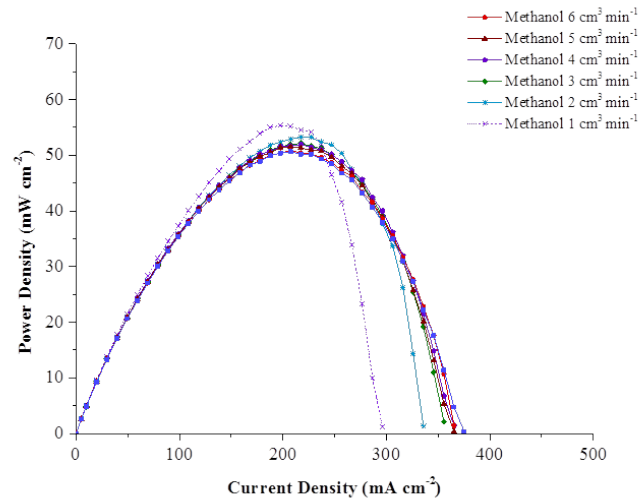
A.1.2.1 Optimised methanol and oxygen flow rate of the the standard 3 (STD3)

A set of experiments was carried out to optimize the methanol flow rate and air flow rate of the new standard produced by procedure II (STD3). The STD3 is tested with a range of methanol flow rates from 1-6 cm³ min⁻¹ and an air flow rates from 400-2000 cm³ min⁻¹. The concentration of methanol was 1M and the cell temperature was sustained at 70 °C.

Graphs in Figure A.7 and A.8 give an comparable information as the initial standard (STD1). The increase of methanol flow rate to 5 cm³ min⁻¹ from 1 cm³ min⁻¹ gives the better performance, nevertheless, STD3 shows similar result although the methanol flow rate goes up to 6 cm³ min⁻¹. The air flow rate adjustment also presents the same trend with the suitable flow rat at 1000 cm³ min⁻¹.

A.1.3 Polarization and power density curves of the stand-ard 5 (STD5) using 1M, 2M and 4M methanol con-centration

(A)



(B)

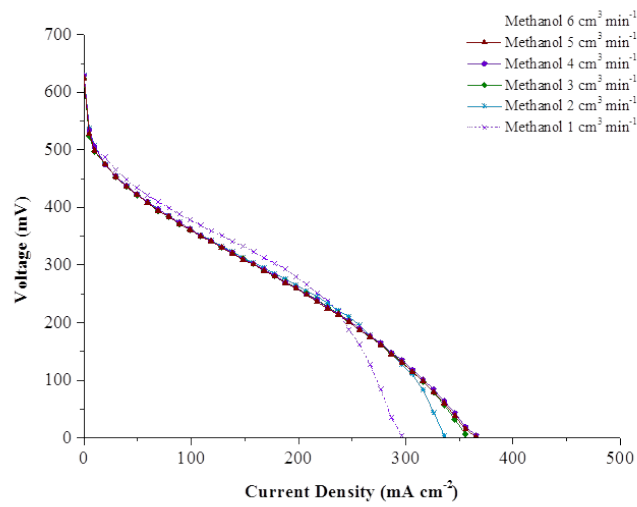


FIGURE A.7: The Performance of STD3 at different methanol flow rates ($1\text{-}6 \text{ cm}^3 \text{ min}^{-1}$)

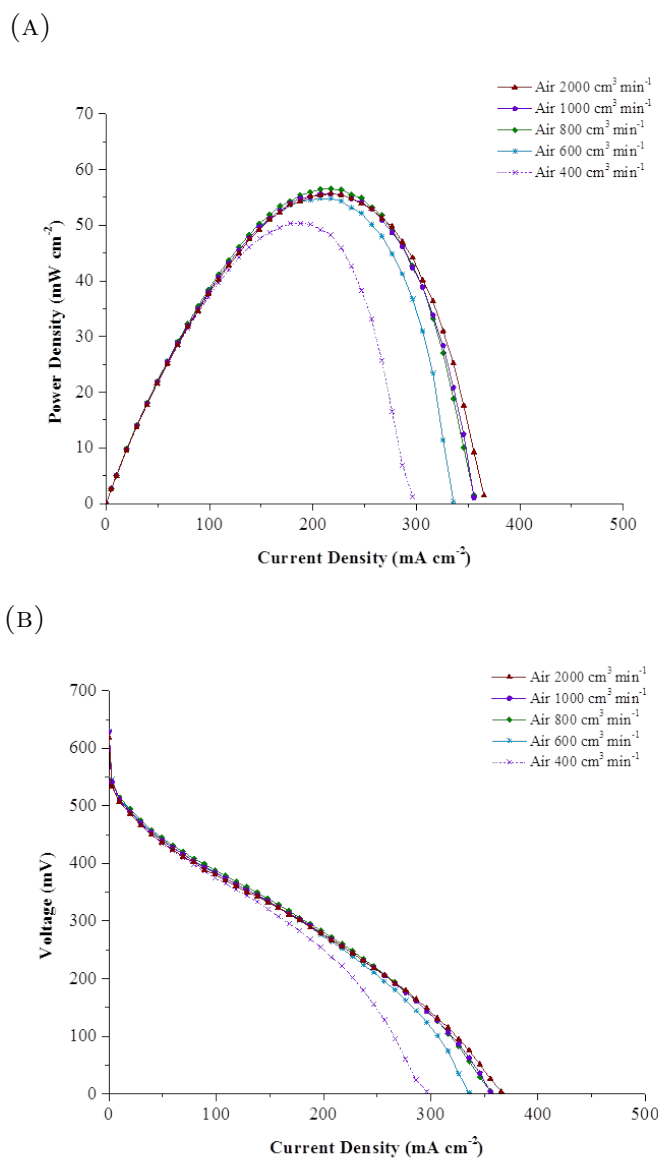
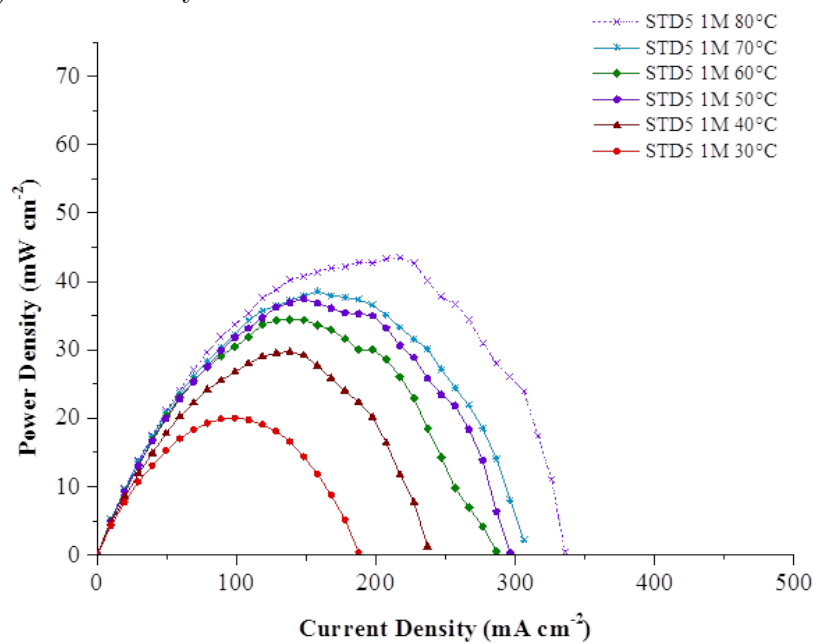


FIGURE A.8: The Performance of STD1 at different air flow rates (400-2000 cm³ min⁻¹)

(A) Power density curve



(B) Polarization curve

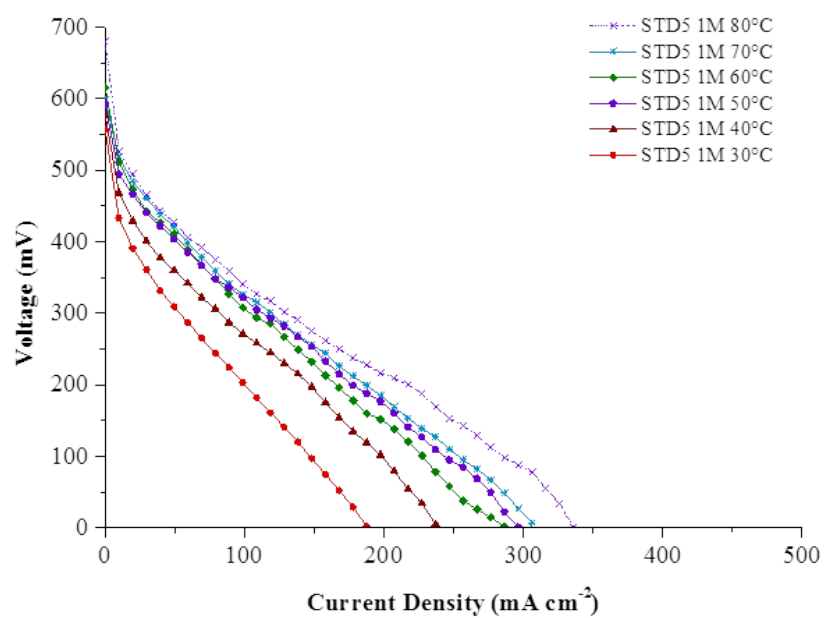
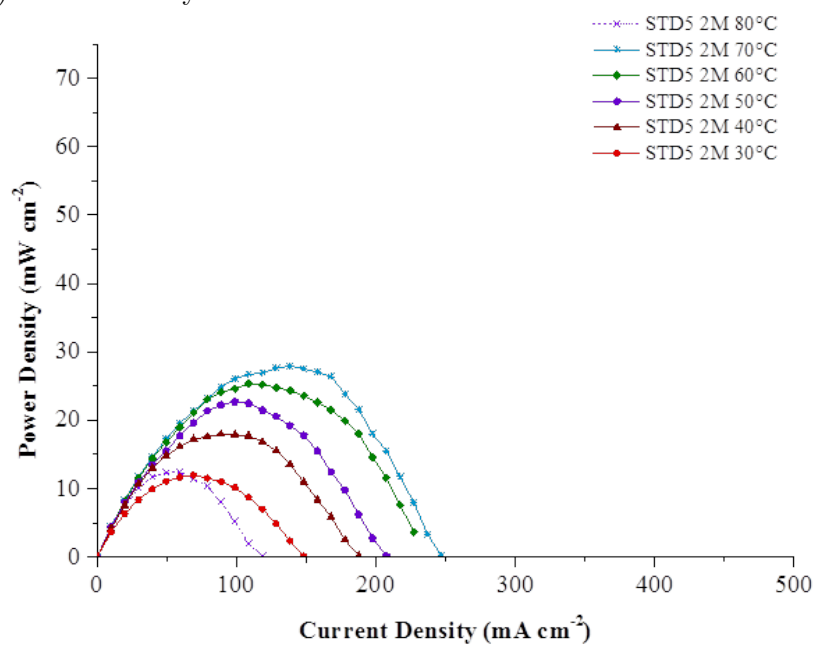


FIGURE A.9: Performance of STD5 at 1 M methanol

(A) Power density curve



(B) Polarization curve

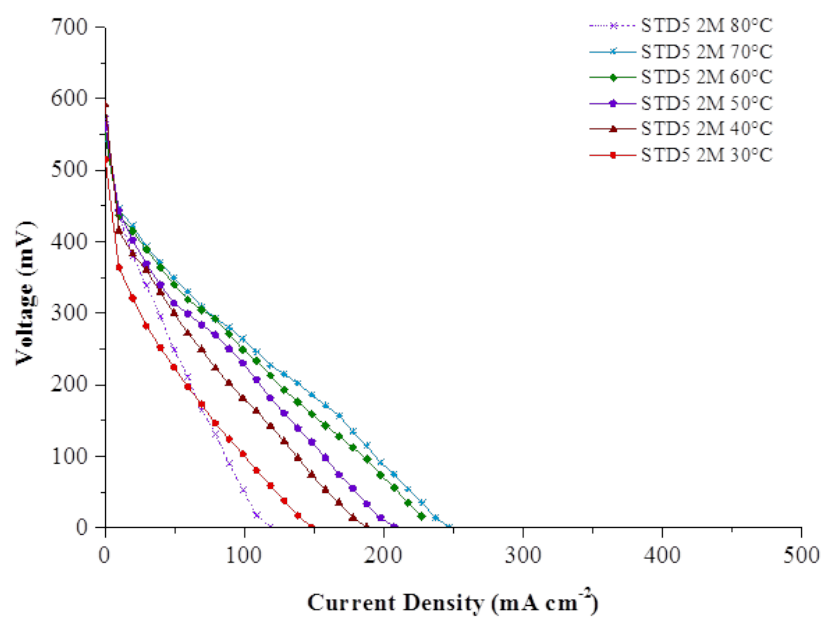
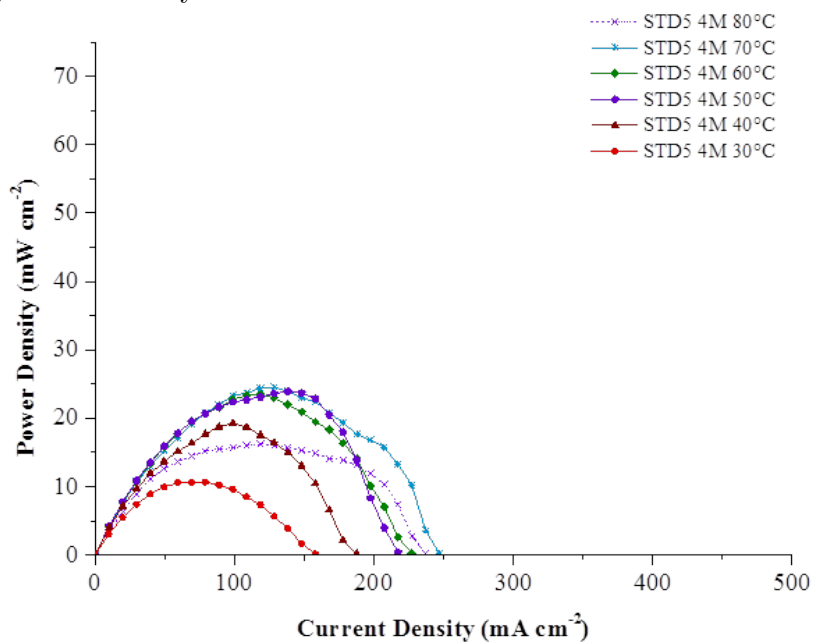


FIGURE A.10: Performance of STD5 at 2 M methanol

(A) Power density curve



(B) Polarization curve

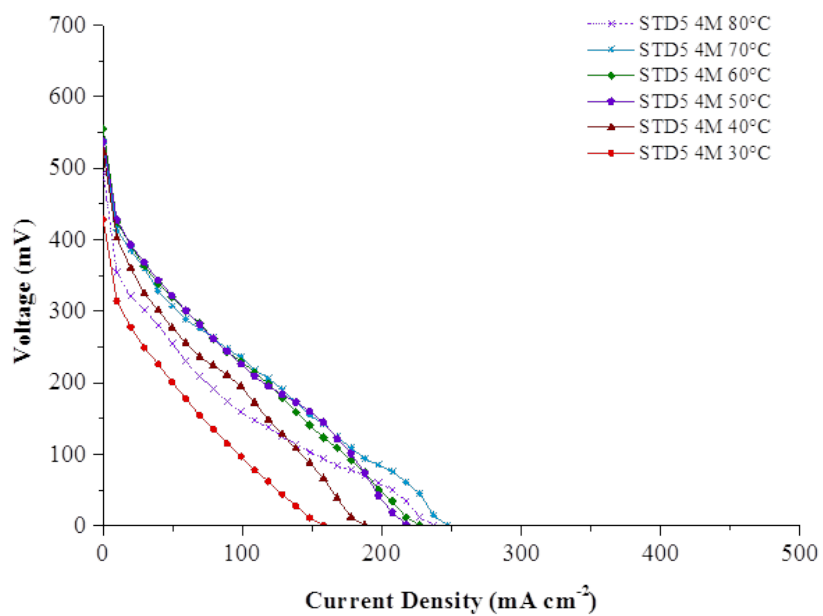


FIGURE A.11: Performance of STD5 at 4 M methanol

A.1.4 Performances of standard membrane electrode assemblies

TABLE A.1: Performances of Standard 1 (STD1)

| Methanol concentration Molar (M) | Temperature °C | Open circuit voltage (mV) | Maximum power density (mW cm ⁻²) | Limiting current density (mA cm ⁻²) |
|--|--------------------------|-------------------------------------|--|---|
| 1 | 30 | 584 | 14.07 | 79.01 |
| | 40 | 594 | 21.29 | 108.64 |
| | 50 | 596 | 25.28 | 128.40 |
| | 60 | 597 | 30.58 | 138.27 |
| | 70 | 599 | 36.50 | 177.78 |
| | 80 | 615 | 42.96 | 217.28 |
| 2 | 30 | 532 | 17.16 | 167.9 |
| | 40 | 545 | 22.82 | 187.65 |
| | 50 | 562 | 30.34 | 217.28 |
| | 60 | 558 | 34.22 | 266.67 |
| | 70 | 566 | 37.78 | 286.42 |
| | 80 | 578 | 37.14 | 276.54 |
| 4 | 30 | 483 | 12.48 | 167.9 |
| | 40 | 510 | 17.69 | 177.78 |
| | 50 | 541 | 23.37 | 187.65 |
| | 60 | 551 | 25.32 | 207.41 |
| | 70 | 551 | 28.21 | 227.16 |
| | 80 | 569 | 28.80 | 207.41 |

TABLE A.2: Performances of Standard 2 (STD2)

| Methanol concentration Molar (M) | Temperature °C | Open circuit voltage (mV) | Maximum power density (mW cm⁻²) | Limiting current density (mA cm⁻²) |
|---|---------------------------|--|---|--|
| 1 | 30 | 463 | 5.78 | 49.38 |
| | 40 | 513 | 10.84 | 79.01 |
| | 50 | 512 | 17.24 | 128.40 |
| | 60 | 555 | 24.30 | 148.15 |
| | 70 | 547 | 28.56 | 197.53 |
| | 80 | 545 | 27.48 | 187.65 |
| 2 | 30 | 456 | 9.26 | 108.64 |
| | 40 | 478 | 15.82 | 148.15 |
| | 50 | 502 | 21.29 | 197.53 |
| | 60 | 512 | 30.14 | 256.79 |
| | 70 | 521 | 36.27 | 306.17 |
| | 80 | 517 | 35.43 | 296.30 |
| 4 | 30 | 435 | 11.06 | 128.40 |
| | 40 | 470 | 15.70 | 167.90 |
| | 50 | 479 | 20.32 | 197.53 |
| | 60 | 478 | 24.06 | 217.28 |
| | 70 | 477 | 25.24 | 237.04 |
| | 80 | 476 | 24.65 | 217.28 |

TABLE A.3: Performances of Standard 3 (STD3)

| Methanol concentration Molar (M) | Temperature °C | Open circuit voltage (mV) | Maximum power density (mW cm⁻²) | Limiting current density (mA cm⁻²) |
|---|---------------------------|--|---|--|
| 1 | 30 | 598 | 19.91 | 158.02 |
| | 40 | 608 | 28.80 | 217.28 |
| | 50 | 623 | 37.63 | 256.79 |
| | 60 | 629 | 46.04 | 316.05 |
| | 70 | 639 | 55.17 | 365.43 |
| | 80 | 649 | 62.92 | 414.81 |
| 2 | 30 | 586 | 24.30 | 237.04 |
| | 40 | 609 | 35.60 | 286.42 |
| | 50 | 622 | 45.04 | 316.05 |
| | 60 | 632 | 55.19 | 355.56 |
| | 70 | 634 | 63.46 | 395.06 |
| | 80 | 634 | 67.28 | 424.69 |
| 4 | 30 | 532 | 16.00 | 197.53 |
| | 40 | 547 | 20.80 | 207.41 |
| | 50 | 561 | 25.30 | 237.04 |
| | 60 | 569 | 28.15 | 256.79 |
| | 70 | 570 | 30.81 | 276.54 |
| | 80 | 559 | 30.66 | 306.17 |

TABLE A.4: Performances of Standard 4 (STD4)

| Methanol concentration Molar (M) | Temperature °C | Open circuit voltage (mV) | Maximum power density (mW cm⁻²) | Limiting current density (mA cm⁻²) |
|---|---------------------------|--|---|--|
| 1 | 30 | 571 | 20.98 | 158.02 |
| | 40 | 591 | 29.39 | 197.53 |
| | 50 | 605 | 38.22 | 256.79 |
| | 60 | 617 | 47.29 | 306.17 |
| | 70 | 625 | 55.19 | 345.68 |
| | 80 | 632 | 62.58 | 395.06 |

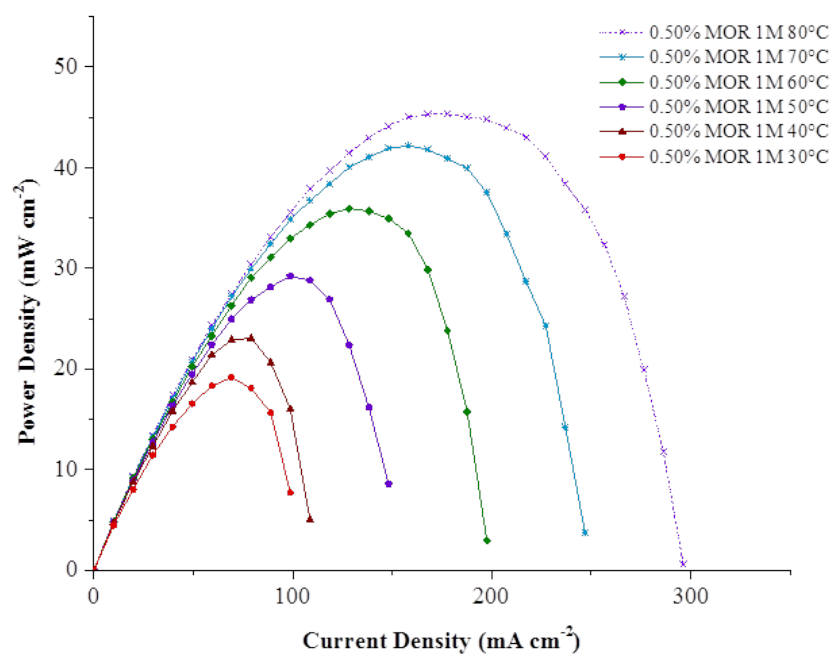
TABLE A.5: Performances of Standard 5 (STD5)

| Methanol concentration Molar (M) | Temperature °C | Open circuit voltage (mV) | Maximum power density (mW cm ⁻²) | Limiting current density (mA cm ⁻²) |
|--|-------------------|---------------------------------|--|---|
| 1 | 30 | 557 | 20.05 | 187.65 |
| | 40 | 577 | 29.73 | 237.04 |
| | 50 | 593 | 37.48 | 296.30 |
| | 60 | 615 | 34.43 | 286.42 |
| | 70 | 599 | 38.56 | 306.17 |
| | 80 | 679 | 43.46 | 335.80 |
| 2 | 30 | 515 | 11.96 | 148.15 |
| | 40 | 591 | 17.96 | 187.65 |
| | 50 | 562 | 22.72 | 207.41 |
| | 60 | 549 | 25.31 | 237.04 |
| | 70 | 547 | 27.93 | 246.91 |
| | 80 | 571 | 12.50 | 118.52 |
| 4 | 30 | 428 | 10.67 | 158.02 |
| | 40 | 522 | 19.26 | 187.65 |
| | 50 | 537 | 23.92 | 217.28 |
| | 60 | 555 | 23.47 | 227.16 |
| | 70 | 535 | 24.52 | 246.91 |
| | 80 | 493 | 16.24 | 237.04 |

A.2 Experimental results of the modified membrane electrode assemblies

A.2.1 Polarization and power density curves of the modified membrane electrode assemblies at 1 M methanol concentration

(A) Power density curve



(B) Polarization curve

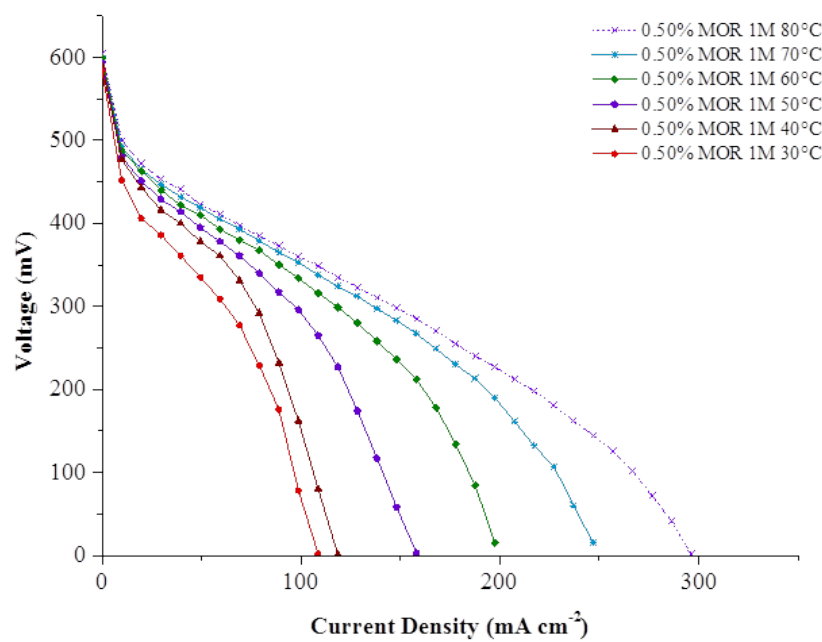
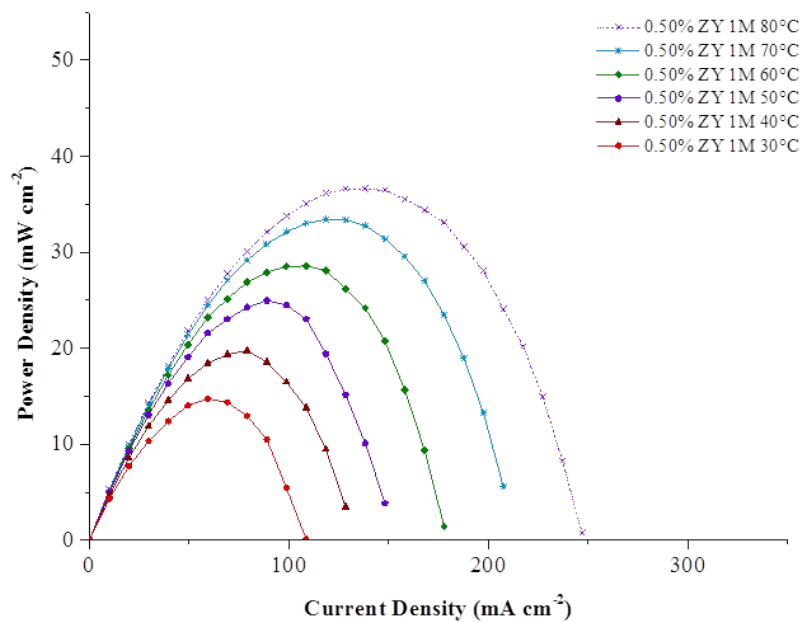


FIGURE A.12: Performance of 0.50% MOR at 1 M methanol

(A) Power density curve



(B) Polarization curve

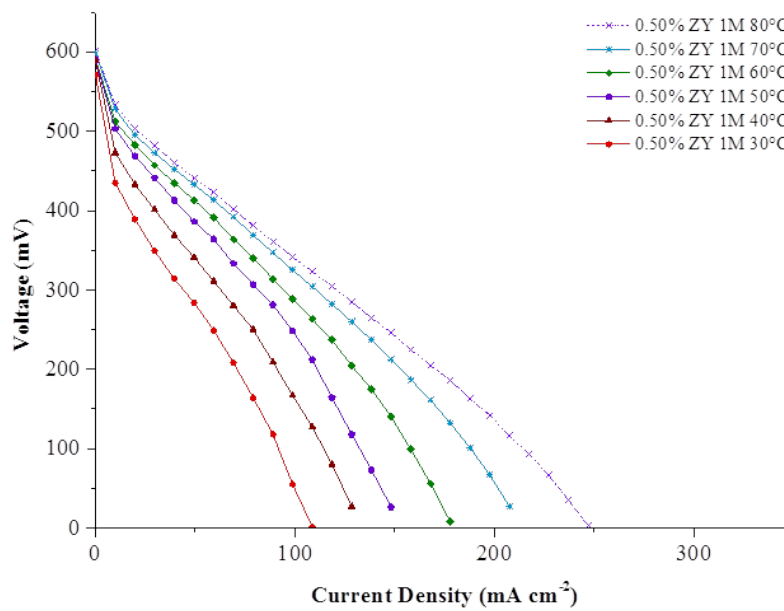
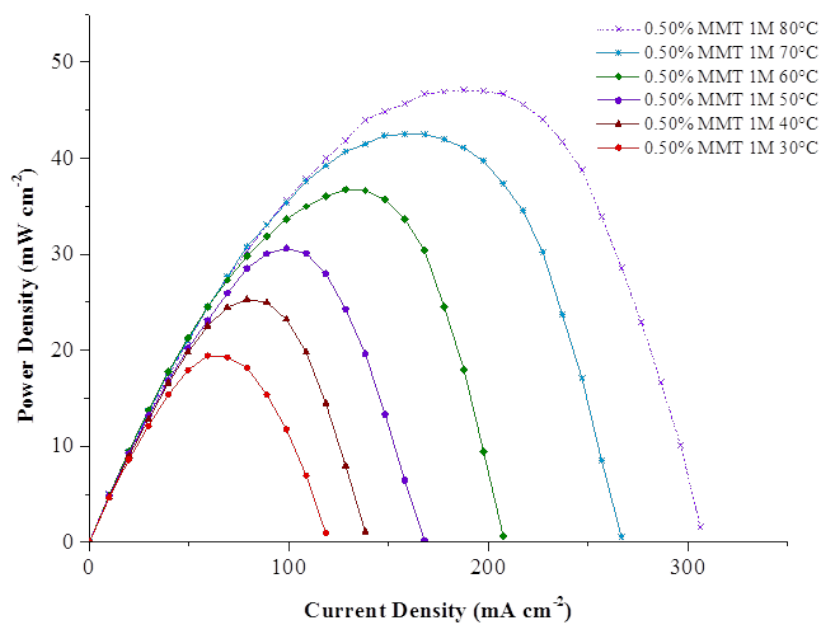


FIGURE A.13: Performance of 0.50% ZY at 1 M methanol

(A) Power density curve



(B) Polarization curve

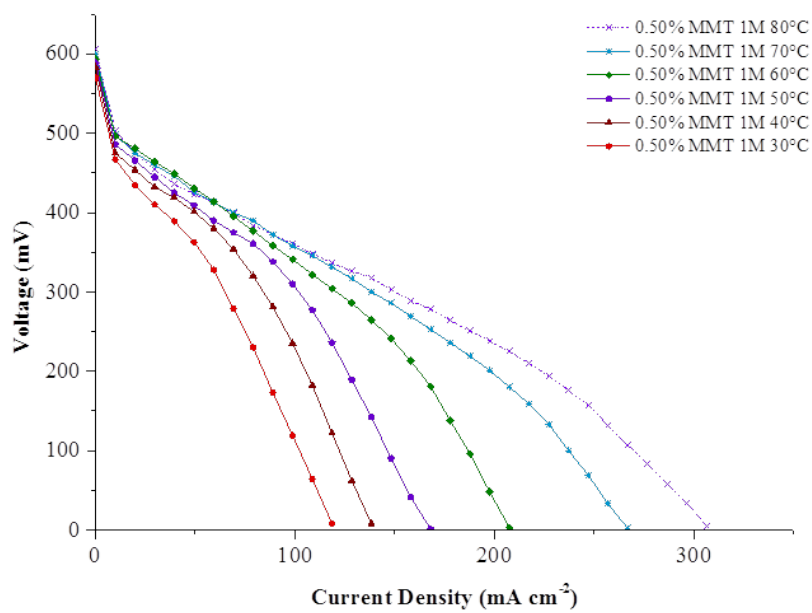
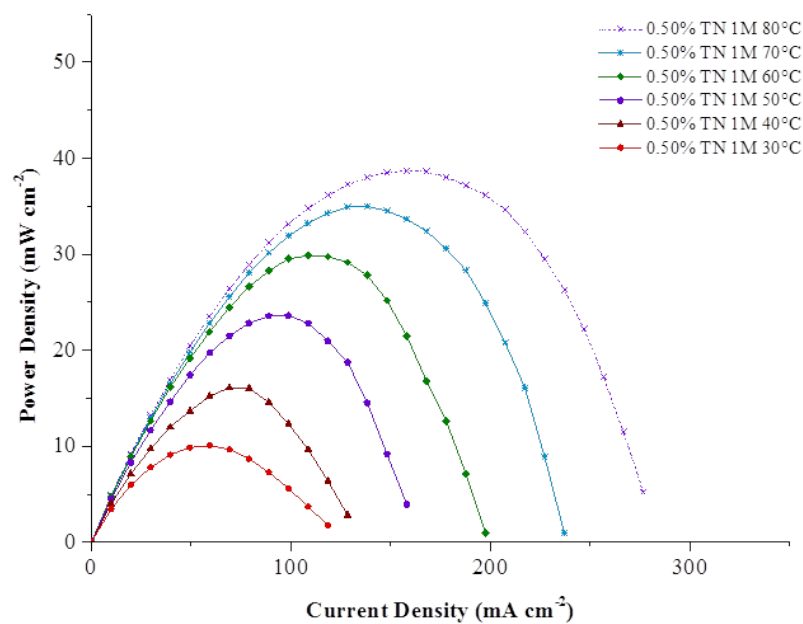


FIGURE A.14: Performance of 0.50% MMT at 1 M methanol

(A) Power density curve



(B) Polarization curve

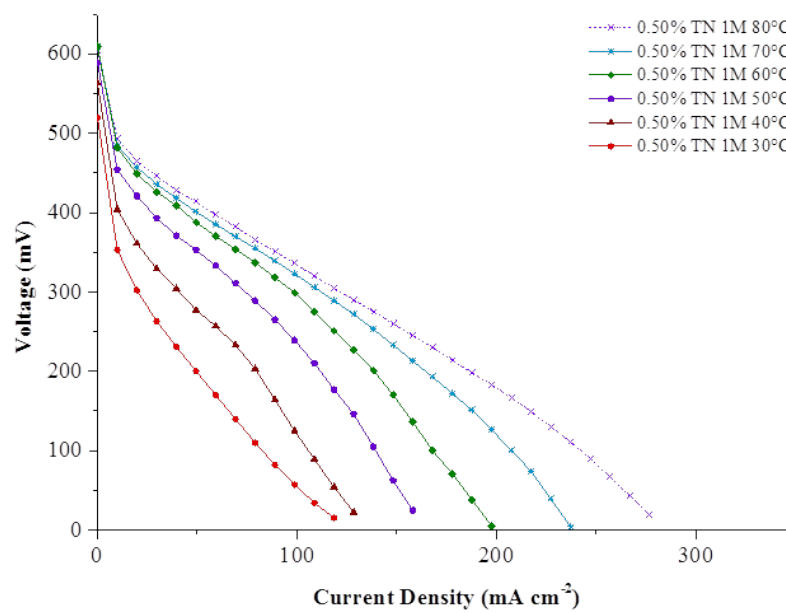
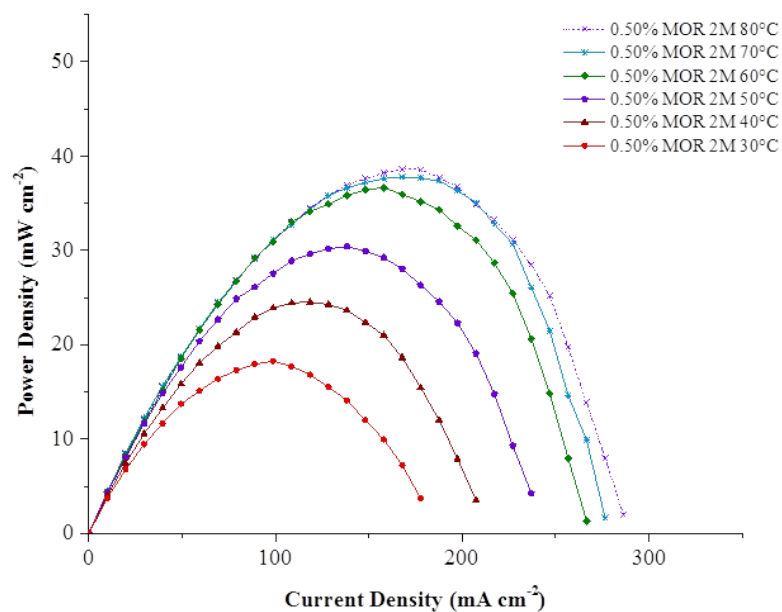


FIGURE A.15: Performance of 0.50% TN at 1 M methanol

A.2.2 Polarization and power density curves of the modified membrane electrode assemblies at 2 M methanol concentration

(A) Power density curve



(B) Polarization curve

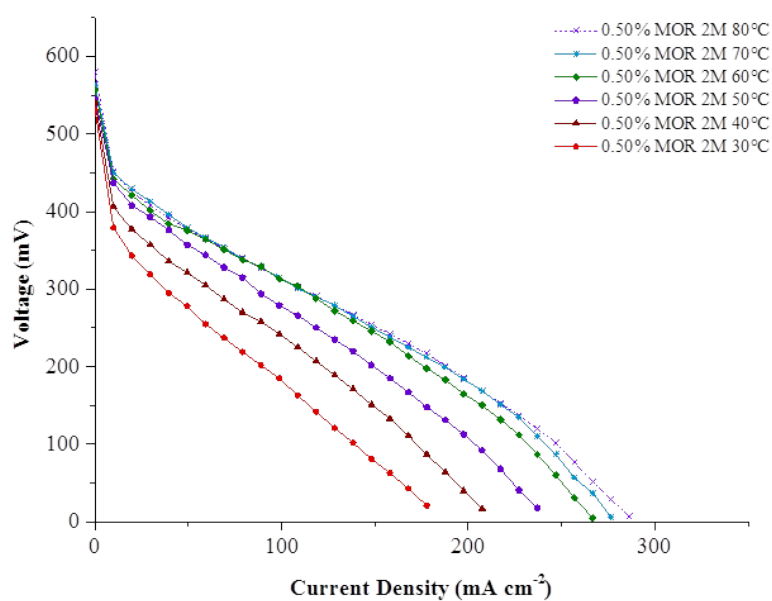
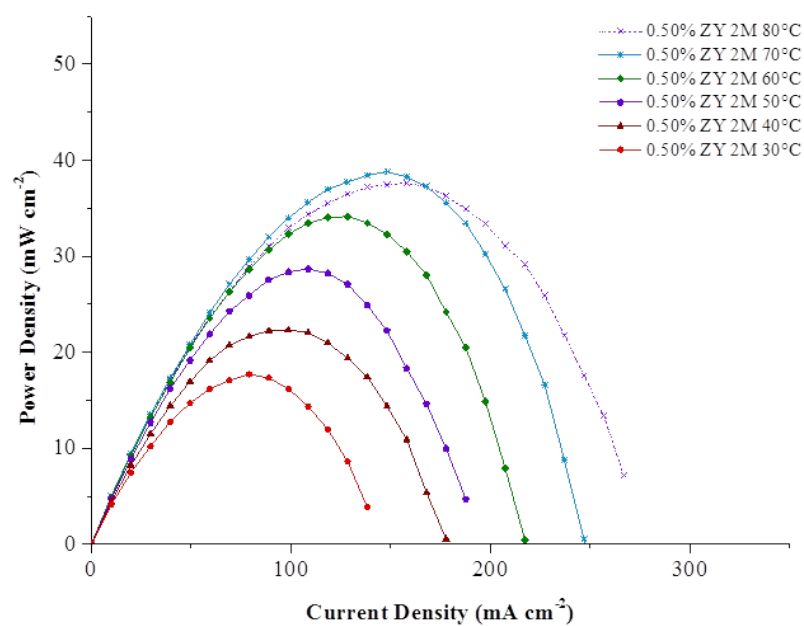


FIGURE A.16: Performance of 0.50% MOR at 2 M methanol

(A) Power density curve



(B) Polarization curve

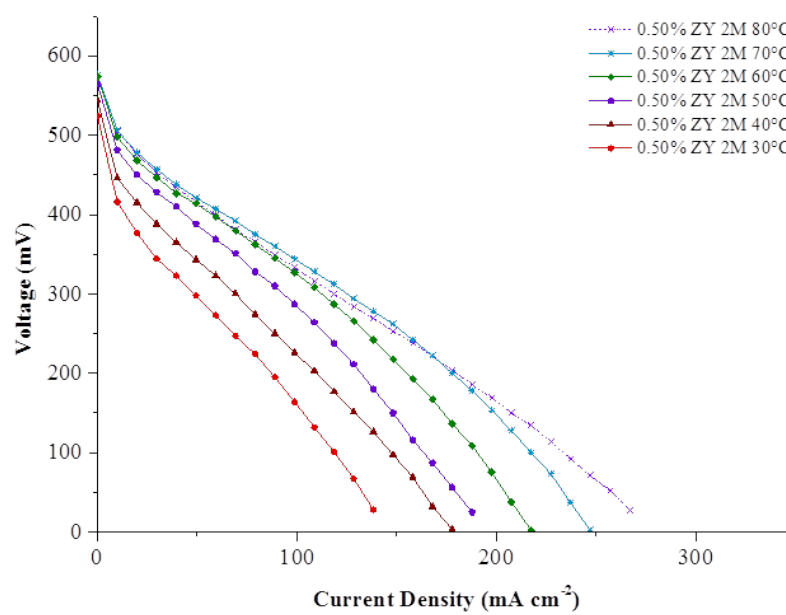
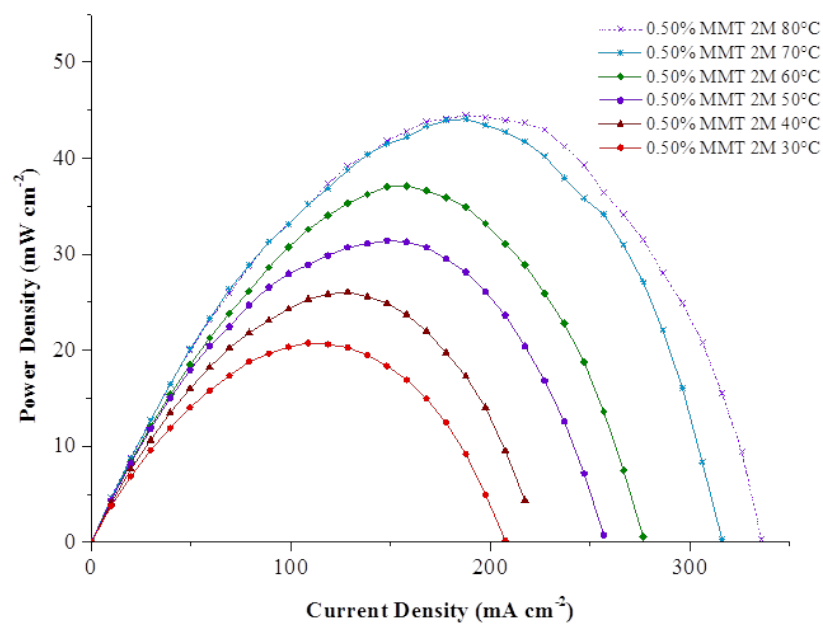


FIGURE A.17: Performance of 0.50% ZY at 2 M methanol

(A) Power density curve



(B) Polarization curve

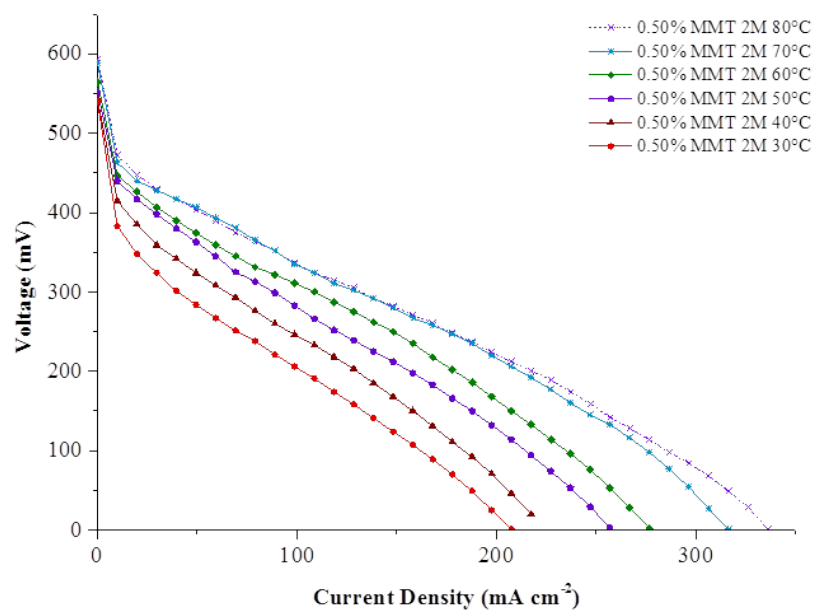
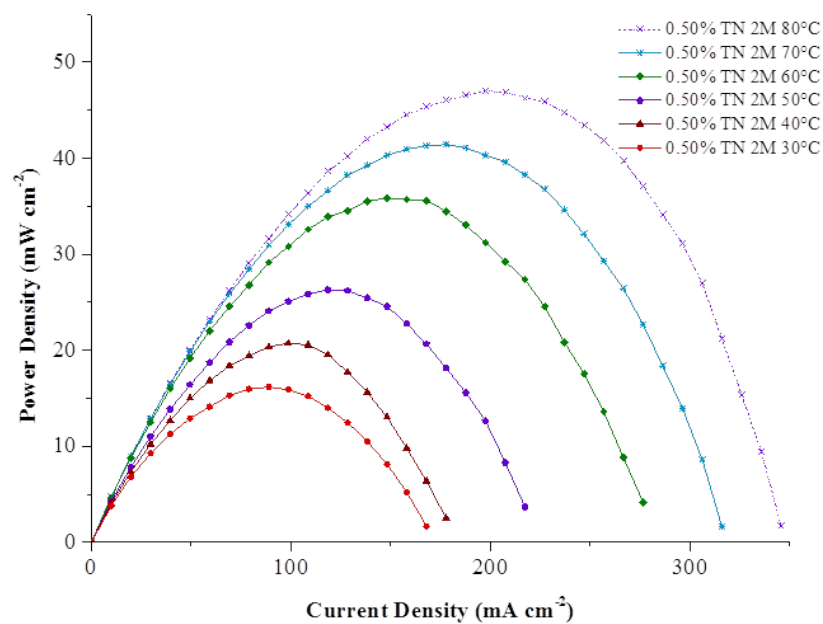


FIGURE A.18: Performance of 0.50% MMT at 2 M methanol

(A) Power density curve



(B) Polarization curve

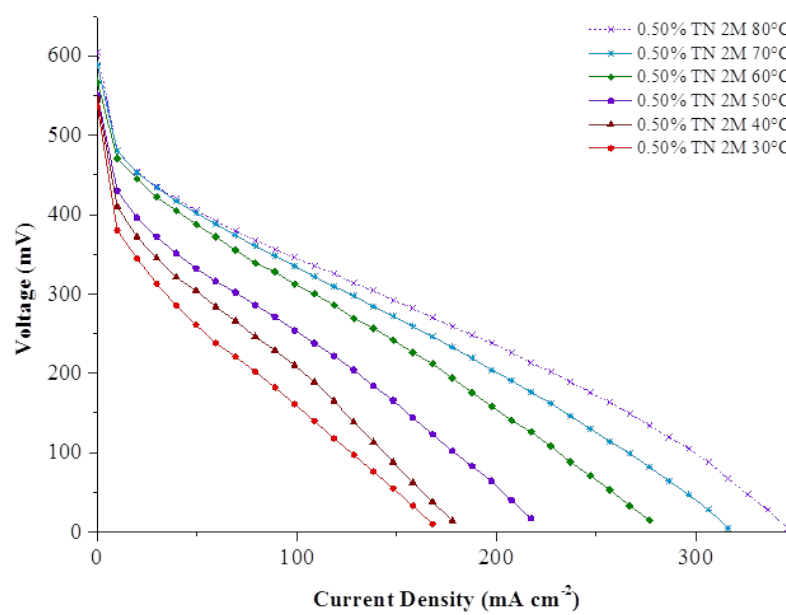
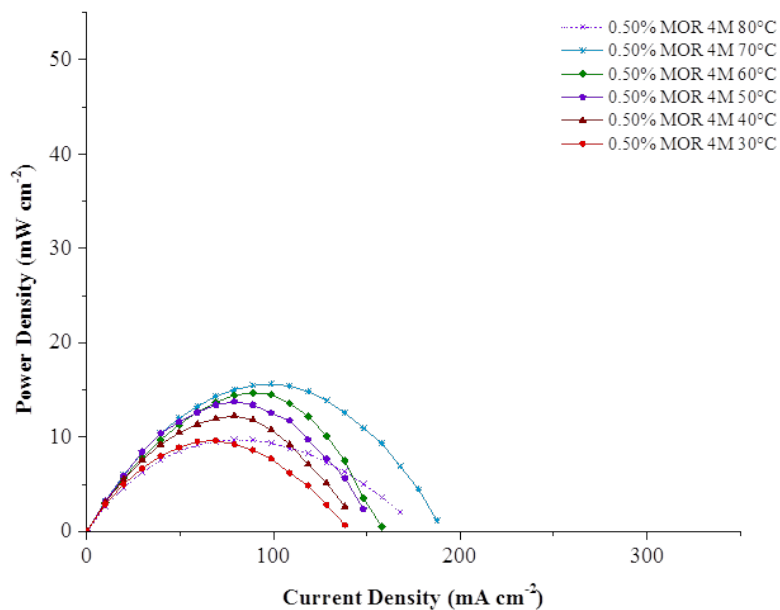


FIGURE A.19: Performance of 0.50% TN at 2 M methanol

A.2.3 Polarization and power density curves of the modified membrane electrode assemblies at 4 M methanol concentration

(A) Power density curve



(B) Polarization curve

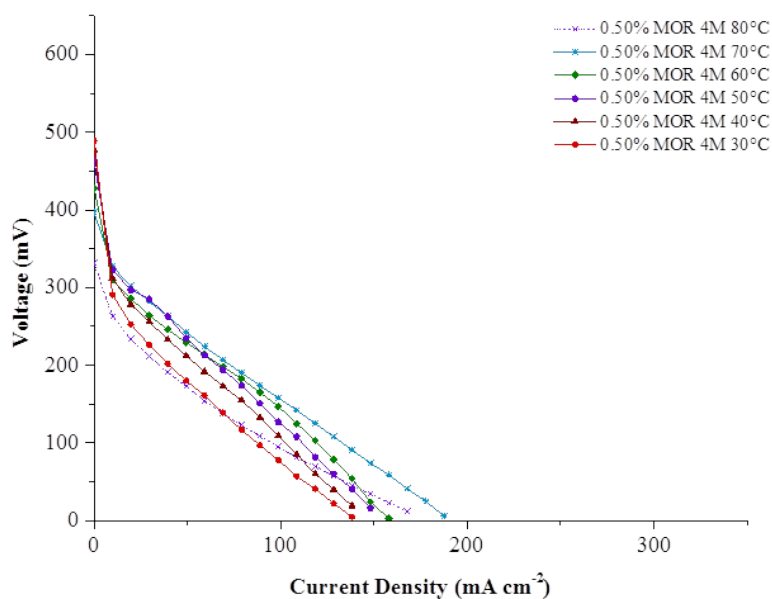
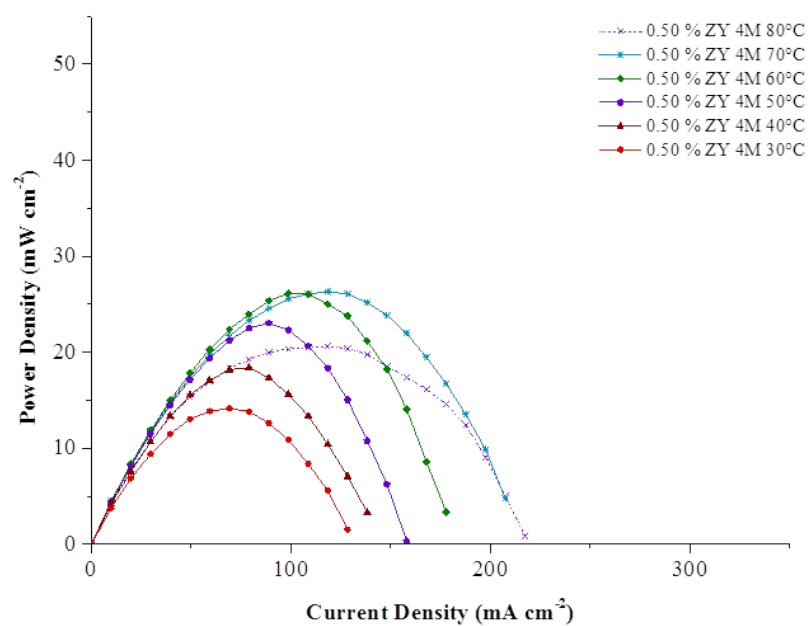


FIGURE A.20: Performance of 0.50% MOR at 4 M methanol

(A) Power density curve



(B) Polarization curve

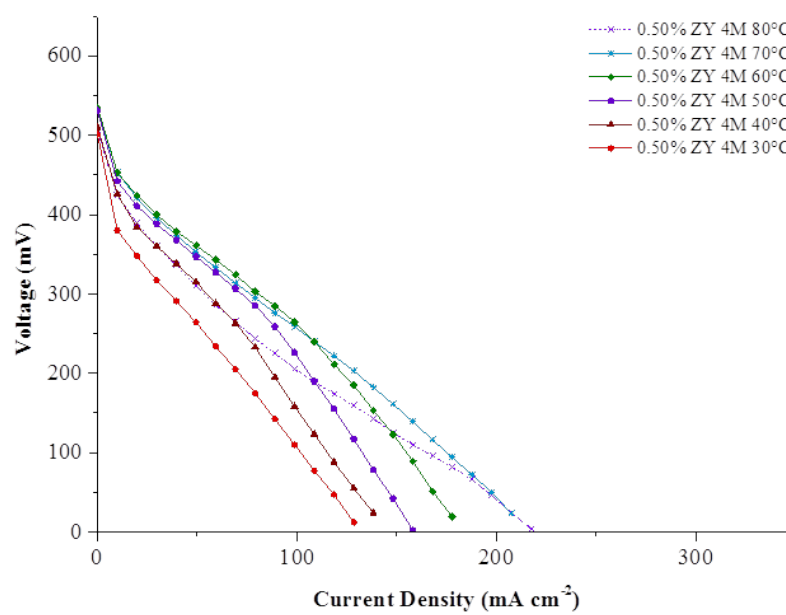
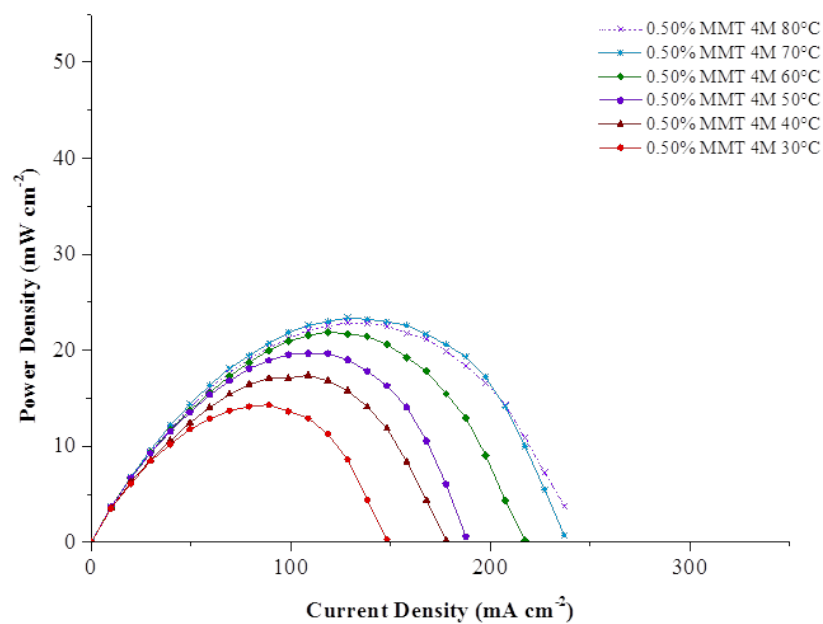


FIGURE A.21: Performance of 0.50% ZY at 4 M methanol

(A) Power density curve



(B) Polarization curve

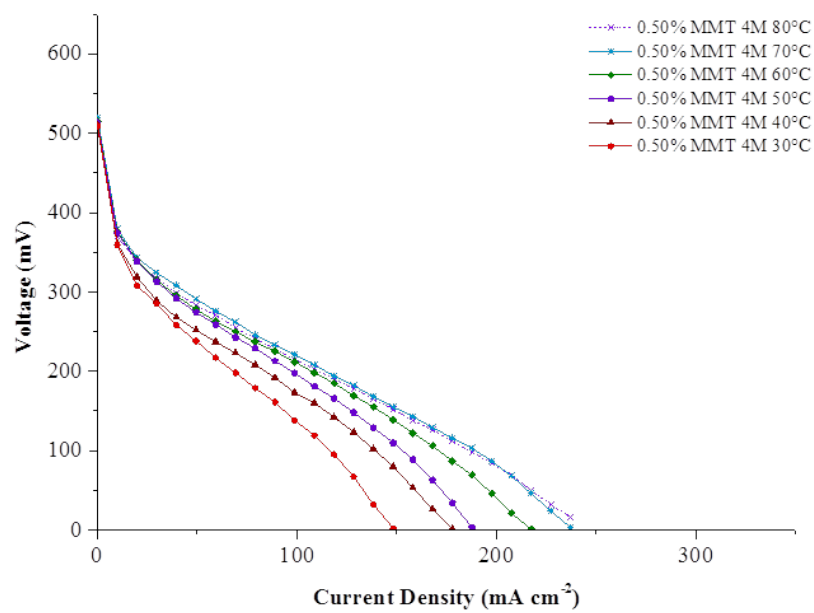
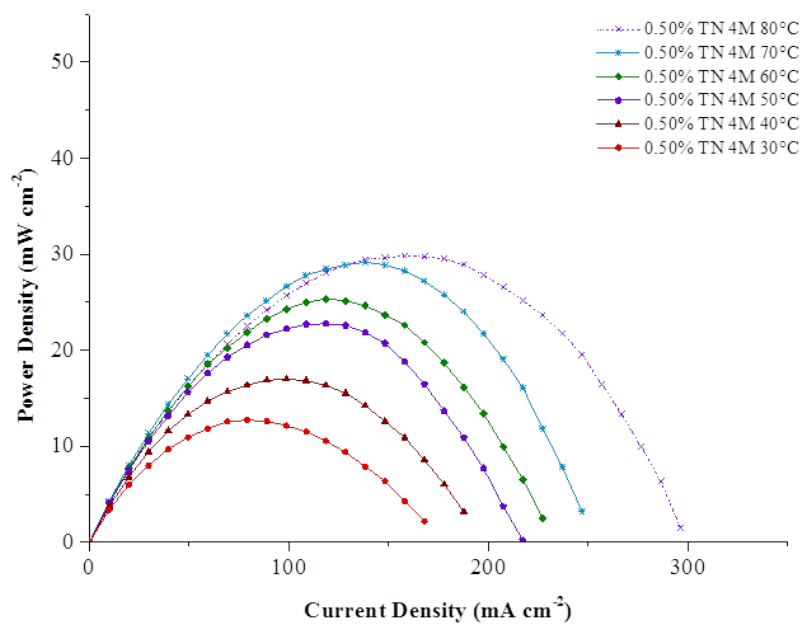


FIGURE A.22: Performance of 0.50% MMT at 4 M methanol

(A) Power density curve



(B) Polarization curve

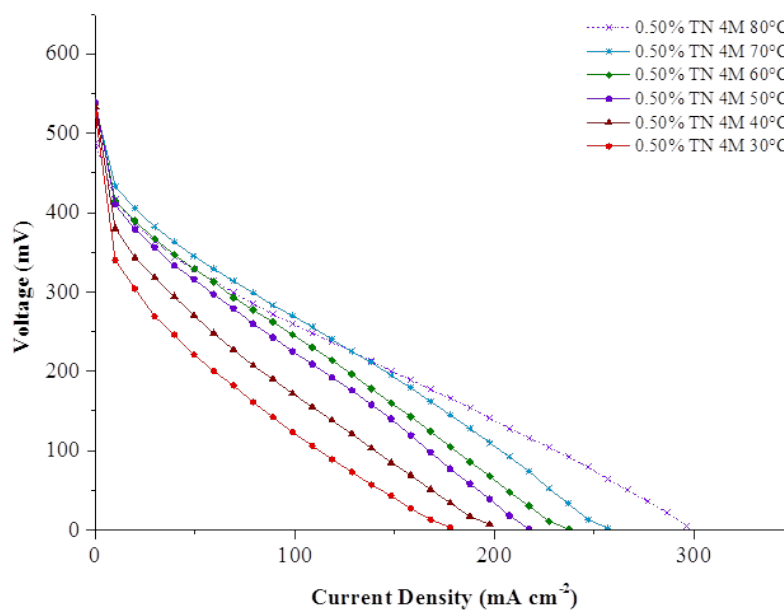


FIGURE A.23: Performance of 0.50% TN at 4 M methanol

A.2.4 Performances of the modified membrane electrode assemblies

TABLE A.6: Performances of the modified membrane electrode assemblies containing 0.50% mordenite (0.50% MOR)

| Methanol concentration Molar (M) | Temperature °C | Open circuit voltage (mV) | Maximum power density (mW cm ⁻²) | Limiting current density (mA cm ⁻²) |
|--|--------------------------|-------------------------------------|--|---|
| 1 | 30 | 583 | 19.15 | 98.77 |
| | 40 | 589 | 23.07 | 108.64 |
| | 50 | 593 | 29.23 | 148.15 |
| | 60 | 599 | 35.95 | 197.53 |
| | 70 | 598 | 42.19 | 246.91 |
| | 80 | 604 | 45.33 | 296.30 |
| 2 | 30 | 531 | 18.27 | 177.78 |
| | 40 | 540 | 24.53 | 207.41 |
| | 50 | 545 | 30.42 | 237.04 |
| | 60 | 557 | 36.66 | 266.67 |
| | 70 | 563 | 37.78 | 276.54 |
| | 80 | 579 | 38.62 | 286.42 |
| 4 | 30 | 489 | 9.61 | 138.27 |
| | 40 | 477 | 12.25 | 138.27 |
| | 50 | 463 | 13.75 | 148.15 |
| | 60 | 428 | 14.67 | 158.02 |
| | 70 | 397 | 15.60 | 187.65 |
| | 80 | 332 | 9.72 | 167.90 |

TABLE A.7: Performances of the modified membrane electrode assemblies containing 0.50% zeolite Y (0.50% ZY)

| Methanol concentration Molar (M) | Temperature °C | Open circuit voltage (mV) | Maximum power density (mW cm⁻²) | Limiting current density (mA cm⁻²) |
|---|---------------------------|--|---|--|
| 1 | 30 | 571 | 14.76 | 108.64 |
| | 40 | 589 | 19.75 | 128.40 |
| | 50 | 590 | 24.98 | 148.15 |
| | 60 | 591 | 28.57 | 177.78 |
| | 70 | 598 | 33.42 | 207.41 |
| | 80 | 602 | 36.64 | 246.91 |
| 2 | 30 | 524 | 17.70 | 138.27 |
| | 40 | 544 | 22.32 | 177.78 |
| | 50 | 564 | 28.68 | 187.65 |
| | 60 | 574 | 34.15 | 217.28 |
| | 70 | 576 | 38.81 | 246.91 |
| | 80 | 576 | 37.61 | 266.67 |
| 4 | 30 | 501 | 14.17 | 128.4 |
| | 40 | 510 | 18.41 | 138.27 |
| | 50 | 531 | 23.02 | 158.02 |
| | 60 | 535 | 26.17 | 177.78 |
| | 70 | 533 | 26.31 | 207.41 |
| | 80 | 507 | 20.62 | 217.28 |

TABLE A.8: Performances of the modified membrane electrode assemblies containing 0.50% montmorillonite (0.50% MMT)

| Methanol concentration Molar (M) | Temperature °C | Open circuit voltage (mV) | Maximum power density (mW cm ⁻²) | Limiting current density (mA cm ⁻²) |
|--|--------------------------|-------------------------------------|--|---|
| 1 | 30 | 570 | 19.44 | 118.52 |
| | 40 | 583 | 25.28 | 138.27 |
| | 50 | 589 | 30.62 | 167.90 |
| | 60 | 593 | 36.72 | 207.41 |
| | 70 | 599 | 42.51 | 266.67 |
| | 80 | 606 | 47.10 | 306.17 |
| 2 | 30 | 540 | 20.75 | 207.41 |
| | 40 | 543 | 26.06 | 217.28 |
| | 50 | 552 | 31.41 | 256.79 |
| | 60 | 565 | 37.14 | 276.54 |
| | 70 | 588 | 44.10 | 316.05 |
| | 80 | 594 | 44.47 | 335.80 |
| 4 | 30 | 509 | 14.31 | 148.15 |
| | 40 | 510 | 17.38 | 177.78 |
| | 50 | 513 | 19.67 | 187.65 |
| | 60 | 515 | 21.93 | 217.28 |
| | 70 | 519 | 23.37 | 237.04 |
| | 80 | 510 | 22.85 | 237.04 |

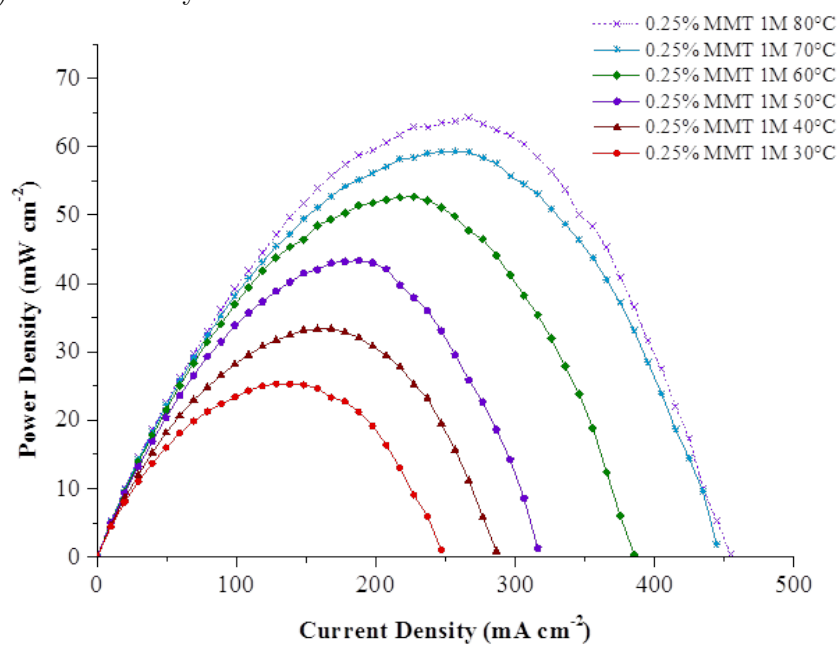
TABLE A.9: Performances of the modified membrane electrode assemblies containing 0.50% titanate (0.50% TN)

| Methanol concentration Molar (M) | Temperature °C | Open circuit voltage (mV) | Maximum power density (mW cm ⁻²) | Limiting current density (mA cm ⁻²) |
|--|--------------------------|-------------------------------------|--|---|
| 1 | 30 | 520 | 10.07 | 118.52 |
| | 40 | 563 | 16.11 | 128.40 |
| | 50 | 589 | 23.60 | 158.02 |
| | 60 | 609 | 29.88 | 197.53 |
| | 70 | 609 | 34.98 | 237.04 |
| | 80 | 604 | 38.72 | 276.54 |
| 2 | 30 | 536 | 16.18 | 167.90 |
| | 40 | 545 | 20.74 | 177.78 |
| | 50 | 550 | 26.31 | 217.28 |
| | 60 | 567 | 35.85 | 276.54 |
| | 70 | 588 | 41.42 | 316.05 |
| | 80 | 605 | 47.01 | 345.68 |
| 4 | 30 | 524 | 12.72 | 167.90 |
| | 40 | 533 | 16.99 | 187.65 |
| | 50 | 539 | 22.76 | 217.28 |
| | 60 | 538 | 25.36 | 227.16 |
| | 70 | 534 | 29.18 | 246.91 |
| | 80 | 487 | 29.87 | 296.30 |

A.3 Experimental results of the new modified membrane electrode assemblies

A.3.1 Polarization and power density curves of the new modified membrane electrode assemblies at 1 M methanol concentration

(A) Power density curve



(B) Polarization curve

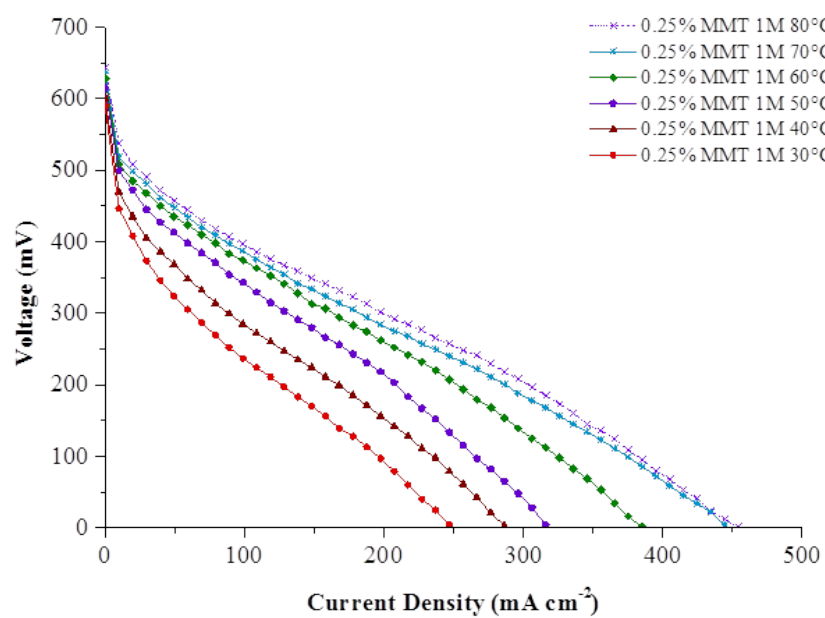
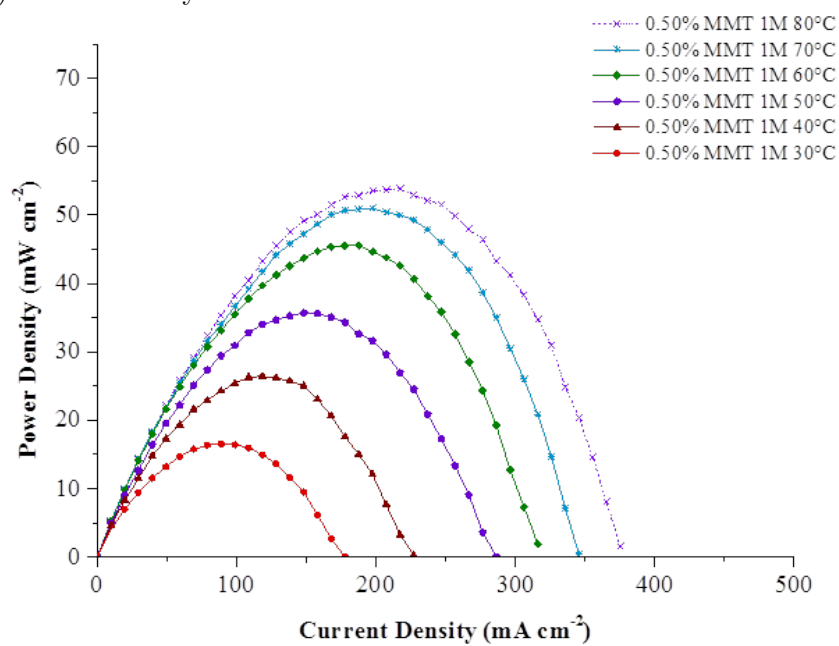


FIGURE A.24: Performance of 0.25% MMT at 1 M methanol

(A) Power density curve



(B) Polarization curve

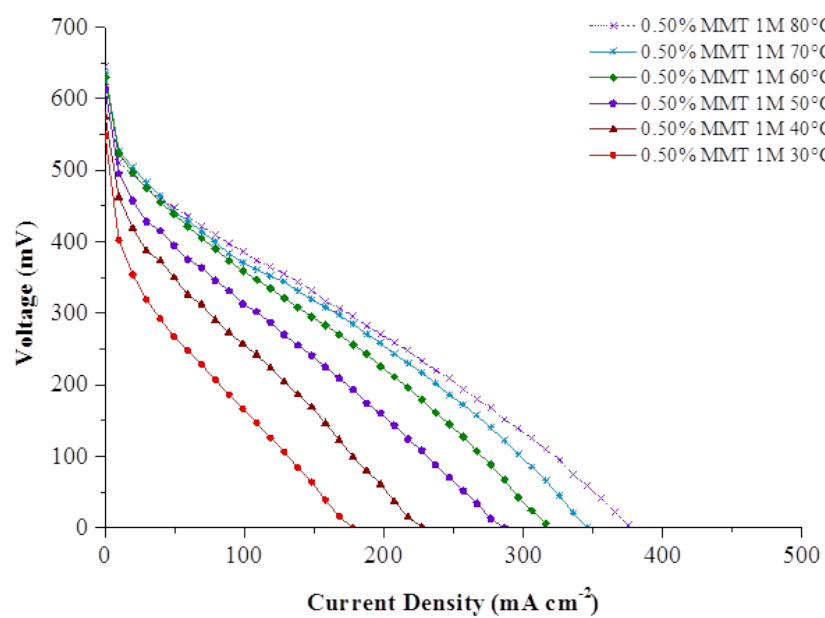
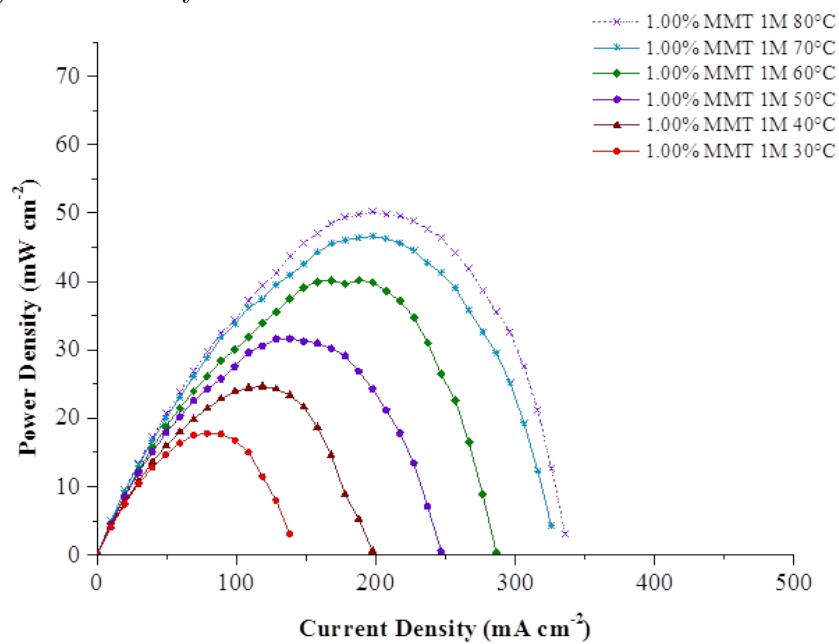


FIGURE A.25: Performance of 0.50% MMT at 1 M methanol

(A) Power density curve



(B) Polarization curve

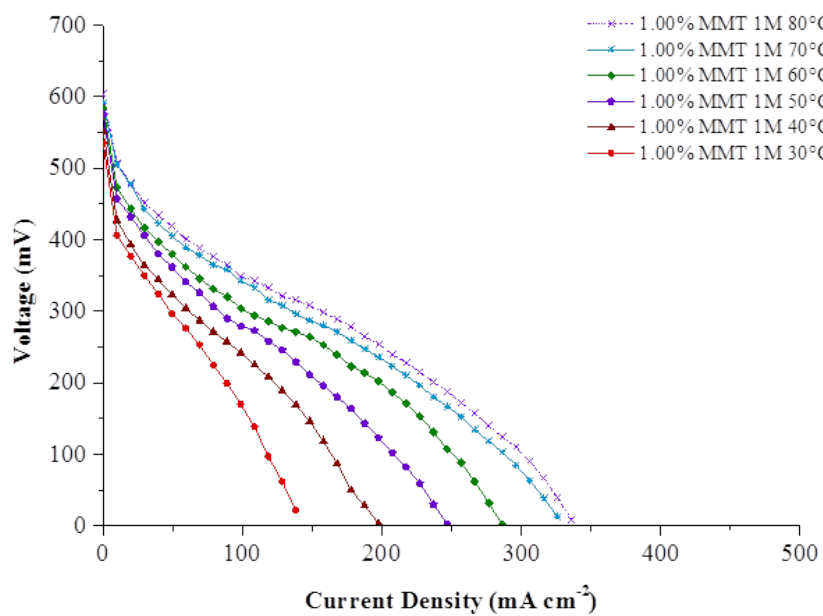
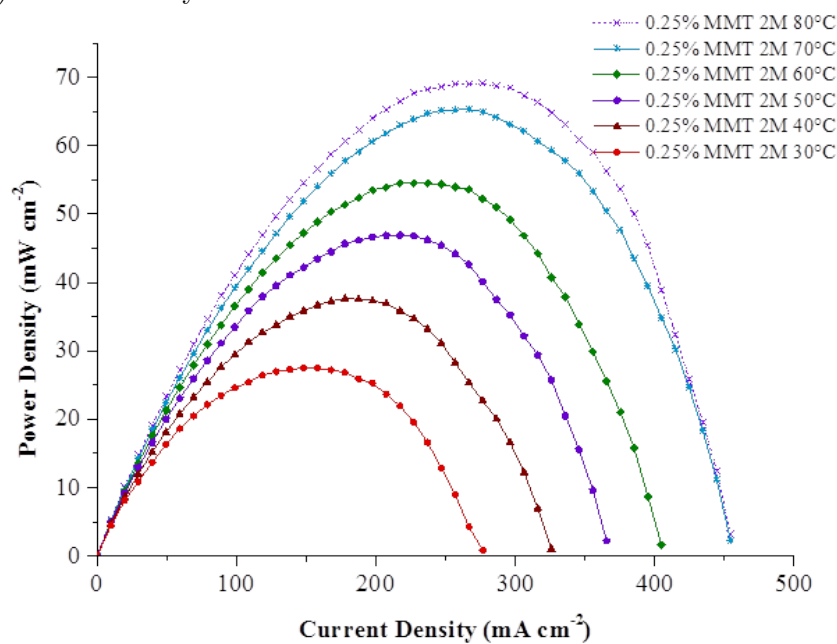


FIGURE A.26: Performance of 1.00% MMT at 1 M methanol

A.3.2 Polarization and power density curves of the new modified membrane electrode assemblies at 2 M methanol concentration

(A) Power density curve



(B) Polarization curve

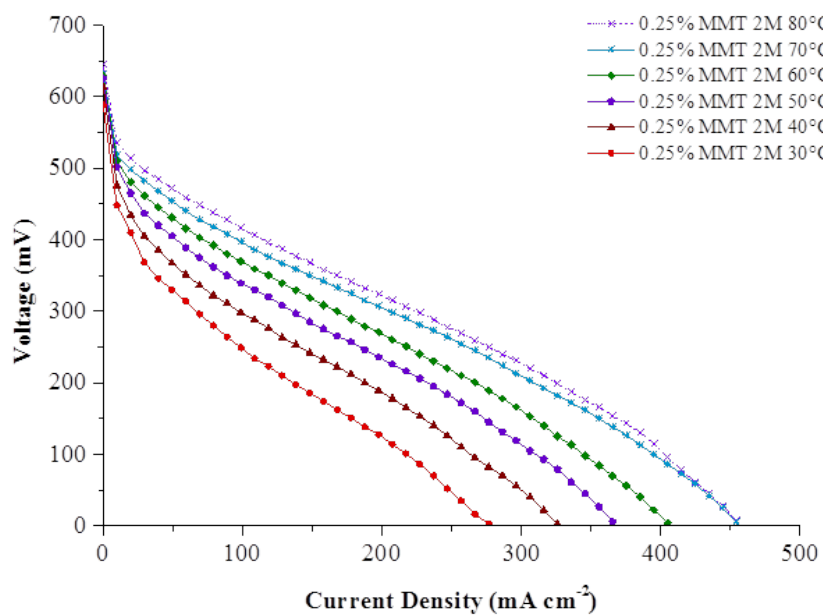
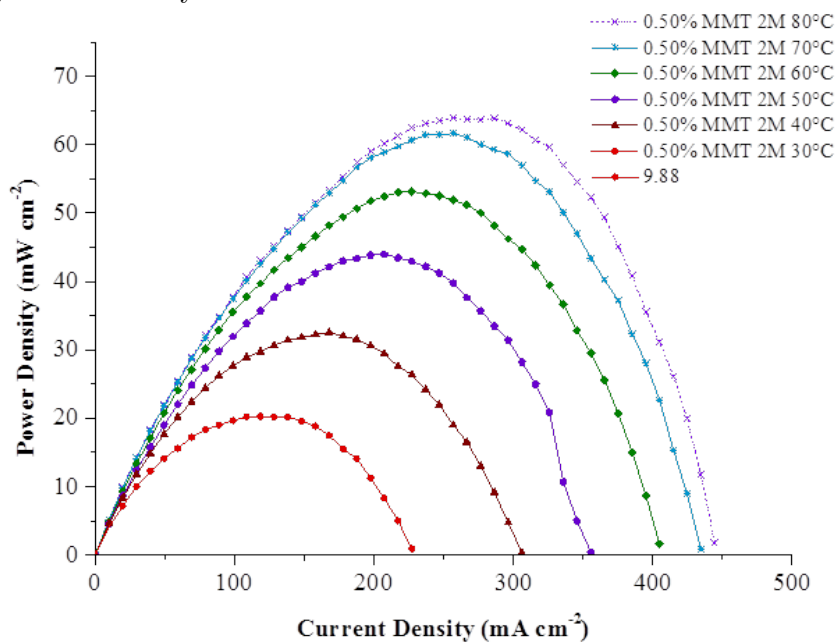


FIGURE A.27: Performance of 0.25% MMT at 2 M methanol

(A) Power density curve



(B) Polarization curve

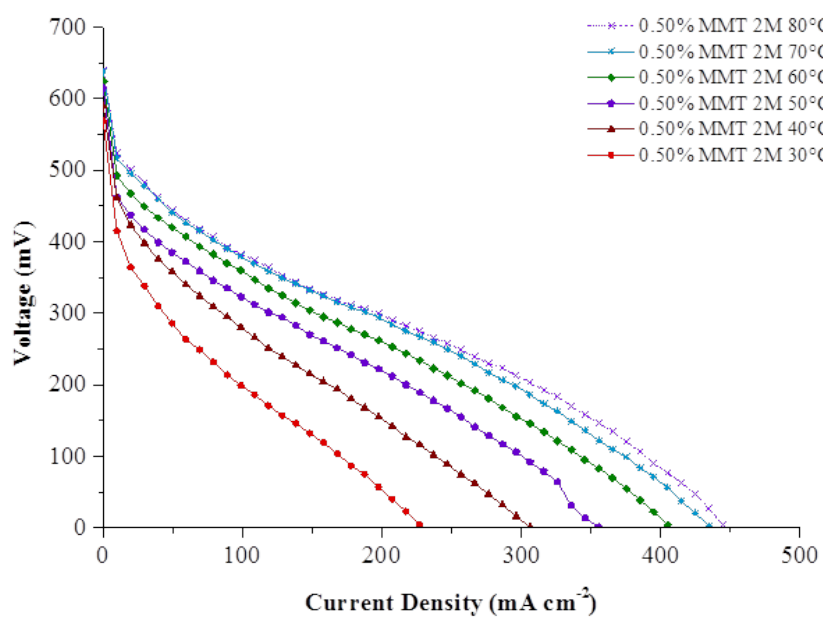
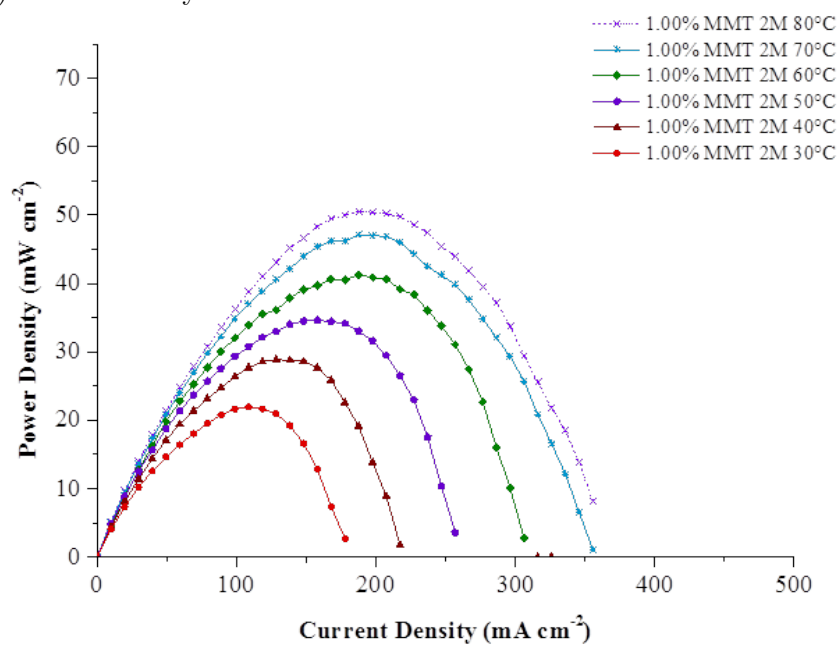


FIGURE A.28: Performance of 0.50% MMT at 2 M methanol

(A) Power density curve



(B) Polarization curve

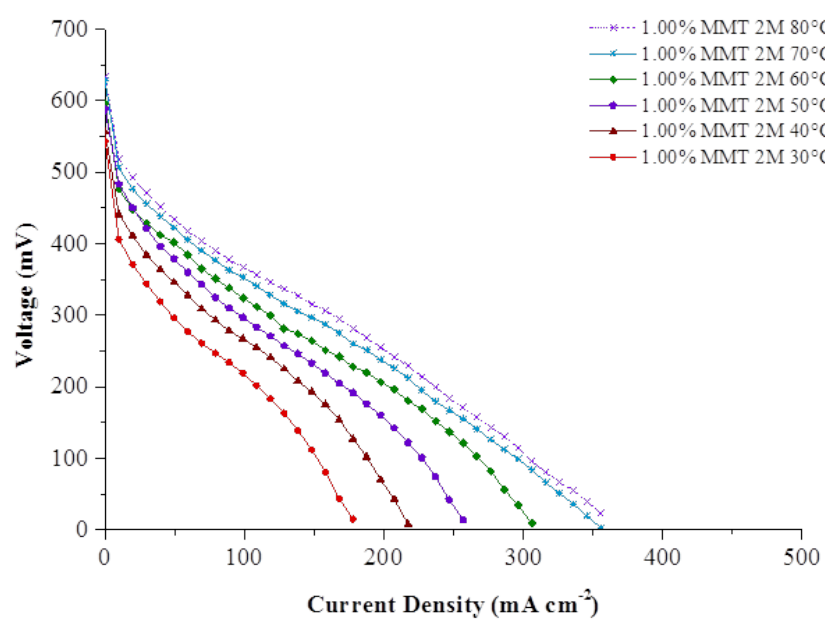
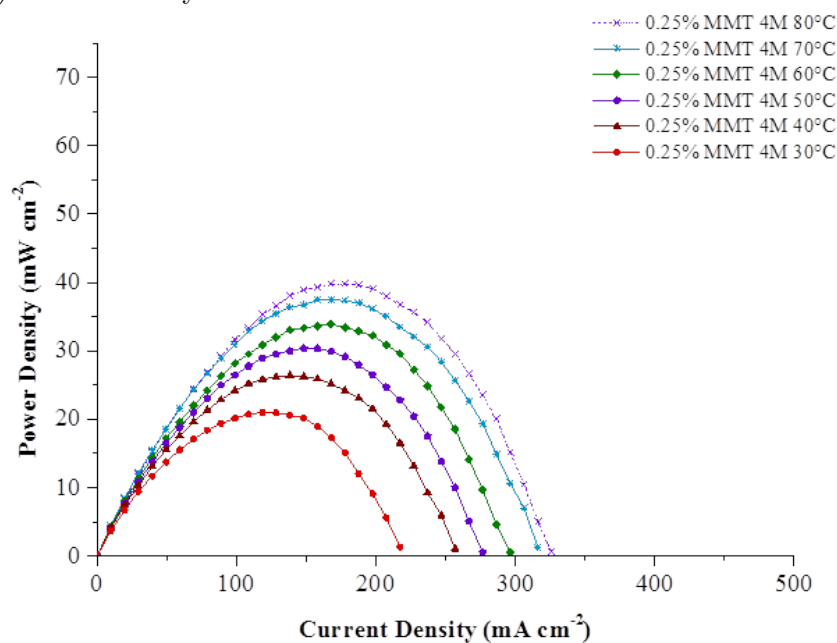


FIGURE A.29: Performance of 1.00%MMT at 2 M methanol

A.3.3 Polarization and power density curves of the new modified membrane electrode assemblies at 4 M methanol concentration

(A) Power density curve



(B) Polarization curve

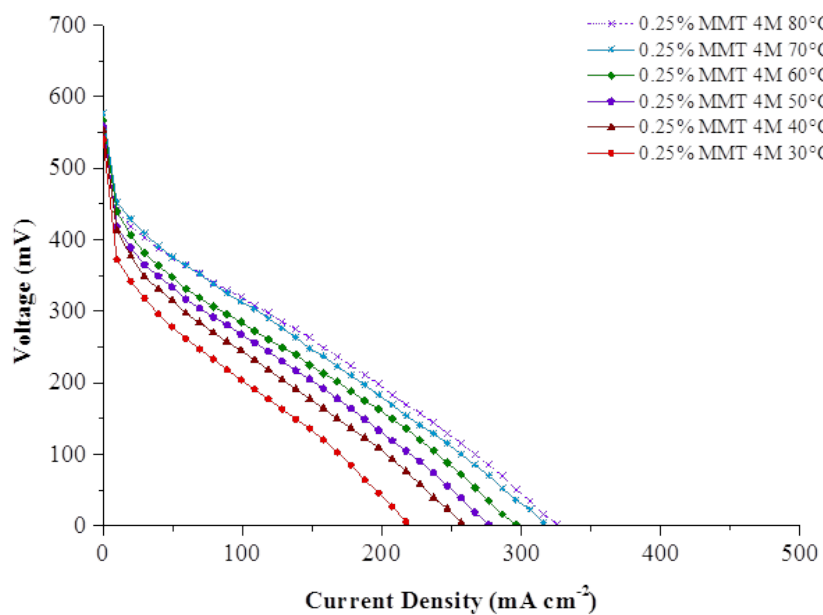
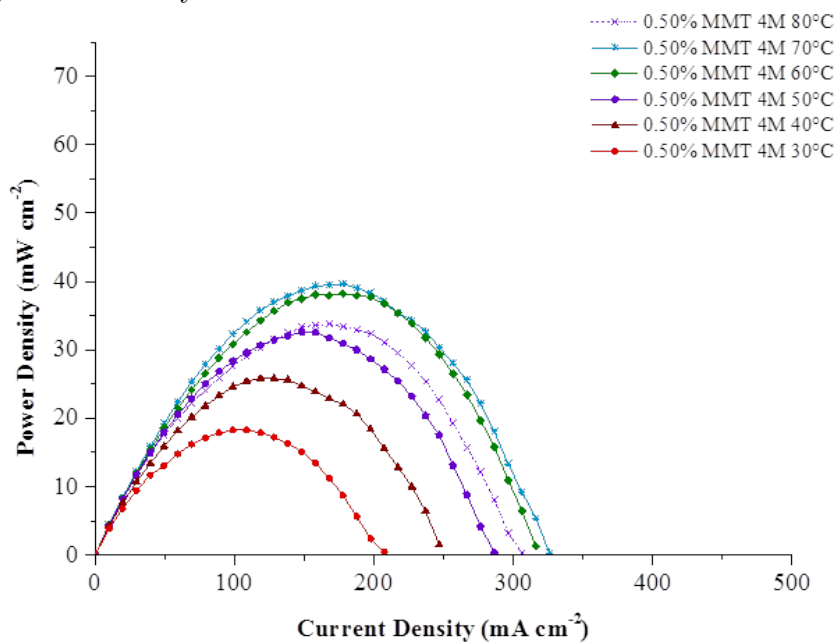


FIGURE A.30: Performance of 0.25% MMT at 4 M methanol

(A) Power density curve



(B) Polarization curve

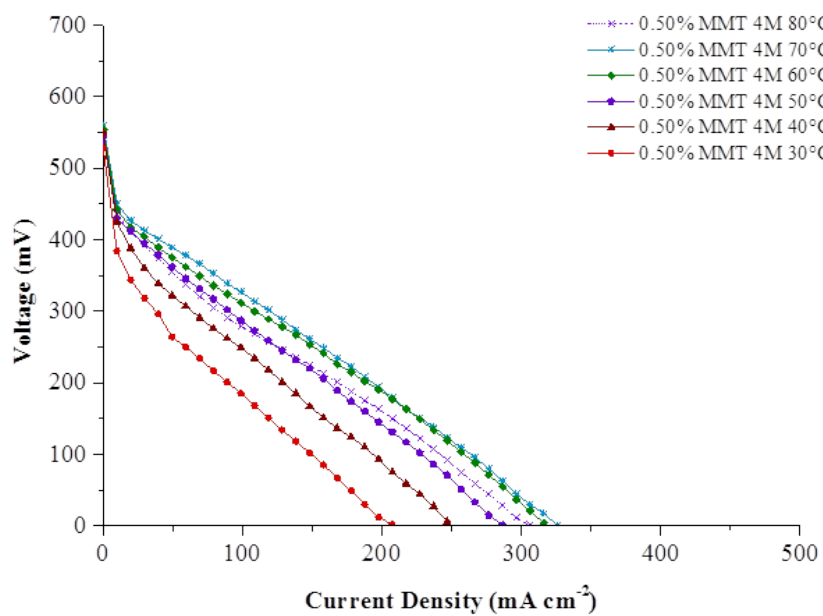
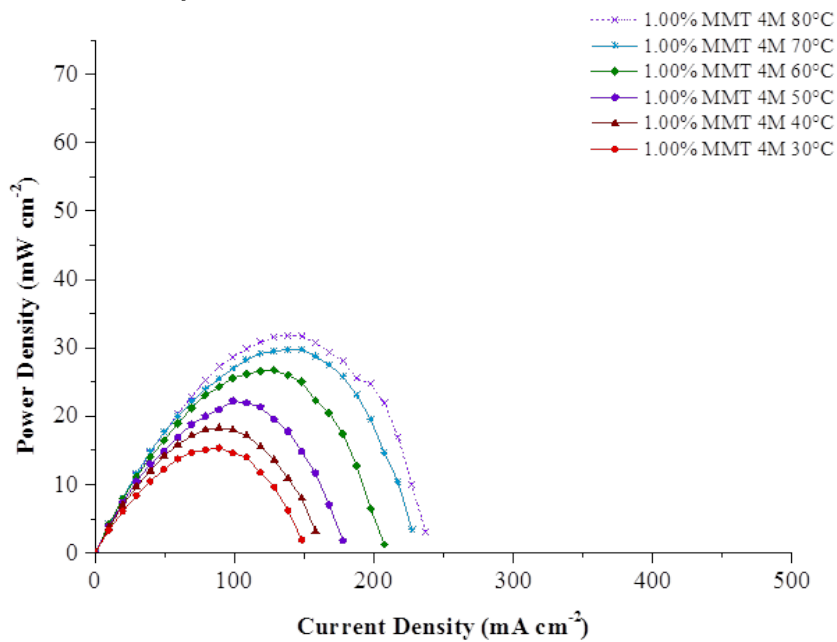


FIGURE A.31: Performance of 0.50% MMT at 4 M methanol

(A) Power density curve



(B) Polarization curve

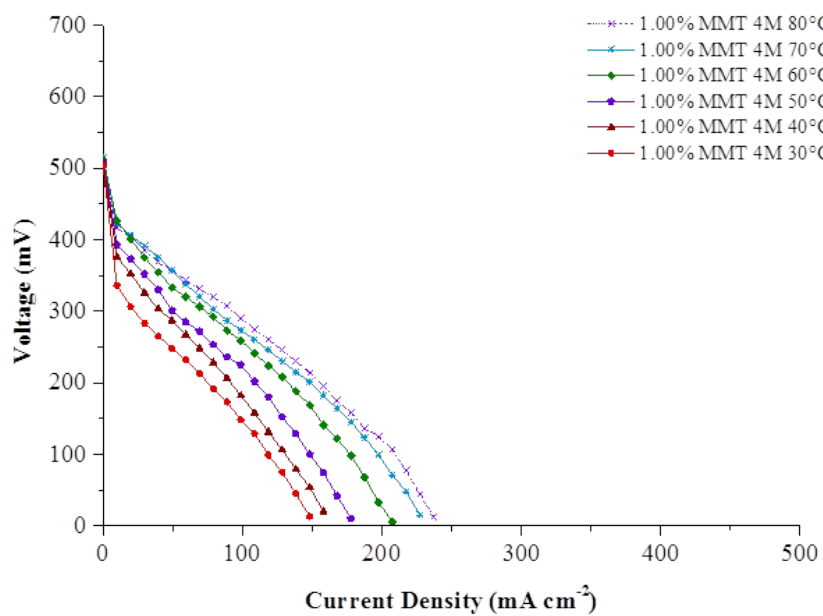


FIGURE A.32: Performance of 1.00% MMT at 4 M methanol

A.3.4 Performances of the new modified membrane electrode assemblies

TABLE A.10: Performances of the modified membrane electrode assemblies containing 0.25% montmorillonite (0.25% MMT)

| Methanol concentration Molar (M) | Temperature °C | Open circuit voltage (mV) | Maximum power density (mW cm ⁻²) | Limiting current density (mA cm ⁻²) |
|--|--------------------------|-------------------------------------|--|---|
| 1 | 30 | 590 | 25.30 | 246.91 |
| | 40 | 600 | 33.41 | 286.42 |
| | 50 | 615 | 43.35 | 316.05 |
| | 60 | 628 | 52.70 | 385.19 |
| | 70 | 628 | 59.32 | 444.44 |
| | 80 | 643 | 64.27 | 454.32 |
| 2 | 30 | 588 | 27.56 | 276.54 |
| | 40 | 613 | 37.69 | 325.93 |
| | 50 | 625 | 46.93 | 365.43 |
| | 60 | 629 | 54.54 | 404.94 |
| | 70 | 632 | 65.33 | 454.32 |
| | 80 | 645 | 69.14 | 454.32 |
| 4 | 30 | 540 | 20.98 | 217.28 |
| | 40 | 553 | 26.41 | 256.79 |
| | 50 | 558 | 30.37 | 276.54 |
| | 60 | 566 | 33.92 | 296.30 |
| | 70 | 576 | 37.45 | 316.05 |
| | 80 | 562 | 39.82 | 325.93 |

TABLE A.11: Performances of the modified membrane electrode assemblies containing 0.50% montmorillonite (0.50% MMT)

| Methanol concentration Molar (M) | Temperature °C | Open circuit voltage (mV) | Maximum power density (mW cm⁻²) | Limiting current density (mA cm⁻²) |
|---|---------------------------|--|---|--|
| 1 | 30 | 548 | 16.53 | 177.78 |
| | 40 | 575 | 26.43 | 227.16 |
| | 50 | 613 | 35.70 | 286.42 |
| | 60 | 630 | 45.60 | 316.05 |
| | 70 | 635 | 50.96 | 345.68 |
| | 80 | 644 | 53.89 | 375.31 |
| 2 | 30 | 569 | 20.27 | 227.16 |
| | 40 | 589 | 32.57 | 306.17 |
| | 50 | 615 | 43.97 | 365.43 |
| | 60 | 624 | 53.16 | 404.94 |
| | 70 | 638 | 61.63 | 434.57 |
| | 80 | 640 | 63.94 | 444.44 |
| 4 | 30 | 528 | 18.27 | 207.41 |
| | 40 | 550 | 25.84 | 246.91 |
| | 50 | 543 | 32.59 | 286.42 |
| | 60 | 554 | 38.22 | 316.05 |
| | 70 | 559 | 39.64 | 325.93 |
| | 80 | 542 | 33.75 | 306.17 |

TABLE A.12: Performances of the modified membrane electrode assemblies containing 1.00% montmorillonite (1.00% MMT)

| Methanol concentration Molar (M) | Temperature °C | Open circuit voltage (mV) | Maximum power density (mW cm⁻²) | Limiting current density (mA cm⁻²) |
|---|---------------------------|--|---|--|
| 1 | 30 | 535 | 17.78 | 138.27 |
| | 40 | 551 | 24.65 | 197.53 |
| | 50 | 575 | 31.66 | 246.91 |
| | 60 | 584 | 40.16 | 286.42 |
| | 70 | 590 | 46.62 | 325.93 |
| | 80 | 603 | 50.17 | 335.80 |
| 2 | 30 | 543 | 21.95 | 177.78 |
| | 40 | 556 | 28.89 | 217.28 |
| | 50 | 588 | 34.61 | 256.79 |
| | 60 | 596 | 41.28 | 306.17 |
| | 70 | 627 | 47.10 | 355.56 |
| | 80 | 634 | 50.48 | 355.56 |
| 4 | 30 | 503 | 15.38 | 148.15 |
| | 40 | 506 | 18.31 | 158.02 |
| | 50 | 509 | 22.22 | 177.78 |
| | 60 | 512 | 26.71 | 207.41 |
| | 70 | 515 | 29.78 | 227.16 |
| | 80 | 508 | 31.80 | 237.04 |

Appendix B

Contact angle measurement

B.1 Contact angle measurement between water droplet and the barrier layers

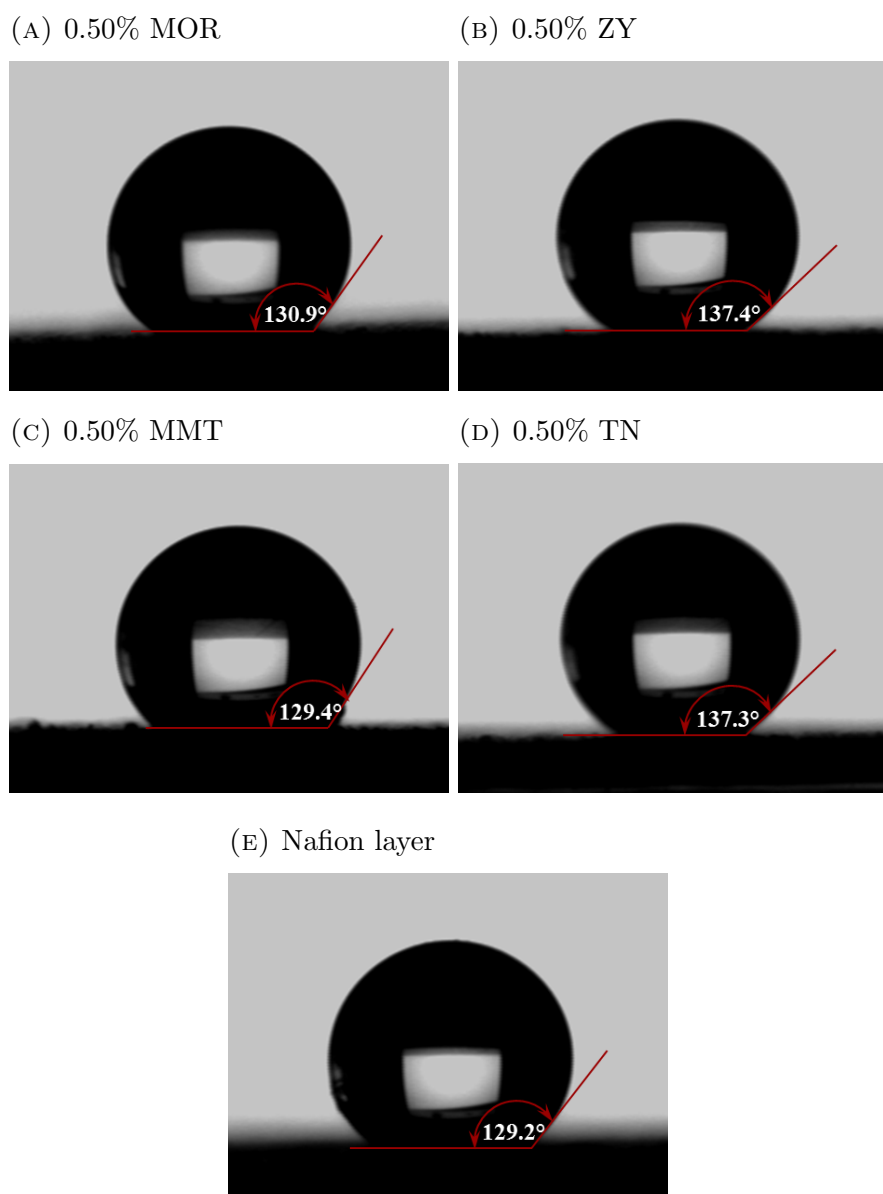


FIGURE B.1: Contact angle measurement between water droplet and the barrier layers containing (A) 0.5% MOR (B) 0.5% ZY (C) 0.5% MMT (D) 0.5% TN (E) Pure Nafion layer (STD)

B.2 Contact angle measurement between 1 M methanol droplet and the barrier layers

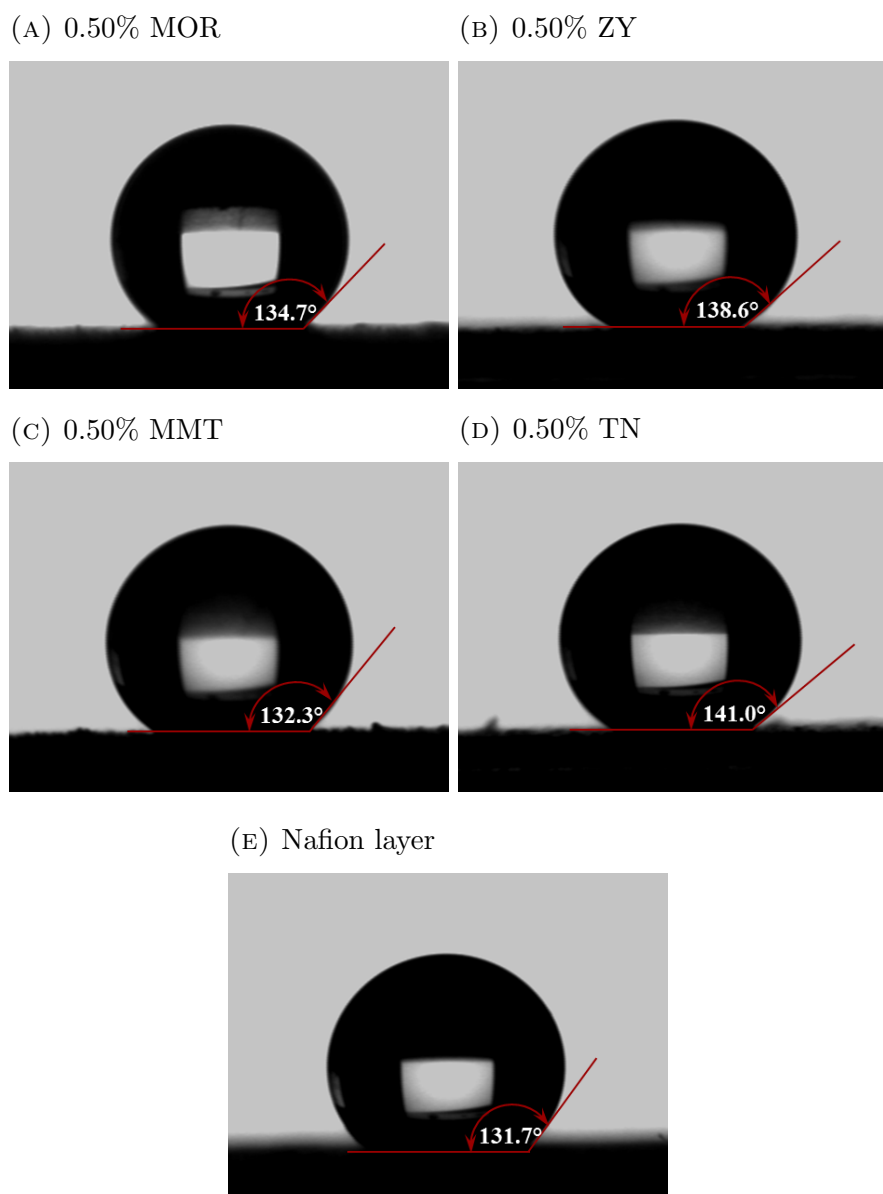


FIGURE B.2: Contact angle measurement between 1 M methanol droplet and the barrier layers containing (A) 0.5% MOR (B) 0.5% ZY (C) 0.5% MMT (D) 0.5% TN (E) Pure Nafion layer (STD)

B.3 Contact angle measurement between 2 M methanol droplet and the barrier layers

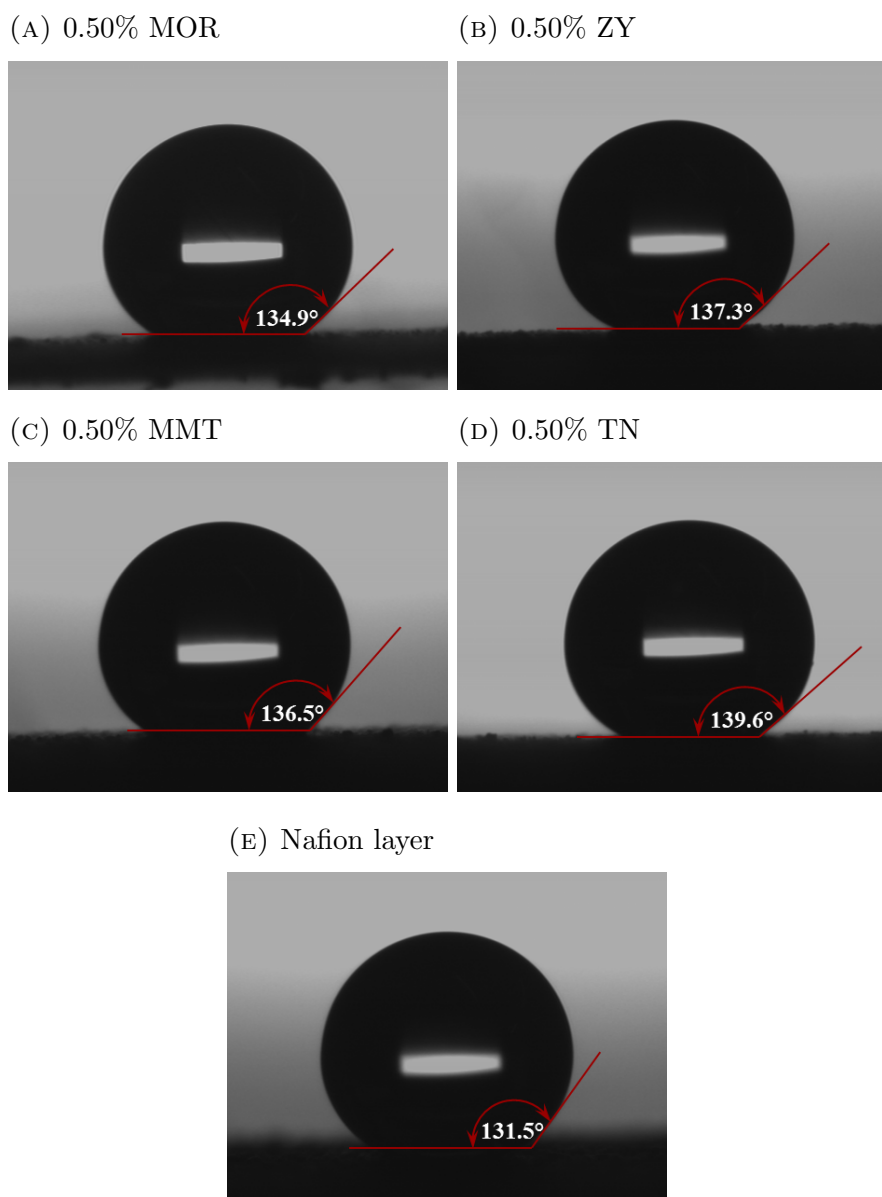


FIGURE B.3: Contact angle measurement between 2 M methanol droplet and the barrier layers containing (A) 0.5% MOR (B) 0.5% ZY (C) 0.5% MMT (D) 0.5% TN (E) Pure Nafion layer (STD)

Appendix C

Presentations

- C. Chailuecha and S. Holmes. The alternative material for direct methanol fuel cell. *Manchester University CEAS Postgraduate Conference*, Manchester, UK, 29 June 2011.
- C. Chailuecha and S. Holmes. Study of new material to improve performance of direct methanol fuel cell technology. *Manchester University CEAS Postgraduate Conference*, Manchester, UK, 15 June 2012.
- C. Chailuecha and S. Holmes. Study of new material to improve performance of direct methanol fuel cell technology. *Manchester University CEAS Postgraduate Conference*, Manchester, UK, 11 June 2013.